QUANTITATIVE ASSESSMENT OF CEREBRAL MICROVASCULATURE USING MACHINE LEARNING AND NETWORK ANALYSIS

A Dissertation

Presented to the Faculty of the Graduate School

of Cornell University

In Partial Fulfillment of the Requirements for the Degree of

Doctor of Philosophy

by

Mohammad Haft Javaherian

May 2019

QUANTITATIVE ASSESSMENT OF CEREBRAL MICROVASCULATURE USING MACHINE LEARNING AND NETWORK ANALYSIS

Mohammad Haft Javaherian, Ph. D.

Cornell University 2019

Vasculature networks are responsible for providing reliable blood perfusion to tissues in health or disease conditions. Volumetric imaging approaches, such as multiphoton microscopy, can generate detailed 3D images of blood vessel networks allowing researchers to investigate different aspects of vascular structures and networks in normal physiology and disease mechanisms. Image processing tasks such as vessel segmentation and centerline extraction impede research progress and have prevented the systematic comparison of 3D vascular architecture across large experimental populations in an objective fashion. The work presented in this dissertation provides complete a fully-automated, open-source, and fast image processing pipeline that is transferable to other research areas and practices with minimal interventions and fine-tuning. As a proof of concept, the applications of the proposed pipeline are presented in the contexts of different biomedical and biological research questions ranging from the stalling capillary phenomenon in Alzheimer's disease to the drought resistance of xylem networks in various tree species and wood types.

BIOGRAPHICAL SKETCH

Mohammad Haft Javaherian traveled around the world along a unique interdisciplinary path to acquire computational mechanics and computer science skills, which are ideal for addressing emerging biomedical problems. He has been eager to build new bridges from artificial intelligence to biomedical science and medicine.

He decided to study civil engineering for his undergraduate program based on his passion for learning about physical laws and their mathematical models that govern high-rise buildings, dams, and bridges, which enable engineers to design those magnificent structures. During his first semester at the University of Tehran, he noticed the possibility of merging his high school computer programming interests with the knowledge of physical laws and mathematical models within the field of computational mechanics. He enhanced his knowledge by taking the system engineering course, which was his first exposure to artificial intelligence.

During his master's program, his main research project was the development of a computer software package that synthesizes virtual microstructure of particle-reinforced composites using generative models that mimics the geometrical and mechanical characteristics of the real fabricated composite material. Subsequently, the synthetic samples were tested using microstructure modeling to estimate the mechanical characteristics of the anticipated material. This synthesized sample generation and testing can potentially replace expensive and time-consuming laboratory fabrication and testing.

He adapted methods from the system engineering course to introduce new empirical and stochastic models using image processing and Markov chain Monte Carlo simulations that translate three-dimensional information of an asphalt mixture to its two-dimensional counterpart.

After his master's program, he realized that these quantitative tools could be used to answer important life science questions, which were more compelling to him. Therefore, he decided to pursue his Ph.D. study in the biomedical engineering field and joined the Schaffer-Nishimura labs. His research interest turned to the microscopic-scale understanding of normal and disease-state physiological processes in different organs and systems such as the central nervous system.

His interdisciplinary education and training are strong foundations that support him in introducing unique approaches to study life science questions in ways not previously possible. His distinctive capability of adopting ideas from many, diverse, research fields to answer a tough life science questions is enhanced with his programming skills and mastery in computational methods in addition to the advanced novel optical techniques developed in our research laboratory. He would like to invest his career in investigating the application of machine learning in biomedical research and medicine in addition to training the next generation of scientists.

ACKNOWLEDGMENTS

It has been an absolute honor and a pleasure working with talented and affable people in the course of my PhD studies at Cornell University. I would like to express my sincere gratitude to my colleagues, friends, and family members for supporting me through this journey.

First, I would like to thank my adviser and co-adviser, Prof. Nozomi Nishimura and Prof. Chris Schaffer. I joined their labs after the tragic loss of my late PhD adviser, Prof. Ephrahim Garcia. Nozomi and Chris flourished my scientific curiosity and eagerness to investigate unknowns with allowing me thinking outside the box and pursuing my passion in other research fields while advising me through the difficulties. I am grateful that they took a chance on me. Beyond the academic settings and on a personal level, their incredible support and kindness made my PhD studies a memorable and pleasant experience that let me forget the difficulties happened prior to joining their labs. I also thanks Prof. Andrew Ruina for his tremendous help and emotional support during that difficult period.

I would also like to thank my committee members. Prof. Mert Sabuncu has been a great resource since I started doing research and applying machine learning and computer vision to biomedical problems. He was receptive in research and helped me to obtain practical experience outside academia. Prof. Joseph Fetcho taught me many tips that allowed me to navigate graduate school very smoothly in the past and academic

career in future, in addition, to being a great resource when I felt lost in the Neuroscience field.

I would like to thank the members of the Schaffer-Nishimura labs. In particular, Dr. Jean Cruz Hernandez and Dr. Oliver Bracko for their experimental work presented in this dissertation in addition to teaching me how to do the surgery myself and how the behavioral test works. Their intellectual support and encouragements were essential. Nancy Uribe Ruiz joined our lab in recently, and I am grateful for the experiments she conducted for brain vasculature networks. I am also grateful to the Master's, undergraduate, and high school students who worked with me extensively and helped me to grow while finishing the research projects together. Linjing Fang helped me with the DeepVess and the Review chapter During her master's program. Victorine Muse helped me with DeepVess and Alzheimer's project measurements. Nash Allan Rahill helped me to investigate the application of DeepVess to the heart vasculature images. Muhammad Ali, Iryna Ivasyk, Lawrence Cheng, Madisen Swallow, Nathaniel Pineda were a great help while trying different prototypes for crowdsourcing and the Alzheimer' project. Saif Azam helped me with the speckle imaging. I wish all of them success in their future endeavors.

Additionally, I thank Yu-Ting Cheng and Dr. David Small for teaching me details of animal surgery and other experimental details as well as Dr. Mike Lamont for inhering my responsibilities and projects in order to move them forward. Many thanks to B56 Weill Hall officemates and close friends who were great moral support during these years. Dr. John Foo for sharing his graduate school experiences, Dr. Jason Jones and Mitch

Pender for helping me to get established when I joined the lab, and Jeffrey Mulligan for being available all the time to discuss scientific and non-scientific matters. Finally, thanks to other Schaffer-Nishimura lab members for their supports: Daniel Rivera, Menansili Mejooli, Dr. Amanda bares, Dr. Poornima Gadamsetty, Dr. Elizabeth Wayne, Silvia Zhang, Dr. Sung Ji Ahn, Dr. Jiahn Choi, Seth Lieberman, Dr. SallyAnne DeNotta, Dr. Chi-Yong Eom, Dr. Kawasi Lett, Dr. Laurie Bizimana, and many other undergraduate students.

I would like to thank our collaborators from Cornell and other institutes around the world. Prof. Sylvie Lorthois (Institut de Mecanique des Fluides de Toulouse in France) was an excellent resource for my work within the Alzheimer's project (allowing me to have experience with human brain vasculature networks), DeepVess, and the fluid simulation of xylem networks. I had a great collaboration with Dr. Amy Smith, Maxime Berg, and Myriam Peyrounette from Sylvie's lab. On the other hand, I had delightful and joyful years of collaboration with Dr. Pietro Michelucci (Human Computation Institute) and his colleagues Ieva Navikiene and Egle Marija Ramanauskaite for the development of StallCatchers. Finally, I would like to thank Annika Huber and Prof. Taryn Bauerle (School of Integrative Plant Science) for their extensive collaboration in the xylem network project.

My gratitude extends to members of my family for their loving support throughout my education. My parents are my long-standing role models and sources of support. Their constant encouragements and continued love were the powerful fuels that allowed me to finish this journey. I owe them a debt of gratitude that can never be repaid. I also thank

my sister for her continued support at a different stage of my life. My gratitude also extends to my wife for her support, friendship, and love. All these years, especially after the birth of our son, she has often been the one holding up the pillars with her love, encouragement, and intellectual depth. Without her support it was not possible to conclude my PhD.

This work was supported by the European Research Council grant 615102 (Nozomi Nishimura), the National Institutes of Health grant AG049952 (Chris Schaffer), the National Institutes of Health grants R01LM012719 and R01AG053949 (Mert Sabuncu), the National Science Foundation Cornell NeuroNex Hub grant (1707312, Mert Sabuncu and Chris Schaffer) and the National Science Foundation (1748377 to Mert Sabuncu).

TABLE OF CONTENTS

LIST OF FIGURES

LIST OF TABLES

LIST OF ABBREVIATIONS

3D-RA	3D Rotational Angiography
BAVM	Brain Arteriovenous Malformation
BB-MRI	Black-Blood Magnetic Resonance Image
CAD	Coronary Artery Disease
CCA	Conventional Catheter Angiography
CT	Computed Tomography
CTA	Computed Tomography Angiography
CTP	Computed Tomography Perfusion
DSA	Digital Subtraction Angiography
EM	Expectation Maximization
FCM	Fuzzy Clustering Methods
ILD	Interstitial Lung Diseases
IPF	Idiopathic Pulmonary Fibrosis
IVUS	Intravascular
MAP	Maximum A Posteriori Probability
Micro-CT	Micro-Computed Tomography
MPM	Multiphoton Microscopy
MRA	Magnetic Resonance Angiographic
MRI	Magnetic Resonance Image
OCT	Optical Coherence Tomography
PC-CT	Phase Contrast Computed Tomography
PC-MRA	Phase Contrast Magnetic Resonance Angiographic
PD-MRI	Proton-Density Magnetic Resonance Image
PSF	Point Spread Function
SNR	Signal-to-Noise Ratio
SRμCT	Synchrotron Radiation-Based Micro-Computed Tomography
SSFP-MRA	Steady-State Free-Precession Magnetic Resonance Angiography
TAVI	Transcatheter Aortic Valve Implantation
TOF-MRA	Time-Of-Flight Magnetic Resonance Angiographic
US	Ultrasound

CHAPTER 1

INTRODUCTION

Current clinical evidence suggests that many cognitive disorders associated with aging, such as dementia and Alzheimer's disease, are correlated with microvascular dysfunction and decreased blood flow (Iadecola, 2004). The underlying mechanisms are unknown and the question of whether vascular dysfunction is a consequence of the disease or one of its causes remains unanswered. Therefore, an understanding of the linkage between Alzheimer's disease and the properties of the brain vascular network is essential (Hirsch, Reichold, Schneider, Székely, & Weber, 2012). However, the methods to systematically and quantitatively describe and compare structures as complex as the brain blood vessels are lacking. This shortage is hampering our ability to analyze the relationship between the structure and function of blood vessels. For instance, we used multiphoton microscopy (Kleinfeld, Mitra, Helmchen, & Denk, 1998; Santisakultarm et al., 2012; Schaffer et al., 2006) to generate three-dimensional images of the brain capillaries in mouse models of Alzheimer's disease and normal mice (Figure 1.1). We developed automated computer vision and machine learning solutions such as DeepVess (Haft-Javaherian et al., 2019) to analyze such images and measure different geometrical and topological metrics within the brain vasculature network. These solutions are now in use in various research labs studying brain, heart, and even in trees. These methods are also used in the data processing backbone for our citizen science crowdsourcing project (*StallCatchers.com*).

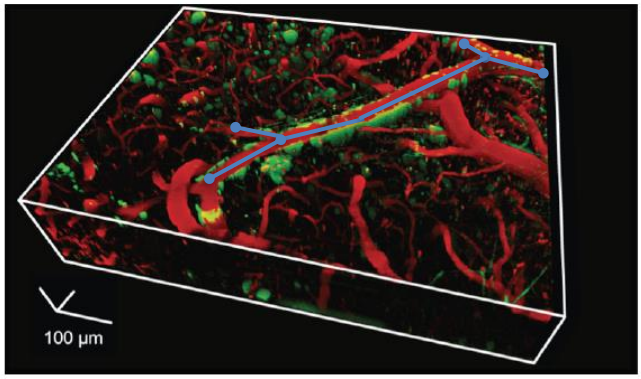

Figure 1.1. Three-dimensional structure of blood vessels in the brain of a mouse model of Alzheimer's disease acquired by in vivo two-photon microscopy. Blood vessels (red), Aβ plaques (green), a sample of the network representation for few vessels (blue).

The work in this dissertation had three main objectives:

Objective 1. Development of a new fully automated open source image processing pipeline to analyze the raw 3D laser microscopy images using computer vision and machine learning.

Objective 2. Development and collection of network metrics to study networks using different topological and geometrical metrics in order to characterize different diseases or survival mechanisms.

Objective 3. Demonstration of the applications of the developed formalism in Objectives 1 and 2 in other research fields such as generation of data using the collaborative crowdsourcing online game project and xylem networks in trees.

Thesis structure

Chapter 2 is a review of the current literature of 3D vessel segmentation and centerline extraction methods. This chapter is the draft of the paper that will be submitted.

Chapter 3 was published in PLoS One and has been reformatted for inclusion in this dissertation. A fully-automated, open source pipeline was developed using the deep convolutional neural networks to segment multiphoton microscopy images and extract the vasculature centerlines. This method generated detailed analysis of the effects of aging and Alzheimer genes on capillary network structure in mouse cortex. I demonstrated the application of this formalism within two different research fields described in Chapter 4, 5 and 6: the study of microvascular dysfunction in Alzheimer's disease and the study of the xylem networks in trees in response to drought and embolism.

Haft-Javaherian, M., Fang, L., Muse, V., Schaffer, C. B., Nishimura, N., & Sabuncu, M. R. (2019). Deep convolutional neural networks for segmenting 3D in vivo multiphoton images of vasculature in Alzheimer disease mouse models. PLOS ONE, 14(3), e0213539. https://doi.org/10.1371/journal.pone.0213539

Chapter 4 was published in Nature Neuroscience and has been reformatted for inclusion in this dissertation. We discovered that leukocyte cells plug about two percent of capillaries in the brains of Alzheimer's disease mouse models. By blocking the leukocyte adhesion, we showed the cerebral blood flow immediately increased, and

cognitive performance rapidly improved. The contribution section reads “MH., G.O. and Y.K. developed custom software for data analysis. M.H. developed custom machine learning algorithms for image segmentation.” I provided novel data analysis and original algorithms which characterized the stalled vessels by several metrics including their topology, relationships to amyloid-beta deposits and morphology.

Cruz Hernández, J. C., Bracko, O., Kersbergen, C. J., Muse, V., Haft-Javaherian, …, Nishimura, N., Schaffer, C. B. (2019). Neutrophil adhesion in brain capillaries reduces cortical blood flow and impairs memory function in Alzheimer’s disease mouse models. Nature Neuroscience, 22(3), 413–420. https://doi.org/10.1038/s41593-018-0329-4

Chapter 5 is on a crowdsourcing citizen science project, i.e., StallCatchers, that utilizes the power of citizen science to perform the task of detecting stalled capillary from images. This time-consuming task is a significant bottleneck for scientific research progress. I developed the image processing pipeline, worked on the validation of the crowd-source analysis, and contributed to generating the first scientific results from this novel method. This chapter is the draft of the paper that will be submitted.

Chapter 6 explores drought resistance of trees with two different wood types and in six species. Similar to blood vessel networks in the brain, tree xylem networks have network structures that contribute to the tree’s resistance to drought and vulnerability to air embolisms that block water flow. In this chapter, we utilized our formalism developed in previous chapters to analyze images of the xylem networks and adapted these methods for extremely large datasets. The 3D xylem images were more than a hundred times larger

than the brain vascular images acquired by multiphoton microscopy. Inspired by methods used to study robustness in brain vascular networks, we also used fluid flow simulations to compare different tree species. This chapter was done in collaboration with Ms. Annika Huber and Prof. Taryn Bauerle at Cornell University in the School of Integrative Plant Science. This is the draft of the paper that will be submitted.

REFERENCES

Cruz Hernández, J. C., Bracko, O., Kersbergen, C. J., Muse, V., Haft-Javaherian, M., Berg, M., … Schaffer, C. B. (2019). Neutrophil adhesion in brain capillaries reduces cortical blood flow and impairs memory function in Alzheimer's disease mouse models. *Nature Neuroscience*, *22*(3), 413–420. https://doi.org/10.1038/s41593-018-0329-4

Haft-Javaherian, M., Fang, L., Muse, V., Schaffer, C. B., Nishimura, N., & Sabuncu, M. R. (2019). Deep convolutional neural networks for segmenting 3D in vivo multiphoton images of vasculature in Alzheimer disease mouse models. *PLOS ONE*, *14*(3), e0213539. https://doi.org/10.1371/journal.pone.0213539

Hirsch, S., Reichold, J., Schneider, M., Székely, G., & Weber, B. (2012). Topology and hemodynamics of the cortical cerebrovascular system. *Journal of Cerebral Blood Flow & Metabolism*, *32*(6), 952–967.

Iadecola, C. (2004). Neurovascular regulation in the normal brain and in Alzheimer's disease. *Nature Reviews Neuroscience*, *5*(5), 347–360. https://doi.org/10.1038/nrn1387

Kleinfeld, D., Mitra, P. P., Helmchen, F., & Denk, W. (1998). Fluctuations and stimulus-induced changes in blood flow observed in individual capillaries in layers 2 through 4 of rat neocortex. *Proceedings of the National Academy of Sciences*, *95*(26), 15741–15746.

Santisakultarm, T. P., Cornelius, N. R., Nishimura, N., Schafer, A. I., Silver, R. T., Doerschuk, P. C., … Schaffer, C. B. (2012). In vivo two-photon excited fluorescence microscopy reveals cardiac- and respiration-dependent pulsatile blood flow in cortical blood vessels in mice. American Journal of Physiology - Heart and Circulatory Physiology, 302(7), H1367–H1377. https://doi.org/10.1152/ajpheart.00417.2011

Schaffer, C. B., Friedman, B., Nishimura, N., Schroeder, L. F., Tsai, P. S., Ebner, F. F., … Kleinfeld, D. (2006). Two-Photon Imaging of Cortical Surface Microvessels

Reveals a Robust Redistribution in Blood Flow after Vascular Occlusion. *PLoS Biol*, *4*(2), e22. https://doi.org/10.1371/journal.pbio.0040022

CHAPTER 2

A REVIEW OF THREE-DIMENSIONAL VESSEL SEGMENTATION METHODS

2.1 Introduction

The circulatory system provides oxygen and nutrients to the entire body and collects the metabolic waste from cells through the vasculature network. Many medical diagnoses and treatments depend heavily on different circulatory system examinations. Likewise, many biomedical researchers are investigating different aspects of this system. Imaging is one of the main methodological approaches used commonly in various biomedical laboratories and medical settings. Extracting the substantial amount of information embedded in cardiovascular images often costs an excessive amount of valuable time of experts who analyze the images before it can be delivered in useful formats to the downstream users ranging from physician and scientists to patients and general public. Image segmentation is an essential image processing task, which is an indispensable part of image analysis pipelines. The primary goal is to locate and label pixels or voxels with different labels, deterministically or stochastically. From a machine learning and data science point of view, this task can be done using supervised on unsupervised approaches. Mainly, the vessel segmentation task is an essential tool for the diagnosis, treatment, surgery planning, prognosis, and biomedical research.

To address the complexity and entanglement of multiple factors within medical and biomedical image analysis, we focus on three different aspects of the 3D vessel

segmentation task. First, we focus on high-level image preprocessing (section 2) and image segmentation methods (section 3) with an emphasis on vasculature images. Second, we discuss organ- and tissue-based vessel segmentations into either vascular networks (section 4) or short segments (section 5). Third, we discussed different pathological vessel segmentation tasks (section 6). To best of our knowledge, currently, Kirbas and Quek (Kirbas & Quek, 2004) and Lesage (Lesage, Angelini, Bloch, & Funka-Lea, 2009) are the most general and extensive vascular segmentation reviews. Therefore, we focused our review mostly on research papers published since 2008.

2.2 Image preprocessing

Preprocessing methods, as low-level pixel intensity operators and logic, filter the unrelated information and enhance targeted image features before the application of main image processing methods. Consequently, they reduce the information entropy to facilitate the main image processing task. These methods may use prior information about acquisition systems or estimate them based on the input image.

For example, pixel-wise intensity transformation can be designed using prior information from neighboring pixels' intensity statistics, the whole image intensity statistics, or the imaging modality used to acquire the input image. Constant thresholding uses no prior information, adaptive thresholding uses neighboring pixels, and the histogram equalizer uses either the whole image data or subset of neighboring pixels. For instance, the log-based intensity transform uses the prior information based on the imaging modality and the segmentation task in order to enhance large vessels and supress other structures in CTA or MRA (Freiman et al., 2009; Samet & Yildirim, 2016).

Prior knowledge of the imaged organs or tissues is a critical requirement for developing effective segmentation methods. The organ-based segmentation and the prior knowledge of the organ's adjacencies produce a target mask that reduces the amount of falsely detected objects and the computational time (Chi et al., 2011). For instance, the skull-stripping algorithm facilitates cerebral tissues isolation (Forkert et al., 2009).

2.2.1 Smoothing and sharpening

Depending on the nature of the images and the main image processing task in hand, different preprocessing techniques ranging from smoothing or sharpening to texture measurements are common fundamental image preprocessing tasks used to prepare the images for the future image procedures. The application of smoothing based on the intensities of neighboring pixels reduces the salt-and-pepper noise and application of methods such as Canny edge detection (Canny, 1987) or wavelet edge highlighting (Korfiatis, Skiadopoulos, Sakellaropoulos, Kalogeropoulou, & Costaridou, 2007) sharpen the image and facilitate edge detections.

The nonlinear smoothing techniques such as Gaussian filtering, Edge Enhancing Diffusion, or Regularized Perona-Malik diffusion (Weickert, 2001) improve the segmentation accuracy with application in CTA and 3D RA images (Firouzian et al., 2011; Meijering, Niessen, Weickert, & Viergever, 2002). On the other hand, bi-Gaussian functions with independent foreground and background scales apply an intra-region smoothing based on the reduced adjacent objects interference (Xiao, Staring, Wang, Shamonin, & Stoel, 2013).

The mathematical morphological filters applya logical operation to the image using a structural element based on the set theory and logical operations. For example, the hit-and-miss filter matches circular shapes along the perpendicular axis or stick shapes along the other axes and leads to segmentation quality improvements (Kim, 2013). Similarly, the morphological top-hat filter reduces the background by subtracting the image from the morphological opening filter application on the image (Jin, Yang, Zhang, & Ding, 2013).

In some cases, the combination of a few preprocessing tasks in addition to one postprocessing algorithm results in a complete segmentation method. Läthén et al. (Läthén, Jonasson, & Borga, 2010) combined line and edge detection using multi-scale quadrature filters to detect distinct objects with lower intensity variation sensitivity. Furthermore, they improved the vessel boundary precision using a min-cut/max-flow algorithm (Marvasti & Acar, 2013)

2.2.2 Image artifact removal

Different imaging techniques may suffer from various artifacts with known or unknown causes. The microscopy image artifacts due to the point spread function (PSF) shape and size causes blurring which can be reduced by deconvolution with the PSF. If there are no independent measures of the PSF, it can be estimated using different reverse-engineering algorithms such as the Richardson-Lucy method and then used in deconvolving the image (Seidel, Edelmann, & Sachse, 2016). The multi-slab acquisition of time-of-flight (TOF) magnetic resonance angiography (MRA) contain inter- and intra-slab boundary intensity variations caused by slab boundary artifacts and poor field

uniformity from the radio frequency coil, respectively. Histogram matching compensates the inter-slice intensity variation artifacts (Kholmovski, Alexander, & Parker, 2002), and the nonparametric methods such as N3 algorithm resolve the intra-slice intensity variation artifacts (Sled, Zijdenbos, & Evans, 1998).

Image intensities in modalities such as PC-MRA fluctuate within the vessel regions due to the blood flow velocity variation and different vessels size, which consequently alter intensity gradients along the vessel centerlines and impair the gradient-based segmentation methods. However, the dramatic signal loss in PC-MRA due to the turbulent blood flows leads is partially recoverable using multiscale filters and local variance (Law & Chung, 2013).

The 3D cerebral CTP scans at multiple time points are affected by severe motion artifacts and the registration of 3D scans over time is the most crucial step in their segmentation and other image analysis. After the motion artifact removal, segmentation can be done simply using thresholding and image analyses such as arteries vs. veins classification (arteriograms and venograms) can be done based on the time to peak measurement of contrast enhancement curves (Mendrik et al., 2010).

Aylward et al. (Aylward, Jomier, Weeks, & Bullitt, 2003) repurposed a similar registration strategy, which is a preprocessing solution for the motion artifact, for vessel segmentation and centerline extraction techniques with less sensitivity to image noise and without assumptions about the local shapes of vessels. They registered the designed vessel templates with the image using both rigid and non-rigid registration methods to segment the vessels and extract the centerlines.

2.2.3 Vesselness measurements

The vesselness filters measure local image texture and orientation to locate vessel-like objects. The Hessian-based vesselness enhancement filters are based on simplified cylindrical tube models and generate low values at bifurcations and boundaries. The strain energy filters based on strain energy density theory from solid mechanics improves the responses at those locations as well (Zhai, Staring, & Stoel, 2016).

Vesselness filters can be defined in the spherical polar coordinate system instead of the Cartesian coordinate system to relax the simplified cylindrical tube model assumption, which resolves the errors at the bifurcations and boundaries (Qian et al., 2007). Similar to the Hessian-based filter, Gabor filtering can be applied in a multiscale fashion to study the image textures based on high-frequency local directionality (Shoujun, Jian, Yongtian, & Wufan, 2010).

The combination of lineness measures and line-direction vectors reduces the partial volume effect in the analysis of small vessels in Hessian-based methods, which happens if an small object smaller than the image resolution is surrounded with low intensity objects and not detectable (Nimura, Kitasaka, & Mori, 2010). The computational cost associated with the Hessian-based multi-scale vesselness measures can be reduced by estimation of each Hessian matrix components using the fractional order differential operators (Gong et al., 2016).

There are multi-scale filters such as the Frangi filter, which measures the vesselness of the image at each voxel at different scales. The multi-scale line filters

applied at different orientations enhance cylindrical structures of vessels and improve their segmentation and visualization (Sato et al., 1997). Similar to the Hessian-based local measurement, the combination of the inward gradient flux through circular cross-sections and non-linear penalizations of asymmetric flux contributions can reduce the false positive rate (Lesage, Angelini, Bloch, & Funka-Lea, 2009). Likewise, filters based on the medial-axis points, which pass a line through each point of the image intersecting the edges of different tubes measuring the distance differences to the nearest edges to facilitate the segmentation (Foruzan, Zoroofi, Sato, & Hori, 2012) with the option of resolving the asymmetric cross-sections artifacts using the isotropic coefficient (Pock, Thomas G, 2004).

2.2.4 Frequency domain

Note that some preprocessing methods are in the frequency domain due to the nature of acquisition systems or image artifacts (Sonka, Hlavac, & Boyle, 2014). For instance, the segmentation task for OCT images are either in the frequency (e.g., using low-pass and high-pass filters) or the space domains. In the case of 1D segmentation in the space domain, only the A-lines that captures the vessels are required to be analyzed based on intensity criteria starting from the shallowest pixel. This intensity-based preprocessing requires 2D or 3D smoothing in order to obtain segmentation continuity (Ughi et al., 2012).

2.3 Vascular segmentation methods

In this section, we discuss the segmentation methods in the context of the vessel segmentation task. The selection of segmentation methods for each task depends on the imaged organ, imaging modality, method availability, and the state-of-the-art methods for the particular task in hand.

2.3.1 Region-based segmentation

The main idea of the region-based segmentation methods is to divide the image into regions that have the maximum homogeneity. The binary homogeneity function is defined based on different characteristics of each voxel or super voxel such as intensity, saliency, direction, and connectivity (Chi et al., 2011). For example, metrics such as gradient vector flow field have high magnitudes at vessel boundaries and in directions toward vessel centerlines (Chen, Sun, & Ong, 2014; Smistad, Elster, & Lindseth, 2014). The regions should satisfy the following two criteria: homogeneity value of each region should be true, and the homogeneity value of the union of each two adjacent regions should be false (Sonka et al., 2014). The homogeneity criteria can have its internal voxel-based inclusion criteria based on neighborhood homogeneity as well. In this scenario, only voxels located in neighborhoods with homogeneity higher than the minimum inclusion criteria are contributing to the homogeneity term of the cost function (Ogiela & Hachaj, 2013). The growing process at different locations within the image can be done simultaneously or can be done vessel branch by vessel branch sequentially (Eiho, Sekiguchi, Sugimoto, Hanakawa, & Urayama, 2004). This method requires initial seed

points provided by experts or obtained from another method such as centerline extraction (Smistad et al., 2014).

The variational region growing approaches utilize the intensity and vesselness terms simultaneously to enforce the target intensity ranges and detect tubular shapes by minimizing the region-descriptor energy function. The variational region growing methods are similar to FCM (see next subsection). The initial seeds required for the variational region growing approaches can be obtained using Hessian-based methods (Lo et al., 2012; Pacureanu, Revol-Muller, Rose, Ruiz, & Peyrin, 2010; Rose, Rose, Revol-Muller, Charpigny, & Odet, 2009). The region growing algorithms combined with noise models can segment the 3D images of vessel laminae, which is the boundary between the lumen and the rest of the tissue, instead of vessel luminal volume by utilizing the detected high-confidence foreground voxels and then converting the detected foreground laminae voxels into 3D isosurface meshes using the marching tetrahedra algorithm (Narayanaswamy et al., 2010).

Researchers resolved some of the known shortcomings of these methods using different techniques. The combination of slice marching and region growing algorithms reduces the leakage and other false positive errors (Zhang, He, Dehmeshki, & Qanadli, 2010). Friman et al. (Friman, Hindennach, & Peitgen, 2008) utilized a vessel template function based on radiuses, directions, and center points to improve the missing vessel end segmentations at low SNR regions after the application of region growing methods.

Note that the inclusion criteria based on the formulated homogeneity function in region-based methods are interchangeable with ensemble models such as the random

forest (Schwier, Hahn, Dahmen, & Dirsch, 2016). Fabijańska et al. (Fabijańska, 2012) used the random walk within consecutive CT slices, slice-by-slice in addition to considering images acquired from other acquisition series.

2.3.2 Fuzzy clustering methods

The segmentation FCM defines the relationship between different regions in the image using fuzzy logic rules in order to include the uncertainties due to the image variations and noise. For example, this statement is a fuzzy rule:

> *"if two sub-regions have similar pixel intensities and if they are comparatively in close distance, there is a higher likelihood that these two sub-regions belong to one region."*

Therefore, the relationships between different sub-regions are considered for all the possible pairs of sub-regions, which make this method very similar to the behavior of a human observer. Hessian-based filtering and spatially-variant mathematical morphology with low computation cost can enhance the fuzzy logic segmentation results (Dufour et al., 2013). Similarly, the addition of line direction vectors of all voxels to the vesselness information improves the FCM results (Wang, Xiong, Huang, Zhou, & Venkatesh, 2012). The second order statistics of image voxels such as angular second moment, contrast correlation, variance, and different inverse moment can be derived using Gray level co-occurrence matrices at different directions and distances that are suitable for the FCM feature extractions (Kumar & Jeyanthi, 2012). A computational cost reduction by a factor of two is achievable by adopting look-up table strategies (Guo,

Huang, Fu, Wang, & Huang, 2015). Guo et al. (Guo et al., 2015) used watershed methods to define the threshold for FCM binarization. The detection of crossing or bifurcation simultaneously with FCM using the structural pattern detection algorithms reduces the merging error (Shoujun et al., 2010).

The expectation maximization (EM) method is the probabilistic counterpart of FCM that changes the segmentation problem into a missing data problem (Zhou et al., 2007). EM defines class prior probabilities and probability density functions to determine class associations. Given an image, EM solves an inverse problem to estimate the parameters of density functions. In the expectation step, EM computes the expected associate probabilities, and in the maximization step, EM estimates the parameters of density functions using likelihood maximization. EM iterates between these two steps until convergence. After convergence, the segmentation results can be acquired using MAP. Analogous to FCM and EM, since the segmentation problems are interchangeable with classification problems for each voxel or group of voxels between background and one or multiple foreground classes, Zheng et al. (Zheng et al., 2011) extracted a set of geometric and image features and used probabilistic boosting tree (Tu, 2005).

2.3.3 Active contour models - Snakes

Kass and colleagues initially introduced the active contour models or snakes for image processing in the 1980s (Kass, Witkin, & Terzopoulos, 1988; Terzopoulos, Witkin, & Kass, 1988; Witkin, Terzopoulos, & Kass, 1987). These models are defined in terms of energy minimizing splines, which depend on the shape and the location of the spline within the target image and tries to match a deformable model to that image. The prior

knowledge about the underlying structure of the image will be incorporated to find the optimal solution. The 3D branching structures can be modeled using high order active contours to define multiscale shapes and interactions between boundaries and from 3D branches (Vazquez-Reina, Miller, Frisken, & Malek, 2008). Freiman et al. (Freiman, Joskowicz, & Sosna, 2009) proposed an energy term based on the vessel surface property to improve the segmentation results at the bifurcations and complex vascular structures. Note that because the introduced evolution is a local process, it is possible to fall into local minimum that result in errors (Reinbacher, Pock, Bauer, & Bischof, 2010).

On the other hand, Terzopoulos and Vasilescu (Terzopoulos & Vasilescu, 1991; Vasilescu & Terzopoulos, 1992) developed a shape reconstruction algorithm based on a deformable mesh using parameter fitting, which was later further improved by including an attractive force derived from the 3D image. Since mesh initialization is critical for precise segmentation, Huang and Goldgof (Huang & Goldgof, 1993) introduced a tracking method for nonrigid structures by dynamically adding or subtracting mesh nodes and correspondingly Delingette et al. (Delingette, Hebert, & Ikeuchi, 1992) developed a dynamic model with both internal smoothness energy and forces derived from input information. Cohen et al. (Cohen & Cohen, 1993) used balloon models to overcome image noise as well as assist with better convergence. The inflating balloon models decrease the computational cost by constructing surfaces from multi-scale images (Chen & Medioni, 1995).

The intensity gradients within a local sphere region, called orientated flux, can be symmetric or antisymmetric and are indicators of regions located at the centers or

boundaries of vessels, respectively. The active counter method evolves using the oriented flux measured for a set of radii unaffected by intensity fluctuation along the vessel centerlines (Law & Chung, 2008). The oriented flux is measured in the Fourier domain in order to decrease computation time (Law & Chung, 2010). Likewise, the reformulation of spherical flux based on divergence theorem, spherical step function, and the convolution operation can be done in the Fourier domain (Law & Chung, 2009b). Since the enforced antipodal-symmetry of the sphere is not appropriate for modeling the bifurcations, cylindrical flux-based higher order tensors can be utilized to detect vasculature and branching together (Cetin & Unal, 2015).

2.3.4 Geometric deformable models - Level set

Parametric methods are the basis of the active counter models (snakes), and partial differential equations are the basis of the geometric deformable models (a.k.a. Level Set (Malladi, Sethian, & Vemuri, 1995)). The main difference is that the optimized geometric curves are non-parametric. The foreground and background are considered as fluid and solid phases, respectively. Based on continuum mechanics, the three forces applied on solid surfaces are the fluid pressure on the solid surfaces, the internal stresses in solid surfaces to maintain the solid integrity, and the external bulk stresses on the surfaces of solids. The fluid pressure deforms the surface along the centerline, the bulk force deforms the surface along the cross-section, and the surface forces control the rate of deformation changes along the surface. These forces can be defined using the second order intensity statistics, and the surface geometry and the surfaces can be modeled using level set functions.

On the other hand, to account for the vessel size variability, the second order intensity statistics of images can be smoothed using Gaussian filters with multiple scale kernels (Law & Chung, 2009a). The small vessels also can be captured using the minimal curvature criteria (Lorigo et al., 2001). Similarly, the MAP of the intensity distribution estimated as a finite mixture of statistical model distributions can be combined with the intensity gradient to perform a fast level set segmentation (Gao et al., 2011).

Caselles et al. (Caselles, Kimmel, & Sapiro, 1997) proposed *Geodesic Active Contours* to avoid trapping in the local minimum, which one can reformulate within the level set framework. The energy function includes an edge detection function with a common choice of exponential functions, which integrates the curve length and image boundaries. Boykov and Kolmogorov (Boykov & Kolmogorov, 2003) combined a similar energy function and minimized it using the graph cut method. In contrast to the active counter models, this contour topology is changeable throughout its evolution. However, there is still a low possibility to be trapped in a local minimum using these energy functions.

Since the image intensity term of the level-set energy function causes higher vessel segmentation errors within small vessels to compare to the larger vessel, its relaxation improves the small vessel segmentation results (Ugurlu, Demirci, Navab, & Celebi, 2011). Similarly, Zhu et al. (Zhu, Xiong, & Jiang, 2012) proposed to add a vessel energy term to facilitate the distinction between tubular objects vs. spherical objects. Alternatively, Ebrahimdoost et al. (Ebrahimdoost et al., 2011) proposed energy-based stopping criteria for the vessel boundary evolution. Similarly, a vesselness-based

regularization can be added to the curvature term of the energy function to expedite the evolution while maintaining the smoothness (Zhu, Xue, Gao, Zhu, & Wong, 2009).

Bresson (Bresson, 2005) and Reinbacher et al. (Reinbacher et al., 2010) introduced the anisotropic weighted total variation energy with a global volumetric constraint and assumed a continuous image domain instead of the formerly discrete domain, which results in a convex energy function. The convex energy functions can be globally optimized independently of the initial solution (Biesdorf, Wörz, Tengg-Kobligk, Rohr, & Schnörr, 2015). Moreover, Unger et al. (Unger, Pock, Trobin, Cremers, & Bischof, 2008) added an energy term based on the user-provided potential function with regularizations to allow the user input incorporation throughout the segmentation process. The second-order directional intensity tensors measured using the diffusion tensor image modeling and tractography can be fed into the geodesic active contour energy function based on the surface term in the Sobolev Space (Mohan, Sundaramoorthi, & Tannenbaum, 2010) or fiber tracking tractography method (Cetin, Demir, Yezzi, Degertekin, & Unal, 2013).

Segmentation methods based on the level-set and curve evolutions (Lorigo et al., 2001) produce vessel wall leakages or under-segmentation in images acquired using different modalities (e.g., intracranial TOF-MRA and cardiac CTA) due to the presence of tissues with vessel-like intensity in the proximity of vessels (Law & Chung, 2009a, 2010). An external constraint term based on the standard deviation of the Gaussian filter was used in Level Set to reduce the segmentation leakages of nonvascular structures (Jin et al., 2013). Because the boundary and initial conditions have strong effects on the

accuracy, initialization methods such as colliding fronts (Piccinelli, Veneziani, Steinman, Remuzzi, & Antiga, 2009) and cube search (Gong et al., 2014) improve the final results. Instead of the devised gradient-based forces used for the level set method, the local phase information filtered by multiscale quadrature can be used alternatively to detect the edges and segment vessels of different diameter with less computational cost (Lathen, Jonasson, & Borga, 2008).

2.3.5 Probabilistic graphical models

The graphical models typically consist of directed or undirected graphs with a set of nodes and edges, in which nodes represent the image voxels classified with a particular label and the edges represent the connection between nodes based on a set of neighborhood criteria. Subsequently, the common graph algorithms such as minimum spanning tree, shortest path, or graph-cuts can be adopted to solve the graph-based segmentation problem.

FCM (Chen, 2012) or quick shift clustering (Chen et al., 2014) can be adapted to obtain the initial segmentation, which is then represented based on the 6-connectivity (when the connected voxels have a shared face) or 26-connectivity (when the connected voxels have a shared face, edge, or corner). Then, graph analysis methods such as graph-cuts coupled with an energy function based on the intensity and boundary penalty terms improve the segmentation result.

Note that the surface smoothness constraint in the graph-cut energy functions (Homann, Vesom, & Noble, 2008) may lead to the elimination of small or detailed

vessels, which can be resolved using submodular constraints (Kitrungrotsakul, Han, Iwamoto, & Chen, 2017). Local graph-cut methods based on regional intensity distributions can be applied iteratively until the minimal change of global results (B. Chen et al., 2014). The sparse graph representation based on elimination of voxels with a very high probability of being the background reduces the memory and computation requirements (Zhai et al., 2016).

2.3.6 Artificial Deep Neural Networks

The artificial neural network (ANN) and specifically deep neural network (DNN) are the most current popular segmentation methods, after the remarkable success of AlexNet in the ImageNet challenge in 2012 (Krizhevsky, Sutskever, & Hinton, 2012), which was the third reincarnation of ANN within the active area of research. ANN can be used for solving any problem that can be reformulated as a classification problem by modeling a black box classifier as a stack of Rosenblatt's Perceptrons (Rosenblatt, 1958) with input nodes, output nodes and hidden nodes in between, which mimics the human neural networks.

Feature extractions for ANN or other clustering and classification methods can be done automatically using an extra set of initial ANN layers or manually. A set of features can be manually engineered through utilizing the preprocessing methods such as Sato or Frangi filters to enhance structures, the offset medialness filter to enhance topologies, and strain energy filter to enhance bifurcations (Zeng et al., 2016). Similarly, k-means methods are suitable for learning filter banks used for feature extraction.

In contrast to traditional ANN, DNN has a much greater number of layers between input and output layers in comparison to the simple three-layer ANN. There are four different common types of DNN: stacked auto-encoders (SAE), deep belief networks (DBN), recurrent neural network (RNN), and convolutional neural network (CNN). Currently, CNN is the most common method among these DNN for biomedical image analysis (Litjens et al., 2017). The first successful CNN work was presented by Lecun et al. (LeCun, Bottou, Bengio, & Haffner, 1998) in 1998 called LeNet-5 used for a digit recognition task in handwritten zip code on mail envelopes.

Merkow et al. (Merkow, Marsden, Kriegman, & Tu, 2016) compared different fully convolutional neural network models for 3D vessel boundary segmentation task. Based on their results, the complete 3D U-Net architecture (i.e., encoding and decoding layers with skip connections) outperforms both 2D and 3D fully convolutional encoder architected adopted from a holistically-nested edge detection model (Xie & Tu, 2015), which produced one of the top accuracy results on the BSDS500 dataset (Martin, Fowlkes, & Malik, 2004). Conversely, Haft-Javaherian et al. (Haft-Javaherian et al., 2019) showed the optimized patch-based CNN architecture with a customized cost function segmentation outperforms 3D U-Net architecture.

Instead of 3D DNN networks, Kitrungrotsakul et al. (Kitrungrotsakul, Han, Iwamoto, Foruzan, et al., 2017) uses three independent 2D sub-networks to process sagittal, coronal, and transversal planes separately. The features extracted from these three independent sub-networks are aggregated at the last layer of the network to produce 3D segmentation of the hepatic vessel in CT images, surpassing 3D CNN performance.

For a survey on deep learning in medical image analysis see the review by Litjens et al. (Litjens et al., 2017).

2.3.7 Centerline extraction Methods

Many medical and biomedical tasks rely on a graph representation of the vasculature network called vessel centerlines. The centerline can be extracted as the primary task based on the raw image or can be a done as a secondary task by skeletonization of the segmentation results. Although centerlines sometimes obtained as a byproduct of segmentation, they can be also used as an initial seed for the segmentation (Gülsün & Tek, 2010; Smistad et al., 2014). The skeletonization methods for the centerline extraction do not perform well in the cases with irregularities and holes in the vessels segmentation results, while the methods without a segmentation step, such as parallel centerline extraction and ridge traversal, do not struggle in those cases (Smistad et al., 2014).

The semi-automated centerline extraction methods often start with a seed point defined by the user and then alternate between prediction and estimation steps to fit a model such as a cylinder to the data (Friman, Hindennach, Kühnel, & Peitgen, 2010; Kerrien et al., 2017; Yureidini, Kerrien, & Cotin, 2012) or solve an optimization problem using a cost function based on the centerline path (Hachaj & Ogiela, 2012; Longair, Baker, & Armstrong, 2011; Türetken, Benmansour, & Fua, 2012). Instead of searching for the optimal path between two centerline seed points based on the 3D trajectory curves of tubular structures, the 3D multi-branch tubular surfaces starting from one seed point

can be identified using 4D curve representation of the structure surfaces based on the 3D sphere representation of points within the tubular structure (Li, Yezzi, & Cohen, 2009).

The crucial requirement for the centerline extraction of large 3D datasets is the ability of local centerline extraction while preserving the global vasculature network continuity (Cassot, Lauwers, Fouard, Prohaska, & Lauwers-Cances, 2006). The segmentation results have different artifacts such as non-smooth boundaries, holes, side-branch discontinuity, or side-branch inclusion. Techniques such as segmentation surface postprocessing (Wala et al., 2011) and robust kernel regression (Schaap et al., 2009) reduce these artifacts. The centerline extraction based on the segmented 3D images of vessel laminae can be done using ray casting and vote accumulation (Narayanaswamy et al., 2010) or cylindrical ellipsoids (Tyrrell et al., 2007). The orientation-based thinning algorithms can be applied in parallel iteratively using different templates until no change is observed (Hu & Cheng, 2015). The segmentation and centerline extraction computation time can be reduced dramatically by utilizing the graphics processing unit (GPU) instead of the central processing unit (CPU) (Bauer, Bischof, & Beichel, 2009; Bauer, Pock, Bischof, & Beichel, 2009; Erdt, Raspe, & Suehling, 2008; Helmberger et al., 2013; Narayanaswamy et al., 2010; Smistad et al., 2014).

The centerline errors such as center points ordering errors and filling inter- and intra-vessel gaps can be resolved using different graph-based techniques such as the shortest path search algorithms (Fetita, Brillet, & Prêteux, 2009; Helmberger et al., 2013) and minimum spanning tree (Kitamura, Li, & Ito, 2012). There are different edge weights that can be considered for finding the shortest path between two vertices including the

Euclidean distance and sum of voxel values along the path using raw intensities or enhances intensities (Lo, Ginneken, & Bruijne, 2010) in addition to the surface information from both the inner and outer walls of the vessel segments (Zhao et al., 2009). Another postprocessing step to improve the centerline quality is simple point removal, which removes the foreground voxels whose removal does not alter the centerline graph representation (Dongen & Ginneken, 2010). Addotomally, a set of logical rules in addition to multiple thinning and dilation applied iteratively improves the skeletonization results (Haft-Javaherian et al., 2019). Algorithms such as 3D dynamic balloon tracking (Zhou et al., 2012) produce more reasonable results compare to thinning algorithms when the task is to extract the large vessels' centerlines within a segmented image containing both large and small vessel. The continuity and smoothness of the final centerline results can be controlled using different techniques such as Laplacian filter and Kalman state estimator (Valencia, Azencot, & Orkisz, 2010).

2.3.8 Bifurcation detection

The vessel bifurcations are detectable by clustering the pixels with high values of a convexity metric measure based on the segmented image using one of the segmentation methods such as k-mean clustering (Almasi & Miller, 2013), level set (Almasi et al., 2015), kernel-based region growing (Almasi et al., 2017), and Bayesian tracking estimation (Zheng, Carr, & Ge, 2013). This methodology may lead to a high rate of false positive bifurcations that require rigorous postprocessing. Almasi et al. (Almasi et al., 2015) reduced the false positive bifurcation candidates by solving an integer linear programming problem with a utility function based on the intensity and structural

information of the graph representation of bifurcations. Pan et al. (Pan, Su, Lai, Liu, & Wu, 2014) used all of the detected vessel bifurcations to construct a minimum spanning tree based on the shortest distance bifurcations and combined it with a strategy that connects the closest pairs of terminal bifurcations to resolve the network discontinuities. The recursive application of the probabilistic sequential Monte Carlo method in addition to the k-means clustering detects both vasculature and the junctions along the vessel tree (Zhao & Bhotika, 2011). The bifurcations detection can be done using geometrical model-based methods with different criteria such as the comparison between parent vessel diameter and daughter vessels' diameters as well as the angle and curvature of the daughter vessels (Wala et al., 2011).

2.4 Vascular networks

2.4.1 Brain

2.4.1.1 Microscopic imaging

Imaging and automatic image analysis of 3D vascular microscopic images are essential tools for researchers studying various biomedical science fields including stem cells (Moore & Lemischka, 2006), neuroscience (Cruz Hernandez et al., 2017), brain tumors (Calabrese et al., 2007), and angiogenesis (Tyrrell et al., 2005). Note that the optimum image processing method should be selected with consideration of the different types of labels and whether the labeling is of the lumen or laminae of vessels. Typical 3D vascular microscopic images artifacts include:

- in vivo raster scanning induced motion artifact,
- low signal to noise ratio and multiscale vessel sizes,
- irregular or extra dense pathological vasculature networks,
- low sensitivity and specificity of labeling dyes,
- in complete labeling within the small vessels,
- large point spreads functions in comparison to the vessel sizes.

To study small vessels and cells with diameters ranges from 2 to 50 μm, an imaging modality with one μm per pixel or smaller resolutions is required based on the Nyquist–Shannon sampling theorem (Wu et al., 2014). On the other hand, the studies that require large fields of views such as the barrel cortex local angiome project (Blinder et al., 2013) need custom image processing toolboxes (Tsai et al., 2009) with large dataset analysis capability.

Different geometrical and topological metrics such as diameter, length, tortuosity, or betweenness centrality measured deterministically or stochastically on the segmentation results can be used to assesses vasculature networks' health and efficiency under different conditions or disease models (Cruz Hernández et al., 2019; Haft-Javaherian et al., 2019).

2.4.1.2 CTA and MRA

There are many different CTA and MRA sequences suitable for various medical diagnosis and treatments. For instance, TOF-MRA has a high contrast between blood serum and tissues that makes is suitable imaging modality for cerebral vascular network imaging (Al-Kwifi, Emery, & Wilman, 2002). It is also possible to acquire more complete

brain vasculature networks using PD-MRI in comparison to PC-MRA and TOF-MRA due to black-blood contrast phenomenon, i.e., low signal blood vessels (Descoteaux, Collins, & Siddiqi, 2008). On the other hand, cerebral CTP scans acquired at a fixed time interval for some time allow the cerebral tissue perfusion assessment for patients with cerebrovascular diseases including acute stroke and subarachnoid hemorrhage (Mendrik et al., 2010). However, repeated imaging over time induces severe motion artifacts requiring registration processes. On the other hand, PC-CT as a non-invasive imaging modality in comparison to the corrosion cast CT is very suitable for vascularization studies because it is possible to perform microscopy imaging of the postmortem histological slices of the same case (Lang et al., 2012). Also, the healthy and pathological animal tissues such as mice and rats can be visualized using SRμCT in both absorption and phase contrast modes (Lang et al., 2012).

For example, TOF-MRI images can be preprocessed (Forkert et al., 2013), and multiscale line filtered (Sato et al., 1997) separately and then combined by a voxel-wise fuzzy logic to weight the high-value intensity of each voxel in any of two images more when the other image has a low intensity (Forkert et al., 2011). Afterward, two different thresholds were applied to seed the level set method and the fuzzy value probability estimation using the Parzen-Window technique (Schmidt-Richberg, Handels, & Ehrhardt, 2009). Additionally, considering the local adaptive energy weights with additional vesselness forces yields better small vessel detection results (Forkert et al., 2013). The TOF-MRA intensity distribution can be models as a finite mixture of statistical model distributions such as Linear Combination of Discrete Gaussians (El-Baz et al., 2012) or a Gaussian distribution for cerebral vasculatures and a Rayleigh

distribution in addition to a set of Gaussian distributions for the surrounding tissues (Gao et al., 2011). A mixture of finite statistical model distributions can be estimated using the EM method and then using MAP to classify the image (Gao et al., 2011).

2.4.2 Lung

The accurate pulmonary vessel segmentation of lung images is required for interventional lung disease diagnosis and treatments as a tool for pre-operation planning and intraoperative assistance in order to avoid any significant vessel damage that has a ubiquities role in the effective image-guided clinical intervention (Zhu et al., 2009). Consequently, the VESSEL12 Challenge (Rudyanto et al., 2014) was hosted by Grand-Challenges and organized in conjunction with the IEEE International Symposium on Biomedical Imaging in 2012 was about lung vessel segmentation in thoracic CT images with different phenotypes as well as characterization of segmentation difficulties in the presence of anatomical abnormalities such as the presence of nodules and dense consolidation.

The lung CT and MR images contain various anatomical information such as ribs, spins, heart, and other vessel segments. Therefore, the vessel segmentation task in the lung is entangled with segmentation of a few other tissues such as pulmonary lobes, fissures, and bronchi (Lassen et al., 2013). For example, The lung field isolation as the first preprocessing step can be performed using different methods such as the knowledge-based segmentation using the prior information of lung intensity ranges (Heussel et al., 2006) and tissue continuities (Lai, Huang, Wang, & Wang, 2016) and application of morphological filters (Dongen & Ginneken, 2010) based on 2D slice-by-slice fashion

(Armato III & Sensakovic, 2004) or 3D volumes (Sun, Zhang, & Duan, 2006). Correspondingly, it is required to exclude the airway walls within the lung a preprocessing step using airway lumen segmentation (Fetita, Ortner, et al., 2009) or the prior information of the wall thickness as a function of lumen diameter (Peters et al., 2007). Then again, the automated detection methods identify the pathological-related errors (Rikxoort, Hoop, Viergever, Prokop, & Ginneken, 2009) and the errors can be reduced based on the abnormality types, e.g. juxtapleural nodules (Pu et al., 2008), prior knowledge of lung regions with high attenuation due to various diseases, e.g. asthma, scleroderma, and emphysema (Prasad et al., 2008), or presence of very dense pathologies requiring atlas-based registrations (Sluimer, Prokop, & Ginneken, 2005).

The candidate seed points required for the semi-automated method can be refined using special filtering based on the distance to the lung mask boundaries or applying morphological erosion filter to the lung mask and utilize it to mask the seed points (Rudyanto et al., 2014). Similarly, the image can be segmented into a fuzzy spherical object representation of blood vessels and nodules and then a tracking algorithm to connect the spheres into the vasculature network based on their connectivity and collinearity (Wu, Agam, Roy, & Armato, 2004).

The Hessian matrix-based methods can detect strong responses based on the scale-space particle sampling (Estépar et al., 2012), and the relevant scales of neighbor voxels can be obtained using multi-label Markov Random Field models enabling the detection of peripheral thin segments thick segments with better connectivity (Geng, Yang, Tan, & Zhao, 2016). On the other hand, the nodules alongside the vessels or fibrosis tissue can

be eliminated as a postprocessing step using shape-based filters based on the medial axis and diameter of vessels (Peters et al., 2007). Additionally, the log transformation based on variance variations to reduces false positive.

2.4.3 Liver

The geometrical properties and territories of liver vasculature network in the vicinity of a tumor facilitate the interventional procedure planning (Chi et al., 2011) or about the liver parenchyma for the liver transplantations (Frericks et al., 2004). Additionally, accurate anatomical dissection helps with avoiding portal osculation, excessive blood loss, and healthy liver tissue injury (Kim, 2013). Accurate vessel segmentation is essential for precise tumor growth estimation (Chen, 2012). Within the liver, it is easier to detect the hepatic artery and bile duct in comparison to the portal vein and hepatic vein due to similar intensity values and twisted structures, especially in cases with abnormalities (Chi et al., 2011). Therefore, the vessel segmentation with inferior vena cava and entrance of portal veins areas are challenging and requires the separation of hepatic and portal veins (Wang, Hansen, Zidowitz, & Hahn, 2014), while it is possible to merely segment the hepatic artery using Canny edge detection (Seo & Park, 2009), dimension reduction using 2D projection (Huang, Wang, Cheng, Huang, & Ju, 2008), or the combination of the vascular intensity Gaussian distribution and Hessian matrix (Kawajiri et al., 2008; Wang et al., 2013).

The small vessels are very hard to detect and even occasionally are missing in the manual segmentations (Chen et al., 2014). The small, precise branches at the liver boundaries can be detected using the hyper-complex edge operator (Ma & Li, 2014),

which replaces the voxel intensity with an eight-dimension octonion containing the neighbors' intensities as well and circularly convoluted with the edge detection operates. Oliveira et al. (Oliveira, Feitosa, & Correia, 2008) detected planes, which fit the hepatic and portal veins, to define the eight distinct liver regions developed by Couinaud facilitating the development of hepatectomies (Couinaud, 1954). The exploitation of the anatomical information and post-order walks of the vessels' graph representation in addition to including 4D enhancement modeling and shape likelihoods improve the segmentation and classification results (Yoshida, Sakas, & Linguraru, 2012).

In clinical practices, the 3D visualizations or information extractions of liver images using common method are extremely beneficial (X. Gao et al., 2011). For example, the maximum intensity projection reduces the 3D information to a 2D image by illustrating the maximum value of voxels along the view angle at each pixel to show the overall vasculature network (Johnson, Prince, & Chenevert, 1998).

2.5 Short segments

2.5.1 Heart

Alongside the importance of heart vessel segmentation in medical settings, biomedical research projects and veterinary care also depend on the imaging the major heart vessels for research studies, diagnosis, and prognosis in order to obtain geometrical measurements, hemodynamics, autoregulation, and tissue oxygen delivery using different imagining modalities such as MRA, Micro-CT, and multiphoton microscopy (Lee,

Beighley, Ritman, & Smith, 2007; Small et al., 2018). The motion of the beating heart presents an additional challenge for vessel identification.

The segmentation methods benefit from prior information about the approximate or precise location of the targeted organ within the image such as the heart in the thorax CT. For example, the prior knowledge of the heart location significantly reduces the computation time and search space because in this case, only the voxels in the proximity of the heart surface require vessel segmentation. This prior information can be obtained based on landmark detection (e.g., aorta, lungs, rib cage, plaques, and/or carina region), mathematical morphology techniques (e.g. blur grey-level hit-or-miss transform) (Bouraoui, Ronse, Baruthio, Passat, & Germain, 2010), adaptive thresholding (Zhou et al., 2012), rigid registration of heart phantom, or estimating the elastic deformation of heart atlas. Furthermore, the usage of several atlases in a multi-atlas fashion by registration of all atlases and fusion of their results improves the segmentation results (Isgum et al., 2009). In some cases, initially, the atlas can be registered rigidly, and then non-rigid registration can be utilized (Isgum et al., 2009). Multi-label myocardium segmentation (e.g., left and right atriums and ventricle, and valves) and heart movement tracking can be done using different techniques such as 4D watershed-cut algorithm (Cousty et al., 2010) or automatic model-based mesh adaptation method (Ecabert et al., 2011).

Similar techniques can be utilized to the locate aorta or the coronary artery within the prior detected heart (Bouraoui et al., 2010). The rib cage can be removed by intensity thresholding and morphological closing (Wang & Smedby, 2010) or closing the anterior

or posterior mediastinum using 2D livewires with a cost function to attract the wire to the interior edge of the sternum and the azygoesophageal recess (Wang & Smedby, 2008). In cases that the heart atlas contains the major vessel segments as well, a vasculature model can be obtained from the atlas and fed into a region growing or level set model to obtain a precise vessel segmentation (Wang, Moreno, & Smedby, 2012).

The blood flow volume and pattern measurements required for diagnosis and prognosis of cardiovascular diseases utilize semi-automated or fully-automated segmentation of thoracic vessels at different cardiac phases based on 2D or 3D PC-MR results in 3D or 4D flow tensors, respectively (Srichai, Lim, Wong, & Lee, 2009). Due to the variation between segmentation results caused by the heart movement and pathological issues, the atlas-based methods achieve reasonable results by registering an atlas to each imaging time point (Bustamante et al., 2015). Rather than utilizing the currently available atlases, atlases can be developed in a supervised fashion by learning the cardiovascular structures and geometries from a set of images (Peters et al., 2008) and then detecting the landmarks using methods such as simulated search (Peters, Ecabert, & Weese, 2005).

2.5.2 Coronary arteries

Coronary arteries supply blood to the heart, and any complication may lead to ischemia or heart attack. Many diagnosis and prognosis procedures depend heavily on the geometrical characteristic of the coronary arteries.

In cases that the heart is detected and located in the image (Zambal, Hladuvka, Kanitsar, & Bühler, 2008), searching algorithms such as cylindrical sampling and pattern fitting can be used to extract the coronary artery vessel tree in addition to handing the branching and terminations using by depth-first search and noise level estimation by Bayesian tracking (Schaap, Smal, Metz, van Walsum, & Niessen, 2007).

The coronary artery images that capture both the lumen-intima and the external elastic membrane of adventitia boundaries (e.g., IVUS) require multilabel segmentations and can be done using the fast-marching method based on the textural gradients (Will, Hermes, Buhmann, & Puzicha, 2000) or the gray level gradient (Destrempes, Roy Cardinal, Allard, Tardif, & Cloutier, 2014). The front propagation of fast-marching method along the local vessel orientation can be constrained using a minimum path cost function (Garcia et al., 2013).

The sub-resolution segmentation is essential for applications that require precise geometrical measurements such as vessel diameters or cross-section profiles for diagnoses or follow-up analyses such as computational fluid mechanics with high sensitivity to small geometrical variations. The methods based on coarse-to-fine fashion initially obtain a rough vessel segmentation and then adapt to segment the image with higher precision than the image resolution. For instance, non-linear regressions based on the image intensity variations along the radial direction result in a sub-resolution segmentation (Schaap et al., 2011).

2.5.3 Carotid arteries

Carotid arteries are located in the neck and supply blood to the head and neck, mainly to the brain. Since the brain has a very low tolerance for blood flow disruption, occlusion or narrowing of carotid arteries may lead to a stroke. MRI is the standard method for the carotid atherosclerosis progression and regression visualization (Underhill, Hatsukami, Fayad, Fuster, & Yuan, 2010). Since BB-MRA and PC-MRA have higher SNR and are non-invasive compared to CTA and CE-MRA, and intensity and gradient information are crucial for carotid lumen segmentation, BB-MRA or PC-MRA are good candidates for quantifying the carotid bifurcation geometries such as angle, area ratio, bulb size, and tortuosity that are correlated with the risk level of the atherosclerosis development (Thomas et al., 2005).

Tang et al. (Tang et al., 2012) proposed utilizing Multispectral MRIs to accurately detect and measure carotid centerlines and geometries, specifically in the pathological conditions. Conversely, the use of local neighboring ray filtering in low-contrast images facilitate the vessel segments' surface detection (Xie, Padgett, Biancardi, & Reeves, 2014). Freiman et al. (Freiman et al., 2009) segmented the carotid arteries using graph min-cut method by considering edge weights based on adaptively coupling of voxel intensity, the intensity prior, and geometric vesselness shape prior. They applied a similar methodology to remove tiny vessel segments and fill vessel discontinuities caused by imaging artifacts.

In cases that the multi-label carotid vessel segmentation (e.g., vessel wall and lumen vs. Background) is required, algorithms have utilized prior knowledge such as the

minimum and maximum separation between the wall and lumen, the segmentation smoothness, and the minimum distribution-based distances such as Bhattacharyya distance (Michailovich, Rathi, & Tannenbaum, 2007) between the label-based intensity distribution models and the intensity distribution of the segmented object (Ukwatta et al., 2013).

2.5.4 Abdominal aorta

There will be more than 15 thousand deaths in the United States due to abdominal aortic aneurysm (Upchurch, Schaub, & others, 2006) and more than 3 million death worldwide due to abdominal organs with malignant tumors between 2014 and 2030 (Maklad et al., 2017). Due to the asymptomatic nature of the abdominal aortic aneurysm, they are not noticeable until the aneurysm ruptures (Cornuz, Sidoti Pinto, Tevaearai, & Egger, 2004). Since the abdominal aorta is the largest human blood vessel, its rupture causes massive internal bleeding with a 90% mortality rate in non-hospitalized cases (Mozaffarian et al., 2016).

Surgical planning for vasculature disruption and reconnection as well as percutaneous stent-graft deployment or medical diagnoses such as arterial occlusive disease or thromboembolism requires accurate knowledge of localizations and geometrical measurements of vasculature network and specifically abdominal aorta. Preprocessing steps such as the segmentation of kidneys, liver, and the abdominal part of the heart based on their morphological, textural, and geometrical information in addition to various bone structures segmentations and lastly postprocessing steps such as 4D curvature analysis (Maklad et al., 2017) facilitate the abdominal aorta segmentation task.

The 3D BB-MRI is the standard for the assessment and volumetric measurements of the abdominal aortic aneurysm and vessel lumens and walls and is more predictive of clinical outcomes (Zhu et al., 2014). Wang et al. (Wang et al., 2017) proposed the use of both CE-MRI and BB-MRI to perform different segmentation based on the mutual information and the geometric active contour using both image series and finally superimposing the final result by their registration results using deformation-based registration methods. Similarly, landmark-based registration methods based on the fiducial markers facilitate the superimposing step (Wörz et al., 2016).

2.5.5 Ascending aorta, aortic arch, and descending aorta

The aorta, the largest artery, begins with the ascending aorta from the left ventricle, reaches the aortic arch, and the continues to the descending aorta. The early detection of congenital aortic disease and consequently the aortic aneurysms and dissections are crucial. The SSFP-MRA (Potthast et al., 2010) has advantages compare to CTA and MRA, which have high risks of renal dysfunction for patients with forthcoming surgery, e.g., aortic endograft procedures, and with a high probability of coexistent cardiovascular and renovascular disease due to repeated diagnostic and prognostic imaging and exposure to ionizing radiation and nephrotoxic contrast agents (Neschis & Fairman, 2004). Nevertheless, low SNR of SSFP-MRA makes the vessel segmentation task more challenging, which can be tackled using the 3D model-based segmentation approach (Müller-Eschner et al., 2014; Worz et al., 2010). Since the two centerlines of ascending and descending aorta may not be spatially co-localized, post-

processing or adapted cost function is required to guarantee the continuity of the centerlines (Zheng et al., 2013).

Due to the prominent intensity of blood within the ascending aorta in CTA and MRA in addition to circular cross-section morphology, the segmentation task turns into the detection of a circular object in each slice. The optimal set of circles consists of one circle per slice and each circle has a high overlap with adjacent slices' circles based on the competing fuzzy connectedness tree (Wang & Smedby, 2008) or virtual contrast injection method (Wang & Smedby, 2010). The precise perimeter of cross-sections can be obtained using region growing or level-set techniques.

The outer aortic cross-sectional boundary can be segmented efficiently using a piecewise constant curvature within a polar-based segmentation model by utilizing the initial aortic centerline estimation to generate multiplanar reformatted image sequence (Deserno, Handels, Meinzer, & Tolxdorff, 2014). Similarly, the initial centerline estimation can be used as the seed points for the geodesic distance transformation and then using each segmented slice as the segmentation seed for the next adjacent slice (Jang et al., 2016). On the other hand, the prior knowledge of the ascending or descending aorta shape and morphology can be used to generate an atlas-based segmentation model (Seada, Hamad, & Mostafa, 2016). The temporal tracking of the centerline can be achieved using the Kalman filter, 3D elliptic cylinder vessel models, and longitudinal intensity-based motion determination (Biesdorf et al., 2011).

2.5.6 Aorta root

The vessel segment between the heart and ascending aorta with aortic valve and the coronary arteries openings and its rupture lead to life-threatening internal bleeding. The localization of lung and the carina tracheae facilitate the detection of the beginning of the aorta root. Feuerstein et al. (Feuerstein, Kitasaka, & Mori, 2009) located a confiding mediastinal bounding box centered at the carina on the mediolateral axis and at the center of lungs bounding box on the anteroposterior and superior-inferior axes with width equal to half of the lung bounding box dimension along the mediolateral axis and the lung bounding box dimension along the anteroposterior and superior-inferior axes. Due to mediastinal anatomy, the aortic arch centerline can be detected using a series of circular Hough transforms (Dasgupta, Mukhopadhyay, Mehre, & Bhattacharyya, 2017; Feuerstein et al., 2009; S. Gao et al., 2017) and the result can be used to segment the aorta root precisely.

The intensity-based elastic image registrations of an image to an aorta root atlas (Biesdorf et al., 2012) or a 3D parametric intensity model generated by convolving an ideal sharp 3D cylinder with another 3D cylinder, which was already convoluted with a 3D Gaussian (Biesdorf, Worz, Tengg-Kobligk, & Rohr, 2009), facilitate the segmentation task. In contrast to the atlas-based models, the parametric intensity models do not require the prior knowledge of atlas and segmentation and produce the templates on-fly. The artifacts caused by calcifications with high intensities can be masked to improve the vascular segmentation accuracy (Elattar et al., 2014).

The severe aortic valve stenosis can be treated using the invasive transcatheter aortic valve implantation (TAVI) procedure. TAVI requires geometrical and morphological information extracted form C-arm CT images for surgery planning and operational guidance such as providing 3-D valve measurements and determining a proper C-arm angulation. Even though it has a lower image quality compared to CT and MRI, C-arm CT captures both 2D and 3D images and overlay the 3D Left Atrium model to the 2D fluoroscopy based on the intrinsic machine coordinate system, while it monitors the physiological status of the patient simultaneously (Gessat et al., 2009; John et al., 2010; Y. Zheng, Yang, John, & Comaniciu, 2014). Since the complete aorta segregation is required (i.e., aortic root, ascending aorta, aortic arch, and descending aorta), Zheng et al. (Zheng et al., 2012) proposed marginal space learning method to localize objects based on their anatomical structures and estimates their scales and orientations.

On the other hand, the atrial fibrillation can be treated using a minimally invasive catheter-based ablation surgery utilizing high radio-frequency energy to ablate the potential sources of abnormal electrical activities (e.g., the ostia of pulmonary veins). An overlay of electro-anatomical maps or real-time 2D fluoroscopic images on the segmented result of left atrium chamber, appendage, and pulmonary veins in ECG-gated MRI or CT images provide essential visual guidance during the surgery (Zheng et al., 2014). In non-gated images, e.g., 3D US, users can define selecting end-diastolic and end-systole in addition to some landmarks, e.g., mitral valve to segment both left atrium and ventricle (Almeida et al., 2014).

2.6 Disease state segmentation

2.6.1 Intracranial aneurysm and BAVM

An intracranial aneurysm is a pathological dilation of a cerebral artery within the Circle of Willis due to weakened vessel walls, and its rupture leads to subarachnoid hemorrhage (Brisman, Song, & Newell, 2006). CTA and 3D-RA are widely-used diagnoses and assessment imaging for intracranial aneurysm (Li et al., 2009). Also, non-invasive modalities such as PC-MRA and TOF-MRA, which do not involve injections and radiations, are preferred for diagnosis and screening (Bogunović et al., 2011).

For instance, CTA intracranial aneurysm images can be segmented using a level set segmentation method such as geodesic active surfaces (Caselles et al., 1997) by incorporating intensity, gradient magnitude, and intensity variance as different energy terms and a single manual seed point within the aneurysm (Firouzian et al., 2011). There are three ways to improve the geodesic active surfaces. First, the multiple-valued neuron classifiers reduce the region-based probability map computation cost (Aizenberg, Aizenberg, & Vandewalle, 2013). Second, utilizing the voxel-based feature scale selection enable the processing of multiscale images (Bogunović et al., 2011). Third, using image intensity standardization, the intensity dependency on the scanning machine can be compensated (Nyúl, Udupa, & others, 1999). On the other hand, because 2D DSA projections are the gold standard for geometrical measurements, Spiegel et al. (Spiegel, Redel, Struffert, Hornegger, & Doerfler, 2011) proposed a snake-based segmentation method for 3D DSA and validated their method by transforming their results into the 2D DSA domain.

The brain arteriovenous malformation (BAVM) is an abnormal direct connection and tangle, i.e., nidus, between arteries and veins without intermediate capillary bed (Byrne, 2005). 2D catheter DSA was the gold standard for diagnostic aneurysm detection (McKinney, Palmer, Truwit, Karagulle, & Teksam, 2008) before the introduction of 3D-RA as the new gold standard (Rooij, Sprengers, Gast, Peluso, & Sluzewski, 2008). Even though DSA and 3D-RA are the standard techniques for the diagnosis and prognosis of BAVM (Friedlander, 2007), researchers explored various image sequences at different stages for the same purpose such as CCA, CTA, TOF-MRA, and PC-MRA (Byrne, 2005; Gauvrit et al., 2006; Remonda et al., 2002; Sanelli, Mifsud, & Stieg, 2004).

Microsurgery is the conventional treatment for BAVM with a diameter less than 3 cm and endovascular embolization (Pik & Morgan, 2000), which requires precise location and geometry of BAVM. Sarieddeen et al. (Sarieddeen et al., 2013) compared KM, FCM, and EM for the BAVM vascular segmentation. They reported similar accuracy across the three methods and the lowest computation time for KM.

2.6.2 Interstitial lung diseases

Lung diseases are the third-leading cause of death in the United States. Interstitial lung diseases (ILD) is a large group of parenchymal lung disorders with unpredictable clinical courses and high mortality rates (Demedts et al., 2001). For instance, the five-year survival-rate of idiopathic pulmonary fibrosis (IPF), major ILD diseases, is about 50% (Xu et al., 2006). The quantitative detection of pulmonary pathology based on various segmentations facilitates the ILD diagnosis and prognosis (Korfiatis, Kalogeropoulou, Karahaliou, Kazantzi, & Costaridou, 2011). The vessel segmentation

within the lung parenchyma field in the presence of abnormalities such as focal abnormalities (Li, Sone, & Doi, 2003) and pulmonary embolism (Zhou et al., 2007) is more challenging compared to healthy state (Shikata, McLennan, Hoffman, & Sonka, 2009). For example, the pattern similarity between reticular patterns and vessel tree segments have similar patterns in lungs parenchyma affected by interstitial pneumonia (Manivila, 2014).

2.6.3 Carotid diseases

Precise severity assessment of carotid diseases is crucial for therapy assignment, which has been shown by the NASCET and ECST trials (European Carotid Surgery Trialists' Collaborative Group and others, 1991; North American Symptomatic Carotid Endarterectomy Trial Collaborators, 1991). Accurate monitoring of carotid disease help patients with managing the risk of stroke given the fact that surgical or non-surgical treatment can prevent many strokes related to carotid atherosclerosis (Gorelick, 1994). There are two classic ways to assess carotid disease severity and monitor atherosclerosis progression: determine the degree of stenosis directly or assess the abnormalities in blood flow velocity indirectly. DSA is the gold standard, but it is invasive and may cause emboli formation during catheterization or adverse allergic reaction to the contrast agent. MRA is an alternative to DSA, but it has the risk of overestimating stenosis due to intravoxel phase dispersion.

Doppler ultrasonography has been increasingly used clinically due to its non-invasive property, albeit it is not able to visualize the details of plaque or its surface and has high intra- and inter-operator variabilities (Gill, Ladak, Steinman, & Fenster, 2000).

The development of 3D US with the ability to visualize plaque and its surface, as well as measure volume of stenosis and the actual atheroma, can better evaluate carotid disease severity and monitor stroke risk (Fenster & Downey, 1996). 3D US imaging is noninvasive and gives 3D information of internal organs and vessels, whose structure can be reconstructed by a 3D segmentation technique.

2.6.4 Coronary artery disease

Coronary artery disease (CAD) is one of the leading causes of death, and nearly one-third of the patients experienced a coronary episode will die in the same year (Mozaffarian et al., 2016). Even though the prevalence of CAD will increase by about 18% by 2030, its mortality rates are decreased since the 1970s in part due to improvements in the clinical presentation patterns of acute myocardium infarction (Mozaffarian et al., 2016). IVUS captures cross-sectional image sequences of vessel walls and plaques by pulling-back a catheter inside arteries blood vessels, and it is the invasive gold standard for studying atherosclerotic diseases (Nissen & Yock, 2001). Invasive coronary angiography (ICA) in adjunction with fractional flow reserve (FFR) measurement is the reference standard for lesion-specific diagnosis of canary artery disease (CAD) (Min et al., 2012; Min, Shaw, & Berman, 2010). Even though coronary CTA as noninvasive imaging method facilitate visualization of CAD and correlates with ICA findings, it cannot capture the hemodynamic and consequently has low precision in ischemia causing obstructive stenosis detection (Meijboom et al., 2008; Schuijf & Bax, 2008).

The narrowing or occlusion of the coronary artery (i.e., stenosis) due to the accumulation of calcium, fat, or cholesterol plaques (i.e., atherosclerosis) compromises the oxygen and nutrition delivery to the heart (i.e., ischemia). The atherosclerotic plaques are divided into two categories of stable vs. unstable based on their rupture possibility, and it may cause irreversible defects to the myocardium or myocardial infarction, (i.e., heart attack) (Kirişli et al., 2013). Therefore, the plaques and vessels identifications, classifications (e.g., types of plaques and vessels), and characterizations (e.g., segmentation and geometrical measurements), especially in the early stage, is indispensable.

Frequently, non-vascular objects such as plaques, stent struts, and guide-wire require segmentation while causing artifacts on the vascular segmentation results. On the other hand, since most of the plaques occur near a bifurcation in the pathological cases, the plaque localization and identification can lead to landmark detections and allow an automatic region of interest detections and image to image registrations (Hemmati, Kamli-Asl, Talebpour, & Shirani, 2015). The external object localization (e.g., guide-wire) is required to eliminate the caused shadow artifacts using different methods such as convex hull approaches (Tung, Shi, Silva, Edwards, & Rueckert, 2011).

2.7 Conclusion

Many medical practices and biomedical research projects focusing on the circulatory system depend profoundly on different imaging techniques and subsequently requires efficient image processing procedures to analyze images time- and cost-effectively. Image segmentation and centerline extraction methods play an essential role

in most of the image processing pipeline. In this review, we examined these important tasks from different angles ranging from fundamental image segmentation methods to organ- and tissue-level vascular segmentation methods divided into the segments and networks in addition to the segmentation of pathological vasculatures.

REFERENCES

Aizenberg, I., Aizenberg, N. N., & Vandewalle, J. P. L. (2013). *Multi-Valued and Universal Binary Neurons: Theory, Learning and Applications*. Springer Science & Business Media.

Al-Kwifi, O., Emery, D. J., & Wilman, A. H. (2002). Vessel contrast at three Tesla in time-of-flight magnetic resonance angiography of the intracranial and carotid arteries. *Magnetic Resonance Imaging*, *20*(2), 181–187. https://doi.org/10.1016/S0730-725X(02)00486-1

Almasi, S., & Miller, E. L. (2013). Microvasculature network identification in 3-D fluorescent microscopy images. *2013 IEEE 10th International Symposium on Biomedical Imaging*, 444–447. https://doi.org/10.1109/ISBI.2013.6556507

Almasi, Sepideh, Ben-Zvi, A., Lacoste, B., Gu, C., Miller, E. L., & Xu, X. (2017). Joint volumetric extraction and enhancement of vasculature from low-SNR 3-D fluorescence microscopy images. *Pattern Recognition*, *63*, 710–718. https://doi.org/10.1016/j.patcog.2016.09.031

Almasi, Sepideh, Xu, X., Ben-Zvi, A., Lacoste, B., Gu, C., & Miller, E. L. (2015). A novel method for identifying a graph-based representation of 3-D microvascular networks from fluorescence microscopy image stacks. *Medical Image Analysis*, *20*(1), 208–223. https://doi.org/10.1016/j.media.2014.11.007

Almeida, N., Barbosa, D., Heyde, B., Mada, R. O., Friboulet, D., Bernard, O., … D'hooge, J. (2014). Semi-automatic left-atrial segmentation from volumetric ultrasound using B-spline explicit active surfaces. *2014 IEEE International Ultrasonics Symposium*, 612–615. https://doi.org/10.1109/ULTSYM.2014.0150

Armato III, S. G., & Sensakovic, W. F. (2004). Automated lung segmentation for thoracic CT: Impact on computer-aided diagnosis. *Academic Radiology*, *11*(9), 1011–1021.

Aylward, S. R., Jomier, J., Weeks, S., & Bullitt, E. (2003). Registration and Analysis of Vascular Images. *International Journal of Computer Vision; New York*, *55*(2–3), 123–138. http://dx.doi.org.proxy.library.cornell.edu/10.1023/A:1026126900358

Bauer, C., Bischof, H., & Beichel, R. (2009). Segmentation of airways based on gradient vector flow. *International Workshop on Pulmonary Image Analysis, Medical Image Computing and Computer Assisted Intervention*, 191–201. Citeseer.

Bauer, C., Pock, T., Bischof, H., & Beichel, R. (2009). Airway tree reconstruction based on tube detection. *Proc. of Second International Workshop on Pulmonary Image Analysis*, 203–213.

Biesdorf, A., Worz, S., Tengg-Kobligk, H. von, & Rohr, K. (2009). Automatic detection of supraaortic branches and model-based segmentation of the aortic arch froM 3D CTA images. *2009 IEEE International Symposium on Biomedical Imaging: From Nano to Macro*, 486–489. https://doi.org/10.1109/ISBI.2009.5193090

Biesdorf, A., Wörz, S., Tengg-Kobligk, H. von, Rohr, K., & Schnörr, C. (2015). 3D segmentation of vessels by incremental implicit polynomial fitting and convex optimization. *2015 IEEE 12th International Symposium on Biomedical Imaging (ISBI)*, 1540–1543. https://doi.org/10.1109/ISBI.2015.7164171

Biesdorf, Andreas, Rohr, K., Feng, D., von Tengg-Kobligk, H., Rengier, F., Böckler, D., … Wörz, S. (2012). *Segmentation and quantification of the aortic arch using joint 3D model-based segmentation and elastic image registration*. *16*(6), 1187–1201. https://doi.org/10.1016/j.media.2012.05.010

Biesdorf, Andreas, Wörz, S., Müller, T., Weber, T. F., Heye, T., Hosch, W., … Rohr, K. (2011). Model-Based Segmentation and Motion Analysis of the Thoracic Aorta from 4D ECG-Gated CTA Images. *Medical Image Computing and Computer-Assisted Intervention – MICCAI 2011*, 589–596. https://doi.org/10.1007/978-3-642-23623-5_74

Blinder, P., Tsai, P. S., Kaufhold, J. P., Knutsen, P. M., Suhl, H., & Kleinfeld, D. (2013). The cortical angiome: an interconnected vascular network with noncolumnar patterns of blood flow. *Nature Neuroscience*, *16*(7), 889–897. https://doi.org/10.1038/nn.3426

Bogunović, H., Pozo, J. M., Villa-Uriol, M. C., Majoie, C. B. L. M., van den Berg, R., Gratama van Andel, H. A. F., … Frangi, A. F. (2011). *Automated segmentation of cerebral vasculature with aneurysms in 3DRA and TOF-MRA using geodesic active regions: An evaluation study*. *38*(1), 210–222. https://doi.org/10.1118/1.3515749

Bouraoui, B., Ronse, C., Baruthio, J., Passat, N., & Germain, P. (2010). *3D segmentation of coronary arteries based on advanced mathematical morphology techniques*. *34*(5), 377–387. https://doi.org/10.1016/j.compmedimag.2010.01.001

Boykov, Y., & Kolmogorov, V. (2003). Computing geodesics and minimal surfaces via graph cuts. *Proceedings Ninth IEEE International Conference on Computer Vision*, 26–33 vol.1. https://doi.org/10.1109/ICCV.2003.1238310

Bresson, X. (2005). *Image segmentation with variational active contours* (PhD Thesis). Verlag nicht ermittelbar.

Brisman, J. L., Song, J. K., & Newell, D. W. (2006). Cerebral Aneurysms. *New England Journal of Medicine*, *355*(9), 928–939. https://doi.org/10.1056/NEJMra052760

Bustamante, M., Petersson, S., Eriksson, J., Alehagen, U., Dyverfeldt, P., Carlhäll, C.-J., & Ebbers, T. (2015). *Atlas-based analysis of 4D flow CMR: Automated vessel segmentation and flow quantification*. *17*, 87. https://doi.org/10.1186/s12968-015-0190-5

Byrne, J. V. (2005). Cerebrovascular malformations. *European Radiology*, *15*(3), 448–452. https://doi.org/10.1007/s00330-004-2634-4

Calabrese, C., Poppleton, H., Kocak, M., Hogg, T. L., Fuller, C., Hamner, B., … Gilbertson, R. J. (2007). A Perivascular Niche for Brain Tumor Stem Cells. *Cancer Cell*, *11*(1), 69–82. https://doi.org/10.1016/j.ccr.2006.11.020

Canny, J. (1987). A Computational Approach to Edge Detection. In *Readings in Computer Vision* (pp. 184–203). https://doi.org/10.1016/B978-0-08-051581-6.50024-6

Caselles, V., Kimmel, R., & Sapiro, G. (1997). Geodesic Active Contours. *International Journal of Computer Vision*, *22*(1), 61–79. https://doi.org/10.1023/A:1007979827043

Cassot, F., Lauwers, F., Fouard, C., Prohaska, S., & Lauwers-Cances, V. (2006). A novel three-dimensional computer-assisted method for a quantitative study of microvascular networks of the human cerebral cortex. *Microcirculation (New York, N.Y.: 1994)*, *13*(1), 1–18. https://doi.org/10.1080/10739680500383407

Cetin, S., Demir, A., Yezzi, A., Degertekin, M., & Unal, G. (2013). *Vessel Tractography Using an Intensity Based Tensor Model with Branch Detection*. *32*(2), 348–363. https://doi.org/10.1109/TMI.2012.2227118

Cetin, S., & Unal, G. (2015). *A Higher-Order Tensor Vessel Tractography for Segmentation of Vascular Structures*. *34*(10), 2172–2185. https://doi.org/10.1109/TMI.2015.2425535

Chen, B., Sun, Y., & Ong, S. H. (2014). Liver Vessel Segmentation Using Graph Cuts with Quick Shift Initialization. In *IFMBE Proceedings*. *The 15th International Conference on Biomedical Engineering* (pp. 188–191). Retrieved from https://link.springer.com/chapter/10.1007/978-3-319-02913-9_48

Chen, X. (2012). Liver vessel tree segmentation based on a hybrid graph cut/fuzzy connectedness method. *Medical Imaging 2012: Image Processing*, *8314*, 83141K. International Society for Optics and Photonics.

Chen, Y., & Medioni, G. (1995). Description of complex objects from multiple range images using an inflating balloon model. *Computer Vision and Image Understanding*, *61*(3), 325–334.

Chi, Y., Liu, J., Venkatesh, S. K., Huang, S., Zhou, J., Tian, Q., & Nowinski, W. L. (2011). *Segmentation of Liver Vasculature from Contrast Enhanced CT Images Using Context-Based Voting*. *58*(8), 2144–2153. https://doi.org/10.1109/TBME.2010.2093523

Cohen, L. D., & Cohen, I. (1993). Finite-element methods for active contour models and balloons for 2-D and 3-D images. *IEEE Transactions on Pattern Analysis & Machine Intelligence*, (11), 1131–1147.

Cornuz, J., Sidoti Pinto, C., Tevaearai, H., & Egger, M. (2004). Risk factors for asymptomatic abdominal aortic aneurysm: systematic review and meta-analysis

of population-based screening studies. *The European Journal of Public Health*, *14*(4), 343–349.

Couinaud, C. (1954). Liver lobes and segments: notes on the anatomical architecture and surgery of the liver. *La Presse Médicale*, *62*(33), 709.

Cousty, J., Najman, L., Couprie, M., Clément-Guinaudeau, S., Goissen, T., & Garot, J. (2010). *Segmentation of 4D cardiac MRI: Automated method based on spatio-temporal watershed cuts*. *28*(8), 1229–1243. https://doi.org/10.1016/j.imavis.2010.01.001

Cruz Hernandez, J. C., Bracko, O., Kersbergen, C. J., Muse, V., Haft-Javaherian, M., Berg, M., … Schaffer, C. B. (2017). Neutrophil adhesion in brain capillaries contributes to cortical blood flow decreases and impaired memory function in a mouse model of Alzheimer's disease. *BioRxiv*. https://doi.org/10.1101/226886

Cruz Hernández, J. C., Bracko, O., Kersbergen, C. J., Muse, V., Haft-Javaherian, M., Berg, M., … Schaffer, C. B. (2019). Neutrophil adhesion in brain capillaries reduces cortical blood flow and impairs memory function in Alzheimer's disease mouse models. *Nature Neuroscience*, *22*(3), 413–420. https://doi.org/10.1038/s41593-018-0329-4

Dasgupta, A., Mukhopadhyay, S., Mehre, S. A., & Bhattacharyya, P. (2017). Morphological Geodesic Active Contour Based Automatic Aorta Segmentation in Thoracic CT Images. In *Advances in Intelligent Systems and Computing*. *Proceedings of International Conference on Computer Vision and Image Processing* (pp. 187–195). Retrieved from https://link.springer.com/chapter/10.1007/978-981-10-2107-7_17

Delingette, H., Hebert, M., & Ikeuchi, K. (1992). Shape representation and image segmentation using deformable surfaces. *Image and Vision Computing*, *10*(3), 132–144.

Demedts, M., Wells, A. U., Antó, J. M., Costabel, U., Hubbard, R., Cullinan, P., … Taylor, A. N. (2001). Interstitial lung diseases: an epidemiological overview. *European Respiratory Journal*, *18*(32 suppl), 2s–16s.

Descoteaux, M., Collins, D. L., & Siddiqi, K. (2008). *A geometric flow for segmenting vasculature in proton-density weighted MRI*. *12*(4), 497–513. https://doi.org/10.1016/j.media.2008.02.003

Deserno, T. M., Handels, H., Meinzer, H.-P., & Tolxdorff, T. (2014). *Polar-Based Aortic Segmentation in 3D CTA Dissection Data Using a Piecewise Constant Curvature Model*. Springer-Verlag.

Destrempes, F., Roy Cardinal, M.-H., Allard, L., Tardif, J.-C., & Cloutier, G. (2014). *Segmentation method of intravascular ultrasound images of human coronary arteries*. *38*(2), 91–103. https://doi.org/10.1016/j.compmedimag.2013.09.004

Dongen, E. van, & Ginneken, B. van. (2010). Automatic segmentation of pulmonary vasculature in thoracic CT scans with local thresholding and airway wall removal. *2010 IEEE International Symposium on Biomedical Imaging: From Nano to Macro*, 668–671. https://doi.org/10.1109/ISBI.2010.5490088

Dufour, A., Tankyevych, O., Naegel, B., Talbot, H., Ronse, C., Baruthio, J., … Passat, N. (2013). *Filtering and segmentation of 3D angiographic data: Advances based on mathematical morphology*. *17*(2), 147–164. https://doi.org/10.1016/j.media.2012.08.004

Ebrahimdoost, Y., Qanadli, S. D., Nikravanshalmani, A., Ellis, T. J., Shojaee, Z. F., & Dehmeshki, J. (2011). Automatic segmentation of Pulmonary Artery (PA) in 3D pulmonary CTA images. *2011 17th International Conference on Digital Signal Processing (DSP)*, 1–5. https://doi.org/10.1109/ICDSP.2011.6004964

Ecabert, O., Peters, J., Walker, M. J., Ivanc, T., Lorenz, C., von Berg, J., … Weese, J. (2011). *Segmentation of the heart and great vessels in CT images using a model-based adaptation framework*. *15*(6), 863–876. https://doi.org/10.1016/j.media.2011.06.004

Eiho, S., Sekiguchi, H., Sugimoto, N., Hanakawa, T., & Urayama, S. (2004). Branch-based region growing method for blood vessel segmentation. *Proceedings of International Society for Photogrammetry and Remote Sensing Congress*, 796–801.

Elattar, M. A., Wiegerinck, E., Planken, R., van Assen, H., Baan, J., Marquering, H., & others. (2014). Automatic segmentation of the aortic root in CT angiography of candidate patients for transcatheter aortic valve implantation. *Medical & Biological Engineering & Computing*, *52*(7), 611–618.

El-Baz, A., Elnakib, A., Khalifa, F., El-Ghar, M. A., McClure, P., Soliman, A., & Gimelrfarb, G. (2012). *Precise Segmentation of 3-D Magnetic Resonance Angiography*. *59*(7), 2019–2029. https://doi.org/10.1109/TBME.2012.2196434

Erdt, M., Raspe, M., & Suehling, M. (2008). Automatic Hepatic Vessel Segmentation Using Graphics Hardware. *Medical Imaging and Augmented Reality*, 403–412. https://doi.org/10.1007/978-3-540-79982-5_44

Estépar, R. S. J., Ross, J. C., Russian, K., Schultz, T., Washko, G. R., & Kindlmann, G. L. (2012). Computational vascular morphometry for the assessment of pulmonary vascular disease based on scale-space particles. *2012 9th IEEE International Symposium on Biomedical Imaging (ISBI)*, 1479–1482. IEEE.

European Carotid Surgery Trialists' Collaborative Group and others. (1991). MRC European Carotid Surgery Trial: interim results for symptomatic patients with severe (70-99%) or with mild (0-29%) carotid stenosis. *Lancet*, *337*(8752), 1235–43.

Fabijańska, A. (2012). Extraction of pulmonary vessels from MDCT thorax scans. *2012 IEEE International Conference on Imaging Systems and Techniques Proceedings*, 63–67. https://doi.org/10.1109/IST.2012.6295486

Fenster, A., & Downey, D. B. (1996). 3-D ultrasound imaging: A review. *IEEE Engineering in Medicine and Biology Magazine*, *15*(6), 41–51.

Fetita, C., Brillet, P.-Y., & Prêteux, F. J. (2009). *Morpho-geometrical approach for 3D segmentation of pulmonary vascular tree in multi-slice CT*. *7259*, 72594F–72594F–12. https://doi.org/10.1117/12.811637

Fetita, C., Ortner, M., Brillet, P.-Y., Prêteux, F., Grenier, P., & others. (2009). A morphological-aggregative approach for 3D segmentation of pulmonary airways from generic MSCT acquisitions. *Proc. of Second International Workshop on Pulmonary Image Analysis*, 215–226.

Feuerstein, M., Kitasaka, T., & Mori, K. (2009). Automated anatomical likelihood driven extraction and branching detection of aortic arch in 3-D chest CT. *Second International Workshop on Pulmonary Image Analysis*, 49–60. Med. Image Comput. Comput. Assist. Interv.(MICCAI).

Firouzian, A., Manniesing, R., Flach, Z. H., Risselada, R., van Kooten, F., Sturkenboom, M. C. J. M., … Niessen, W. J. (2011). *Intracranial aneurysm segmentation in 3D CT angiography: Method and quantitative validation with and without prior noise filtering*. *79*(2), 299–304. https://doi.org/10.1016/j.ejrad.2010.02.015

Forkert, N. D., Schmidt-Richberg, A., Fiehler, J., Illies, T., Möller, D., Handels, H., & Säring, D. (2011). *Fuzzy-based Vascular Structure Enhancement in Time-of-Flight MRA Images for Improved Segmentation*. *50*(1), 74–83. https://doi.org/10.3414/ME10-02-0003

Forkert, Nils Daniel, Säring, D., Fiehler, J., Illies, T., Möller, D., & Handels, H. (2009). Automatic brain segmentation in Time-of-Flight MRA images. *Methods of Information in Medicine*, *48*(5), 399–407. https://doi.org/10.3414/ME9237

Forkert, Nils Daniel, Schmidt-Richberg, A., Fiehler, J., Illies, T., Möller, D., Säring, D., … Ehrhardt, J. (2013). *3D cerebrovascular segmentation combining fuzzy vessel enhancement and level-sets with anisotropic energy weights*. *31*(2), 262–271. https://doi.org/10.1016/j.mri.2012.07.008

Foruzan, A. H., Zoroofi, R. A., Sato, Y., & Hori, M. (2012). *A Hessian-based filter for vascular segmentation of noisy hepatic CT scans*. *7*(2), 199–205. https://doi.org/10.1007/s11548-011-0640-y

Freiman, M., Joskowicz, L., & Sosna, J. (2009, February 1). *A variational method for vessels segmentation: algorithm and application to liver vessels visualization*. *7261*, 72610H. https://doi.org/10.1117/12.810611

Freiman, Moti, Broide, N., Natanzon, M., Nammer, E., Shilon, O., Weizman, L., … Sosna, J. (2009). Vessels-Cut: A Graph Based Approach to Patient-Specific Carotid Arteries Modeling. *Modelling the Physiological Human*, 1–12. https://doi.org/10.1007/978-3-642-10470-1_1

Frericks, B. B., Caldarone, F. C., Nashan, B., Savellano, D. H., Stamm, G., Kirchhoff, T. D., … Galanski, M. (2004). *3D CT modeling of hepatic vessel architecture and volume calculation in living donated liver transplantation*. *14*(2), 326–333. https://doi.org/10.1007/s00330-003-2161-8

Friedlander, R. M. (2007). Arteriovenous Malformations of the Brain. *New England Journal of Medicine*, *356*(26), 2704–2712. https://doi.org/10.1056/NEJMcp067192

Friman, O., Hindennach, M., & Peitgen, H. O. (2008). Template-based multiple hypotheses tracking of small vessels. *2008 5th IEEE International Symposium on Biomedical Imaging: From Nano to Macro*, 1047–1050. https://doi.org/10.1109/ISBI.2008.4541179

Friman, Ola, Hindennach, M., Kühnel, C., & Peitgen, H.-O. (2010). Multiple hypothesis template tracking of small 3D vessel structures. *Medical Image Analysis*, *14*(2), 160–171. https://doi.org/10.1016/j.media.2009.12.003

Gao, S., van 't Klooster, R., Brandts, A., Roes, S. D., Alizadeh Dehnavi, R., de Roos, A., … van der Geest, R. J. (2017). *Quantification of common carotid artery and descending aorta vessel wall thickness from MR vessel wall imaging using a fully automated processing pipeline*. *45*(1), 215–228. https://doi.org/10.1002/jmri.25332

Gao, X., Uchiyama, Y., Zhou, X., Hara, T., Asano, T., & Fujita, H. (2011). A Fast and Fully Automatic Method for Cerebrovascular Segmentation on Time-of-Flight (TOF) MRA Image. *Journal of Digital Imaging*, *24*(4), 609–625. https://doi.org/10.1007/s10278-010-9326-1

Garcia, M. P., Velut, J., Boulmier, D., Leclercq, C., Garreau, M., Haigron, P., & Toumoulin, C. (2013). *Coronary Vein Extraction in MSCT Volumes Using Minimum Cost Path and Geometrical Moments*. *17*(2), 336–345. https://doi.org/10.1109/JBHI.2013.2245420

Gauvrit, J.-Y., Oppenheim, C., Nataf, F., Naggara, O., Trystram, D., Munier, T., … Meder, J.-F. (2006). Three-dimensional dynamic magnetic resonance angiography for the evaluation of radiosurgically treated cerebral arteriovenous

malformations. *European Radiology*, *16*(3), 583–591. https://doi.org/10.1007/s00330-005-0011-6

Geng, H., Yang, J., Tan, W., & Zhao, D. (2016). *3D Multi-Scale Pulmonary Vascular Segmentation Algorithm Based on Multi-Label MRF Optimization*. *6*(7), 1794–1798. https://doi.org/10.1166/jmihi.2016.1892

Gessat, M., Merk, D. R., Falk, V., Walther, T., Jacobs, S., Nöttling, A., & Burgert, O. (2009). A planning system for transapical aortic valve implantation. *Medical Imaging 2009: Visualization, Image-Guided Procedures, and Modeling*, *7261*, 72611E. International Society for Optics and Photonics.

Gill, J. D., Ladak, H. M., Steinman, D. A., & Fenster, A. (2000). *Accuracy and variability assessment of a semiautomatic technique for segmentation of the carotid arteries from three-dimensional ultrasound images*. *27*(6), 1333–1342. https://doi.org/10.1118/1.599014

Gong, Z.-X., Tan, W., Song, Y.-H., Geng, H., Ren, F.-L., Liang-Chen, ., … Zhang, J. (2016). *Segmentation of Pulmonary Blood Vessels Based on Fractional Differentiation in 3D Chest CT Images*. *6*(7), 1746–1749. https://doi.org/10.1166/jmihi.2016.1883

Gong, Z.-X., Tan, W.-J., Yang, J.-Z., Xu, M., Bian, Z., & Zhao, D.-Z. (2014). *A Carotid Vasculature Segmentation Method for Computed Tomography Angiography*. *4*(6), 912–915. https://doi.org/10.1166/jmihi.2014.1341

Gorelick, P. B. (1994). Stroke prevention. An opportunity for efficient utilization of health care resources during the coming decade. *Stroke*, *25*(1), 220–224.

Gülsün, M. A., & Tek, H. (2010, February 1). *Segmentation of carotid arteries by graph-cuts using centerline models*. *7625*, 762530. https://doi.org/10.1117/12.845638

Guo, X., Huang, S., Fu, X., Wang, B., & Huang, X. (2015). *Vascular segmentation in hepatic CT images using adaptive threshold fuzzy connectedness method*. *14*, 57. https://doi.org/10.1186/s12938-015-0055-z

Hachaj, T., & Ogiela, M. R. (2012). Evaluation of Carotid Artery Segmentation with Centerline Detection and Active Contours without Edges Algorithm.

Multidisciplinary Research and Practice for Information Systems, 468–478. https://doi.org/10.1007/978-3-642-32498-7_35

Haft-Javaherian, M., Fang, L., Muse, V., Schaffer, C. B., Nishimura, N., & Sabuncu, M. R. (2019). Deep convolutional neural networks for segmenting 3D in vivo multiphoton images of vasculature in Alzheimer disease mouse models. *PLOS ONE*, *14*(3), e0213539. https://doi.org/10.1371/journal.pone.0213539

Helmberger, M., Urschler, M., Pienn, M., Balint, Z., Olschewski, A., & Bischof, H. (2013). *Pulmonary Vascular Tree Segmentation from Contrast-Enhanced CT Images*. Retrieved from http://arxiv.org/abs/1304.7140

Hemmati, H., Kamli-Asl, A., Talebpour, A., & Shirani, S. (2015). *Semi-automatic 3D segmentation of carotid lumen in contrast-enhanced computed tomography angiography images*. *31*(8), 1098–1104. https://doi.org/10.1016/j.ejmp.2015.08.002

Heussel, C. P., Achenbach, T., Buschsieweke, C., Kuhnigk, J., Weinheimer, O., Hammer, G., … Kauczor, H. U. (2006). [Quantification of pulmonary emphysema in multislice-CT using different software tools]. *RoFo: Fortschritte auf dem Gebiete der Rontgenstrahlen und der Nuklearmedizin*, *178*(10), 987–998. https://doi.org/10.1055/s-2006-926823

Homann, H., Vesom, G., & Noble, J. A. (2008). Vasculature segmentation of CT liver images using graph cuts and graph-based analysis. *2008 5th IEEE International Symposium on Biomedical Imaging: From Nano to Macro*, 53–56. https://doi.org/10.1109/ISBI.2008.4540930

Hu, X., & Cheng, Y. (2015). *Centerline-based vessel segmentation using graph cuts*. *9443*, 94432E–94432E–5. https://doi.org/10.1117/12.2179082

Huang, S., Wang, B., Cheng, M., Huang, X., & Ju, Y. (2008). *The use of a projection method to simplify portal and hepatic vein segmentation in liver anatomy*. *92*(3), 274–278. https://doi.org/10.1016/j.cmpb.2008.05.008

Huang, W.-C., & Goldgof, D. B. (1993). Adaptive-size meshes for rigid and nonrigid shape analysis and synthesis. *IEEE Transactions on Pattern Analysis and Machine Intelligence*, *15*(6), 611–616.

Isgum, I., Staring, M., Rutten, A., Prokop, M., Viergever, M. A., & Ginneken, B. van. (2009). *Multi-Atlas-Based Segmentation with Local Decision Fusion—Application to Cardiac and Aortic Segmentation in CT Scans*. *28*(7), 1000–1010. https://doi.org/10.1109/TMI.2008.2011480

Jang, Y., Jung, H. Y., Hong, Y., Cho, I., Shim, H., & Chang, H.-J. (2016). Geodesic Distance Algorithm for Extracting the Ascending Aorta from 3D CT Images [Research article]. Retrieved July 3, 2017, from https://www.hindawi.com/journals/cmmm/2016/4561979/abs/

Jin, J., Yang, L., Zhang, X., & Ding, M. (2013). *Vascular Tree Segmentation in Medical Images Using Hessian-Based Multiscale Filtering and Level Set Method*. *2013*, e502013. https://doi.org/10.1155/2013/502013

John, M., Liao, R., Zheng, Y., Nöttling, A., Boese, J., Kirschstein, U., … Walther, T. (2010). System to guide transcatheter aortic valve implantations based on interventional C-arm CT imaging. *International Conference on Medical Image Computing and Computer-Assisted Intervention*, 375–382. Springer.

Kass, M., Witkin, A., & Terzopoulos, D. (1988). Snakes: Active contour models. *International Journal of Computer Vision*, *1*(4), 321–331.

Kawajiri, S., Zhou, X., Zhang, X., Hara, T., Fujita, H., Yokoyama, R., … Hoshi, H. (2008). *Automated segmentation of hepatic vessels in non-contrast X-ray CT images*. *1*(2), 214–222. https://doi.org/10.1007/s12194-008-0031-4

Kerrien, E., Yureidini, A., Dequidt, J., Duriez, C., Anxionnat, R., & Cotin, S. (2017). *Blood vessel modeling for interactive simulation of interventional neuroradiology procedures*. *35*, 685–698. https://doi.org/10.1016/j.media.2016.10.003

Kholmovski Eugene G., Alexander Andrew L., & Parker Dennis L. (2002). Correction of slab boundary artifact using histogram matching. *Journal of Magnetic Resonance Imaging*, *15*(5), 610–617. https://doi.org/10.1002/jmri.10094

Kim, D.-Y. (2013). *Hepatic vessel segmentation on contrast enhanced CT image sequence for liver transplantation planning*. *2013*. https://doi.org/10.4236/jbise.2013.64063

Kirbas, C., & Quek, F. (2004). A Review of Vessel Extraction Techniques and Algorithms. *ACM Comput. Surv.*, *36*(2), 81–121. https://doi.org/10.1145/1031120.1031121

Kirişli, H. A., Schaap, M., Metz, C. T., Dharampal, A. S., Meijboom, W. B., Papadopoulou, S. L., … van Walsum, T. (2013). *Standardized evaluation framework for evaluating coronary artery stenosis detection, stenosis quantification and lumen segmentation algorithms in computed tomography angiography*. *17*(8), 859–876. https://doi.org/10.1016/j.media.2013.05.007

Kitamura, Y., Li, Y., & Ito, W. (2012). Automatic coronary extraction by supervised detection and shape matching. *2012 9th IEEE International Symposium on Biomedical Imaging (ISBI)*, 234–237. https://doi.org/10.1109/ISBI.2012.6235527

Kitrungrotsakul, T., Han, X.-H., Iwamoto, Y., & Chen, Y.-W. (2017). Automatic and Robust Vessel Segmentation in CT Volumes Using Submodular Constrained Graph. *Innovation in Medicine and Healthcare 2017*, 57–66. https://doi.org/10.1007/978-3-319-59397-5_7

Kitrungrotsakul, T., Han, X.-H., Iwamoto, Y., Foruzan, A. H., Lin, L., & Chen, Y.-W. (2017). *Robust hepatic vessel segmentation using multi deep convolution network*. *10137*, 1013711–1013711–6. https://doi.org/10.1117/12.2253811

Korfiatis, P. D., Kalogeropoulou, C., Karahaliou, A. N., Kazantzi, A. D., & Costaridou, L. I. (2011). *Vessel Tree Segmentation in Presence of Interstitial Lung Disease in MDCT*. *15*(2), 214–220. https://doi.org/10.1109/TITB.2011.2112668

Korfiatis, P., Skiadopoulos, S., Sakellaropoulos, P., Kalogeropoulou, C., & Costaridou, L. (2007). Combining 2D wavelet edge highlighting and 3D thresholding for lung segmentation in thin-slice CT. *The British Journal of Radiology*, *80*(960), 996–1004. https://doi.org/10.1259/bjr/20861881

Krizhevsky, A., Sutskever, I., & Hinton, G. E. (2012). Imagenet classification with deep convolutional neural networks. *Advances in Neural Information Processing Systems*, 1097–1105.

Kumar, I. V., & Jeyanthi, S. (2012). Vascular segmentation of interstitial pneumonia patterns in lung using MDCT. *Vascular*, *2*(1).

Lai, J., Huang, Y., Wang, Y., & Wang, J. (2016). *Three-Dimensions Segmentation of Pulmonary Vascular Trees for Low Dose CT Scans*. *1*(17), 1–15. https://doi.org/10.1007/s11220-016-0138-3

Lang, S., Müller, B., Dominietto, M. D., Cattin, P. C., Zanette, I., Weitkamp, T., & Hieber, S. E. (2012). Three-dimensional quantification of capillary networks in healthy and cancerous tissues of two mice. *Microvascular Research*, *84*(3), 314–322. https://doi.org/10.1016/j.mvr.2012.07.002

Lassen, B., Rikxoort, E. M. van, Schmidt, M., Kerkstra, S., Ginneken, B. van, & Kuhnigk, J. M. (2013). Automatic Segmentation of the Pulmonary Lobes from Chest CT Scans Based on Fissures, Vessels, and Bronchi. *IEEE Transactions on Medical Imaging*, *32*(2), 210–222. https://doi.org/10.1109/TMI.2012.2219881

Lathen, G., Jonasson, J., & Borga, M. (2008). Phase based level set segmentation of blood vessels. *2008 19th International Conference on Pattern Recognition*, 1–4. https://doi.org/10.1109/ICPR.2008.4760970

Läthén, G., Jonasson, J., & Borga, M. (2010). *Blood vessel segmentation using multi-scale quadrature filtering*. *31*(8), 762–767. https://doi.org/10.1016/j.patrec.2009.09.020

Law, M. W. K., & Chung, A. C. S. (2013). *Segmentation of Intracranial Vessels and Aneurysms in Phase Contrast Magnetic Resonance Angiography Using Multirange Filters and Local Variances*. *22*(3), 845–859. https://doi.org/10.1109/TIP.2012.2216274

Law, Max W. K., & Chung, A. C. S. (2008). Three-Dimensional Curvilinear Structure Detection Using Optimally Oriented Flux. *Computer Vision – ECCV 2008*, 368–382. https://doi.org/10.1007/978-3-540-88693-8_27

Law, Max W. K., & Chung, A. C. S. (2009a). A Deformable Surface Model for Vascular Segmentation. *Medical Image Computing and Computer-Assisted Intervention – MICCAI 2009*, 59–67. https://doi.org/10.1007/978-3-642-04271-3_8

Law, Max W. K., & Chung, A. C. S. (2009b). *Efficient Implementation for Spherical Flux Computation and Its Application to Vascular Segmentation*. *18*(3), 596–612. https://doi.org/10.1109/TIP.2008.2010073

Law, Max W. K., & Chung, A. C. S. (2010). An Oriented Flux Symmetry Based Active Contour Model for Three-Dimensional Vessel Segmentation. *Computer Vision – ECCV 2010*, 720–734. https://doi.org/10.1007/978-3-642-15558-1_52

LeCun, Y., Bottou, L., Bengio, Y., & Haffner, P. (1998). Gradient-based learning applied to document recognition. *Proceedings of the IEEE*, *86*(11), 2278–2324.

Lee, J., Beighley, P., Ritman, E., & Smith, N. (2007). *Automatic segmentation of 3D micro-CT coronary vascular images*. *11*(6), 630–647. https://doi.org/10.1016/j.media.2007.06.012

Lesage, D., Angelini, E. D., Bloch, I., & Funka-Lea, G. (2009). Design and study of flux-based features for 3D vascular tracking. *2009 IEEE International Symposium on Biomedical Imaging: From Nano to Macro*, 286–289. https://doi.org/10.1109/ISBI.2009.5193040

Lesage, David, Angelini, E. D., Bloch, I., & Funka-Lea, G. (2009). A review of 3D vessel lumen segmentation techniques: Models, features and extraction schemes. *Medical Image Analysis*, *13*(6), 819–845. https://doi.org/10.1016/j.media.2009.07.011

Li, H., Yezzi, A., & Cohen, L. (2009). 3D Multi-branch Tubular Surface and Centerline Extraction with 4D Iterative Key Points. *Medical Image Computing and Computer-Assisted Intervention – MICCAI 2009*, 1042–1050. https://doi.org/10.1007/978-3-642-04271-3_126

Li, Qi, Lv, F., Li, Y., Li, K., Luo, T., & Xie, P. (2009). Subtraction CT angiography for evaluation of intracranial aneurysms: comparison with conventional CT angiography. *European Radiology*, *19*(9), 2261–2267. https://doi.org/10.1007/s00330-009-1416-4

Li, Qiang, Sone, S., & Doi, K. (2003). Selective enhancement filters for nodules, vessels, and airway walls in two- and three-dimensional CT scans. *Medical Physics*, *30*(8), 2040–2051. https://doi.org/10.1118/1.1581411

Litjens, G., Kooi, T., Bejnordi, B. E., Setio, A. A. A., Ciompi, F., Ghafoorian, M., … Sánchez, C. I. (2017). A Survey on Deep Learning in Medical Image Analysis. *ArXiv:1702.05747 [Cs]*. Retrieved from http://arxiv.org/abs/1702.05747

Lo, P., Ginneken, B. van, & Bruijne, M. de. (2010). Vessel tree extraction using locally optimal paths. *2010 IEEE International Symposium on Biomedical Imaging: From Nano to Macro*, 680–683. https://doi.org/10.1109/ISBI.2010.5490083

Lo, Pechin, Van Ginneken, B., Reinhardt, J. M., Yavarna, T., De Jong, P. A., Irving, B., … others. (2012). Extraction of airways from CT (EXACT'09). *IEEE Transactions on Medical Imaging*, *31*(11), 2093–2107.

Longair, M. H., Baker, D. A., & Armstrong, J. D. (2011). Simple Neurite Tracer: open source software for reconstruction, visualization and analysis of neuronal processes. *Bioinformatics*, *27*(17), 2453–2454. https://doi.org/10.1093/bioinformatics/btr390

Lorigo, L. M., Faugeras, O. D., Grimson, W. E. L., Keriven, R., Kikinis, R., Nabavi, A., & Westin, C.-F. (2001). CURVES: Curve evolution for vessel segmentation. *Medical Image Analysis*, *5*(3), 195–206. https://doi.org/10.1016/S1361-8415(01)00040-8

Ma, Y., & Li, X. (2014). *Hepatic vessel segmentation from computed tomography using three-dimensional hyper-complex edge detection operator*. *9069*, 90690K–90690K–6. https://doi.org/10.1117/12.2050193

Maklad, A. S., Matsuhiro, M., Suzuki, H., Kawata, Y., Niki, N., Shimada, M., & Iinuma, G. (2017). *A hybrid 3D region growing and 4D curvature analysis-based automatic abdominal blood vessel segmentation through contrast enhanced CT*. *10134*, 101344C–101344C–7. https://doi.org/10.1117/12.2254327

Malladi, R., Sethian, J. A., & Vemuri, B. C. (1995). Shape modeling with front propagation: A level set approach. *IEEE Transactions on Pattern Analysis and Machine Intelligence*, *17*(2), 158–175.

Manivila, K. D. (2014). Automatic vessel segmentation of lung affected patterns in MDCT using decision tree classification. *Middle-East Journal of Scientific Research*, *22*(11), 1679–1685.

Martin, D. R., Fowlkes, C. C., & Malik, J. (2004). Learning to detect natural image boundaries using local brightness, color, and texture cues. *IEEE Transactions on Pattern Analysis & Machine Intelligence*, (5), 530–549.

Marvasti, N. B., & Acar, B. (2013). Assessment of MRF based joint scale selection and segmentation for 3D liver vessel segmentation task. *2013 21st Signal Processing and Communications Applications Conference (SIU)*, 1–4. https://doi.org/10.1109/SIU.2013.6531368

McKinney, A. M., Palmer, C. S., Truwit, C. L., Karagulle, A., & Teksam, M. (2008). Detection of Aneurysms by 64-Section Multidetector CT Angiography in Patients Acutely Suspected of Having an Intracranial Aneurysm and Comparison with Digital Subtraction and 3D Rotational Angiography. *American Journal of Neuroradiology*, *29*(3), 594–602. https://doi.org/10.3174/ajnr.A0848

Meijboom, W. B., Mieghem, C. A. G. V., Pelt, N. van, Weustink, A., Pugliese, F., Mollet, N. R., … Feyter, P. J. de. (2008). Comprehensive Assessment of Coronary Artery Stenoses: Computed Tomography Coronary Angiography Versus Conventional Coronary Angiography and Correlation with Fractional Flow Reserve in Patients With Stable Angina. *Journal of the American College of Cardiology*, *52*(8), 636–643. https://doi.org/10.1016/j.jacc.2008.05.024

Meijering, E., Niessen, W., Weickert, J., & Viergever, M. (2002). Diffusion-enhanced visualization and quantification of vascular anomalies in three-dimensional rotational angiography: Results of an in-vitro evaluation. *Medical Image Analysis*, *6*(3), 215–233. https://doi.org/10.1016/S1361-8415(02)00081-6

Mendrik, A., Vonken, E., van Ginneken, B., Smit, E., Waaijer, A., Bertolini, G., … Prokop, M. (2010). *Automatic segmentation of intracranial arteries and veins in four-dimensional cerebral CT perfusion scans*. *37*(6), 2956–2966. https://doi.org/10.1118/1.3397813

Merkow, J., Marsden, A., Kriegman, D., & Tu, Z. (2016). Dense Volume-to-Volume Vascular Boundary Detection. *Medical Image Computing and Computer-Assisted Intervention – MICCAI 2016*, 371–379. https://doi.org/10.1007/978-3-319-46726-9_43

Michailovich, O., Rathi, Y., & Tannenbaum, A. (2007). Image Segmentation Using Active Contours Driven by the Bhattacharyya Gradient Flow. *Trans. Img. Proc.*, *16*(11), 2787–2801. https://doi.org/10.1109/TIP.2007.908073

Min, J. K., Leipsic, J., Pencina, M. J., Berman, D. S., Koo, B.-K., Mieghem, C. van, … Mauri, L. (2012). Diagnostic Accuracy of Fractional Flow Reserve from Anatomic CT Angiography. *JAMA*, *308*(12), 1237–1245. https://doi.org/10.1001/2012.jama.11274

Min, J. K., Shaw, L. J., & Berman, D. S. (2010). The Present State of Coronary Computed Tomography Angiography: A Process in Evolution. *Journal of the American College of Cardiology*, *55*(10), 957–965. https://doi.org/10.1016/j.jacc.2009.08.087

Mohan, V., Sundaramoorthi, G., & Tannenbaum, A. (2010). Tubular Surface Segmentation for Extracting Anatomical Structures from Medical Imagery. *IEEE Transactions on Medical Imaging*, *29*(12), 1945–1958. https://doi.org/10.1109/TMI.2010.2050896

Moore, K. A., & Lemischka, I. R. (2006). Stem Cells and Their Niches. *Science*, *311*(5769), 1880–1885. https://doi.org/10.1126/science.1110542

Mozaffarian, D., Benjamin, E. J., Go, A. S., Arnett, D. K., Blaha, M. J., Cushman, M., … Subcommittee, on behalf of the A. H. A. S. C. and S. S. (2016). Heart disease and stroke statistics-2016 update a report from the American Heart Association. *Circulation*, *133*(4), e38–e48. https://doi.org/10.1161/CIR.0000000000000350

Müller-Eschner, M., Müller, T., Biesdorf, A., Wörz, S., Rengier, F., Böckler, D., … von Tengg-Kobligk, H. (2014). *3D morphometry using automated aortic segmentation in native MR angiography: an alternative to contrast enhanced MRA? 4*(2), 80–87. https://doi.org/10.3978/j.issn.2223-3652.2013.10.06

Narayanaswamy, A., Dwarakapuram, S., Bjornsson, C. S., Cutler, B. M., Shain, W., & Roysam, B. (2010). *Robust Adaptive 3-D Segmentation of Vessel Laminae from Fluorescence Confocal Microscope Images and Parallel GPU Implementation*. *29*(3), 583–597. https://doi.org/10.1109/TMI.2009.2022086

Neschis, D. G., & Fairman, R. M. (2004). Magnetic resonance imaging for planning aortic endograft procedures. *Seminars in Vascular Surgery*, *17*, 135–143. Elsevier.

Nimura, Y., Kitasaka, T., & Mori, K. (2010). *Blood vessel segmentation using line-direction vector based on Hessian analysis*. *7623*, 76233Q–76233Q–9. https://doi.org/10.1117/12.844672

Nissen, S. E., & Yock, P. (2001). Intravascular ultrasound: novel pathophysiological insights and current clinical applications. *Circulation*, *103*(4), 604–616.

North American Symptomatic Carotid Endarterectomy Trial Collaborators. (1991). Beneficial effect of carotid endarterectomy in symptomatic patients with high-grade carotid stenosis. *New England Journal of Medicine*, *325*(7), 445–453.

Nyúl, L. G., Udupa, J. K., & others. (1999). On standardizing the MR image intensity scale. *Image*, *1081*.

Ogiela, M. R., & Hachaj, T. (2013). *Automatic segmentation of the carotid artery bifurcation region with a region-growing approach*. *22*(3), 033029–033029. https://doi.org/10.1117/1.JEI.22.3.033029

Oliveira, D. A. B., Feitosa, R. Q., & Correia, M. M. (2008). Automatic Couinaud Liver and Veins Segmentation from CT Images. *BIOSIGNALS (1)*, 249–252.

Pacureanu, A., Revol-Muller, C., Rose, J.-L., Ruiz, M. S., & Peyrin, F. (2010). Vesselness-guided variational segmentation of cellular networks from 3D micro-CT. *2010 IEEE International Symposium on Biomedical Imaging: From Nano to Macro*, 912–915. IEEE.

Pan, X. C., Su, H. R., Lai, S. H., Liu, K. C., & Wu, H. S. (2014). 3D Liver Vessel Reconstruction from CT Images. *2014 2nd International Conference on 3D Vision*, *2*, 75–81. https://doi.org/10.1109/3DV.2014.96

Peters, J., Ecabert, O., Lorenz, C., von Berg, J., Walker, M. J., Ivanc, T. B., … Weese, J. (2008). *Segmentation of the heart and major vascular structures in cardiovascular CT images*. *6914*, 691417–691417–12. https://doi.org/10.1117/12.768494

Peters, Jochen, Ecabert, O., & Weese, J. (2005). Feature optimization via simulated search for model-based heart segmentation. *International Congress Series*, *1281*, 33–38. https://doi.org/10.1016/j.ics.2005.03.023

Peters, R. J., Marquering, H. A., Dogan, H., Hendriks, E. A., de Roos, A., Reiber, J. H., & Stoel, B. C. (2007). Labeling the pulmonary arterial tree in CT images for automatic quantification of pulmonary embolism. *Medical Imaging 2007: Computer-Aided Diagnosis*, *6514*, 65143Q. International Society for Optics and Photonics.

Piccinelli, M., Veneziani, A., Steinman, D. A., Remuzzi, A., & Antiga, L. (2009). A Framework for Geometric Analysis of Vascular Structures: Application to Cerebral Aneurysms. *IEEE Transactions on Medical Imaging*, *28*(8), 1141–1155. https://doi.org/10.1109/TMI.2009.2021652

Pik, J. H. T., & Morgan, M. K. (2000). Microsurgery for Small Arteriovenous Malformations of the Brain: Results in 110 Consecutive Patients. *Neurosurgery*, *47*(3), 571–577. https://doi.org/10.1097/00006123-200009000-00006

Pock, Thomas G. (2004). *Robust segmentation of tubular structures in 3D volume data*. Technische Universit¨at Graz, Graz.

Potthast, S., Mitsumori, L., Stanescu, L. A., Richardson, M. L., Branch, K., Dubinsky, T. J., & Maki, J. H. (2010). Measuring aortic diameter with different MR techniques: Comparison of three-dimensional (3D) navigated steady-state free-precession (SSFP), 3D contrast-enhanced magnetic resonance angiography (CE-MRA), 2D T2 black blood, and 2D cine SSFP. *Journal of Magnetic Resonance Imaging*, *31*(1), 177–184.

Prasad, M. N., Brown, M. S., Ahmad, S., Abtin, F., Allen, J., da Costa, I., … Goldin, J. G. (2008). Automatic Segmentation of Lung Parenchyma in the Presence of Diseases Based on Curvature of Ribs. *Academic Radiology*, *15*(9), 1173–1180. https://doi.org/10.1016/j.acra.2008.02.004

Pu, J., Roos, J., Yi, C. A., Napel, S., Rubin, G. D., & Paik, D. S. (2008). Adaptive border marching algorithm: Automatic lung segmentation on chest CT images.

Computerized Medical Imaging and Graphics, *32*(6), 452–462. https://doi.org/10.1016/j.compmedimag.2008.04.005

Qian, X., Brennan, M. P., Dione, D. P., Dobrucki, W. L., Jackowski, M. P., Breuer, C. K., … Papademetris, X. (2007). Detection of Complex Vascular Structures using Polar Neighborhood Intensity Profile. *2007 IEEE 11th International Conference on Computer Vision*, 1–8. https://doi.org/10.1109/ICCV.2007.4409172

Reinbacher, C., Pock, T., Bauer, C., & Bischof, H. (2010). Variational segmentation of elongated volumetric structures. *2010 IEEE Computer Society Conference on Computer Vision and Pattern Recognition*, 3177–3184. https://doi.org/10.1109/CVPR.2010.5539771

Remonda, L., Senn, P., Barth, A., Arnold, M., Lövblad, K.-O., & Schroth, G. (2002). Contrast-Enhanced 3D MR Angiography of the Carotid Artery: Comparison with Conventional Digital Subtraction Angiography. *American Journal of Neuroradiology*, *23*(2), 213–219.

Rikxoort, E. M. van, Hoop, B. de, Viergever, M. A., Prokop, M., & Ginneken, B. van. (2009). Automatic lung segmentation from thoracic computed tomography scans using a hybrid approach with error detection. *Medical Physics*, *36*(7), 2934–2947. https://doi.org/10.1118/1.3147146

Rooij, W. J. van, Sprengers, M. E., Gast, A. N. de, Peluso, J. P. P., & Sluzewski, M. (2008). 3D Rotational Angiography: The New Gold Standard in the Detection of Additional Intracranial Aneurysms. *American Journal of Neuroradiology*, *29*(5), 976–979. https://doi.org/10.3174/ajnr.A0964

Rose, J.-L., Rose, J.-L., Revol-Muller, C., Charpigny, D., & Odet, C. (2009). Shape prior criterion based on Tchebichef moments in variational region growing. *2009 16th IEEE International Conference on Image Processing (ICIP)*, 1081–1084. IEEE.

Rosenblatt, F. (1958). The perceptron: A probabilistic model for information storage and organization in the brain. *Psychological Review*, *65*(6), 386.

Rudyanto, R. D., Kerkstra, S., van Rikxoort, E. M., Fetita, C., Brillet, P.-Y., Lefevre, C., … van Ginneken, B. (2014). Comparing algorithms for automated vessel segmentation in computed tomography scans of the lung: the VESSEL12 study.

Medical Image Analysis, *18*(7), 1217–1232. https://doi.org/10.1016/j.media.2014.07.003

Samet, R., & Yildirim, Z. (2016). A New Methodology for Blood Vessel Segmentation on Lung CT Images. *2016 Nicograph International (NicoInt)*, 1–7. https://doi.org/10.1109/NicoInt.2016.1

Sanelli, P. C., Mifsud, M. J., & Stieg, P. E. (2004). Role of CT Angiography in Guiding Management Decisions of Newly Diagnosed and Residual Arteriovenous Malformations. *American Journal of Roentgenology*, *183*(4), 1123–1126. https://doi.org/10.2214/ajr.183.4.1831123

Sarieddeen, F., El Berbari, R., Imad, S., Baki, J. A., Hamad, M., Blanc, R., … Chenoune, Y. (2013). Image Clustering Framework for BAVM Segmentation in 3DRA Images: Performance Analysis. *World Academy of Science, Engineering and Technology, International Journal of Computer, Electrical, Automation, Control and Information Engineering*, *7*(1), 116–120.

Sato, Y., Nakajima, S., Atsumi, H., Koller, T., Gerig, G., Yoshida, S., & Kikinis, R. (1997). 3D multi-scale line filter for segmentation and visualization of curvilinear structures in medical images. In *CVRMed-MRCAS'97* (pp. 213–222). https://doi.org/10.1007/BFb0029240

Schaap, M., Walsum, T. van, Neefjes, L., Metz, C., Capuano, E., Bruijne, M. de, & Niessen, W. (2011). *Robust Shape Regression for Supervised Vessel Segmentation and its Application to Coronary Segmentation in CTA*. *30*(11), 1974–1986. https://doi.org/10.1109/TMI.2011.2160556

Schaap, Michiel, Neefjes, L., Metz, C., Giessen, A. van der, Weustink, A., Mollet, N., … Niessen, W. (2009). Coronary Lumen Segmentation Using Graph Cuts and Robust Kernel Regression. *Information Processing in Medical Imaging*, 528–539. https://doi.org/10.1007/978-3-642-02498-6_44

Schaap, Michiel, Smal, I., Metz, C., van Walsum, T., & Niessen, W. (2007). Bayesian Tracking of Elongated Structures in 3D Images. In N. Karssemeijer & B. Lelieveldt (Eds.), *Information Processing in Medical Imaging* (pp. 74–85). Springer Berlin Heidelberg.

Schmidt-Richberg, A., Handels, H., & Ehrhardt, J. (2009). Integrated Segmentation and Non-linear Registration for Organ Segmentation and Motion Field Estimation in 4D CT Data. *Methods of Information in Medicine*, *48*(4), 344–349. https://doi.org/10.3414/ME9234

Schuijf, J. D., & Bax, J. J. (2008). CT angiography: an alternative to nuclear perfusion imaging? *Heart*, *94*(3), 255–257. https://doi.org/10.1136/hrt.2006.105833

Schwier, M., Hahn, H. K., Dahmen, U., & Dirsch, O. (2016). *Segmentation of vessel structures in serial whole slide sections using region-based context features*. *9791*, 97910E–97910E–14. https://doi.org/10.1117/12.2216497

Seada, N. A., Hamad, S., & Mostafa, M. G. M. (2016). Automatically Seeded Region Growing Approach for Automatic Segmentation of Ascending Aorta. *Proceedings of the 10th International Conference on Informatics and Systems*, 127–132. https://doi.org/10.1145/2908446.2908479

Seidel, T., Edelmann, J.-C., & Sachse, F. B. (2016). *Analyzing Remodeling of Cardiac Tissue: A Comprehensive Approach Based on Confocal Microscopy and 3D Reconstructions*. *44*(5), 1436–1448. https://doi.org/10.1007/s10439-015-1465-6

Seo, J. J., & Park, J. W. (2009). Automatic Segmentation of Hepatic Vessels in Abdominal MDCT Image. *2009 Fourth International Conference on Computer Sciences and Convergence Information Technology*, 420–424. https://doi.org/10.1109/ICCIT.2009.82

Shikata, H., McLennan, G., Hoffman, E. A., & Sonka, M. (2009). *Segmentation of Pulmonary Vascular Trees from Thoracic 3D CT Images*. *2009*, 24:1–24:11. https://doi.org/10.1155/2009/636240

Shoujun, Z., Jian, Y., Yongtian, W., & Wufan, C. (2010). *Automatic segmentation of coronary angiograms based on fuzzy inferring and probabilistic tracking*. *9*, 40. https://doi.org/10.1186/1475-925X-9-40

Sled, J. G., Zijdenbos, A. P., & Evans, A. C. (1998). A nonparametric method for automatic correction of intensity nonuniformity in MRI data. *IEEE Transactions on Medical Imaging*, *17*(1), 87–97. https://doi.org/10.1109/42.668698

Sluimer, I., Prokop, M., & Ginneken, B. van. (2005). Toward automated segmentation of the pathological lung in CT. *IEEE Transactions on Medical Imaging*, *24*(8), 1025–1038. https://doi.org/10.1109/TMI.2005.851757

Small, D. M., Jones, J. S., Tendler, I. I., Miller, P. E., Ghetti, A., & Nishimura, N. (2018). Label-free imaging of atherosclerotic plaques using third-harmonic generation microscopy. *Biomedical Optics Express*, *9*(1), 214–229. https://doi.org/10.1364/BOE.9.000214

Smistad, E., Elster, A. C., & Lindseth, F. (2014). GPU accelerated segmentation and centerline extraction of tubular structures from medical images. *International Journal of Computer Assisted Radiology and Surgery*, *9*(4), 561–575. https://doi.org/10.1007/s11548-013-0956-x

Sonka, M., Hlavac, V., & Boyle, R. (2014). *Image processing, analysis, and machine vision*. Cengage Learning.

Spiegel, M., Redel, T., Struffert, T., Hornegger, J., & Doerfler, A. (2011). *A 2D driven 3D vessel segmentation algorithm for 3D digital subtraction angiography data*. *56*(19), 6401. https://doi.org/10.1088/0031-9155/56/19/015

Srichai, M. B., Lim, R. P., Wong, S., & Lee, V. S. (2009). Cardiovascular applications of phase-contrast MRI. *American Journal of Roentgenology*, *192*(3), 662–675.

Stafford Johnson, D. B., Prince, M. R., & Chenevert, T. L. (1998). Magnetic resonance angiography: A review. *Academic Radiology*, *5*(4), 289–305. https://doi.org/10.1016/S1076-6332(98)80230-4

Sun, X., Zhang, H., & Duan, H. (2006). 3D Computerized Segmentation of Lung Volume with Computed Tomography. *Academic Radiology*, *13*(6), 670–677. https://doi.org/10.1016/j.acra.2006.02.039

Tang, H., van Walsum, T., van Onkelen, R. S., Hameeteman, R., Klein, S., Schaap, M., … Niessen, W. J. (2012). *Semiautomatic carotid lumen segmentation for quantification of lumen geometry in multispectral MRI*. *16*(6), 1202–1215. https://doi.org/10.1016/j.media.2012.05.014

Terzopoulos, D., & Vasilescu, M. (1991). Sampling and reconstruction with adaptive mesh. *Proceedings. 1991 IEEE Computer Society Conference on Computer Vision and Pattern Recognition*, 70–75. IEEE.

Terzopoulos, D., Witkin, A., & Kass, M. (1988). Symmetry-seeking models and 3D object reconstruction. *International Journal of Computer Vision, 1*(3), 211–221.

Thomas Jonathan B., Antiga Luca, Che Susan L., Milner Jaques S., Hangan Steinman Dolores A., Spence J. David, … Steinman David A. (2005). Variation in the Carotid Bifurcation Geometry of Young Versus Older Adults. *Stroke*, *36*(11), 2450–2456. https://doi.org/10.1161/01.STR.0000185679.62634.0a

Tsai, P. S., Kaufhold, J. P., Blinder, P., Friedman, B., Drew, P. J., Karten, H. J., … Kleinfeld, D. (2009). Correlations of neuronal and microvascular densities in murine cortex revealed by direct counting and colocalization of nuclei and vessels. *The Journal of Neuroscience: The Official Journal of the Society for Neuroscience*, *29*(46), 14553–14570. https://doi.org/10.1523/JNEUROSCI.3287-09.2009

Tu, Z. (2005). Probabilistic Boosting-Tree: Learning Discriminative Models for Classification, Recognition, and Clustering. *ICCV*, *2*, 2.

Tung, K. P., Shi, W. Z., Silva, R. D., Edwards, E., & Rueckert, D. (2011). Automatical vessel wall detection in intravascular coronary OCT. *2011 IEEE International Symposium on Biomedical Imaging: From Nano to Macro*, 610–613. https://doi.org/10.1109/ISBI.2011.5872481

Türetken, E., Benmansour, F., & Fua, P. (2012). Automated reconstruction of tree structures using path classifiers and Mixed Integer Programming. *2012 IEEE Conference on Computer Vision and Pattern Recognition*, 566–573. https://doi.org/10.1109/CVPR.2012.6247722

Tyrrell, J. A., Tomaso, E. di, Fuja, D., Tong, R., Kozak, K., Jain, R. K., & Roysam, B. (2007). Robust 3-D Modeling of Vasculature Imagery Using Superellipsoids. *IEEE Transactions on Medical Imaging*, *26*(2), 223–237. https://doi.org/10.1109/TMI.2006.889722

Tyrrell, James A., Mahadevan, V., Tong, R. T., Brown, E. B., Jain, R. K., & Roysam, B. (2005). *A 2-D/3-D model-based method to quantify the complexity of microvasculature imaged by in vivo multiphoton microscopy*. *70*(3), 165–178. https://doi.org/10.1016/j.mvr.2005.08.005

Ughi, G. J., Adriaenssens, T., Onsea, K., Kayaert, P., Dubois, C., Sinnaeve, P., … D'hooge, J. (2012). *Automatic segmentation of in-vivo intra-coronary optical coherence tomography images to assess stent strut apposition and coverage*. *28*(2), 229–241. https://doi.org/10.1007/s10554-011-9824-3

Ugurlu, D., Demirci, S., Navab, N., & Celebi, M. S. (2011). A Vessel Segmentation Method for MRA Images Based on Multi-scale Analysis and Level Set Framework. *3rd International MICCAI-Workshop on Computation and Visualization on (Intra) Vascular Imaging*.

Ukwatta, E., Yuan, J., Rajchl, M., Qiu, W., Tessier, D., & Fenster, A. (2013). 3-D Carotid Multi-Region MRI Segmentation by Globally Optimal Evolution of Coupled Surfaces. *IEEE Transactions on Medical Imaging*, *32*(4), 770–785. https://doi.org/10.1109/TMI.2013.2237784

Underhill, H. R., Hatsukami, T. S., Fayad, Z. A., Fuster, V., & Yuan, C. (2010). MRI of carotid atherosclerosis: clinical implications and future directions. *Nature Reviews Cardiology*, *7*(3), 165–173. https://doi.org/10.1038/nrcardio.2009.246

Unger, M., Pock, T., Trobin, W., Cremers, D., & Bischof, H. (2008). TVSeg-Interactive Total Variation Based Image Segmentation. *BMVC, 31*, 44–46. Citeseer.

Upchurch, G. R., Schaub, T. A., & others. (2006). Abdominal aortic aneurysm. *Am Fam Physician*, *73*(7), 1198–204.

Valencia, L. F., Azencot, J., & Orkisz, M. (2010). Algorithm for Blood-Vessel Segmentation in 3D Images Based on a Right Generalized Cylinder Model: Application to Carotid Arteries. *Computer Vision and Graphics*, 27–34. https://doi.org/10.1007/978-3-642-15910-7_4

Vasilescu, M., & Terzopoulos, D. (1992). Adaptive meshes and shells: Irregular triangulation, discontinuities, and hierarchical subdivision. *Proceedings 1992*

IEEE Computer Society Conference on Computer Vision and Pattern Recognition, 829–832. IEEE.

Vazquez-Reina, A., Miller, E., Frisken, S., & Malek, A. (2008). *Multiscale Shape Priors for 3D Branching Structures in Vasculature Segmentation*.

Wala, J., Fotin, S., Lee, J., Jirapatnakul, A., Biancardi, A., & Reeves, A. (2011). *Automated segmentation of the pulmonary arteries in low-dose CT by vessel tracking*. Retrieved from http://arxiv.org/abs/1106.5460

Wang, C., Moreno, R., & Smedby, Ö. (2012). Vessel segmentation using implicit model-guided level sets. *MICCAI Workshop" 3D Cardiovascular Imaging: A MICCAI Segmentation Challenge", Nice France, 1st of October 2012*.

Wang, C., & Smedby, O. (2008). An automatic seeding method for coronary artery segmentation and skeletonization in CTA. *The Insight Journal*, *43*, 1–8.

Wang, C., & Smedby, Ö. (2010). *Integrating automatic and interactive methods for coronary artery segmentation: let the PACS workstation think ahead*. *5*(3), 275–285. https://doi.org/10.1007/s11548-009-0393-z

Wang, L., Hansen, C., Zidowitz, S., & Hahn, H. K. (2014). *Segmentation and separation of venous vasculatures in liver CT images*. *9035*, 90350Q–90350Q–8. https://doi.org/10.1117/12.2043406

Wang, Yan, Seguro, F., Kao, E., Zhang, Y., Faraji, F., Zhu, C., … Liu, J. (2017). *Segmentation of lumen and outer wall of abdominal aortic aneurysms from 3D black-blood MRI with a registration based geodesic active contour model*. *40*, 1–10. https://doi.org/10.1016/j.media.2017.05.005

Wang, Yi, Fang, B., Pi, J., Wu, L., Wang, P. S., & Wang, H. (2013). Automatic multi-scale segmentation of intrahepatic vessel in CT images for liver surgery planning. *International Journal of Pattern Recognition and Artificial Intelligence*, *27*(01), 1357001.

Wang, Z., Xiong, W., Huang, W., Zhou, J., & Venkatesh, S. K. (2012). *A fuzzy clustering vessel segmentation method incorporating line-direction information*. *8314*, 83143I–83143I–8. https://doi.org/10.1117/12.919106

Weickert, J. (2001). Applications of nonlinear diffusion in image processing and computer vision. *Acta Math. Univ. Comenianae, 70*(1), 33–50.

Will, S., Hermes, L., Buhmann, J. M., & Puzicha, J. (2000). On learning texture edge detectors. *Proceedings 2000 International Conference on Image Processing (Cat. No. 00CH37101), 3*, 877–880. IEEE.

Witkin, A., Terzopoulos, D., & Kass, M. (1987). Signal matching through scale space. *International Journal of Computer Vision*, *1*(2), 133–144.

Wörz, S., Hoegen, P., Liao, W., Müller-Eschner, M., Kauczor, H.-U., von Tengg-Kobligk, H., & Rohr, K. (2016, March 1). *Framework for quantitative evaluation of 3D vessel segmentation approaches using vascular phantoms in conjunction with 3D landmark localization and registration*. *9784*, 978419. https://doi.org/10.1117/12.2216091

Worz, S., Tengg-Kobligk, H. v, Henninger, V., Rengier, F., Schumacher, H., Bockler, D., … Rohr, K. (2010). *3-D Quantification of the Aortic Arch Morphology in 3-D CTA Data for Endovascular Aortic Repair*. *57*(10), 2359–2368. https://doi.org/10.1109/TBME.2010.2053539

Wu, C., Agam, G., Roy, A. S., & Armato, S. G., III. (2004, May 1). *Regulated morphology approach to fuzzy shape analysis with application to blood vessel extraction in thoracic CT scans*. *5370*, 1262–1270. https://doi.org/10.1117/12.533175

Wu, J., He, Y., Yang, Z., Guo, C., Luo, Q., Zhou, W., … Gong, H. (2014). 3D BrainCV: Simultaneous visualization and analysis of cells and capillaries in a whole mouse brain with one-micron voxel resolution. *NeuroImage*, *87*, 199–208. https://doi.org/10.1016/j.neuroimage.2013.10.036

Xiao, C., Staring, M., Wang, Y., Shamonin, D. P., & Stoel, B. C. (2013). Multiscale Bi-Gaussian Filter for Adjacent Curvilinear Structures Detection with Application to Vasculature Images. *IEEE Transactions on Image Processing*, *22*(1), 174–188. https://doi.org/10.1109/TIP.2012.2216277

Xie, S., & Tu, Z. (2015). *Holistically-Nested Edge Detection*. 1395–1403. Retrieved from http://openaccess.thecvf.com/content_iccv_2015/html/Xie_Holistically-Nested_Edge_Detection_ICCV_2015_paper.html

Xie, Y., Padgett, J., Biancardi, A. M., & Reeves, A. P. (2014). *Automated aorta segmentation in low-dose chest CT images*. *9*(2), 211–219. https://doi.org/10.1007/s11548-013-0924-5

Xu, Y., van Beek, E. J. R., Hwanjo, Y., Guo, J., McLennan, G., & Hoffman, E. A. (2006). Computer-aided Classification of Interstitial Lung Diseases Via MDCT: 3D Adaptive Multiple Feature Method (3D AMFM). *Academic Radiology*, *13*(8), 969–978. https://doi.org/10.1016/j.acra.2006.04.017

Yoshida, H., Sakas, G., & Linguraru, M. G. (2012). *Liver Segmental Anatomy and Analysis from Vessel and Tumor Segmentation via Optimized Graph Cuts*. Springer.

Yureidini, A., Kerrien, E., & Cotin, S. (2012). *Robust RANSAC-based blood vessel segmentation*. *8314*, 83141M–83141M–8. https://doi.org/10.1117/12.911670

Zambal, S., Hladuvka, J., Kanitsar, A., & Bühler, K. (2008). Shape and appearance models for automatic coronary artery tracking. *The Insight Journal*, *4*.

Zeng, Y. Z., Zhao, Y. Q., Liao, M., Zou, B. J., Wang, X. F., & Wang, W. (2016). *Liver vessel segmentation based on extreme learning machine*. *32*(5), 709–716. https://doi.org/10.1016/j.ejmp.2016.04.003

Zhai, Z., Staring, M., & Stoel, B. C. (2016). *Lung vessel segmentation in CT images using graph-cuts*. *9784*, 97842K–97842K–8. https://doi.org/10.1117/12.2216827

Zhang, J., He, Z., Dehmeshki, J., & Qanadli, S. D. (2010). Segmentation of pulmonary artery based on ct angiography image. *2010 Chinese Conference on Pattern Recognition (CCPR)*, 1–5. IEEE.

Zhao, F., & Bhotika, R. (2011). Coronary artery tree tracking with robust junction detection in 3D CT Angiography. *2011 IEEE International Symposium on Biomedical Imaging: From Nano to Macro*, 2066–2071. https://doi.org/10.1109/ISBI.2011.5872819

Zhao, Fei, Zhang, H., Wahle, A., Thomas, M. T., Stolpen, A. H., Scholz, T. D., & Sonka, M. (2009). *Congenital aortic disease: 4D magnetic resonance segmentation and quantitative analysis*. *13*(3), 483–493. https://doi.org/10.1016/j.media.2009.02.005

Zheng, M., Carr, J. J., & Ge, Y. (2013). Automatic Aorta Detection in Non-contrast 3D Cardiac CT Images Using Bayesian Tracking Method. *Medical Computer Vision. Large Data in Medical Imaging*, 130–137. https://doi.org/10.1007/978-3-319-05530-5_13

Zheng, Y., John, M., Liao, R., Nottling, A., Boese, J., Kempfert, J., … Comaniciu, D. (2012). *Automatic Aorta Segmentation and Valve Landmark Detection in C-Arm CT for Transcatheter Aortic Valve Implantation*. *31*(12), 2307–2321. https://doi.org/10.1109/TMI.2012.2216541

Zheng, Y., Yang, D., John, M., & Comaniciu, D. (2014). *Multi-Part Modeling and Segmentation of Left Atrium in C-Arm CT for Image-Guided Ablation of Atrial Fibrillation*. *33*(2), 318–331. https://doi.org/10.1109/TMI.2013.2284382

Zheng, Yefeng, Loziczonek, M., Georgescu, B., Zhou, S. K., Vega-Higuera, F., & Comaniciu, D. (2011). *Machine learning based vesselness measurement for coronary artery segmentation in cardiac CT volumes*. *7962*, 79621K–79621K–12. https://doi.org/10.1117/12.877233

Zhou, C., Chan, H.-P., Chughtai, A., Patel, S., Hadjiiski, L. M., Wei, J., & Kazerooni, E. A. (2012). *Automated coronary artery tree extraction in coronary CT angiography using a multiscale enhancement and dynamic balloon tracking (MSCAR-DBT) method*. *36*(1), 1–10. https://doi.org/10.1016/j.compmedimag.2011.04.001

Zhou, C., Chan, H.-P., Sahiner, B., Hadjiiski, L. M., Chughtai, A., Patel, S., … Kazerooni, E. A. (2007). Automatic multiscale enhancement and segmentation of pulmonary vessels in CT pulmonary angiography images for CAD applications. *Medical Physics*, *34*(12), 4567–4577. https://doi.org/10.1118/1.2804558

Zhu, C., Sadat, U., Patterson, A. J., Teng, Z., Gillard, J. H., & Graves, M. J. (2014). 3D high-resolution contrast enhanced MRI of carotid atheroma—a technical update. *Magnetic Resonance Imaging*, *32*(5), 594–597.

Zhu, Q., Xiong, H., & Jiang, X. (2012). Pulmonary Blood Vessels and Nodules Segmentation via Vessel Energy Function and Radius-Variable Sphere Model. *2012 IEEE Second International Conference on Healthcare Informatics, Imaging and Systems Biology*, 121–121. https://doi.org/10.1109/HISB.2012.46

Zhu, X., Xue, Z., Gao, X., Zhu, Y., & Wong, S. T. C. (2009). VOLES: Vascularity-Oriented LEvel Set algorithm for pulmonary vessel segmentation in image guided intervention therapy. 2009 IEEE International Symposium on Biomedical Imaging: From Nano to Macro, 1247–1250. https://doi.org/10.1109/ISBI.2009.5193288

CHAPTER 3

DEEP CONVOLUTIONAL NEURAL NETWORKS FOR SEGMENTING 3D IN VIVO MULTIPHOTON IMAGES OF VASCULATURE IN ALZHEIMER DISEASE MOUSE MODELS

3.1 Abstract

The health and function of tissue rely on its vasculature network to provide reliable blood perfusion. Volumetric imaging approaches, such as multiphoton microscopy, are able to generate detailed 3D images of blood vessels that could contribute to our understanding of the role of vascular structure in normal physiology and in disease mechanisms. The segmentation of vessels, a core image analysis problem, is a bottleneck that has prevented the systematic comparison of 3D vascular architecture across experimental populations. We explored the use of convolutional neural networks to segment 3D vessels within volumetric in vivo images acquired by multiphoton microscopy. We evaluated different network architectures and machine learning techniques in the context of this segmentation problem. We show that our optimized convolutional neural network architecture with a customized loss function, which we call DeepVess, yielded a segmentation accuracy that was better than state-of-the-art methods, while also being orders of magnitude faster than the manual annotation. To explore the effects of aging and Alzheimer's disease on capillaries, we applied DeepVess to 3D images of cortical blood vessels in young and old mouse models of Alzheimer's disease and wild type littermates. We found little difference in the distribution of capillary

diameter or tortuosity between these groups but did note a decrease in the number of longer capillary segments (> 75μm) in aged animals as compared to young, in both wild type and Alzheimer's disease mouse models.

3.2 Introduction

The performance of organs and tissues depend critically on the delivery of nutrients and removal of metabolic products by the vasculature. Blood flow deficits due to disease related factors or aging often leads to functional impairment [1]. In particular, the brain has essentially no energy reserve and relies on the vasculature to provide uninterrupted blood perfusion [2].

Multiple image modalities can be used to study vascular structure and dynamics, each offering tradeoffs between the smallest vessels that can be resolved and the volume of tissue that can be imaged. Recent work with several modalities, including photoacoustic microscopy [3], optical coherence tomography [4], and multiphoton microscopy (MPM) [5], enable individual capillaries to be resolved in 3D over volumes approaching 1 mm^3 in living animals. The analysis of such images is one of the most critical and time-consuming tasks of this research, especially when it has to be done manually.

For example, in our own work we investigated the mechanisms leading to reduced brain blood flow in mouse models of Alzheimer's disease (AD), which required extracting topology from capillary networks each with $\sim 1,000$ vessels from dozens of animals. The manual tracing of these networks required $\sim 40\times$ the time required to acquire the images, greatly slowing research progress [6]. The labor involved in such tasks limits our ability to

investigate the vital link between capillary function and many different diseases. Many studies have shown anatomical and physiological differences in microvasculature associated both with age and AD, such as changes in composition of large vessel walls' smooth muscles [7], increased collagen VI in microvascular basement membranes and their thickening in AD [8], and age-associated reduction of microvascular plasticity and the ability of the vessels to respond appropriately to changes in metabolic demand [9].

In this paper, we consider the segmentation of vessels, a core image analysis problem that has received considerable attention [10, 11]. As in other segmentation and computer vision problems, in recent years deep neural networks (DNNs) have offered state-of-the-art performance [12]. DNN approaches often rely on formulating the problem as supervised classification (or regression), where a neural network model is trained on some (manually) labeled data. For a survey on deep learning in medical image analysis, see a recent review by Litjens et al. [12].

Here, we explore the use of a convolutional neural network (CNN) to segment 3D vessels within volumetric in vivo MPM images. In vivo MPM imaging of blood vessels has the advantage that it captures the size and shape of vessels without introducing artifacts from postmortem tissue processing. However, blood flow generates features which must be accommodated in the vessel segmentation. We conduct a thorough study of different network architectures and machine learning techniques in the context of this segmentation problem. We apply the final model, which we call DeepVess, on image stacks of cortical blood vessels in mouse models of AD and wild type (WT) littermates. Our experimental results show that DeepVess yields segmentation accuracy that is better

than current state-of-the-art, while being orders of magnitude faster than the manual annotation (20-30 hours manual work vs. 10 minutes computation time). The segmentation method developed in this work provides robust and efficient analysis which enabled us to quantify and compare capillary diameters and other vascular parameters from in vivo cortex images across multiple animals, with varying age as well as across WT mice and AD models.

3.3 Related work

Blood vessel segmentation is one of the most common and time-consuming tasks in biomedical image analysis. This problem can either be approached in 2D or 3D, depending on the specifics of the application and analytic technique. The most established blood vessel segmentation methods are developed for 2D retinography [13] and 3D CT/MRI [11].

Among segmentation methods, region-based methods are well-known for their simplicity and low computational cost [14]. For example, Yi et al. [15] developed a 3D region growing vessel segmentation method based on local cube tracking. In related work, Mille et al. [16] used a 3D parametric deformable model based on the explicit representation of a vessel tree to generate centerlines. In recent years, these traditional segmentation methods have become less popular and are considered to be limited in comparison to deep learning methods, because they require handcrafted filters, features, or logical rules and often yield lower accuracy.

Today, in problems that are closely related to ours, various deep learning techniques dominate state-of-the-art. For instance, in a recent Kaggle challenge for

diabetic retinopathy detection within color fundus images, deep learning was used by most of the 661 participant teams, including the top four teams. Interestingly, those top four methods surpassed the average human accuracy. Subsequently, Gulshan et al. [17] adopted the Google Inception V3 network [18] for this task and reached the accuracy of seven ophthalmologists combined. For retinal blood vessel segmentation, Wu et al. [19] used a CNN-based approach to extract the entire connected vessel tree. Fu et al. [20] proposed to add a conditional random fields (CRF) to post-process the CNN segmentation output. They further improved their method by replacing the CRF with a recurrent neural network (RNN), which allows them to train the complete network in an end-to-end fashion [21]. Further, Maninis et al. [22] addressed retinal vessel and optic disc segmentation problems using one CNN network and could surpass the human expert.

There are 3D capillary image datasets in mice [14] and human [23] that were segmented using traditional segmentation methods and have illustrated the scientific value of such information, but few such datasets are available.

To the best of our knowledge, there are only two studies that used deep learning for our problem: vascular image analysis of multi-photon microscopy (MPM) images. The first one is by Teikari et al. [24] who proposed a hybrid 2D-3D CNN architecture to produce state-of-the-art vessel segmentation results in 3D microscopy images. The main limitation of their method was the use of 2D convolutions and 2D conditional random fields (CRF)s, which restrict the full exploitation of the information along the third dimension. The second study was conducted by Bates et al. [25], where the authors applied a convolutional long short-term memory RNN to extract 3D vascular centerlines

of endothelial cells. Their approach was based on the U-net architecture [26], which is a well-known fully convolutional network [27] widely used for biomedical image segmentation. Bates and colleagues achieved state-of-the-art results in terms of centerline extraction; nevertheless, they reported that certain vessels in the images were combined in the automatic segmentation. Finally, we consider the 3D U-Net [28], which is the volumetric version of the U-net architecture [26] and is regarded by many as state-of-the-art for microscopy image segmentation problems.

3.4 Data and methods

The proposed vasculature segmentation method for 3D in vivo MPM images, DeepVess, consists of (i) pre-processing to remove in vivo physiological motion artifacts due to respiration and heartbeat, (ii) applying a 3D CNN for binary segmentation of the vessel tree, and (iii) post-processing to remove artifacts such as network discontinuities and holes.

3.4.1 Data

3.4.1.1 Animals

All animal procedures were approved by the Cornell University Institutional Animal Care and Use Committee and were performed under the guidance of the Cornell Center for Animal Resources and Education. We used double transgenic mice (B6.Cg-Tg (APPswe, PSEN1dE9) 85Dbo/J, referred to as APP/PS1 mice) that express two human proteins associated with early onset AD, a chimeric mouse/human amyloid precursor protein (Mo/HuAPP695swe) and a mutant human presenilin1 (PS1-dE9), which is a

standard model of AD and typically develops amyloid-beta plaque deposition around 6 months of age [29]. Littermate WT mice (C57BL/6) served as controls. Animals were of both sexes and ranged in age from 18 to 31 weeks for young mice and from 50 to 64 weeks for the old mice (6 WT and 6 AD at each age, for a total of 24 mice).

3.4.1.2 In vivo imaging of cortical vasculature

We use a locally-designed multiphoton microscope [30] for in vivo imaging of the brain vasculature. Glass-covered craniotomies were prepared over parietal cortex, as described previously [6, 31, 32]. For cranial window implantation and imaging, mice were anesthetized with 3% isoflurane and then maintained on 1.5% isoflurane in 100% oxygen. Mice were injected with 0.05 mg/100g of mouse weight glycopyrrolate (Baxter Inc.) or 0.005 mg/100g atropine (intramuscular 54925-063-10, Med-Pharmex Inc.). At time of surgery as well as 1 and 2 days after mice received 0.025 mg/100g dexamethasone (subcutaneous 07-808-8194, Phoenix Pharm Inc.), and 0.5 mg/100g ketoprofen (intramuscular, Zoetis Inc.). Bupivacaine (0.1 ml, 0.125%, Hospira Inc.) was subcutaneously injected at the incision site. Animals were injected with 1 ml/100g mouse 5% (w/v) glucose in normal saline subcutaneously every hour during imaging and surgery. Body temperature was maintained at 37^{o}C with a feedback-controlled heating blanket (40-90-8D DC, FHC). Mice were euthanized with pentobarbital overdose after their last imaging session.

We waited at least three weeks after the surgery before imaging to give time for the mild surgically-induced inflammation to subside. Windows typically remained clear for as long as 20 weeks. This technique allows us to map the architecture of the

vasculature throughout the top 500 μm of the cortex. Briefly, the blood plasma of an anesthetized mouse was labeled with an intravenous injection of Texas Red labeled dextran (70 KDa, Life Technologies). The two-photon excited fluorescence intensity was recorded while the position of the focus of a femtosecond laser pulse train was scanned throughout the brain, providing a three-dimensional image of the vasculature [30]. Imaging was done using 800-nm or 830-nm, 75-fs pulses from a Ti:Sapphire laser oscillator (MIRA HP, pumped by a Verdi-V18, or Vision S, Coherent). Lasers were scanned by galvonometric scanners and focused into the sample using a 1.0 NA, 20X water-immersion objective lens (Carl Zeiss, Inc.). Image stacks were acquired with 645/45 nm (center wavelength/bandwidth) bandpass filters. The ScanImage software package [33] was used to control the whole system. Image stacks were taken with a range of magnifications resulting in lateral voxel sizes from 0.45 to 1.71 μm/pixel, but always 1 μm in the axial direction.

3.4.1.3 Expert annotation

We implemented a protocol to facilitate the manual 3D segmentation task using ImageJ, an open-source image processing software package [34] (supplementary material). Two people, one expert and one less experienced, each manually segmented a motion artifact corrected (see below), 256 × 256 × 200 voxels (292 × 292 × 200 μm3) image from an AD mouse, independently, which took about 20 and 30 hours, respectively. The second annotator was trained by the expert and then had several months of practice prior to performing this task. These data were used to estimate inter-human segmentation variation. We treated the expert labels as the "gold standard" segmentation

and used the second annotator's labels to compare variability in manual segmentation. All other comparisons were made with respect to the gold standard segmentation as the ground truth. This dataset was divided into independent (i.e., non-overlapping) training, validation, and testing sub-parts (50%-25%-25%), all spanning the entire depth of the stack. The training and validation datasets were used in the optimization of CNN architectures, while the test dataset was kept unused until the end of our architecture design optimization process and used for the final unbiased evaluation. We repeated this process 4 times, by varying the test data and thus effectively conducting 4-fold cross-validation. We note that architecture optimization was only done in the first fold. Additionally, six independent 3D images (different mice and different voxel size) acquired by Cruz Hernandez et al. [6] were labeled by an expert to examine the generalization of DeepVess. The detailed properties of these images are in S3 Table. With this paper, we also have made all images and expert annotations publicly available at: *https://doi.org/10.7298/X4FJ2F1D*

3.4.2 Preprocessing

Motion artifacts caused by physiological movements are one of the major challenges for 3D segmentation of in vivo MPM images. Furthermore, global linear transformation models cannot compensate for the local nonuniform motion artifacts, for example, due to a breath occurring part way though the raster scanning for an MPM image. In this study, we adopted the non-rigid non-parametric diffeomorphic demons image registration tool implemented based on the work of Thirion [35] and Vercauteren et al. [36]. Our approach is to register each slice to the previous slice, starting from the

first slice as the fixed reference. The diffeomorphic demons algorithm aims to match the intensity values between the reference image and deformed image, where cost is computed as the mean squared error. The smoothness prior on the deformation field is implemented via an efficient Gaussian smoothing of gradient fields, and invertibility is ensured via concatenation of small deformations. This kernel is effectively encouraging the deformation field to be smooth, thus regularizing the ill-posed non-linear registration problem. Based on our experiments, a Gaussian kernel with the standard deviation of 1.3 was chosen for the regularization of the registration algorithm. Next, in our pre-processing steps, the 1-99% range of the image intensities in the input image patch were linearly mapped between 0 and 1, and the extreme 1% of voxels were clipped at 0 and 1. This step, we found, helps with generalizing the model to work well with images taken from other MPM platforms by adapting normalization parameters to the acquisition systems and image statistics utilizing most of the intensity rang. To facilitate comparison between different datasets, image volumes were resampled to have 1 μm^3 voxel for comparisons.

3.4.3 Convolutional neural network architectures

Our aim in this work is to design a system that takes an input stack of images (in 3D) and produces a segmentation of vessels as a binary volume of the same size. For this task, as we elaborate below, we explored different CNN architectures using validation performance as our guiding metric. Our baseline CNN architecture starts with a 3D input image patch (tile), which has 33 × 33 × 5 voxels (in x, y, and z directions). The first convolution layer uses a 7 × 7 × 5 voxel kernel with 32 features to capture 3D structural

information within the neighborhood of the targeted voxel. The output of this layer, 32 nodes of 27 × 27 × 1 voxel images, enter a max pooling layer with a 2 × 2 kernel and 2 × 2 strides. Another convolution layer with 5 × 5 × 1 kernel and 64 features, followed by a similar max pooling layer are then applied before the application of the fully connected dense layer with 1024 hidden nodes and dropout [37] with a probability value of 50%. The output is a two-node layer, which represents the probability that the pixel at the center of the input patch belongs to tissue vs. vessel. The CNN takes an input 3D patch and produces a segmentation label for the central voxel. All the convolution layers have a bias term and rectified linear unit (ReLU) as the element-wise nonlinear activation function. Starting from this baseline CNN architecture, we optimized the network architecture hyperparameters with a greedy algorithm.

Different kernel sizes for the 3D convolution layers were explored in our experiments. Note that each choice in the architecture parameters (including the kernel size) corresponded to a different input patch size. As the validation results summarized in S1 Table indicate, the best performing baseline architecture had an input patch size of 33 × 33 × 7. Based on this result we chose an input patch size of 33 × 33 × 7 as the optimal field of view (FOV) for segmentation. We then explored the effect of the number of convolutional and max pooling layers. As summarized in S2 Table, the best architecture had three 3D convolution layers with a 3 × 3 × 3 voxel kernel, a max pooling layer, followed by two convolution layers with a 3 × 3 voxel kernel, and a max pooling layer. The output of the last max pooling layer is reshaped to a fully-connected layer followed by a 1024-node fully-connected layer and the last fully-connected layer, which is

reshaped to the output patch size. Note that there is no difference in spatial resolution (i.e., voxel dimensions) between the input and output patches.

Finally, we investigated the performance for different output patch sizes, ranging from 1 voxel to $5 \times 5 \times 5$ voxels and found that performance was improved further when the output is the segmentation of the central $5 \times 5 \times 1$ patch and not just a single voxel. A larger output area has the advantage of accounting for the structural relationship between adjacent voxels in their segmentation. The optimal CNN architecture scheme is shown in Figure 3.1.

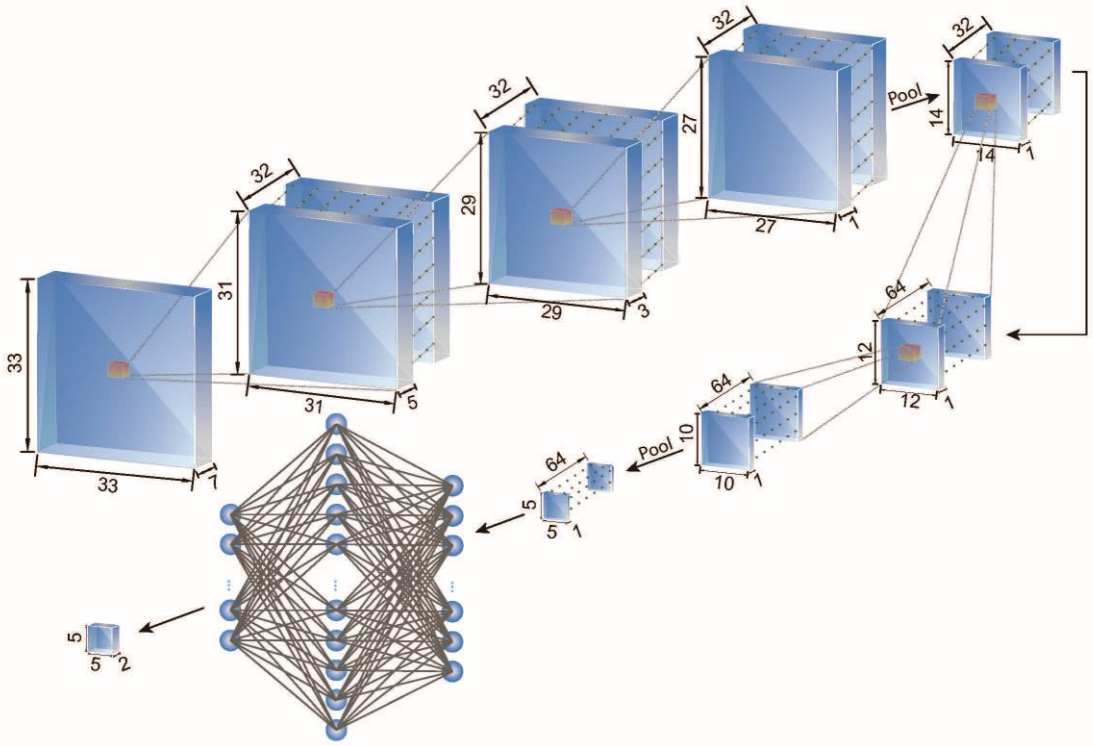

Figure 3.1. The optimal 3D CNN architecture.

The field of view (FOV), i.e. the input patch size is 33 × 33 × 7 voxels and the output is the segmentation of the 5 × 5 × 1 patch (region of interest, ROI) at the center of the patch. The convolution kernels are 3 × 3 × 3 voxels for all the layers and ReLU is used as the element-wise nonlinear activation function. The first three convolution layers have 32 channels and are followed by pooling. The second three convolution layers have 64 channels. The output of convolution layers is 5 × 5 × 1 voxels with 64 channels, which is fed to a fully connected neural network with a 1024-node hidden layer. The final result has 5 × 5 × 1 voxels with two channels representing the probability of the foreground and background label associations.

3.4.4 Performance metrics

There are different performance metrics to compare agreement between an automated segmentation method and a "ground truth" (GT) human annotation. In the context of binary segmentation, the foreground (F) will be the positive class, and the negative class will correspond to the background (B). Therefore, true positive (TP) can be measured as the total number of voxels where both the automatic and human segmentation labels are foreground. True Negative (TN), False Positive (FP) and False Negative (FN) can be defined in a similar fashion.

Based on these, we can compute sensitivity and specificity. For example, sensitivity is the percentage of GT foreground voxels that are labeled by the automatic segmentation (ASeg) correctly. Mathematically, we have:

$$sensitivity = P(y = f|GT = F) = \frac{TP}{TP + FN} \quad (1)$$

$$specificity = P(y = B|GT = B) = \frac{TN}{TN + FP} \quad (2)$$

The Dice coefficient (DC), Jaccard index (JI), and modified Hausdorff distance (MHD) are another set of commonly used segmentation performance metrics. JI is defined as the ratio between the number of voxels labeled as foreground by both GT and ASeg, to the total number of voxels that are called foreground by either GT and ASeg. DC is very similar to JI, except it values TP twice as much as FP and FN. JI and DC are useful metrics when the number of the foreground voxels is much less than background

and the detection accuracy of the foreground voxels is more important compared to background voxel detection, which is the case for 3D imaging of vasculature.

$$JI = P(y = F \cap FT = F | y = F \cup GT = F) = \frac{TP}{TP + FP + FN} \tag{3}$$

$$DC = \frac{2\,JI}{1 + JI} = \frac{2\,TP}{2\,TP + FP + FN} \tag{4}$$

On the other hand, MHD [38] quantifies accuracy in terms of distances between boundaries, which might be appropriate when considering tubular structures. For each boundary point in image **A** ($a \in$ A), the closest Euclidean distance ($d(a, b) = ||a - b||_2$) to any boundary point inside image **B** ($b \in$ B) is first calculated, $d(a, \mathrm{B}) = min_{b \in \mathrm{B}} ||a - b||_2$). This is then averaged over all boundary points in A: $\frac{1}{N_a} \sum_{a \in \mathrm{A}} d(a, \mathrm{B})$ [39]. MHD is then defined as:

$$MHD = max\left[\sum_{a \in \mathrm{A}} d(a, \mathrm{B}), \sum_{b \in \mathrm{B}} d(b, \mathrm{A})\right] \tag{5}$$

$$d(a, \mathrm{B}) = min_{b \in \mathrm{B}} \|a - b\|_2 \tag{6}$$

Note that in the segmentation setting, **A** and **B** can represent the foreground boundaries in the automatic and GT segmentations, respectively. Finally, we can compute the MHD on centerlines instead of boundaries, a metric we call MHD-CL.

3.4.5 Training and implementation details

In training our segmentation algorithms, we used a customized cross-entropy loss function designed for our highly unbalanced datasets (where foreground voxels comprise only a small fraction of the volume), measured over all voxels but TN (i ∈ {TP, FP, FN}), defined as:

$$Loss = \sum_{\mathrm{i} \in \{\mathrm{TP,FP,FN}\}} -|y_i \log(p_i) + (1 - y_i) \log(1 - p_i)| \qquad (7)$$

y_i is the GT label and p_i is the model's output as the probability of the target voxel i belonging to the foreground. Note that in Eq. (7), true negative voxels have no contribution, effectively reducing the influence of the dominant background. We trained our model using *Adam* stochastic optimization [40] with a learning rate of 10^{-4} for 100 epochs during architecture exploration and a learning rate of 10^{-6} for 30,000 epochs during the fine tuning of model parameters for the proposed architecture with mini-batch size of 1000 samples (based on GPU memory constraints and results of our experiments with smaller mini-batch size, which did not improve the optimization results). The fine tuning took one month on one NVIDIA TITAN X GPU. We implemented our models in Python using Tensorflow[41].

3.4.6 Post-processing

CNN segmentation results contain some segmentation artifact such as holes inside the vessels, rough boundaries, or isolated small objects. In order to remove these artifacts, the holes within the vessels were filled. This was followed by application of a 3D mean

filter with a 3 × 3 × 3 voxel kernel and the removal of small foreground objects, e.g. smaller than 100 voxels. This result was used to compare to the gold standard.

3.4.7 Analysis of vasculature centrelines

To characterize the cortical vasculature of the experimental animals, we identified capillary segments by calculating centerlines from the segmented image data. Our centerline extraction method includes dilation and thinning operations, in addition to some centerline artifact removal steps. The binary segmentation image was first thinned using the algorithm developed by Lee et al. [42]. The result was then dilated using a spherical kernel with a radius of 5-voxels to improve the vessel connectivity, which was followed by mean filtering with a 3 × 3 × 3 voxel kernel and removing holes from each cross section. Next, a thinning step was applied again to obtain the new centerline result. The original segmented image was dilated using a spherical kernel with a radius of 1-voxel to act as the mask for the centerlines with the goal of improving the centerline connectivity. The following rules were applied to the resulting centerlines repeatedly until no further changes could be done. A vessel is a segment between two bifurcations.

1) Remove any vessels with one end not connected to the network (i.e., dead end) and with length smaller than 11 voxels.
2) Remove single voxels connected to a junction.
3) Remove single voxels with no connections.
4) Remove vessel loops with length of one or two voxels.

Finally, the centerline network representation (i.e. nodes, edges, and their properties) was extracted. (The centerline extraction was applied on both manual and automated segmentations.)

3.5 Results

We conducted a systematic evaluation of several network architecture parameters in order to optimize segmentation accuracy of images of mouse cortex vasculature from MPM. Features of in vivo MPM images include motion artifacts due to respiration and heartbeat. Because vessels are visualized by an injection of dye that labels the blood plasma, unlabeled red blood cells appear as dark spots and streaks moving through the vessel lumen (arrows in Figure 3.2). Images are acquired by raster scanning through the tissue and each vessel is captured in several images. The imaging speed has a significant influence on these features and in in vivo experiments, imaging is often relatively slow, such that these features become prominent [43]. We emphasize that our exploration was based on performance on the validation dataset and the final results presented reflect the model accuracy on an independent test dataset. The detailed performance results for some of the tested architectures are reported in Table S 3.1 and Table S 3.2. The optimal architecture, DeepVess, was trained on the training data until the model accuracy stopped improving and no overfitting was observed (30,000 epochs). Figure S1 shows the JI learning curve over 30,000 epochs, for training, validation, and test datasets. The constant gap between JI of the training and validation datasets, which represent generalization error, confirms that we are not strongly overfitting.

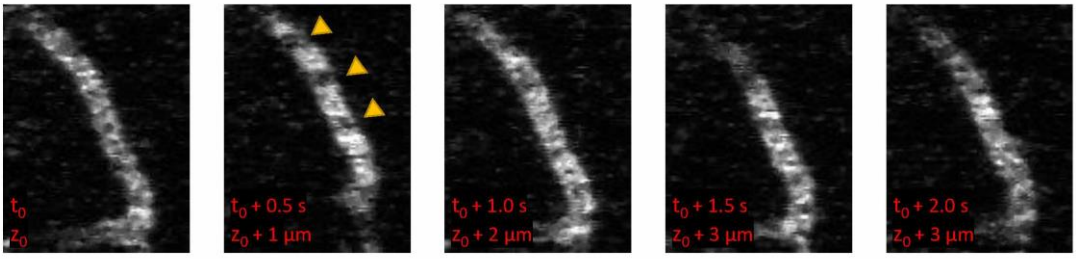

Figure 3.2. In vivo MPM images of a capillary.

Because MPM images are acquire by raster scanning, images at different depths (z) are acquired with a time lag (t). Unlabeled red blood cells moving through the lumen cause dark spots and streaks and result in variable patterns within a single vessel.

Furthermore, we implemented two state-of-the-art methods [24, 28], and an improved version of the method of Teikari et al. [24], where we changed the 2D convolutional kernels into 3D kernels and inserted a fully connected neural network layer at the end, based on the suggestion in the discussion of their paper. Table 3.1 summarizes the comparison between the performance of our optimal architecture based on the 4-fold cross-validation results, with and without the post-processing step, comparing to two state-of-the-art methods and a second human annotator to provide a measure of the inter-human variability. These results, as well as Figure S1 demonstrate that DeepVess outperforms the state-of-the-art methods [24, 28] in terms of sensitivity, Dice index, Jaccard index, and boundary modified Hausdorff distance; and approaches human performance in terms of Dice and Jaccard. The proposed method does not outperform the benchmarks in specificity, indicating a slightly higher rate of false positive voxels. Yet we note that the relatively lower specificity is still very high (97%).

Table 3-1. The comparison of our proposed CNN architecture (DeepVess), manual annotation by a trained person, and two state-of-the-art methods [24, 28] to the gold standard of the expert human annotation based on the 4-fold cross-validation results. DeepVess surpassed both human annotator and two state-of-the-art methods in terms of sensitivity as well as Dice index, Jaccard index, and boundary modified Hausdorff distance, which are the three metrics that are widely used in segmentation.

	Sensitivity	*Specificity*	***Dice***	***Jaccard***	***MHD***
Second human annotator	81.07%	98.70%	82.35%	70.40%	1.50
Original Teikari et al. [24]	62.44%	**98.65%**	69.69%	55.06%	3.20
Çiçek et al. [28]	70.01%	98.21%	72.69%	59.41%	3.55
Improved [24] in this study	69.55%	98.39%	74.03%	59.96%	3.16
DeepVess	89.91%	97.00%	81.62%	69.13%	2.26
DeepVess with post-processing	**89.95%**	97.00%	**81.63%**	**69.15%**	**2.25**

In MPM, the variation in the signal to noise as a function of imaging depth leads to changes in image quality between image slices. The performance of a segmentation method should therefore be assessed by analyzing slices separately. Figure 3.3 illustrates the boxplot of slice-wise Dice index values from the x-y planes within the 3D MPM image dataset. DeepVess had a higher Dice index values in comparison to the Teikari et al. and the trained annotator's results. However, there was more variation compared to the other two results, which implies the possibility and need for further improvements.

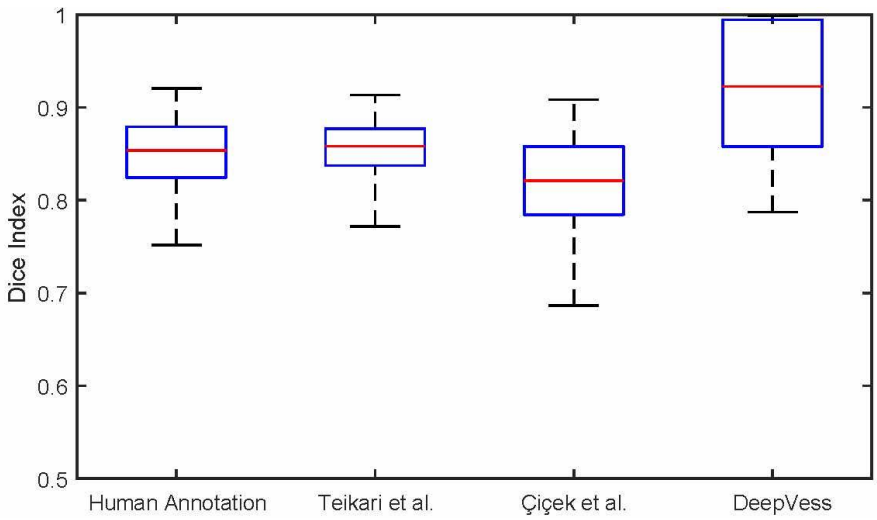

Figure 3.3. Slice-wise Dice index of DeepVess vs. manual annotation by a trained person and the state-of-the-art methods [24, 28] compared to the gold standard of the expert human annotation. The central red mark is the median, and the top and bottom of the box is the third and first quartiles, respectively. The whiskers indicate the range of data. DeepVess has higher median value in comparison to the Teikari et al. [24], Cicek et al. [28], and the human annotator (Wilcoxon signed-rank test, $p = 2.98e-23$, $p = 2.59e-32$, and $p = 2.8e-28$, respectively).

The generalization of the model was studied by testing an independent dataset annotated by our expert consisting of 6 separate 3D MPM images acquired from 1 AD and 5 WT mice (Table S 3.3) and the results are summarized in Table S 3.4. DeepVess outperforms both the state-of-the-art methods [24, 28] on the second dataset in terms of sensitivity, Dice index, Jaccard index, and boundary MHD. Similar to the test dataset results, specificity was slightly lower. These results illustrate the generalization of our model on new MPM images with different image quality and captured from different mouse models and with different voxels sizes. Figure 3.4.A illustrates the image intensity

and three models overlaid on the image for a cross-section extracted from a 3D image from the independent dataset (Table S 3.4 #1). Figure 3.4.B-E are magnified version of three cases within Figure 3.4.A. The main sources of failure in the vessel segmentations of 3D in vivo MPM images are low SNR at deeper cross-sections (Figure 3.4.C) and unlabeled, moving red blood cells in the vessel lumen, which cause dark spots and streaks (Figure 3.4.B and D). The patchy segmentations due to unlabeled red blood cells result in unconnected and isolated vasculature centerlines and network. The DeepVess architecture has fully connected layers and thus might be exploiting some spatially varying properties of the signal (as in the variation of contrast as a function of depth) that a fully convolutional architecture such as U-Net might not be able to exploit. Elsewhere, in the absence of such difficulties, all three models segment the vessels largely accurately.

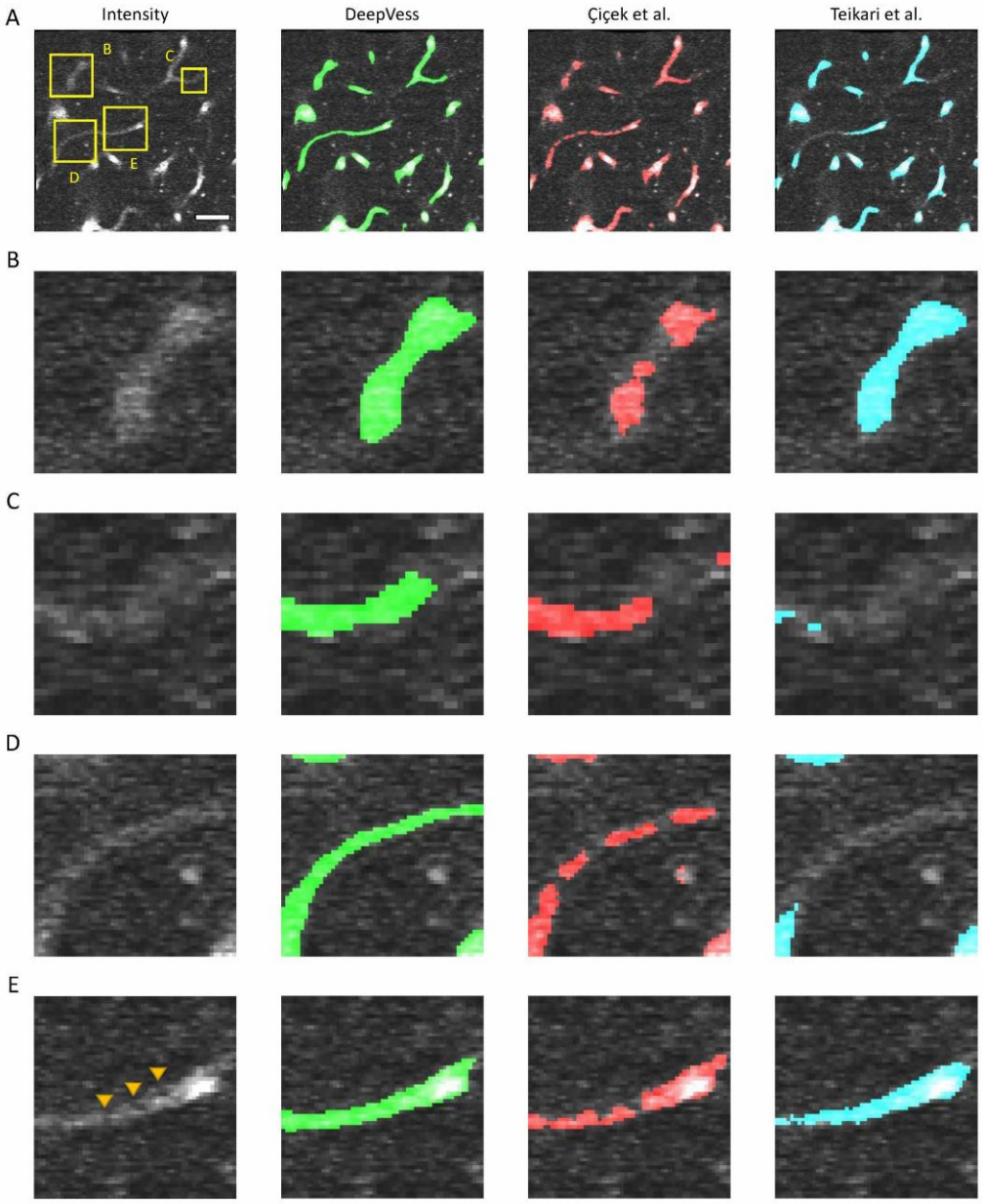

Figure 3.4. Comparison of DeepVess and the state-of-the-art methods [24, 28] in a 3D image cross-section obtained from an independent dataset (S4 Table #1) not used during the training. (A) An image frame with intensity in gray and overlay of segmentation from each method. (B-E) magnified view of four cases within A. The three models overlaid on the complete 3D image is made available online in Supplemental Materials. Scale bar is 50µm.

We next examined the quality of the vessel centerlines derived from the different segmentations. Using the centerline modified Hausdorff distance (CL MHD) as a centerline extraction accuracy metric, DeepVess (CL MHD [DeepVess] = 3.03) is substantially better than the state-of-the-art methods (CL MHD [Teikari et al.] = 3.72, CL MHD [Cicek et al.] = 6.13). But there is still room for improvement in terms of automatic centerline extraction as neither automatic methods yielded scores as good as the trained human annotator (CL MHD [human annotator] = 2.73). In order to test the accuracy of geometrical measurements, the vessel diameter, a sensitive metric, was selected. We measured the diameter of 100 vessels manually by averaging ten 2D measurements per vessel to compare with the DeepVess's results (Figure S 3.2) We observed that there is no significant difference between manually measured diameters and DeepVess's results (paired t-test, $n = 100$, $p = 0.34$).

3.6 Discussion

The segmentation of 3D vasculature images is a laborious task that slows down the progress of biomedical research and constrains the use of imaging in clinical practice. There has been significant research into tackling this problem via image analysis methods that reduce or eliminate human involvement. In this work, we presented a CNN approach, which surpasses the state-of-the-art vessel segmentation methods [24, 28] as well as a trained human annotator. The proposed algorithm, DeepVess, segments 3D in vivo vascular MPM images with more than ten million voxels in ten minutes on a single

NVIDIA TITAN X GPU, a task that takes 30 hours for a trained human annotator to complete manually.

In order to characterize the performance of DeepVess, we compared the automated segmentation to an expert manual segmentation (Figure 3.5). Here, we visualized three slices with different qualities of segmentation results. The 3D rendering of the mouse brain vasculature shown in Fig 5 indicates the location of these top, middle, and bottom slices representing typical high, medium, and low segmentation quality, respectively. Top layers are very similar, and differences are visible at the bottom layers, which have low SNR.

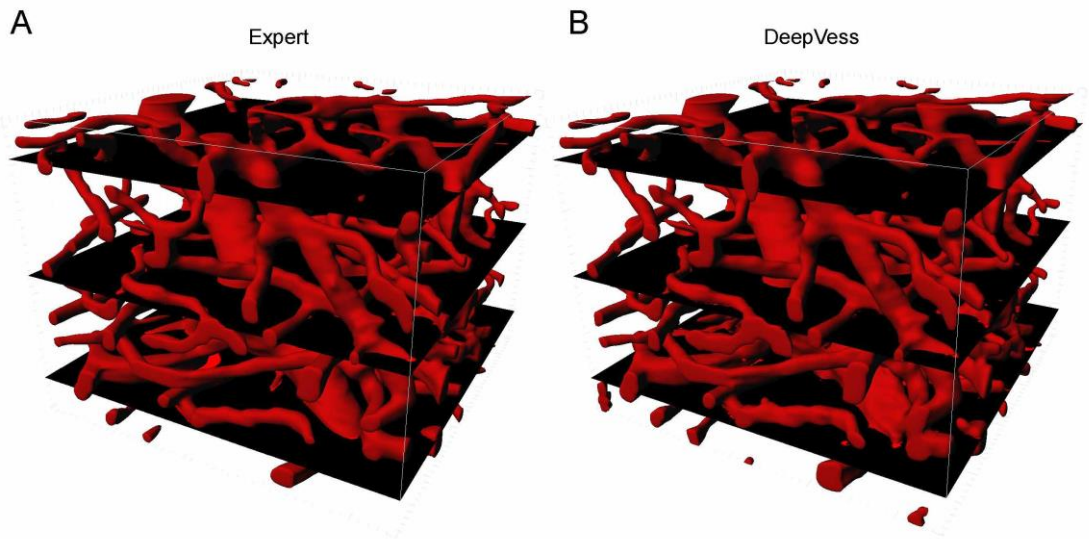

Figure 3.5. 3D rendering of (A) the expert's manual and (B) DeepVess segmentation results.

The top, middle, and bottom black plains correspond to the high, medium, and low-quality examples, respectively, which are analyzed further in the Discussion (Fig 6). Each volume is 256 × 256 × 200 voxels (292 × 292 × 200 μm3).

We used 50% dropout during test-time [44] and computed Shannon's entropy for the segmentation prediction at each voxel to quantify the uncertainty in the automated segmentation. Higher entropy represents higher segmentation uncertainty at a particular voxel. The entropy results together with the comparison between DeepVess and the expert segmentations for those three planes are illustrated in Figure 3.6. The left column contains the intensity gray-scale images of these examples. The segmentation results of the DeepVess and the expert are superimposed on the original gray-scale image with red (DeepVess) and green (the expert), as shown in the middle column. Yellow represents agreement between DeepVess and the expert. The right column shows the entropy of each example estimated via test time dropout. We observe that, in general, DeepVess has higher uncertainty at the boundaries of vessels. The disagreement with ground truth is also mostly concentrated at the boundaries. Images from deeper within the brain tissue that often have lower image contrast and higher noise levels due to the nature of MPM, suffer from more segmentation errors. These images can often be challenging even for expert humans. Arrows in Figure 3.6.C highlight examples of these difficulties. The error example 1 illustrates the case where the expert ignored bright pixels around the vessel lumen based on their knowledge of the underlying physiology and experience with MPM images of brain that postulate a rounded lumen instead of a jittery and rough lumen, despite a very strong signal. The error example 2 illustrates a low intensity vessel junction that was judged to be an artifact by humans based on experience or information from other image planes. The error example 3 illustrates the case where a small vessel does not exhibit a strong signal and it is not connected to another major vessel.

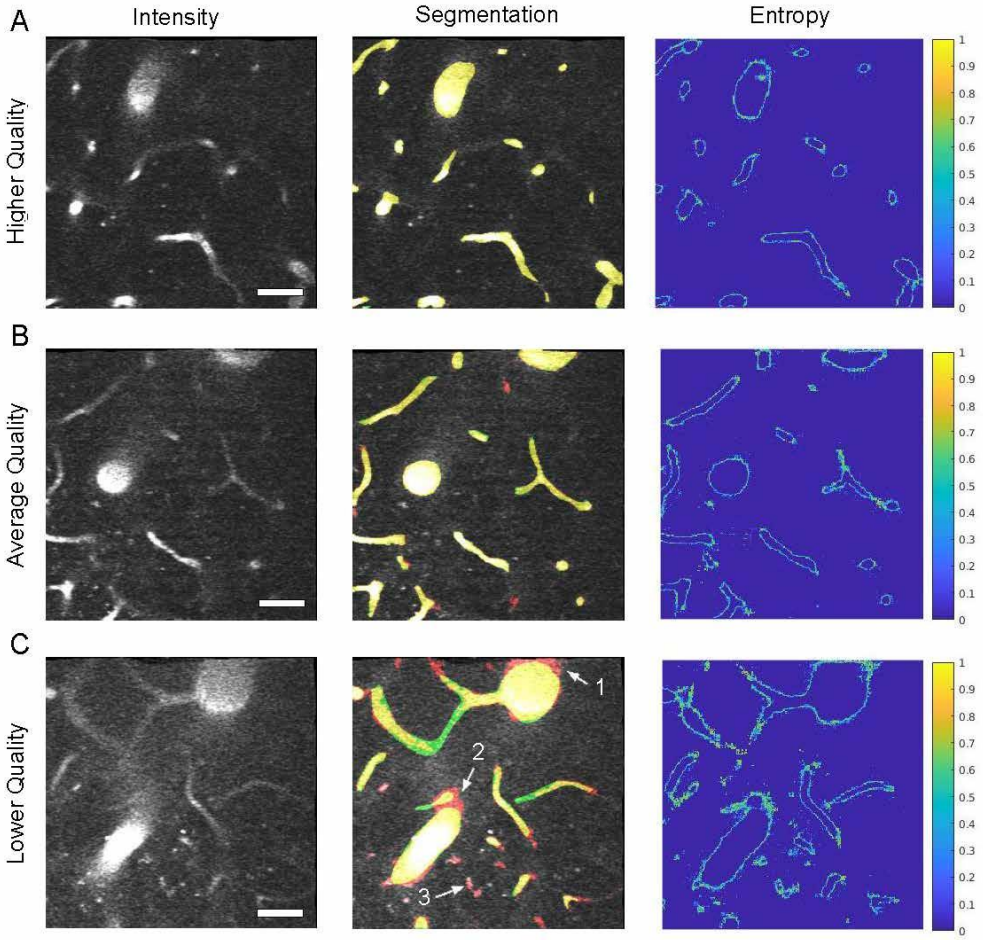

Figure 3.6. Comparison of DeepVess and the gold standard human expert segmentation results in image planes as shown in Figure 3.5. Imaging is generally higher quality at planes closer to the sample surface. (Left column) Image intensity shown with gray scale after motion artifact removal. The dark spots within the vessels are red blood cells that do not take up the injected dye. (Middle column) Comparison between DeepVess (red) and the expert (green) segmentation results overlaid on images. Yellow shows agreement between the two segmentations. (Right column) Shannon entropy, which is a metric of DeepVess segmentation uncertainty computed with 50% dropout at test-time [44]. The boundaries of vessels with high entropy values, shown in warmer colors, demonstrate the uncertainty of DeepVess results at those locations. Scale bar is 50 μm.

DeepVess implements pre- and post-processing tools to deal with in vivo MPM images that suffer from different motion artifacts. DeepVess is freely available at *https://github.com/mhaft/DeepVess* and can be used immediately by researchers who use MPM for vasculature imaging. Also, our model can be fine-tuned further by adjusting the intensity normalization step to utilize a different part of the intensity range and training samples for other 3D vasiform structures or other imaging modalities. Similar to many machine learning solutions, DeepVess' performance depends on specific image features and the performance will degrade in cases where the tissues are labeled differently (e.g. vessel walls are labeled instead of blood serum) or the images intensities are concentrated in a small portion of the intensity range.

Although in vivo measurements present unique challenges to image segmentation, such as the red blood cell motion, in our case, we have shown that DeepVess successfully handles these challenges. Postmortem techniques all change the vessel diameters in the tissue processing. Hence, we believe that in vivo imaging is the best strategy to quantify vessel diameters. While features such as topology and length might not be affected by postmortem processing, in vivo imaging with MPM is important for capillary diameter measurements. Two-photon microscopy has been used to validate histology in many studies ([5, 14, 45–48]) and comparisons with other labeling techniques are quite common.

While DeepVess offers very high accuracy in the problem we consider, there is room for further improvement and validation, in particular in the application to other vasiform structures and modalities. For example, other types of (e.g., non-convolutional)

architectures such as long short-term memory (LSTM) can be examined for this problem. Likewise, a combined approach that treats segmentation and centerline extraction methods together, such as the method proposed by Bates et al. [25] in a single complete end-to-end learning framework might achieve higher centerline accuracy levels.

3.7 Application to Alzheimer's mouse models

3.7.1 Capillary alteration caused by aging and Alzheimer's disease

In vivo imaging with multiphoton microscopy of capillary beds is free of distortions in vessel structure caused by postmortem tissue processing that can result in artifacts such as altered diameters [5]. However, the images often suffer from poor signal to noise and motion artifacts. An additional challenge is that unlabeled, moving red blood cells in the vessel lumen cause dark spots and streaks that move over time. Disease models are often especially challenging because inflammation and tissue damage can further degrade imaging conditions.

Strong correlations between vascular health, brain blood flow and AD suggest that mapping the microvascular network is critical to the understanding of cognitive health in aging [49]. To explore this question, we imaged the cortical vascular networks in young and old mouse models of AD (young AD and old AD) and their young and old WT littermates (young WT and old WT). Imaged volumes ranged from 230 × 230 to 600 × 600 μm^2 in x-y and 130 to 459 μm in the z direction. We imaged 6 animals per group, with at least 3000 capillary segments analyzed for each group.

The resulting 3D stacks of images were preprocessed, segmented with DeepVess, and post-processed as discussed in the previous sections. Centerlines were extracted, and individual vessel segments were identified. To analyze capillaries while excluding arterioles and venules, only vessel segments less than 10 μm in diameter were included [6, 50, 51]. For the vascular parameters of segment length, diameter, and tortuosity considered here, previous work has shown that AD mouse models have increased tortuosity in cortical penetrating arterioles as compared to WT mice [52, 53]. Our analysis of capillaries excluded these vessels. Three metrics were selected to characterize the vascular network. For each capillary segment, we calculated the diameter averaged along the length (Fig 7.A), the length (Figure 3.7.B), and the tortuosity, defined as the length divided by the Euclidean distance between the two ends (Figure w.7.C). The distributions of capillary diameter, length, and tortuosity varied little between young and old mice or between WT and AD genotype (Table 3.2). There were subtle shifts (~ 0.25 μm) in the diameter distribution between groups, but no clear differences across old/young or WT/AD and the differences in means were small compared to the standard deviation (6-27% of SD). However, we observed a decrease in the number of longer length (> 75μm) capillaries in older animals as compared to young in both WT and AD mice shown by a rightward shift in the cumulative distribution function curve (Figure w.7.B and Table 3.2).

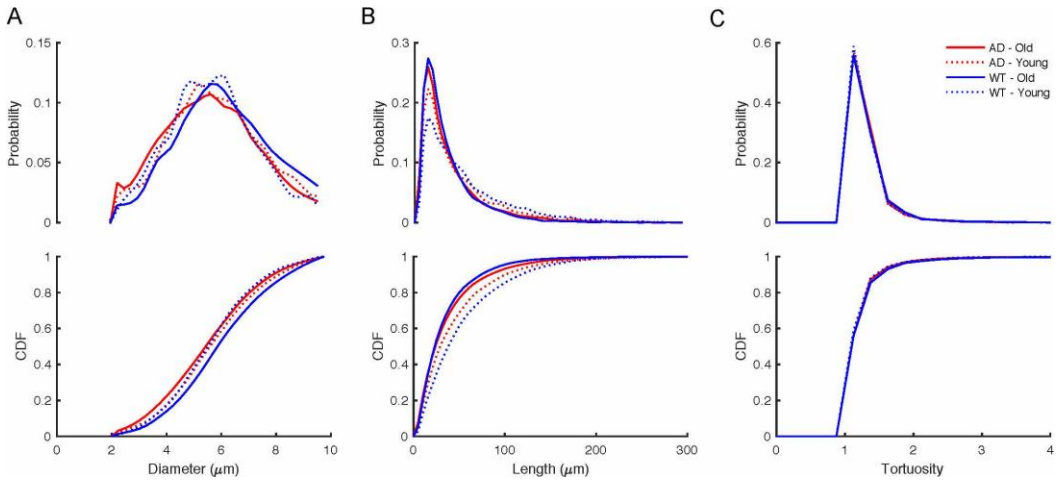

Figure 3.7. Comparison of capillaries between young and old mice with WT and AD genotype (6 mice in each group).

The relative probability and cumulative distribution function (CDF) of the (A) diameters, (B) length, and (C) tortuosity based on all capillaries aggregated within each of the four groups. We compared these metrics between the groups using Kruskal-Wallis test followed by Bonferroni multiple comparison correction [54] (Table 3.2).

Table 3-2. Comparison between metrics distributions between different groups using Kruskal-Wallis test followed by Bonferroni multiple comparison correction. Δμ is the difference between the mean values of the two tested groups.

	Diameter (μm)		**Length (μm)**		**Tortuosity**	
	$\Delta\mu$	**P-value**	$\Delta\mu$	**P-value**	$\Delta\mu$	**P-value**
AD-Old vs. AD-Young	0.206	2.61E-7	7.908	7.5E-22	0.016	0.798
AD-Old vs. WT-Old	0.475	2.93E-27	2.787	0.055	0.019	0.645
AD-Old vs. WT-Young	0.095	1.20E-5	16.16	6.9E-67	0.018	0.321
AD-Young vs. WT-Old	0.269	6.39E-9	10.69	1.14E-27	0.035	0.027
AD-Young vs. WT-Young	0.110	0.012	8.252	9.12E-17	1.50E-3	1.000
WT-Old vs. WT-Young	0.379	1.1E-14	18.95	2.1E-63	0.037	0.036

3.7.2 Aging and Alzheimer's disease have little effect on capillary characteristics

Using a large database of vessel segments measured in three dimensions, we surprisingly found only very small differences between groups that were dwarfed by the variance in capillary diameter or tortuosity between young and old animals or between WT and AD mouse models. The automation provided by DeepVess enabled the evaluation across a very large number of vessels in a large group size. The strong agreement between the measurements based on DeepVess and the manual measurements by Cruz Hernandez et al. [6], confirms that the proposed pipeline yields unbiased and accurate metrics to analyze capillary segments. There was a decrease in the number of long capillary segments in the aged animals compared to young in both the WT and AD groups. Note that the reported metrics only represent the parietal region of cortex and that regional variability can affect our results. These finding may not generalize across all ages and mouse models of AD and could be different in other regions of the brain. Sonntag et al. [1] argue that changes in vasculature due to aging might be non-linear and multi-phasic. For instance, two studies showed that the capillary density increases during adulthood and then declines in more advanced age [55, 56]. As summarized in Table 3.3, several previous studies have characterized the average diameters of cortical capillaries in mice and showed high variability in results suggesting that methodological variations make comparison between studies difficult. Other studies that compared AD models and WT also found negligible or no difference in capillary diameters. Heinzer et al. compared a different mouse model (APP23) using MRA and found no difference between WT and

AD mice [57]. The same group also compared the effects of "VEGF overexpression" model and WT using SRμCT and also found little difference [58].

There are a wide range of imaging approaches used in these various studies and data from both live animal and postmortem analysis is included. It is possible that some of these differences emerge when tissues are processed rather than measured in vivo as was done here. Studies based on sectioned tissue sample the 3D vascular architecture differently so it is difficult to make direct comparisons between datasets. Measures of capillaries depend on the definition of capillaries. Here it was based on a threshold diameter of 10μm, which could explain some of the variability in the literature. Not surprisingly given the differences in approach and sample preparation, there is significant disagreement between reported average diameters. Some differences may, however, reflect differences in vasculature across strains and ages of animals.

Therefore, the proposed fully automated objective segmentation of 3D in vivo images of the vasculature can be used to reduce the variability due to sample preparation and imaging/analysis approach, allowing such strain and age differences to be elucidated clearly.

Table 3-3. Comparison of measured mouse capillary diameters from different studies.

Study	Background	Trans gene	Phenotype	Age (week)	Imaging Modality	Vessel Diameter
This study	C57/BL6	-	WT	18-31	*in vivo* 2PEF	5.81 ± 1.62
This study	C57/BL6	-	WT	50-64	*in vivo* 2PEF	6.19 ± 1.76
This study	C57/BL6	APP/PS1	AD	18-31	*in vivo* 2PEF	5.92 ± 1.76
This study	C57/BL6	APP/PS1	AD	50-64	*in vivo* 2PEF	5.71 ± 1.77
Boero et al. [59]	BALB/C	-	WT	11	postmortem optical imaging	$2.48 - 2.70\ \mu m$
Drew et al. [60]	C57/BL6	-	WT	-	*in vivo* 2PEF	$2.9 \pm 0.5\ \mu m$
Blinder et al. [5]	C57/BL6	-	WT	-	*in vivo* optical img.,	$2 - 5.3\ \mu m$
Hall et al. [61]	C57/BL6J	NG2-	WT	-	*in vivo* 2PEF	$4.4 \pm 0.1\ \mu m$
Gutierrez-Jiménez et al. [51]	C57/BL6	NTac	WT	13-15	*in vivo* 2PEF	$4.1 - 4.5\ \mu m$
Cudmore et al. [62]	C57/BL6	Tie2-Cre :mTmG	WT	13-21, 64, 97	*in vivo* 2PEF	$5.03 \pm 1.18\ \mu m$
Meyer et al. [63]	C57/BL6	APP23 & -	AD & WT	12-108	postmortem histology	$4 - 6\ \mu m$
Tsai et al. [14]	Swiss	-	WT	-	*in vivo* 2PEF	$3.97 - 4.11$
Tsai et al. [14]	C57/BL6	-	WT	-	*in vivo* 2PEF	$3.97 - 4.11$
Heinzer et al. [57]	C57/BL6	APP23	WT	52	MRA	$14 \pm 5\ \mu m$
Heinzer et al. [57]	C57/BL6	APP23	AD	52	MRA	$14 \pm 5\ \mu m$
Heinzer et al. [64]	C57/BL6	APP23	AD	44	$SR\mu CT$	$8.9\ \mu m$
Heinzer et al. [58]	C57/BL6	-	WT	16	$SR\mu CT$	$5.6 \pm 27.9\ \mu m$
Heinzer et al. [58]	C57/BL6	C3H/He:NSE	other	16	$SR\mu CT$	$5.5 \pm 29.3\ \mu m$
Serduc et al. [65]	Swiss nude	-	WT	5	*in vivo* 2PEF	$4 - 6\ \mu m$
Vérant et al. [50]	Swiss nude	-	WT	5	*in vivo* 2PEF	$8.2 \pm 1.4\ \mu m$

3.8 Conclusions

Here, we presented DeepVess, a 3D CNN segmentation method together with essential pre- and post-processing steps, to fully automate the vascular segmentation of 3D in vivo MPM images of murine brain vasculature. DeepVess promises to expedite biomedical research on the differences in angioarchitecture and the impact of such

differences by removing the laborious, time consuming, and subjective manual segmentation task from the analysis pipelines in addition to elimination of subjective image analysis results. We hope the availability of our open source code and reported results will facilitate and motivate the adoption of this method by researchers and practitioners.

3.9 Data availability statement

All data underlying these findings is publicly available at Cornell's eCommons online archive: *https://doi.org/10.7298/X4FJ2F1D*

3.10 Declarations of interest

none

3.11 Supplementary materials

3.11.1 Manual 3D segmentation protocol using ImageJ.

First, we created a new hyper-stack (File menu → New) with 3D voxel size and bit depth similar to the original image (e.g. a 16-bit 1024 × 1024 × 500 voxel hyper-stack). The original image and the new hyper-stack were then merged (Image menu → Color) into a multi-channel hyper-stack, which contained both the raw data and the segmentation results. On each image (in the x-y plane) the expert drew segmentation boundaries using the free hand tool and fill function (F key) while the second channel is selected using scrollbar. The Color Picker and Channels Tool (Image menu → Color) in

addition to the Reverse CZT option (Edit menu → Options → Miscellaneous) were used to expedite the segmentation process.

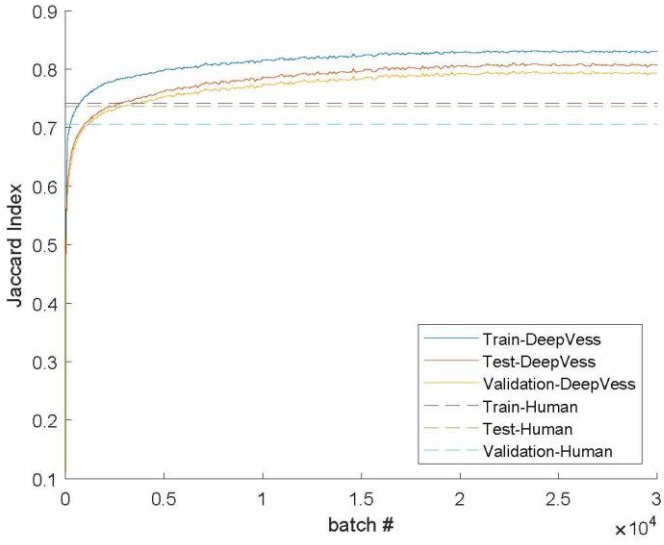

Figure S 3.1. Jaccard as a measure of the model accuracy.

The DeepVess results surpass the trained human annotator result at all three train, validation, and test datasets. The human annotator and DeepVess results are shown in dashed and solid lines respectively. The constant difference between DeepVess and the human annotator's results confirm the avoidance of overfitting.

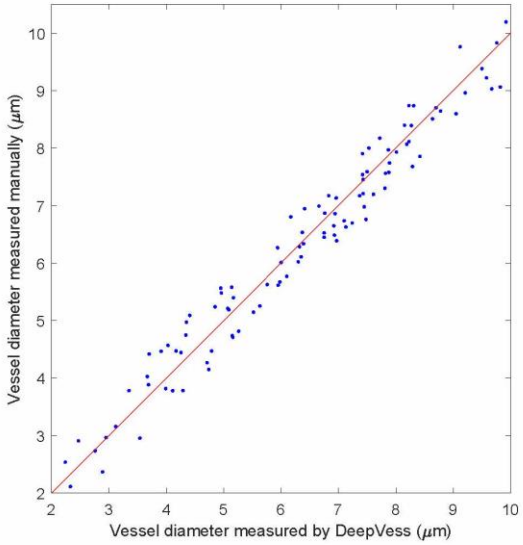

Figure S 3.2. The vessel diameters measured manually in comparison to the DeepVess's results.

There is no significant difference between two measurements (paired t-test, n = 100, p = 0.34).

Table S 3-1. The results of investigating different field of view sizes.

	Architecture	***FOV***
N1	C 7x7x5 - P - C 5x5 - P - NN	33x33x5
N2	C 7x7x9 - P - C 5x5 - P - NN	33x33x9
N3	C 7x7x15 - P - C 5x5 - P - NN	33x33x15
N4	C 7x7x31 - P - C 5x5 - P - NN	33x33x31
N5	C 7x7x5 - P - C 5x5 - P - NN	85x85x5
N6	C 7x7x7 - P - C 5x5 - P - NN	25x25x7
N7	C 7x7x7 - P - C 5x5 - P - NN	33x33x7
N8	C 7x7x7 - P - C 5x5 - P - NN	41x41x7
N9	C 9x9x9 - P - C 5x5 - P - NN	41x41x9

	Sensitivity	***Specificity***	***Dice***	***Jaccard***	***MHD***
N1	93.10%	98.15%	87.11%	77.17%	1.38
N2	87.39%	98.87%	87.40%	77.62%	1.15
N3	91.69%	98.31%	87.09%	77.13%	1.61
N4	89.94%	98.21%	85.69%	74.96%	2.19
N5	91.15%	98.23%	86.43%	76.11%	1.46
N6	90.22%	98.61%	87.71%	78.11%	1.03
N7	91.57%	98.49%	87.89%	78.40%	1.20
N8	91.01%	98.34%	86.86%	76.77%	1.85
N9	93.23%	97.61%	84.81%	73.63%	2.38

Table S 3-2. The results of investigating different architectures.

	Architecture	*FOV*
N10	C 7x7x7 - P - C 5x5 - P - 2*NN	33x33x7
N11	3*C 3x3x3 - P - 3*C 3x3 - P - NN	33x33x7
N12	4*C 5x5x5 - P - 3*C 5x5 - P - NN	41x41x9
N13	4*C 3x3x3 - P - 3*C 3x3 - P - NN	41x41x9
N14	C 7x7x7 - P - C 5x5x5 - P - NN	25x25x25
N15	3*C 3x3x3 - P - 2*C 3x3x3 - P - NN	33x33x33
N16	3*C 3x3x3 - P - 2*C 3x3 - P - NN	41x41x41
N17	3*C 3x3x3 - P - 2*C 3x3 - P - NN	31x31x31
N18	3*C 3x3x3 - P - 2*C 3x3 - P - NN	49x49x49
N19	3*C 3x3x3 - P - 2*C 3x3 - P - NN	33x33x7
N20	previous architecture for ROI 5x5	33x33x7
N20P	previous architecture+post proc.	33x33x7

	Sensitivity	*Specificity*	*Dice*	*Jaccard*	*MHD*
N10	89.61%	98.33%	86.06%	75.53%	1.63
N11	93.71%	97.83%	86.00%	75.44%	1.87
N12	83.78%	98.68%	84.43%	73.05%	1.82
N13	93.45%	98.15%	87.30%	77.46%	1.48
N14	91.57%	98.49%	87.89%	78.40%	1.20
N15	90.29%	98.40%	86.77%	76.63%	5.98
N16	6.31%	93.76%	7.17%	3.72%	9.45
N17	14.82%	85.51%	10.71%	5.66%	9.48
N18	30.40%	72.32%	13.85%	7.44%	9.50
N19	92.89%	98.31%	87.74%	78.15%	1.16
N20	95.15%	98.40%	89.33%	80.71%	1.58
N20P	95.09%	98.47%	89.65%	81.24%	1.04

Table S 3-3. The properties of six 3D images not used for training acquired from different mice included in the second independent dataset.

	Image Size (voxel)	*Voxel Size* (μm^3)	*Z evaluation interval*	*Background*	*Trans gene*	*Phenotype*
1	256 × 256 × 100	1.14 × 1.14 × 1	1 μm	C57/BL6	APP/PS1	AD
2	256 × 256 × 250	0.95 × 0.95 × 1	25 μm	C57/BL6	APP/PS1	WT
3	256 × 256 × 25	0.95 × 0.95 × 1	1 μm	C57/BL6	APP/PS1	WT
4	256 × 256 × 25	0.95 × 0.95 × 1	1 μm	C57/BL6	APP/PS1	WT
5	256 × 256 × 25	0.95 × 0.95 × 1	1 μm	C57/BL6	APP/PS1	WT
6	256 × 256 × 25	0.95 × 0.95 × 1	1 μm	C57/BL6	APP/PS1	WT

Table S 3-4. The results of DeepVess and the state-of-the-art methods on the second independent dataset from subjects not used for the model training (S3 Table).

DeepVess surpass both of them in terms of sensitivity, Dice index, Jaccard index, and boundary modified Hausdorff distance (MHD).

	Sensitivity	***Specificity***	***Dice***	***Jaccard***	***MHD***
Teikari et al. [24]	67.7%	99.3%	74.9%	60.6%	1.73
3D U-Net [28]	72.4%	99.3%	78.5%	64.9%	1.45
DeepVess	**85.5**%	98.7%	**83.5**%	**71.8**%	**1.41**

REFERENCES

Sonntag WE, Eckman DM, Ingraham J, Riddle DR. Regulation of cerebrovascular aging. In: Riddle DR, editor. Brain aging: models, methods, and mechanisms. Boca Raton, FL: CRC Press/Taylor & Francis; 2007. p. 279–304.

Hossmann K. Viability thresholds and the penumbra of focal ischemia. Annals of neurology. 1994;36(4):557–565.

Lin L, Yao J, Zhang R, Chen CC, Huang CH, Li Y, et al. High-speed photoacoustic microscopy of mouse cortical microhemodynamics. Journal of biophotonics. 2017;10(6-7):792–798.

Erdener ŞE, Tang J, Sajjadi A, Kılıç K, Kura S, Schaffer CB, et al. Spatio-temporal dynamics of cerebral capillary segments with stalling red blood cells. Journal of Cerebral Blood Flow & Metabolism. 2017; p. 0271678X17743877.

Blinder P, Tsai PS, Kaufhold JP, Knutsen PM, Suhl H, Kleinfeld D. The cortical angiome: an interconnected vascular network with noncolumnar patterns of blood flow. Nature neuroscience. 2013;16(7):889–897.

Cruz Hernández JC, Bracko O, Kersbergen CJ, Muse V, Haft-Javaherian M, Berg M, et al. Neutrophil adhesion in brain capillaries contributes to cortical blood flow decreases and impaired memory function in mouse models of Alzheimer's disease. Nature Neuroscience In press. 2019.

Kalaria RN. Cerebral vessels in ageing and Alzheimer's disease. Pharmacology & therapeutics. 1996;72(3):193–214.

Farkas E, Luiten PG. Cerebral microvascular pathology in aging and Alzheimer's disease. Progress in neurobiology. 2001;64(6):575–611.

Riddle DR, Sonntag WE, Lichtenwalner RJ. Microvascular plasticity in aging. Ageing research reviews. 2003;2(2):149–168.

Kirbas C, Quek F. A review of vessel extraction techniques and algorithms. ACM Computing Surveys (CSUR). 2004;36(2):81–121.

Lesage D, Angelini ED, Bloch I, Funka-Lea G. A review of 3D vessel lumen segmentation techniques: Models, features and extraction schemes. Medical image analysis. 2009;13(6):819–845.

Litjens G, Kooi T, Bejnordi BE, Setio AAA, Ciompi F, Ghafoorian M, et al. A survey on deep learning in medical image analysis. Medical Image Analysis. 2017;42(Supplement C):60 – 88.

Fraz MM, Remagnino P, Hoppe A, Uyyanonvara B, Rudnicka AR, Owen CG, et al. Blood vessel segmentation methodologies in retinal images–a survey. Computer methods and programs in biomedicine. 2012;108(1):407–433.

Tsai PS, Kaufhold JP, Blinder P, Friedman B, Drew PJ, Karten HJ, et al. Correlations of neuronal and microvascular densities in murine cortex revealed by direct counting and colocalization of nuclei and vessels. Journal of Neuroscience. 2009;29(46):14553–14570.

Yi J, Ra JB. A locally adaptive region growing algorithm for vascular segmentation. International Journal of Imaging Systems and Technology. 2003;13(4):208–214.

Mille J, Cohen LD. Deformable tree models for 2D and 3D branching structures extraction. In: Computer Vision and Pattern Recognition Workshops, 2009. CVPR Workshops 2009. IEEE Computer Society Conference on. IEEE; 2009. p. 149–156.

Gulshan V, Peng L, Coram M, Stumpe MC, Wu D, Narayanaswamy A, et al. Development and validation of a deep learning algorithm for detection of diabetic retinopathy in retinal fundus photographs. Jama. 2016;316(22):2402–2410.

Szegedy C, Vanhoucke V, Ioffe S, Shlens J, Wojna Z. Rethinking the inception architecture for computer vision. In: Proceedings of the IEEE Conference on Computer Vision and Pattern Recognition; 2016. p. 2818–2826.

Wu A, Xu Z, Gao M, Buty M, Mollura DJ. Deep vessel tracking: A generalized probabilistic approach via deep learning. In: Biomedical Imaging (ISBI), 2016 IEEE 13th International Symposium on. IEEE; 2016. p. 1363–1367.

Fu H, Xu Y, Wong DWK, Liu J. Retinal vessel segmentation via deep learning network and fully- connected conditional random fields. In: Biomedical

Imaging (ISBI), 2016 IEEE 13th International Symposium on. IEEE; 2016. p. 698–701.

Fu H, Xu Y, Lin S, Wong DWK, Liu J. Deepvessel: Retinal vessel segmentation via deep learning and conditional random field. In: International Conference on Medical Image Computing and Computer- Assisted Intervention. Springer; 2016. p. 132–139.

Maninis KK, Pont-Tuset J, Arbeláez P, Van Gool L. Deep retinal image understanding. In: International Conference on Medical Image Computing and Computer-Assisted Intervention. Springer; 2016. p. 140– 148.

Lorthois S, Lauwers F, Cassot F. Tortuosity and other vessel attributes for arterioles and venules of the human cerebral cortex. Microvascular research. 2014; 91:99–109.

Teikari P, Santos M, Poon C, Hynynen K. Deep learning convolutional networks for multiphoton microscopy vasculature segmentation. arXiv preprint arXiv:160602382. 2016.

Bates R, Irving B, Markelc B, Kaeppler J, Muschel R, Grau V, et al. Extracting 3D Vascular Structures from Microscopy Images using Convolutional Recurrent Networks. arXiv preprint arXiv:170509597. 2017.

Ronneberger O, Fischer P, Brox T. U-net: Convolutional networks for biomedical image segmentation.

In: International Conference on Medical Image Computing and Computer-Assisted Intervention. Springer; 2015. p. 234–241.

Long J, Shelhamer E, Darrell T. Fully convolutional networks for semantic segmentation. In: Proceedings of the IEEE Conference on Computer Vision and Pattern Recognition; 2015. p. 3431–3440.

Çiçek Ö, Abdulkadir A, Lienkamp SS, Brox T, Ronneberger O. 3D U-Net: learning dense volumetric segmentation from sparse annotation. In: International Conference on Medical Image Computing and Computer-Assisted Intervention. Springer; 2016. p. 424–432.

Jankowsky JL, Fadale DJ, Anderson J, Xu GM, Gonzales V, Jenkins NA, et al. Mutant presenilins specifically elevate the levels of the 42 residue β-amyloid peptide in vivo:

evidence for augmentation of a 42-specific γ secretase. Human molecular genetics. 2003;13(2):159–170.

Denk W, Strickler JH, Webb WW, et al. Two-photon laser scanning fluorescence microscopy. Science. 1990;248(4951):73–76.

Holtmaat A, Bonhoeffer T, Chow DK, Chuckowree J, De Paola V, Hofer SB, et al. Long-term, high-resolution imaging in the mouse neocortex through a chronic cranial window. Nature protocols. 2009;4(8):1128–1144.Shih AY, Driscoll JD, Drew PJ, Nishimura N, Schaffer CB, Kleinfeld D. Two-photon microscopy as a tool to study blood flow and neurovascular coupling in the rodent brain. Journal of Cerebral Blood Flow & Metabolism. 2012;32(7):1277–1309.

Pologruto TA, Sabatini BL, Svoboda K. ScanImage: flexible software for operating laser scanning microscopes. Biomedical engineering online. 2003;2(1):13.

Abràmoff MD, Magalhães PJ, Ram SJ. Image processing with ImageJ. Biophotonics international. 2004;11(7):36–42.

Thirion JP. Image matching as a diffusion process: an analogy with Maxwell's demons. Medical image analysis. 1998;2(3):243–260.

Vercauteren T, Pennec X, Perchant A, Ayache N. Diffeomorphic demons: Efficient non-parametric image registration. NeuroImage. 2009;45(1): S61–S72.

Srivastava N, Hinton GE, Krizhevsky A, Sutskever I, Salakhutdinov R. Dropout: a simple way to prevent neural networks from overfitting. Journal of machine learning research. 2014;15(1):1929–1958.

Dubuisson MP, Jain AK. A modified Hausdorff distance for object matching. In: Pattern Recognition, 1994. Vol. 1-Conference A: Computer Vision & Image Processing., Proceedings of the 12th IAPR International Conference on. vol. 1. IEEE; 1994. p. 566–568.

Huttenlocher DP, Klanderman GA, Rucklidge WJ. Comparing images using the Hausdorff distance. IEEE Transactions on pattern analysis and machine intelligence. 1993;15(9):850–863.

Kingma D, Ba J. Adam: A method for stochastic optimization. arXiv preprint arXiv:14126980. 2014.

Abadi M, Agarwal A, Barham P, Brevdo E, Chen Z, Citro C, et al. Tensorflow: Large-scale machine learning on heterogeneous distributed systems. arXiv preprint arXiv:160304467. 2016.

Lee TC, Kashyap RL, Chu CN. Building skeleton models via 3-D medial surface axis thinning algorithms. CVGIP: Graphical Models and Image Processing. 1994;56(6):462–478.

Jones JS, Small DM, Nishimura N. In Vivo Calcium Imaging of Cardiomyocytes in the Beating Mouse Heart with Multiphoton Microscopy. Frontiers in physiology. 2018; 9:969.

Gal Y, Ghahramani Z. Dropout as a Bayesian approximation: Representing model uncertainty in deep learning. In: international conference on machine learning; 2016. p. 1050–1059.

So PT, Kim H, Kochevar IE. Two-photon deep tissue ex vivo imaging of mouse dermal and subcutaneous structures. Optics express. 1998;3(9):339–350.

So PT, Dong CY, Masters BR, Berland KM. Two-photon excitation fluorescence microscopy. Annual review of biomedical engineering. 2000;2(1):399–429.

Tsai PS, Friedman B, Ifarraguerri AI, Thompson BD, Lev-Ram V, Schaffer CB, et al. All-optical histology using ultrashort laser pulses. Neuron. 2003;39(1):27–41.

Zoumi A, Lu X, Kassab GS, Tromberg BJ. Imaging coronary artery microstructure using second- harmonic and two-photon fluorescence microscopy. Biophysical journal. 2004;87(4):2778–2786.

Iadecola C. Neurovascular regulation in the normal brain and in Alzheimer's disease. Nature reviews Neuroscience. 2004;5(5):347.

Vérant P, Serduc R, Van Der Sanden B, Rémy C, Vial JC. A direct method for measuring mouse capillary cortical blood volume using multiphoton laser scanning microscopy. Journal of Cerebral Blood Flow & Metabolism. 2007;27(5):1072–1081.

Guti´errez-Jim´enez E, Cai C, Mikkelsen IK, Rasmussen PM, Angleys H, Merrild M, et al. Effect of electrical forepaw stimulation on capillary transit-time heterogeneity (CTH). Journal of Cerebral Blood Flow & Metabolism. 2016;36(12):2072–2086.

Dorr A, Sahota B, Chinta LV, Brown ME, Lai AY, Ma K, et al. Amyloid-β-dependent compromise of microvascular structure and function in a model of Alzheimer's disease. Brain. 2012;135(10):3039–3050.

Lai AY, Dorr A, Thomason LA, Koletar MM, Sled JG, Stefanovic B, et al. Venular degeneration leads to vascular dysfunction in a transgenic model of Alzheimer's disease. Brain. 2015;138(4):1046–1058.

Milliken GA, Johnson DE. Analysis of messy data volume 1: designed experiments. vol. 1. CRC Press; 2009.

Wilkinson J, Hopewell J, Reinhold H. A quantitative study of age-related changes in the vascular architecture of the rat cerebral cortex. Neuropathology and applied neurobiology. 1981;7(6):451–462.

Hunziker O, Abdel'al S, Schulz U. The aging human cerebral cortex: a stereological characterization of changes in the capillary net. Journal of gerontology. 1979;34(3):345–350.

Heinzer S, Krucker T, Stampanoni M, Abela R, Meyer EP, Schuler A, et al. Hierarchical bioimaging and quantification of vasculature in disease models using corrosion casts and microcomputed tomography. In: Proc. SPIE. vol. 5535. SPIE Bellingham, WA, USA; 2004. p. 65–76.

Heinzer S, Kuhn G, Krucker T, Meyer E, Ulmann-Schuler A, Stampanoni M, et al. Novel three- dimensional analysis tool for vascular trees indicates complete micro-networks, not single capillaries, as the angiogenic endpoint in mice overexpressing human VEGF 165 in the brain. Neuroimage. 2008;39(4):1549–1558.

Boero JA, Ascher J, Arregui A, Rovainen C, Woolsey TA. Increased brain capillaries in chronic hypoxia. Journal of applied physiology. 1999;86(4):1211–1219.

Drew PJ, Shih AY, Kleinfeld D. Fluctuating and sensory-induced vasodynamics in rodent cortex extend arteriole capacity. Proceedings of the National Academy of Sciences. 2011;108(20):8473–8478.

Hall CN, Reynell C, Gesslein B, Hamilton NB, Mishra A, Sutherland BA, et al. Capillary pericytes regulate cerebral blood flow in health and disease. Nature. 2014;508(7494):55–60.

Cudmore RH, Dougherty SE, Linden DJ. Cerebral vascular structure in the motor cortex of adult mice is stable and is not altered by voluntary exercise. Journal of Cerebral Blood Flow & Metabolism. 2016; p. 0271678X16682508.

Meyer EP, Ulmann-Schuler A, Staufenbiel M, Krucker T. Altered morphology and 3D architecture of brain vasculature in a mouse model for Alzheimer's disease. Proceedings of the National Academy of Sciences. 2008;105(9):3587–3592.

Heinzer S, Krucker T, Stampanoni M, Abela R, Meyer EP, Schuler A, et al. Hierarchical microimaging for multiscale analysis of large vascular networks. Neuroimage. 2006;32(2):626–636.

Serduc R, Vérant P, Vial JC, Farion R, Rocas L, Rémy C, et al. In vivo two-photon microscopy study of short-term effects of microbeam irradiation on normal mouse brain microvasculature. International Journal of Radiation Oncology* Biology* Physics. 2006;64(5):1519–1527.

CHAPTER 4

NEUTROPHIL ADHESION IN BRAIN CAPILLARIES REDUCES CORTICAL BLOOD FLOW AND IMPAIRS MEMORY FUNCTION IN ALZHEIMER'S DISEASE MOUSE MODELS

4.1 List of Haft-Javaherian's contributions

- Author contributions section (4.7) reads: *"... **MH.**, G.O. and Y.K. developed custom software for data analysis. **M.H.** developed custom machine learning algorithms for image segmentation. ... . J.C.C.H., O.B., N.N. and C.B.S. wrote the paper with contributions from **M.H.**, M.C.C., L.P., C.L., C.I.* and S.L. All authors edited and commented on the manuscript."
- Figure 4.1: Panel E, F, and G
- Figure 4.2: Panel D and E
- Figure S 4.1: Panel A
- Figure S 4.2: Panel A, B, C, D
- Method Section: Quantification of capillary network topology and capillary segment stalling.
- Method Section: Variations in quantification of capillary network topology and capillary segment stalling for 5xFAD mice
- Method Section: Amyloid plaque segmentation and density analysis

4.2 Abstract

Cerebral blood flow (CBF) reductions in Alzheimer's disease (AD) patients and related mouse models have been recognized for decades, but the underlying mechanisms and resulting consequences on AD pathogenesis remain poorly understood. In APP/PS1 and 5xFAD mice we found that an increased number of cortical capillaries had stalled blood flow as compared to wildtype animals, largely due to neutrophils that adhered in capillary segments and blocked blood flow. Administration of antibodies against the neutrophil marker Ly6G reduced the number of stalled capillaries, leading to an immediate increase in CBF and to rapidly improved performance in spatial and working memory tasks. This study identified a novel cellular mechanism that explains the majority of the CBF reduction seen in two mouse models of AD and demonstrated that improving CBF rapidly improved short-term memory function. Restoring cerebral perfusion by preventing neutrophil adhesion may provide a novel strategy for improving cognition in AD patients.

4.3 Introduction

Alzheimer's disease (AD) is the most common form of dementia in the elderly, worldwide. AD is characterized by a rapid and progressive cognitive decline accompanied by several pathological features, such as the accumulation of amyloid-beta (Aβ) plaques in brain tissue and along blood vessels as cerebral amyloid angiopathy, the hyperphosphorylation of tau proteins and formation of neurofibrillary tangles in neurons, increased density and activation of inflammatory cells, and ultimately the death of neurons and other brain cells[1].

Vascular dysfunction is implicated in the pathogenesis of AD. Many of the primary risk factors for AD are associated with compromised vascular structure and function, such as obesity, diabetes, atherosclerosis, and hypertension[2]. Brain blood flow is also severely compromised in AD, with both patients with AD[3-5] and mouse models of AD[6-8], which express mutated genes that encode for amyloid precursor protein (APP), exhibiting cortical cerebral blood flow (cCBF) reductions of ~25% early in disease development. Several mechanisms for this hypoperfusion had been proposed including constriction of brain arterioles[9], loss of vascular density[10], and changes in neural activity patterns and/or in neurovascular coupling[11,12], but a full understanding of the underlying mechanisms for CBF reduction in AD has not emerged.

These large blood flow decreases could contribute to the cognitive symptoms of AD and drive disease progression. Cognitive functions, such as attention, were immediately impaired by CBF reductions of ~20% in healthy humans[13]. When CBF was chronically reduced by ~35% in wildtype (wt) mice, spatial memory deficits were observed, accompanied by pathological changes in the brain including increased inflammation[14]. In addition, impairing blood flow in AD mouse models led to an increase in Aβ deposition, suggesting that blood flow deficits can worsen Aβ pathology[14,15]. These data suggest that the decreased CBF in AD likely contributes to both the cognitive dysfunction and to disease progression.

Because CBF reductions have been a recognized and important aspect of AD, yet have not been well explained, we sought to uncover the cellular basis for these flow reductions in the APP/PS1 and 5xFAD mouse models of APP overexpression.

4.4 Results

To investigate cortical hypoperfusion in AD, we used *in vivo* two-photon excited fluorescence (2PEF) microscopy to image the cortical vasculature in APP/PS1 mice[16] (Fig. 4.1.a) and looked for occluded vessels (Figure 4.1.b). We observed no obstructions in arterioles or venules, but about 1.8% of capillaries in APP/PS1 mice had stalled blood flow, while age- and sex-matched, wt littermates had 0.4% of capillaries not flowing (Figure 4.1.c, video S 4.1 and S 4.2). The number of stalled capillaries was elevated by 12 weeks of age in APP/PS1 mice and remained elevated throughout disease progression (Figure 4.1.d). Flowing and stalled capillaries (Figure 4.1.e) had about the same distance distribution relative to the nearest penetrating arteriole (Figure 4.1.f) or ascending venule (Figure 4.1.g). The incidence of capillary stalling did not increase with Aβ plaque density (Figure S 4.1a) and was the same in awake and anesthetized animals (video S 4.3 and S 4.4; Figure S 4.1.b). Capillary stalling was similarly elevated in 5-6 month old 5xFAD (Figure S 4.2.a) and 10-13 month old TgCRND8 mice[17] (Figure S 4.3), two different mouse model of APP overexpression.

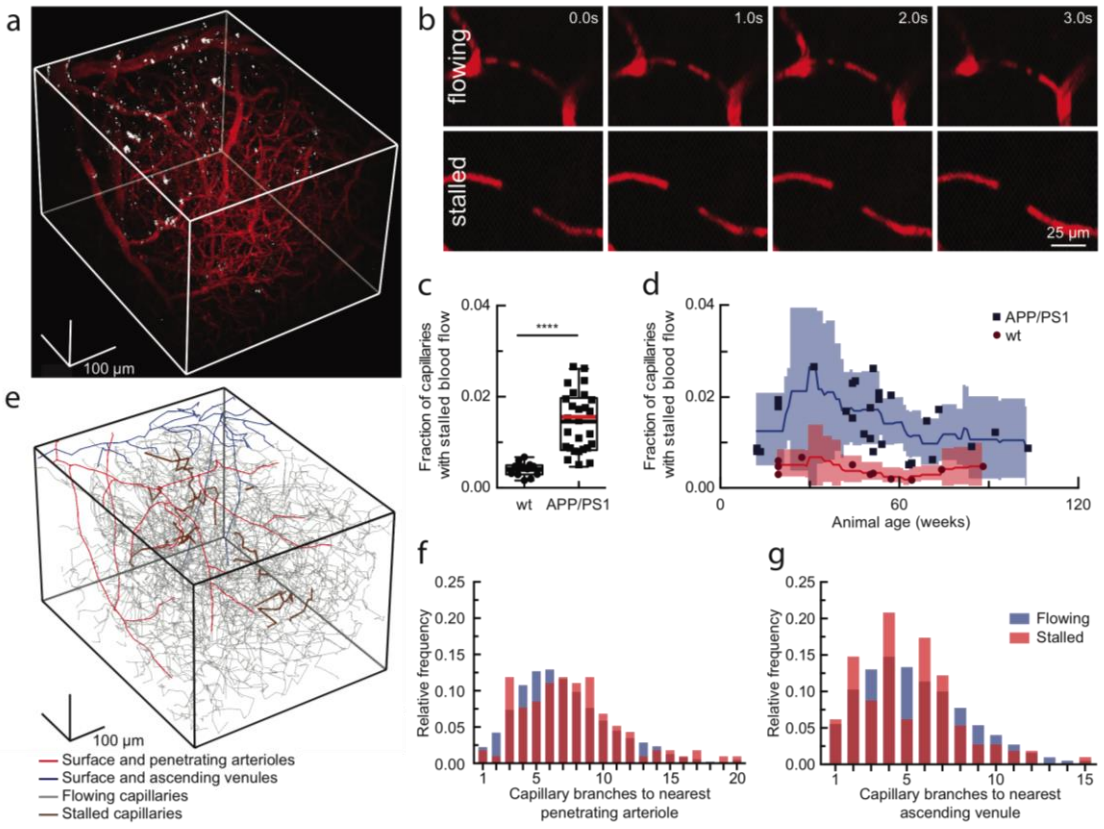
a
100 µm
b
flowing
stalled
0.0s
1.0s
2.0s
3.0s
25 µm
c
Fraction of capillaries with stalled blood flow
0.04
0.02
0.00
****
wt
APP/PS1
d
Fraction of capillaries with stalled blood flow
APP/PS1
wt
0
60
120
Animal age (weeks)
e
100 µm
Surface and penetrating arterioles
Surface and ascending venules
Flowing capillaries
Stalled capillaries
f
Relative frequency
0.25
0.20
0.15
0.10
0.05
0.00
1
5
10
15
20
Capillary branches to nearest penetrating arteriole
g
Relative frequency
Flowing
Stalled
1
5
10
15
Capillary branches to nearest ascending venule

Figure 4.1. 2PEF imaging of mouse cortical vasculature revealed a higher fraction of plugged capillaries in APP/PS1 mice.

(a) Rendering of 2PEF image stack of cortical vasculature (red; Texas Red dextran) and amyloid deposits (white; methoxy-X04). (b) Individual brain capillaries were scored as flowing or stalled based on the motion of unlabeled blood cells (black) within the fluorescently labeled blood plasma (red). (c) Fraction of capillaries with stalled blood flow in APP/PS1 and wt mice. (APP/PS1: n = 28 mice (7 female, 21 male), ~22,400 capillaries, and wt: n = 12 mice (10 female, 2 male), ~9,600 capillaries; Two-tailed Mann-Whitney, $p=6.8 \times 10^{-9}$; Boxplot: whiskers extend 1.5 times the difference between the value of the 75th and 25th percentile, median=black line and mean= red line.) (d) same data in c shown as a function of animal age. Each data point represents the fraction of capillaries stalled in one mouse, with a minimum of 800 capillaries scored per mouse. Curves represent sliding averages with a 10-week window and shaded areas represent 95% confidence intervals. Data from one outlier mouse not shown in c and d: APP/PS1, 42 weeks, 4.4% stalled. (e) Tracing of the vascular network in panel a, with stalled capillaries indicated in brown. (f) and (g) Histograms showing the topological location of flowing and stalled capillaries in APP/PS1 mice relative to the nearest penetrating arteriole and ascending venule, respectively (n = 8 mice (5 female, 3 male), 120 stalled and ~8,700 flowing capillaries).

Using labeling strategies to distinguish leukocytes, platelets, and RBCs (Figure 4.2.a), we found the majority of stalled capillary segments in APP/PS1 mice contained a leukocyte, sometimes with and sometimes without one or more RBCs also present in the capillary segment (Figure 4.2.b). We injected a low dose of fluorescently labeled antibodies against Ly6G, a neutrophil surface marker (0.1 mg/kg animal weight, intravenous), and found that the vast majority of capillary stalls had a labeled cell present (Figure 4.2.c; 26 of 30 identified capillary stalls across four mice were labeled). Stalled capillaries had a modestly smaller average diameter than flowing capillaries (Figure 4.2.d), but no difference in the density of nearby Aβ deposits (Figure 4.2.e). Most plugged capillaries were transiently stalled with a half-life of less than 5 min, while one-third remained stalled for 15 min and 10% began flowing and then re-stalled within 15 min (Figure 4.2.f; Figure S 4.4). We also observed that some capillary segments alternated between flowing and stalled in repeated imaging sessions over weeks (Figure 4.2.g). The same capillaries were stalled across multiple imaging sessions about ten times as frequently as predicted by a statistical model that assumed each capillary had an equal probability of being stalled at any time point (Figure 4.2.h). Taken together, these data suggest that the capillary stalls were caused by leukocytes (likely neutrophils based on the specificity of Ly6G expression[18]) plugging a distinct subset of capillary segments.

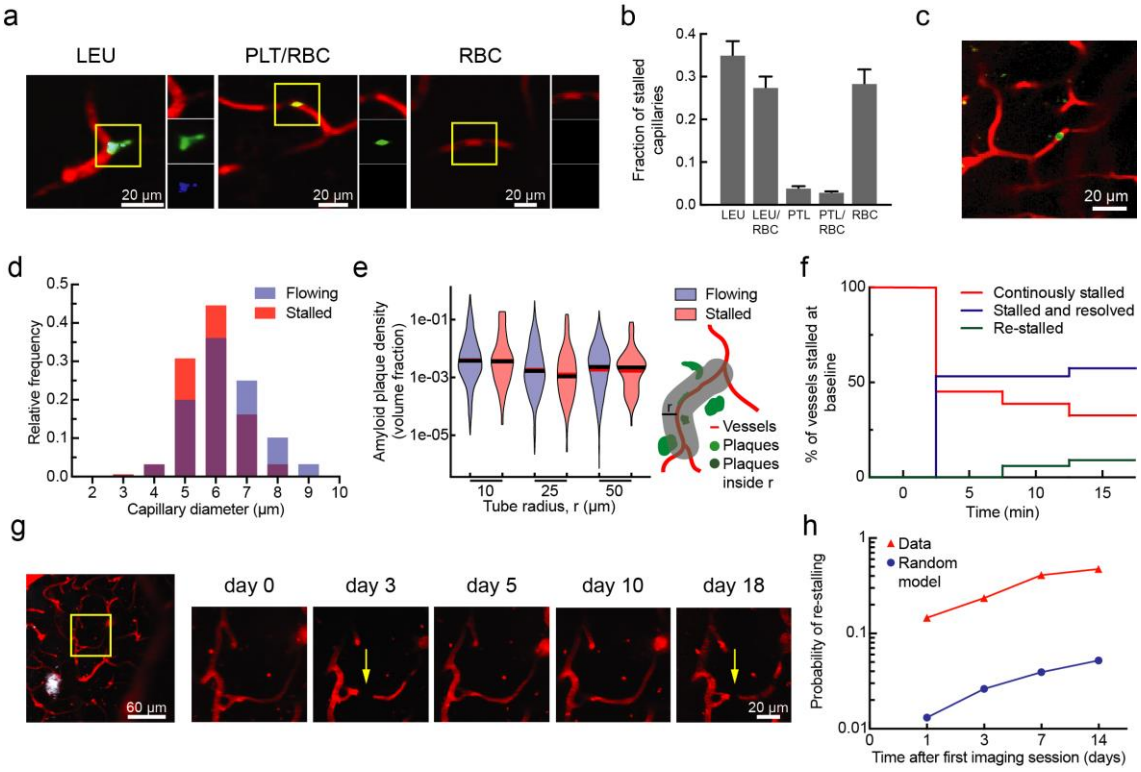

Figure 4.2. Characterization of the cause, location, and dynamics of capillary occlusions in APP/PS1 mice.

(a) 2PEF images of stalled capillaries that contained a leukocyte (LEU, left), platelet aggregates (PLT) and RBCs (center), or only RBCs (right), distinguished by fluorescent labels (red: Texas Red-labeled blood plasma; green: rhodamine 6G-labeled leukocytes and platelets; blue: Hoechst-labeled leukocyte nuclei). (b) Fraction of stalled capillaries in APP/PS1 mice that contained LEU, one or more RBCs, and PLT, distinguishing cases of LEU only, LEU with one or more RBCs, PLT only, PLT with RBCs, and RBCs only (n = 6 mice (3 female, 3 male) and 106 stalls; error bars represent 95% confidence intervals based on binomial statistics.) (c) Projection of 2PEF image stack showing an anti-Ly6G labeled cell in a stalled capillary (red: Texas Red-labeled blood plasma; green: anti-Ly6G-Alexa 488 (0.1 mg/kg animal weight, intravenous). (d) Histogram of the diameter of flowing and stalled capillaries in APP/PS1 mice (Averages: 5.8±0.84 µm (stalled), 6.3±1.1 µm (flowing) (mean±SD);

Two-tailed Mann-Whitney, p=0.000020; n = 7 mice (4 female, 3 male), 116 stalled and ~8,400 flowing capillaries). (e) Violin plot of the density of amyloid deposits within tubes of different radii that followed the capillary centerline for flowing and stalled capillary segments in APP/PS1 mice (n = 7 mice (4 female, 3 male), 116 stalled and ~8,400 flowing capillaries). The vertical range of the violin plot represents the full range of measured values, while the width of the violin indicates the frequency of those values. The red (black) horizontal line indicates the mean (median) value. (f) Fraction of stalled capillaries that remained stalled (red), resumed flowing (green), or resumed flowing and then re-stalled (blue) over 15 minutes in APP/PS1 mice (n = 3 mice (all male), 31 capillary segments). (g) 2PEF images of the same capillary alternately stalled (arrows) and flowing over several weeks (white: methoxy-X04). (h) Probability of an initially stalled capillary to be observed stalled again at any subsequent imaging time point, showing both real observations in APP/PS1 mice and predictions from a model that assumed each capillary had an equal probability of stalling at each time point (n=4 mice (2 female, 2 male), 49 stalled capillaries followed from the first imaging session).

We serendipitously found that administration of a much higher dose of fluorescently-labeled antibodies against Ly6G (α-Ly6G; 4 mg/kg animal weight, intraperitoneal) reduced the number of stalled capillaries within 10 min (Figure 4.3.a and Figure S 4.5). Isotype control (Iso-Ctr) antibodies did not impact capillary stalling. Using flow cytometry (Figure S 4.6.a) we found that α-Ly6G administration led to no change in the number of circulating neutrophils at three hours (Figure S 4.6.b) but did lead to ~50% depletion by six hours (Figure S 4.6.c) and near complete depletion by 24 hours (Figure 4.6.d). Median volumetric blood flow in penetrating arterioles, measured using 2PEF (Figure 4.3.b) and characterizing blood flow into the cortex, increased by 26% in young (3-4 months) and 32% in aged (11-14 months) APP/PS1 mice one hour after α-Ly6G administration (Figure 4.3.c). This increase in penetrating arteriole blood flow was due to an increase in RBC speed and not an increase in vessel diameter (Figure S 4.7.a and b). Penetrating arterioles with lower baseline flow tended to show larger flow increases (Figure S 4.7.c). Iso-Ctr antibodies did not change penetrating arteriole blood flow in APP/PS1 mice, nor did α-Ly6G in wt animals (Figure S 4.3.c). We also used arterial spin labeled MRI (ASL-MRI) to measure cCBF in 7-9-month old animals (Figure 4.3.d). At baseline, average cCBF in APP/PS1 mice was 17% lower than in wt animals (Figure 4.3.e). cCBF increased by 13% in APP/PS1 mice at ~5 hr after α-Ly6G administration, recovering about two-thirds of the deficit relative to wt animals, but was unchanged in APP/PS1 mice given Iso-Ctr antibodies or wt mice given α-Ly6G (Figure 4.3.e). To establish the timeline for these CBF increases, we used multi-exposure laser speckle contrast imaging to quantify changes in CBF over the first three hours after antibody administration in APP/PS1 mice. CBF increased within the first 10 min after α-Ly6G

administration and remained elevated over the three hours (Figure S 4.8). Isotype control antibodies did not lead to significant changes in CBF (Figure S 4.8). In 5-6-month-old 5xFAD mice we also found that α-Ly6G administration led to a reduction in the number of stalled capillaries (Figure S 4.2.a) and an increase in blood flow in cortical penetrating arterioles (Figure S 4.2.b-d) within an hour. Thus, administration of α-Ly6G led to a rapid reduction in the number of capillary stalls that was accompanied by a rapid increase in cCBF in APP/PS1 and 5xFAD mice. In contrast, when antibodies against LFA-1 were administered to 11-13-month-old APP/PS1 mice, we did not observe a rapid decrease in the number of stalled capillaries. Instead, we found that capillary stalls were reduced, and penetrating arteriole blood flow was increased at one day after antibody injection, when circulating leukocytes had been depleted (Figure S 4.9). Across all antibody and control treatments in APP/PS1 mice, penetrating arteriole flows increased (decreased) when the number of stalled capillaries decreased (increased) (Figure S 4.9.g).

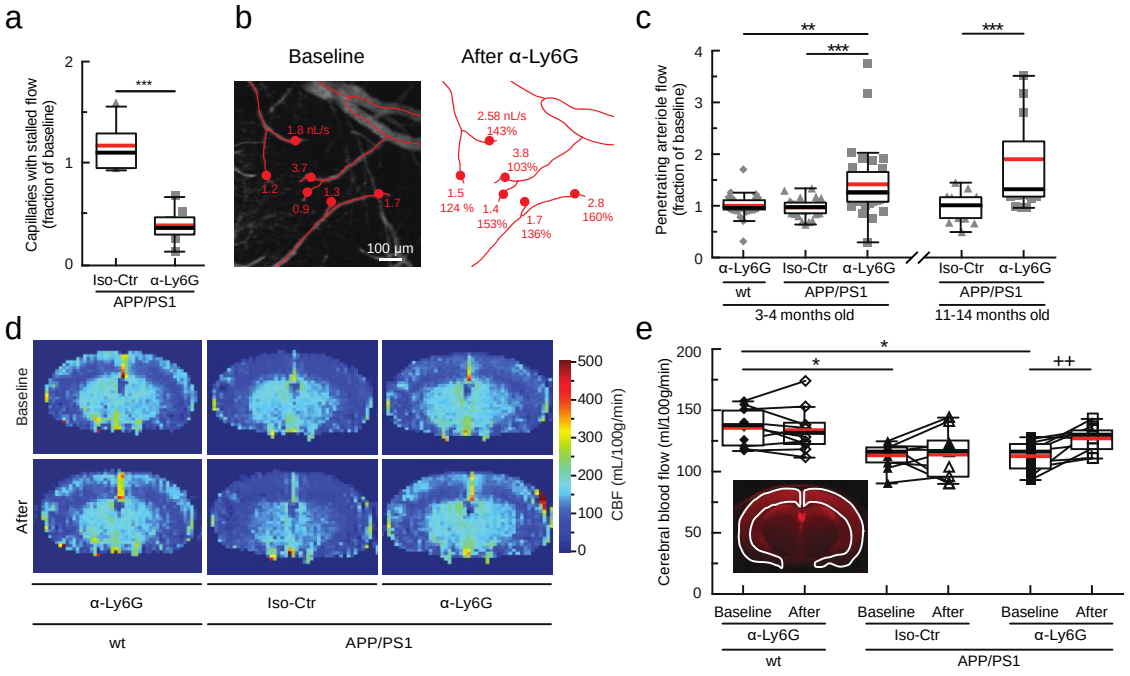

Figure 4.3. Administration of antibodies against Ly6G reduced the number of stalled capillaries and increased cCBF in APP/PS1 mice.

(a) Number of capillaries with stalled blood flow ~1 hr after α-Ly6G or Iso-Ctr antibody administration (4 mg/kg animal weight, intraperitoneal) shown as a fraction of the number of stalled capillaries at baseline in APP/PS1 mice (α-Ly6G: n = 6 mice (3 female, 3 male), ~4,800 capillaries; Iso-Ctr: n = 6 mice (5 female, 1 male), ~4,800 capillaries; two-tailed Mann-Whitney, p=0.0004). (b) Projection of 2PEF image stack of brain surface vasculature, with surface (red lines) and penetrating (red dots) arterioles identified. For each penetrating arteriole, volumetric blood flow is indicated at baseline (left) and after α-Ly6G administration (right), along with the percentage of baseline flow. (c) Volumetric blood flow in penetrating arterioles measured 60-90 min after α-Ly6G or Iso-Ctr antibody administration in young and old APP/PS1 mice and wt control animals shown as a fraction of baseline arteriole flow (young APP/PS1 Iso-Ctr: n = 5 mice (1 female, 4 male), 32 arterioles; old APP/PS1 Iso-Ctr: n = 3 mice (1 female, 2 male), 18 arterioles; young wt α-Ly6G: n = 5 mice (3 female, 2 male), 30 arterioles; young APP/PS1 α-Ly6G: n = 5 (2 female, 3

male), 33 arterioles; old APP/PS1 α-Ly6G: n = 3 mice (all male), 22 arterioles; one-way Kruskal-Wallis ANOVA with post-hoc using Dunn's multiple comparison correction: young wt α-Ly6G vs. young APP/PS1 α-Ly6G p = 0.0023; young APP/PS1 Iso-Ctr vs. young APP/PS1 α-Ly6G p = 0.0000012; old APP/PS1 Iso-Ctr vs. old APP/PS1 α-Ly6G p = 0.00055). (d) CBF map measured using ASL-MRI at baseline and ~5 hr after administration of α-Ly6G or Iso-Ctr antibodies in APP/PS1 and wt mice. (e) cCBF measurements (ASL-MRI, inset indicates ROI on T2 MRI image) at baseline and ~5 hr after administration of α-Ly6G or Iso-Ctr antibodies in APP/PS1 and wt mice (wt α-Ly6G: n = 10 mice, APP/PS1 α-Ly6G: n = 10 mice, APP/PS1 Iso-Ctr: n = 10 mice; Ordinary one-way ANOVA with post hoc using Tukey's multiple comparison correction to compare across groups: baseline wt α-Ly6G vs. baseline APP/PS1 α-Ly6G p=0.011; baseline wt α-Ly6G vs. baseline APP/PS1 Iso-Ctr p=0.014; Paired t-test to compare baseline and after treatment within a group: baseline APP/PS1 α-Ly6G vs. after APP/PS1 α-Ly6G p=0.0058). All boxplots are defined as: whiskers extend 1.5 times the difference between the value of the 75th and 25th percentile, median=black line and mean= red line.

We next tested whether α-Ly6G administration improves cognitive function in APP/PS1 (Figure 4.4.a) and 5xFAD mice. In the object replacement (OR) test of spatial short-term memory (Figure 4.4.b), a single dose of α-Ly6G in ~11-month old APP/PS1 mice improved performance to the level of wt animals at 3 and 24 hours after administration (Figure 4.4.c; Figure S 4.10.a). APP/PS1 mice treated with Iso-Ctr antibodies showed no change, nor did wt animals with α-Ly6G (Figure 4.4.c). In ~ 6-month-old 5xFAD mice, a single dose of α-Ly6G improved animal performance in the OR task at 24 hours, with this trend evident at 3 hours (Figure 4.11.a and b). Similarly, α-Ly6G improved performance of APP/PS1 and 5xFAD mice in the Y-maze test of working memory (Figure 4.4d, Figure S 4.10.b, and Figure S 4.11.c and d). We detected no improvement in sensory-motor function (balance beam walk, Figure S 4.12.a-d) nor in depression- and anxiety-like behavior (forced swim, Figure S 4.12.e) in APP/PS1 mice with α-Ly6G. To exclude an antibody specific effect we repeated the OR and Y-maze behavioral tests in another cohort of APP/PS1 mice before and after administration of α-LFA-1 antibodies and found improved performance on both tests at 24 hours (Figure S 4.13.a-d).

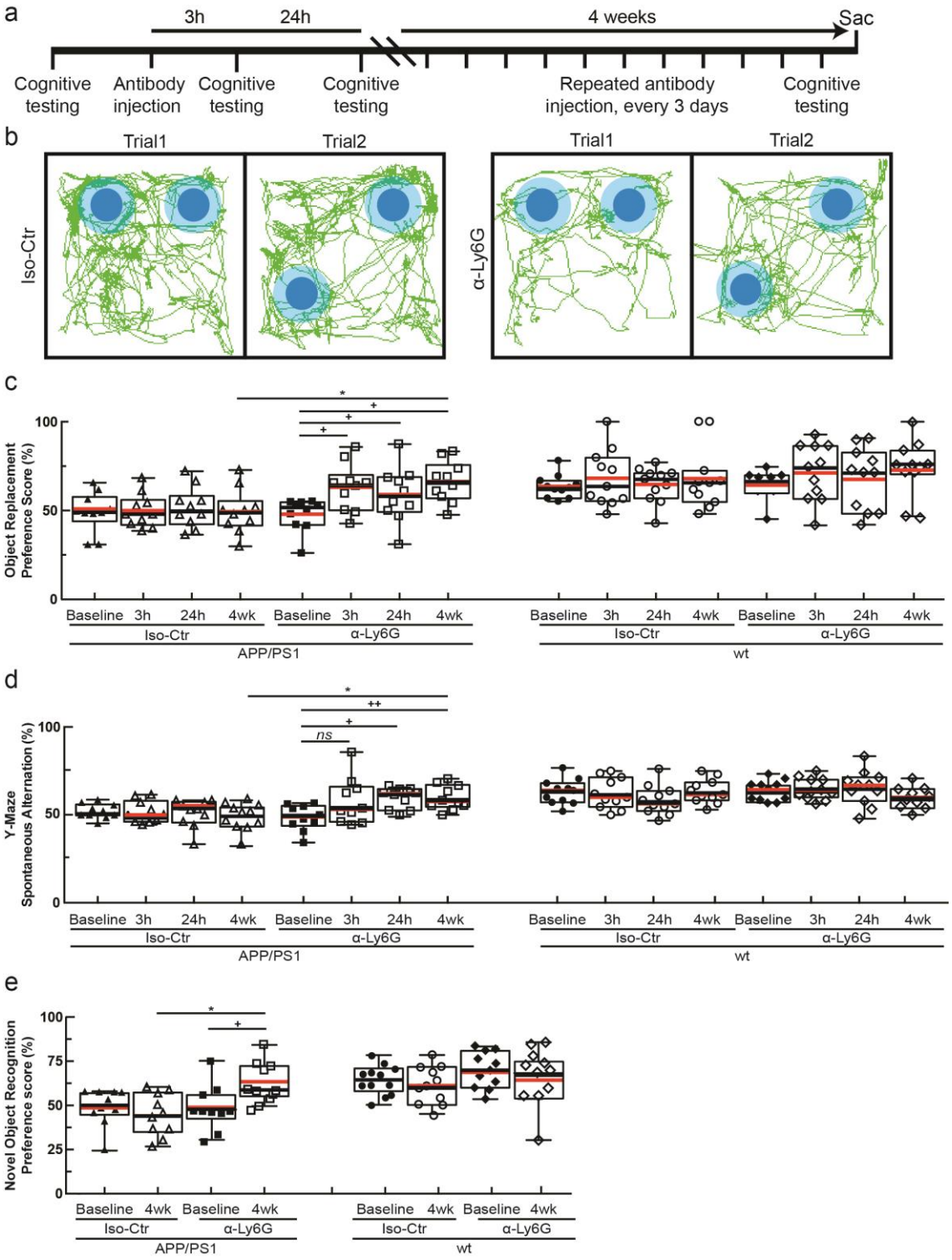
a
3h
24h
4 weeks
Sac
Cognitive testing
Antibody injection
Cognitive testing
Cognitive testing
Repeated antibody injection, every 3 days
Cognitive testing
b
Trial1
Trial2
Trial1
Trial2
Iso-Ctr
α-Ly6G
c
Object Replacement Preference Score (%)
100
50
0
Baseline 3h 24h 4wk Baseline 3h 24h 4wk
Iso-Ctr
α-Ly6G
APP/PS1
Baseline 3h 24h 4wk Baseline 3h 24h 4wk
Iso-Ctr
α-Ly6G
wt
d
Y-Maze Spontaneous Alternation (%)
ns
e
Novel Object Recognition Preference score (%)
100
75
50
25
0
Baseline 4wk Baseline 4wk
Iso-Ctr
α-Ly6G
APP/PS1
Baseline 4wk Baseline 4wk
Iso-Ctr
α-Ly6G
wt

Figure 4.4. Administration of α-Ly6G improved short-term memory.

(a) Experimental timeline for behavioral studies. (b) Tracking of mouse nose location from video recording during training and trial phases of OR task taken 3-5 hr after administration of α-Ly6G or Iso-Ctr antibodies in APP/PS1 mice (representative tracing maps). (c) Preference score in OR task and (d) spontaneous alternation in Y-maze task for APP/PS1 and wt mice at baseline and at 3 hr and 24 hr after a single administration of α-Ly6G or Iso-Ctr antibodies, and after 4 weeks of treatment every three days. (e) Preference score in NOR task for APP/PS1 and wt mice at baseline and after 4 weeks of treatment every three days. (APP/PS1 Iso-Ctr: n=10 mice (5 female, 5 female), APP/PS1 α-Ly6G: n=10 mice (5 female, 5 male), wt α-Ly6G: n=11 mice (7 female, 4 male), wt Iso-Ctr: n=11 mice (8 female, 3 male); one-way Kruskal-Wallis ANOVA with post-hoc using Dunn's multiple comparison correction to compare across groups: Object replacement APP/PS1 4wk Iso-Ctr vs. α-Ly6G p=0.029; Y-maze APP/PS1 4wk Iso-Ctr vs. α-Ly6G p=0.037; Novel object APP/PS1 4wk Iso-Ctr vs. α-Ly6G p=0.038; Friedman one-way repeated measures non-parametric ANOVA to compare baseline and after treatment results within a group: Object replacement APP/PS1 α-Ly6G baseline vs. 3 h p=0.0055, baseline vs. 24h p=0.016, baseline vs. 4wk p=0.045; Y-maze APP/PS1 α-Ly6G baseline vs. 24h p=0.13, baseline vs 4wk p=0.036; two-tailed Wilcoxon matched-pairs signed rank test to compare baseline and post-treatment with novel object APP/PS1 α-Ly6G baseline vs 4wk p=0.039.) All boxplots are defined as: whiskers extend 1.5 times the difference between the value of the 75th and 25th percentile, median=black line and mean= red line. All data in this figure represents the aggregation of two independently-conducted sets of behavioral experiments.

We continued to treat the APP/PS1 mice that received α-Ly6G with additional doses of α-Ly6G every three days for a month, resulting in depletion of neutrophils (Figure S 4.6.e). After this regimen, APP/PS1 mice exhibited short-term memory performance that matched wt animals in OR (Figure 4.4.c), Y-maze (Figure 4.4.d), and novel object recognition (NOR) (Figure 4.4.e; Figure S 4.10.c and d). We saw no improvement in sensory-motor function (Figure S 4.12.a-d) nor in depression- and anxiety-like behavior (Figure S 4.12.e).

Because one of the clearance pathways for Aβ is through the vasculature[19] we assessed whether improving cCBF with α-Ly6G decreases the concentration of Aβ monomers and aggregates. Using enzyme-linked immunosorbent assays (ELISAs) of brain extracts from the animals that received one month of antibody treatment, we found that α-Ly6G reduced the concentration of $A\beta_{1-40}$ compared to Iso-Ctr antibodies (Figure 4.5.a), while the concentration of $A\beta_{1-42}$ (Figure 4.5.b) and aggregates of Aβ (Figure S 4.14.d) remained unchanged. We saw no difference in the number and density of Aβ plaques between α-Ly6G and Iso-Ctr treated animals (Figure S 4.14.a – c).

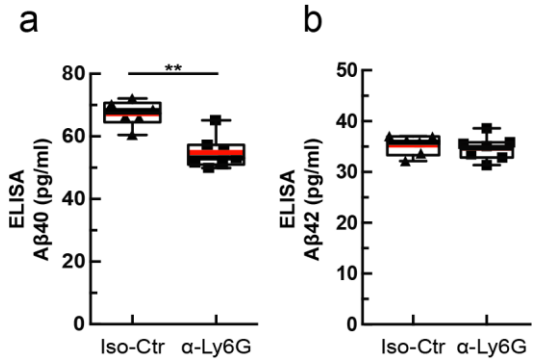

Figure 4.5. Administration of α-Ly6G for one month decreased the concentration of Aβ1-40 in APP/PS1 mice.

ELISA measurements of (a) Aβ1-40 and (b) Aβ1-42 monomer concentrations after 4 weeks of treatment every three days (Iso-Ctr: n=6 mice (4 female, 2 male) and α-Ly6G: n=7 mice (4 female, 3 male); two-tailed Mann-Whitney p=0.0023). Boxplots are defined as: whiskers extend 1.5 times the difference between the value of the 75th and 25th percentile, median=black line and mean= red line.

Finally, we addressed the question of how only ~2% of capillaries being stalled could explain the dramatic blood flow changes we observed after α-Ly6G administration. Because each occluded capillary decreases blood flow in up- and down-stream vessels[20], a small number of stalled capillaries could have an outsized impact on CBF. To estimate the magnitude of this impact and to compare how the topology of the cortical capillary network influences the result, we simulated blood flow in vascular networks from a 1 mm^3 volume of mouse parietal cortex (Figure 4.6.a)[21], a 6 mm^3 volume of human cortex (Figure 4.6.b)[22], and a synthetic periodic network of order three (Figure S 4.15.a) using a non-linear model of microvascular blood flow[23] (see Supplementary Methods and Supplementary Note). cCBF decreased linearly with an increasing fraction of stalled

capillaries, without any threshold effect, across all three networks (Figure 4.6.c), demonstrating that, on average, each single capillary occlusion has a similar, and cumulative, impact on blood flow. Moreover, the slope of the CBF decrease with increasing capillary stalls was almost identical between the mouse, human, and artificial networks, suggesting that capillary stalling may impact CBF similarly across three-dimensional capillary networks with three vessels connected at each node. Quantitatively, these simulations predicted a ~5% (10%) deficit in cCBF due to 2% (4%) of capillaries stalled (relative to the case with no capillary stalls), which is smaller than the increase in CBF we observed with 2PEF and ASL-MRI measurements after α-Ly6G administration.

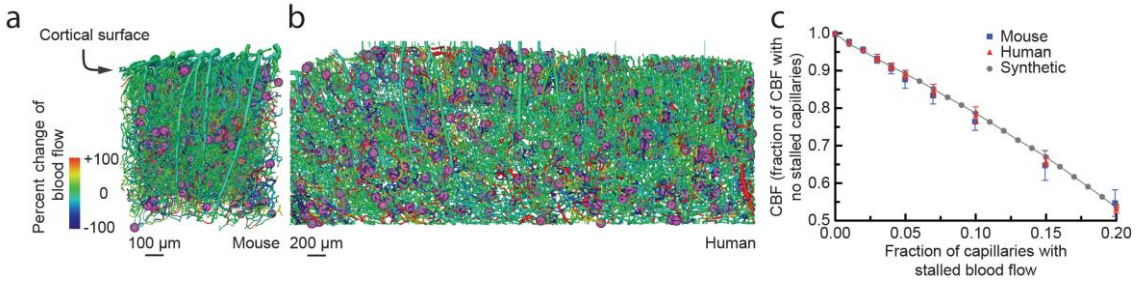

Figure 4.6. Simulations predicted a similar CBF decrease in mouse and human cortical capillary networks with increasing fraction of capillaries with stalled flow.

Spatial maps of simulated blood flow changes caused by stalling of 2% of capillaries (indicated by purple spheres) in an mouse cortical vascular network (a, data on the structure and connectivity of murine cortical vascular network from [44]), and a human network (b, data on the structure and connectivity of human cortical vascular network from [22]). (c) Normalized cortical perfusion as a function of the fraction of capillaries that were occluded, expressed as a fraction of the perfusion with no occlusions, in mouse, human, and synthetic networks (data points represent the mean and error bars represent the SD across five independent simulations).

4.5 Discussion

In this study, we aimed to uncover the cellular mechanisms contributing to reduced cCBF in AD and to determine the impact of this reduced cCBF on cognitive function. Brain blood flow reductions occur in the vast majority of dementia patients, including those with AD. These blood flow reductions are one of the earliest features of AD progression[3,24]. Mouse models that express mutant APP also show comparable reductions in CBF[6-8].

Previous studies have implicated a variety of potential mechanisms in the CBF reductions seen in AD. Amyloid beta monomers were found to drive vasoconstriction in brain arterioles that could contribute to a reduction in resting CBF[9]. In AD, there is a faster loss of vascular density with age, which could reduce cerebral perfusion[10]. In addition to decreases in baseline perfusion, the regulation of blood flow in the brain is compromised in AD. Vessel diameter changes in response to CO_2 inhalation, blood pressure changes, and changes in local neural activity are all attenuated in AD patients and mouse models of APP overexpression[25]. This loss of dynamic regulation of cerebral blood flow could also contribute to cognitive impacts. Indeed, recent work showed that restoring cerebrovascular function, by angiotensin receptor inhibition or by reducing vascular oxidative stress, led to improved cognitive function[12,26,27].

Our data reveal that neutrophil plugging of individual capillary segments is a previously unrecognized mechanism that significantly contributes to the CBF reduction in AD mouse models. The rapid resolution of the capillary stalls after α-Ly6G treatment suggests the stalls are caused by receptor-mediated interactions of neutrophils with the

capillary endothelium[28], likely due to increased endothelial inflammation. Ly6G has long been appreciated as a neutrophil-specific marker[29]. Consistent with our findings, it has recently been shown that inhibiting Ly6G signaling leads to decreased migration of neutrophils toward sites of inflammation by modulating β2-integrin-dependent adhesion[28]. There may, however, be other mechanisms that contribute to the reduction in capillary stalling after α-Ly6G treatment. We observed that stalled capillaries had a modestly smaller diameter, on average, than flowing capillaries and a receptor-mediated increase in the mechanical stiffness of neutrophils that was blocked by α-Ly6G might allow for easier deformation and passage of neutrophils through the narrowed capillaries[30]. While some mouse models of AD have shown severe alterations in the topology of the cortical vascular network, recent work has shown that there are relatively minor differences in the capillary density and tortuosity between APP/PS1 and wt mice, suggesting differences in vascular structure likely do not underlie the increase in capillary stalling in APP/PS1 mice[31,32].

Capillary obstructions due to tissue inflammation have been observed in a variety of organ systems (typically at higher incidence than observed here) and have been shown to contribute to the pathology and disease development[33-39]. Inflammation is a persistent and well-recognized feature of AD and previous work has demonstrated an increase in inflammatory adhesion receptors on endothelial cells[40-42], which likely underlies the capillary stalling we observed. A significant contributor to this inflammation is increased reactive oxygen species (ROS) induced by brain exposure to Aβ oligomeric aggregates[26]. These ROS cause a loss of cerebrovascular flow regulation and likely drive the expression

of leucocyte-binding receptors on the endothelial cell surface, such as ICAM1 and VCAM1. Our observation that some capillary segments were more likely to stall suggests that the underlying vascular inflammation may not be uniform.

While here our focus has been on increased leukocyte adherence causing a subset of capillaries to be transiently stalled due to a firmly adhered leukocyte, this increased leukocyte adherence likely also contributes to slowed, but not stalled, flow in other capillary segments when a leukocyte is present. Our experimental approach does not enable us to readily detect such slowed vessels. Our simulations included only the impact of completely stalled vessels, which may have contributed to the model's underestimation of the increase in CBF after α-Ly6G administration. However, the simulations predicted a similar sensitivity of brain blood flow to capillary stalling in humans and mice, suggesting that, if capillary stalling occurs in AD patients, significant blood flow improvements could be achieved.

We observed spatial and working memory improvements within 24 hours after treatment with antibodies against Ly6G and/or LFA-1 in multiple mouse models of AD. The temporal correlation between reduced capillary stalling/blood flow increase and the improvement in cognitive function suggests that a mismatch between neuronal energy metabolism and delivery of energy substrates through blood flow contributes to the cognitive deficit in these AD mouse models.

We also observed improved cognitive function after one month of treatment with α-Ly6G, which depletes neutrophils, in APP/PS1 mice, measured during the antibody therapy. Because of the persistent depletion of neutrophils during this treatment, we

expect that capillary stalling was reduced and brain blood flow increased throughout the month, including during cognitive testing, which likely contributed to the improved cognitive performance. In previous work by Zenaro, et al., treatment with antibodies that deplete neutrophils (α-GR-1, α-LFA-1, and α-Ly6G) for one month in multiple AD mouse models (3xTg and 5xFAD), remarkably, led to a persistent improvement in cognitive performance, measured a month after the end of antibody therapy[42]. This persistent improvement in cognitive function was attributed to a decrease in the number of neutrophils present in the brain parenchyma due to their antibody-mediated depletion and a resulting decrease in neuroinflammation, and it is likely this mechanism contributed to the improvement in cognitive performance we observed after one month of antibody therapy. Taken together, these studies show that neutrophil interactions in the vasculature and parenchyma of the brain play a crucial role in the impaired cognitive function observed in multiple mouse models of amyloid-beta overexpression.

Without a firm understanding of the underlying mechanisms that caused reduced CBF in AD, no medical approach to increasing brain blood flow has been developed or tested in humans. In a limited series of experiments in severe AD patients, a piece of omentum, which is known to secrete angiogenic factors and encourage new vessel growth, was surgically placed on the surface of the brain. In the patients that showed an increased CBF as a result, there were signs of improved cognitive function[5,43]. Accordingly, improving CBF by interfering with neutrophil adhesion could be a promising therapeutic approach for AD.

4.6 Acknowledgments

This work was supported by the National Institutes of Health grants AG049952 (CBS), NS37853 (CI), and AG031620 (NN), the Alzheimer's Drug Discovery Foundation (CBS), the Alzheimer's Art Quilt Initiative (CBS), the BrightFocus Foundation (CBS), European Research Council grant 615102 (SL), the DFG German Research Foundation (OB), a National Science Foundation Graduate Research Fellowship (JCH), the L'Oréal Fellowship for Women in Science (NN), and used computing resources at CALMIP (SL). We thank Frédéric Lauwers for the human vascular data, Philibert Tsai, Pablo Blinder and David Kleinfeld for the mouse vascular data, and Maria Gulinello for guidance on behavior experiments. Finally, we thank Joseph R. Fetcho, Jesse H. Goldberg, and Michael I. Kotlikoff for commenting on the manuscript.

4.7 Author contributions:

JCCH, OB, SL, NN, and CBS conceived the study. JCCH, OB, and CJK performed the *in vivo* imaging experiments. MH, GO and YK developed custom software for data analysis. MH developed custom machine learning algorithms for image segmentation. OB conducted the behavioral studies. LP and CI conducted the ALS-MRI experiments. DR conducted laser speckle imaging studies. MB, MP, VD, AS, YD and SL performed the blood flow simulations. MCC and SS did the stall analyses in the TgCNRD8 mouse model. JCCH, OB, CJK, VM, LKV, II, YK, JZ, JDB, and ED contributed to the analysis of *in vivo* imaging experiments. JCCH, OB, NN and CBS

wrote the paper with contributions from MH, MCC, LP, CL, CI, and SL. All authors edited and commented on the manuscript.

4.8 Competing interests statement

The authors declare no competing interests.

4.9 Methods

4.9.1 Animals and surgical preparation

All animal procedures were approved by the Cornell Institutional Animal Care and Use Committee (protocol numbers: 2009-0043 and 2015-0029) and were performed under the guidance of the Cornell Center for Animal Resources and Education. We used adult transgenic mice as mouse models of AD, including the APP/PS1 line (B6.Cg-Tg (APPswe, PSEN1dE9) 85Dbo/J; MMRRC_034832-JAX, The Jackson Laboratory)[45] and the 5xFAD line (B6SJL-Tg(APPSwFlLon,PSEN1 *M146L*L286V)6799Vas/Mmjax; MMRRC Stock No: 34840-JAX, The Jackson Laboratory)[46]. Littermate wild-type mice (C57BL/6) were used as controls. Animals were of both sexes and ranged in age from 12 to 100 weeks.

For cranial window implantation, mice were anesthetized under 3% isoflurane on a custom-built stereotactic surgery frame and then maintained on ~1.5% isoflurane in 100% oxygen. Once unresponsive to a toe pinch, mice were given 0.05 mg per 100 g of mouse weight of glycopyrrolate (Baxter Inc.) or 0.005 mg/100 g of atropine (54925-063-10, Med-Pharmex Inc.) to prevent lung secretions, 0.025 mg/100 g of dexamethasone

(07-808-8194, Phoenix Pharm Inc.) to reduce post-surgical inflammation, and 0.5 mg/100 g of ketoprofen (Zoetis Inc.) to reduce post-surgical inflammation and provide post-surgical analgesia. Glycopyrrolate and ketoprofen were injected intramuscularly, while atropine and dexamethasone were injected subcutaneously. Bupivacaine (0.1 ml, 0.125%) (Hospira Inc.) was subcutaneously administered at the incision site to provide a local nerve block. Animals were provided 1 ml per 100 g of mouse weight of 5% (w/v) glucose in normal saline subcutaneously every hour during the procedure. We used a thermometer and feedback-controlled heating blanket (40-90-8D DC, FHC) to maintain body temperature at 37 °C. The head was shaved and washed 3 times with alternating 70% (v/v) ethanol and iodine solutions (AgriLabs). A 6-mm diameter craniotomy was performed over the cerebral cortex using a high-speed drill (HP4-917-21, Fordom) using bits with diameters of 1.4, 0.9, 0.7, and 0.5 mm (Fine Science Tools) for different steps in the craniotomy procedure. The craniotomy was then covered with a sterile 8-mm diameter glass coverslip (11986309, Thermo Scientific), glued onto the remaining skull with cyanoacrylate adhesive (Loctite) and dental cement (Co-Oral-Ite Dental). All procedures were done using sterile technique.

Once the craniotomy was completed, mice were returned to their cages and given injections of 0.025 mg/100 g of dexamethasone and 0.5 mg/100 g of ketoprofen subcutaneously 1 and 2 days after surgery, and all cages were placed over a heating pad during this period. Animals were given at least two weeks to recover from cranial window implantation before experimentation to minimize inflammation from the surgical procedure. Animals were excluded from further study if the clarity of the imaging window was insufficient for 2PEF imaging.

4.9.2 In vivo two-photon microscopy

During imaging sessions, mice were anesthetized with 3% isoflurane, placed on a custom stereotactic frame, and were given glycopyrrolate or atropine and glucose as described above. During imaging, anesthesia was maintained with ~1.5% isoflurane in 100% oxygen, with small adjustments to the isoflurane made to maintain the respiratory rate at ~1 Hz. The mouse was kept at 37 °C with a feedback-controlled heating pad.

To fluorescently label the microvasculature, Texas Red dextran (40 µl, 2.5%, MW = 70,000 kDA, Thermo Fisher Scientific) in saline was injected retro-orbitally immediately prior to imaging. In some animals, amyloid beta (Aβ) deposits were labeled using methoxy-X04[47]. In early experiments using methoxy-X04 obtained directly from Prof. Klunk at the University of Pittsburgh, we retro-orbitally injected 40 µL of 1 mg/ml methoxy-X04 in 0.9% saline (adjusted to pH 12 with 0.1 N NaOH) immediately prior to imaging. In later experiments using methoxy-X04 available commercially from Tocris, we intraperitoneally injected methoxy-X04 (dissolved in DMSO at 100 mM) one day prior to imaging at a dose of 1 mg/100 g. We observed no obvious differences in the amyloid labeling between these two administration approaches. In some animals, leukocytes and blood platelets were labeled with a retro-orbital injection of Rhodamine 6G (0.1 ml, 1 mg/ml in 0.9% saline, Acros Organics, Pure)[38]. Leukocytes were distinguished from blood platelets with a retro-orbital injection of Hoechst 33342 (50 µl, 4.8 mg/ml in 0.9% saline, Thermo Fisher Scientific). Texas Red (and methoxy-X04, when given retro-orbitally) were dosed in a single syringe, while Rhodamine 6G and Hoechst were dosed together in a second syringe.

Three-dimensional images of the cortical vasculature and measurement of red blood cell flow speeds in specific vessels were obtained via a custom-built two-photon excited fluorescence (2PEF) microscope. Imaging was done using 830-nm, 75-fs pulses from a Ti:Sapphire laser oscillator (MIRA HP pumped by a Verdi-V18 or Vision S, Coherent) and 900-nm, 75-fs pulses from a second Ti:Sapphire laser oscillator (Vision S, Coherent). Lasers were scanned by galvonometric scanners (1 frame/s) and focused into the sample using a 20× water-immersion objective lens for high-resolution imaging (numerical aperture (NA) = 1.0, Carl Zeiss Microscopy; or NA = 0.95, Olympus), or a 4× objective for mapping of the cortical surface vasculature (NA = 0.28, Olympus). The emitted fluorescence was detected on either a two-channel detection system or, for later data sets, on an upgraded four-channel detection system. On the two-channel system, the fluorescence was split by a 600-nm long pass dichroic and two successive image stacks were acquired first with 645/45 nm (center wavelength/bandwidth) and 575/25 nm bandpass filters to image Texas Red and Rhodamine 6G, respectively, and then with 645/65 nm and 460/50 nm filters to image Texas Red and both methoxy-X04 and Hoescht (on the same channel), all under 830-nm excitation. On the four-channel system, a secondary long-pass dichroic at 520 nm was followed by tertiary long-pass dichroics at 458 nm and one at either 562 or 605 nm. Emission was detected on four photomultiplier tubes through the following emission filters: 417/60 nm for Hoechst, 494/41 nm for methoxy-X04, 550/49 nm for Rhodamine 6G, and 641/75 nm for Texas Red. Laser excitation was 830 nm except when trying to image deep cortical tissue in animals where only Texas Red was present in which case 900-nm excitation was used. Laser scanning and data acquisition was controlled by ScanImage software[48]. To visualize the cortical

vasculature, stacks of images spaced by 1 μm axially were taken to a cortical depth of 300-500 μm.

For imaging of neutrophils labeled with anti-Ly6G antibodies labeled with Alexa488, imaging was performed on a custom-built 2PEF microscope at the Wellman Center for Photomedicine. In these animals, neutrophils were labeled with a tail vein injection of anti-Ly6G-Alexa 488 (0.1 mg/kg animal weight, 127626-Biolegend) at the same time as the labeling of blood plasma with Texas Red dextran. Imaging was done using 750-nm, 80-fs pulses from a Ti:Sapphire laser oscillator (Spectra-Physics Mai Tai). The laser beam was scanned by polygon scanners (30 frames/s) and focused into the sample using a 40x water-immersion objective lens for high-resolution imaging (NA = 0.80, Olympus), or a 10x objective for mapping of the cortical surface vasculature (NA = 0.30, Olympus). The emitted fluorescence was detected on photomultiplier tubes through the following emission filters: 525/50 nm for Alexa-488 and 605/50 nm for Texas Red. Laser scanning and data acquisition was controlled by custom built software. Stacks of images spaced by 1 μm axially were taken to a cortical depth of 100-200 μm.

4.9.3 Quantification of capillary network topology and capillary segment stalling

The 2PEF images of vascular networks were manually traced in three-dimensions to create a vectorized skeleton that represents the cortical vasculature using custom-written tracing software. The researchers producing these tracings were blinded to the genotype of the animal and any treatment it had received. Volumes of these image stacks where vessels could not be readily identified and traced were excluded from all analysis. These regions were typically deep and near the edges of the imaged volume, or

occasionally directly underneath a large surface vessel. Vessel segments were classified as surface and penetrating arterioles, capillaries, or ascending and surface venules. All vessels smaller than 10 μm in diameter were classed as capillaries. Large surface arterioles were distinguished from large surface venules based on morphology (arterioles were smaller diameter, had smoother walls and less tortuosity, and tended to branch more symmetrically and in Y-shape junctions as compared to venules). Other arterioles or venules were classed by tracing their connectivity to these readily identifiable large vessels.

Each capillary segment in these images was then manually classed as either flowing or stalled based on the motion of RBCs during the entire time each capillary was visible in the 3D image stack. The Texas Red dextran labels the blood plasma, but not the blood cells, so RBCs and other blood cells show up as dark patches in the vessel lumen. The motion of these dark patches indicates flowing blood cells. Each capillary segment was visible in a minimum of ~5 successive frames in the 3D image stack, or for ~5 s (capillaries not oriented parallel to the cortical surface were observed for significantly more frames). We scored a capillary segment as stalled if we did not see motion of the RBCs and other cells in the capillary segment over this observation time. This manual scoring of capillaries as flowing or stalled was performed with the researcher blinded to the genotype and treatment status of the animal. In addition, this scoring was performed using only the image data visible on the Texas Red imaging channel. All animals included in our analysis had at least 800 capillary segments scored as flowing or stalled. Animals with fewer characterized capillaries were excluded.

Using the traced vascular network, the topologically shortest path from each flowing or stalled capillary to the nearest penetrating arteriole and ascending venule was calculated using Dijkstra's algorithm[49].

4.9.4 Distinguishing causes of capillary stalls

In some animals, once capillary stalls were identified we used the additional fluorescent labels to determine what was blocking blood flow in the capillary segment. Stalled capillary segments with a cell-shaped object labeled with both Rhodamine 6G and Hoechst present were scored as having a leukocyte. Stalled segments with punctate objects labeled with Rhodamine 6G alone were scored as having platelet aggregates. Stalled capillary segments with only RBCs present were classed as RBC stalls. We determined what fraction of stalled capillaries had only a leukocyte, a leukocyte with one or more RBCs present, only platelet aggregates, platelet aggregates with RBCs, and only RBCs. With this labeling scheme, we were unable to reliably distinguish platelet aggregates when a leukocyte was present. Additional experiments used a low-dose of Alexa 488 labeled anti-Ly6G antibodies to assess the type of leukocyte associated with capillary stalls.

We assessed if the diameter of flowing and stalled capillaries was different, on average. First, image stacks were linearly interpolated to have an isotropic 1 μm voxel size. To reduce the salt and pepper noise in the vascular images, we filtered using a 3D 5 x 5 x 5 pixel Gaussian filter. We then corrected for unevenness in the image intensity by filtering the image (85 x 85 pixel sized mean filter) and subtracting this from the Gaussian filtered image. The resulting image was binarized using Otsu's method[50]. Finally, objects

smaller than 1000 voxels were eliminated, where voxels were considered part of the same connected object whenever they shared at least a corner. We then used this binarized image to correct the manual tracing of the vasculature by shifting the centerline, so it was equidistant from the vessel boundaries (done within a 10-μm neighborhood to avoid confusion between neighboring capillaries). Every 5 μm along the centerline of each capillary segment, we estimated the vessel radius by finding the closest distance from the centerline to the vessel boundary. Measurements of less than 2 μm or more than 10 μm were excluded as they likely reflected imaging artifacts, and we averaged across all measurements for each capillary segment.

4.9.5 Administration of antibodies against Ly6G or LFA-1 to interfere with capillary stalling

We treated APP/PS1 and 5xFAD mice with intraperitoneal injections of monoclonal antibodies against lymphocyte antigen 6 complex, locus G (Ly6G) (α-Ly6G, clone 1A8, 4 mg/kg, BD Biosciences) or an isotype control antibody (Rat IgG2a, κ, 4 mg/kg, BD Biosciences). In addition, APP/PS1 mice were treated with retroorbital or intraperitoneal injections of monoclonal antibodies against Lymphocyte Functional Antigen 1 (α-LFA-1; M17/4 clone, BD Biosciences; 4 mg/kg). The same cortical capillary bed was imaged in anesthetized mice immediately before and at 60-90 min after treatment. Mice were randomly assigned to receive treatment or isotype control antibodies and the experimenter was blinded to both mouse genotype and whether the antibody was the treatment or control during the experiment. Quantification of stalled

capillaries was performed by researchers blinded to imaging time, animal genotype, and treatment type.

4.9.6 Behavior experiments

All experiments were performed under red light in an isolated room. The position of the mouse's nose was automatically traced by Viewer III software (Biobserve, Bonn, Germany). In addition to the automatic results obtained by Viewer III software, a blinded experimenter independently scored mouse behavior manually. Animals were taken into the behavior room one-hour prior to the experiment. Behavioral analysis was conducted at baseline and at 3 and 24 h after injection with α-Ly6G, α-LFA-1, or isotype control antibodies (IP 4 mg/kg). The α-Ly6G treated APP/PS1 mice were then treated every three days for four weeks (IP 2 mg/kg) and behavior experiments were repeated. The OR, Y-maze, balance beam walk, and forced swim tests were performed at all time points. The NOR task was performed only at baseline and the 4-week time point to avoid animals becoming accustomed to the objects. For experiments with APP/PS1 mice and α-Ly6G, animals were ~11 months of age at the start of the experiment. For experiments with APP/PS1 mice and α-LFA-1, animals were 11-13 months of age. For experiments with 5xFAD mice and α-Ly6G, animals were 5-6 months of age. Mice were randomly assigned to receive treatment or isotype control antibodies and the experimenter was blinded to both mouse genotype and whether the antibody was the treatment or control during the experiment.

4.9.6.1 Object replacement test:

The object replacement (OR) task evaluated spatial memory performance. All objects used were first validated in a separate cohort of mice to ensure that no intrinsic preference or aversion was observed, and animals explored all objects similarly. Exploration time for the objects was defined as any time when there was physical contact with an object (whisking, sniffing, rearing on, or touching the object) or when the animal was oriented toward the object and the head was within 2 cm of the object. In trial 1, mice were allowed to explore two identical objects for 10 min in the arena and then returned to their home cage for 60 min. Mice were then returned to the testing arena for 3 min with one object moved to a novel location (trial 2). Care was taken to ensure that the change of placement alters both the intrinsic relationship between objects (e.g. a rotation of the moved object) and the position relative to internal visual cues (e.g. new location in the arena; one wall of testing arena had a pattern). At subsequent time points, new object positions and new pairs of objects (from the validated pool of objects) were used to maintain animal interest. In addition to using the tracking software to determine the object exploration times, the time spent at each object was manually scored by an independent experimenter who was blinded to the genotype and treatment. The preference score (%) for OR tasks was calculated as ([exploration time of the novel object]/[exploration time of both objects]) × 100 from the data in trial 2. Automated tracking and manual scoring yielded similar results across groups, so we report the automated tracking results.

4.9.6.2 Y-Maze:

The Y-Maze task was used to measure working memory by quantifying spontaneous alternation between arms of the maze. The Y-maze consisted of three arms at 120° and was made of light grey plastic. Each arm was 6-cm wide and 36-cm long and had 12.5-cm high walls. The maze was cleaned with 70% ethanol after each mouse. A mouse was placed in the Y-maze and allowed to explore for 6 min. Mouse behavior was monitored, recorded, and analyzed using the Viewer software. A mouse was considered to have entered an arm if the whole body (except for the tail) entered the arm and to have exited if the whole body (except for the tail) exited the arm. If an animal consecutively entered three different arms, it was counted as an alternating trial. Because the maximum number of triads is the total number of arm entries minus 2, the spontaneous alternation score was calculated as (number of alternating triads)/(total number of arm entries − 2).

4.9.6.3 Novel object recognition test:

The novel object recognition (NOR) task measures recognition memory and is based on rodents' innate preference for exploring novel objects. This test was conducted only in the animals at baseline and after 4 weeks of treatment. The testing approach was identical to the OR task, but with a novel object placed at the location of one of the initial objects in trial 2. To exclude preference bias for particular objects in the first trial one animal would see two of object A and another animal two of object B. In the second trial to test for preference for a novel object, both animals see one of object A and one of object B. For the repeat of the test at 4 weeks, we used new objects C and D.

4.9.7 ELISA assay

After the conclusion of the behavior experiments, the APP/PS1 animals that had received α-Ly6G or isotype control antibodies every 3 days for a month were sacrificed by lethal injection of pentobarbital (5 mg/100 g). Brains were quickly extracted and divided along the centerline. One half was immersed in 4% paraformaldehyde in phosphate buffered saline (PBS) for later histological analysis and the other half was snap frozen in liquid nitrogen.

The frozen APP/PS1 mouse hemi-brains (Iso-Ctr: n=6, 11.5-12.5 months old; α-Ly6G: n=7, 11.5-12.5 months old) were weighed and homogenized in 1 ml PBS containing complete protease inhibitor (Roche Applied Science) and 1 mM AEBSF (Sigma) using a Dounce homogenizer. The homogenates were then sonicated and centrifuged at 14,000 g for 30 min at 4° C. The supernatant (PBS-soluble fraction) was removed and stored at −80° C. The pellet was re-dissolved in 0.5 ml 70% formic acid, sonicated, and centrifuged at 14,000 g for 30 min at 4° C, and the supernatant was removed and neutralized using 1M Tris buffer at pH 11. Protein concentration was measured in the PBS soluble fraction and the formic acid soluble fraction using the Pierce BCA Protein Assay (Thermo Fischer Scientific). The PBS soluble fraction extracts were diluted 1:5. Formic acid extracts were diluted 1:1 after neutralization. These brain extracts were analyzed by sandwich ELISA for Aβ1-40, Aβ1-42, and Aβ aggregates using commercial ELISA kits and following the manufacturer's protocol (Aβ1-40: KHB3481; Aβ1-42: KHB3441; Aβ aggregates: KHB3491, Thermo Fisher Scientific). The Aβ concentration was calculated by comparing the sample absorbance with the absorbance

of known concentrations of synthetic Aβ1–40 and Aβ1–42 standards on the same plate. Data was acquired with a Synergy HT plate reader (Biotek) and analyzed using Gen5 software (BioTek) and Prism (Graphpad).

4.9.8 Statistical analysis

Boxplots were created using Prism7 (GraphPad). The box extends between the values for the 25th and 75th percentile of the data. The whiskers extend 1.5 times the difference between the value of the 75th and 25th percentile of the data from the top and bottom of the box. Values lying outside the whiskers were defined as outliers and the mean was computed excluding these outliers. The median is indicated with a black horizontal line inside the box, while the mean is indicated with a red horizontal line. Violin plots were created using the statistical software package, R[51].

Data in all groups was tested for normality using D'Agostino-Pearson omnibus normality test. Parametric statistics were used only if the data in all groups in the comparison were normally distributed. The statistical significance of differences between multiple groups was determined using one-way analysis of variance (ANOVA) followed by Tukey's multiple comparison correction for normally distributed data and using one-way Kruskal-Wallis ANOVA followed by Dunn's multiple comparison correction for data with a non-normal distribution. To compare baseline and post-treatment measurements at multiple time points with non-normal data, the Friedman one-way repeated measures non-parametric ANOVA followed by Dunn's multiple comparison correction was used. Statistical comparisons between two groups were performed using the Student's t test or paired t test for normally distributed data or using the Mann-

Whitney test or Wilcoxon matched-pairs test for data with a non-normal distribution. P-values smaller than 0.05 were considered statistically significant. All statistical analysis was performed using Prism7 (GraphPad).

We use a standardized set of significance indicators across all figures in this manuscript. For comparisons between groups: *p<0.05, **p<0.01, ***p<0.001, ****p<0.0001. For matched comparisons before and after treatment: +p<0.05, ++p<0.01. Details of the groups compared, animal and capillary numbers, sex distributions, statistical tests, exact p-values, and explanatory notes for individual panels are included in the figure captions.

4.9.9 Additional methodological details

Additional information on the methods used in this study are available in the Supplementary Methods.

4.9.10 Data availability

The raw data reported in this manuscript are archived at https://doi.org/10.7298/9PR3-D773.

4.9.11 Code availability

Code for 3D tracing, vessel segmentation, analysis of linescan data, and determination of amyloid density around capillaries can be obtained by contacting NN or CBS. Code for simulation of blood flow in vascular networks can be obtained by contacting SL.

References

1 Wang, J., Gu, B. J., Masters, C. L. & Wang, Y. J. A systemic view of Alzheimer disease - insights from amyloid-beta metabolism beyond the brain. Nature reviews. Neurology 13, 612-623, doi:10.1038/nrneurol.2017.111 (2017).

2 Santos, C. Y. et al. Pathophysiologic relationship between Alzheimer's disease, cerebrovascular disease, and cardiovascular risk: A review and synthesis. Alzheimer's & dementia 7, 69-87, doi:10.1016/j.dadm.2017.01.005 (2017).

3 Iturria-Medina, Y. et al. Early role of vascular dysregulation on late-onset Alzheimer's disease based on multifactorial data-driven analysis. Nature communications 7, 11934, doi:10.1038/ncomms11934 (2016).

4 Dai, W. et al. Mild cognitive impairment and alzheimer disease: patterns of altered cerebral blood flow at MR imaging. Radiology 250, 856-866, doi:10.1148/radiol.2503080751 (2009).

5 Wolters, F. J. et al. Cerebral Perfusion and the Risk of Dementia: A Population-Based Study. Circulation, doi:10.1161/CIRCULATIONAHA.117.027448 (2017).

6 Wiesmann, M. et al. Hypertension, cerebrovascular impairment, and cognitive decline in aged AbetaPP/PS1 mice. Theranostics 7, 1277-1289, doi:10.7150/thno.18509 (2017).

7 Li, H. et al. Vascular and parenchymal amyloid pathology in an Alzheimer disease knock-in mouse model: interplay with cerebral blood flow. Molecular neurodegeneration 9, 28, doi:10.1186/1750-1326-9-28 (2014).

8 Niwa, K., Kazama, K., Younkin, S. G., Carlson, G. A. & Iadecola, C. Alterations in cerebral blood flow and glucose utilization in mice overexpressing the amyloid precursor protein. Neurobiology of disease 9, 61-68, doi:10.1006/nbdi.2001.0460 (2002).

9 Niwa, K. et al. A beta-peptides enhance vasoconstriction in cerebral circulation. American journal of physiology. Heart and circulatory physiology 281, H2417-2424 (2001).

10 Farkas, E. & Luiten, P. G. Cerebral microvascular pathology in aging and Alzheimer's disease. Progress in neurobiology 64, 575-611 (2001).

11 Chen, Y. et al. Voxel-level comparison of arterial spin-labeled perfusion MRI and FDG-PET in Alzheimer disease. Neurology 77, 1977-1985, doi:10.1212/WNL.0b013e31823a0ef7 (2011).

12 Royea, J., Zhang, L., Tong, X. K. & Hamel, E. Angiotensin IV Receptors Mediate the Cognitive and Cerebrovascular Benefits of Losartan in a Mouse Model of Alzheimer's Disease. The Journal of neuroscience : the official journal of the Society for Neuroscience 37, 5562-5573, doi:10.1523/JNEUROSCI.0329-17.2017 (2017).

13 Marshall, R. S. et al. Recovery of brain function during induced cerebral hypoperfusion. Brain : a journal of neurology 124, 1208-1217 (2001).

14 Wang, L. et al. Chronic cerebral hypoperfusion induces memory deficits and facilitates Abeta generation in C57BL/6J mice. Experimental neurology 283, 353-364, doi:10.1016/j.expneurol.2016.07.006 (2016).

15 Hattori, Y. et al. Gradual Carotid Artery Stenosis in Mice Closely Replicates Hypoperfusive Vascular Dementia in Humans. Journal of the American Heart Association 5, doi:10.1161/JAHA.115.002757 (2016).

16 Radde, R. et al. Abeta42-driven cerebral amyloidosis in transgenic mice reveals early and robust pathology. EMBO reports 7, 940-946, doi:10.1038/sj.embor.7400784 (2006).

17 Chishti, M. A. et al. Early-onset amyloid deposition and cognitive deficits in transgenic mice expressing a double mutant form of amyloid precursor protein 695. The Journal of biological chemistry 276, 21562-21570, doi:10.1074/jbc.M100710200 (2001).

18 Hasenberg, A. et al. Catchup: a mouse model for imaging-based tracking and modulation of neutrophil granulocytes. Nature methods 12, 445-452, doi:10.1038/nmeth.3322 (2015).

19 Deane, R., Bell, R. D., Sagare, A. & Zlokovic, B. V. Clearance of amyloid-beta peptide across the blood-brain barrier: implication for therapies in Alzheimer's disease. CNS & neurological disorders drug targets 8, 16-30 (2009).

20 Nishimura, N. et al. Targeted insult to subsurface cortical blood vessels using ultrashort laser pulses: three models of stroke. Nature methods 3, 99-108, doi:10.1038/nmeth844 (2006).

21 Tsai, P. S. et al. Correlations of neuronal and microvascular densities in murine cortex revealed by direct counting and colocalization of nuclei and vessels. The Journal of neuroscience : the official journal of the Society for Neuroscience 29, 14553-14570, doi:10.1523/JNEUROSCI.3287-09.2009 (2009).

22 Lauwers, F., Cassot, F., Lauwers-Cances, V., Puwanarajah, P. & Duvernoy, H. Morphometry of the human cerebral cortex microcirculation: general characteristics and space-related profiles. NeuroImage 39, 936-948, doi:10.1016/j.neuroimage.2007.09.024 (2008).

23 Lorthois, S., Cassot, F. & Lauwers, F. Simulation study of brain blood flow regulation by intra-cortical arterioles in an anatomically accurate large human vascular network. Part II: flow variations induced by global or localized modifications of arteriolar diameters. NeuroImage 54, 2840-2853, doi:10.1016/j.neuroimage.2010.10.040 (2011).

24 Roher, A. E. et al. Cerebral blood flow in Alzheimer's disease. Vascular health and risk management 8, 599-611, doi:10.2147/VHRM.S34874 (2012).

25 Iadecola, C. The Neurovascular Unit Coming of Age: A Journey through Neurovascular Coupling in Health and Disease. Neuron 96, 17-42, doi:10.1016/j.neuron.2017.07.030 (2017).

26 Park, L. et al. Nox2-derived radicals contribute to neurovascular and behavioral dysfunction in mice overexpressing the amyloid precursor protein. Proceedings

of the National Academy of Sciences of the United States of America 105, 1347-1352, doi:10.1073/pnas.0711568105 (2008).

27 Park, L. et al. Innate immunity receptor CD36 promotes cerebral amyloid angiopathy. Proceedings of the National Academy of Sciences of the United States of America 110, 3089-3094, doi:10.1073/pnas.1300021110 (2013).

28 Wang, J. X. et al. Ly6G ligation blocks recruitment of neutrophils via a beta2-integrin-dependent mechanism. Blood 120, 1489-1498, doi:10.1182/blood-2012-01-404046 (2012).

29 Daley, J. M., Thomay, A. A., Connolly, M. D., Reichner, J. S. & Albina, J. E. Use of Ly6G-specific monoclonal antibody to deplete neutrophils in mice. Journal of leukocyte biology 83, 64-70, doi:10.1189/jlb.0407247 (2008).

30 Lavkan, A. H., Astiz, M. E. & Rackow, E. C. Effects of proinflammatory cytokines and bacterial toxins on neutrophil rheologic properties. Critical care medicine 26, 1677-1682 (1998).

31 Bennett, R. E. et al. Tau induces blood vessel abnormalities and angiogenesis-related gene expression in P301L transgenic mice and human Alzheimer's disease. Proceedings of the National Academy of Sciences of the United States of America 115, E1289-E1298, doi:10.1073/pnas.1710329115 (2018).

32 Mohammad Haft-Javaherian, L. F., Victorine Muse, Chris B. Schaffer, Nozomi Nishimura, Mert R. Sabuncu. Deep convolutional neural networks for segmenting 3D in vivo multiphoton images of vasculature in Alzheimer disease mouse models. arXiv preprint arXiv:1801.00880. (2018).

33 Villringer, A. et al. Imaging of leukocytes within the rat brain cortex in vivo. Microvascular research 42, 305-315 (1991).

34 Ishikawa, M. et al. Leukocyte plugging and cortical capillary flow after subarachnoid hemorrhage. Acta neurochirurgica 158, 1057-1067, doi:10.1007/s00701-016-2792-6 (2016).

35 Kloner, R. A. No-reflow phenomenon: maintaining vascular integrity. Journal of cardiovascular pharmacology and therapeutics 16, 244-250, doi:10.1177/1074248411405990 (2011).

36 Engler, R. L., Schmid-Schonbein, G. W. & Pavelec, R. S. Leukocyte capillary plugging in myocardial ischemia and reperfusion in the dog. The American journal of pathology 111, 98-111 (1983).

37 Chibber, R., Ben-Mahmud, B. M., Chibber, S. & Kohner, E. M. Leukocytes in diabetic retinopathy. Current diabetes reviews 3, 3-14 (2007).

38 Santisakultarm, T. P. et al. Stalled cerebral capillary blood flow in mouse models of essential thrombocythemia and polycythemia vera revealed by in vivo two-photon imaging. Journal of thrombosis and haemostasis : JTH 12, 2120-2130, doi:10.1111/jth.12738 (2014).

39 Ilesanmi, O. O. Pathological basis of symptoms and crises in sickle cell disorder: implications for counseling and psychotherapy. Hematology reports 2, e2, doi:10.4081/hr.2010.e2 (2010).

40 Zuliani, G. et al. Markers of endothelial dysfunction in older subjects with late onset Alzheimer's disease or vascular dementia. Journal of the neurological sciences 272, 164-170, doi:10.1016/j.jns.2008.05.020 (2008).

41 Iadecola, C. Vascular and Metabolic Factors in Alzheimer's Disease and Related Dementias: Introduction. Cellular and molecular neurobiology 36, 151-154, doi:10.1007/s10571-015-0319-y (2016).

42 Zenaro, E. et al. Neutrophils promote Alzheimer's disease-like pathology and cognitive decline via LFA-1 integrin. Nature medicine 21, 880-886, doi:10.1038/nm.3913 (2015).

43 Goldsmith, H. S. Alzheimer's disease can be treated: Why the delay? Surgical neurology international 8, 133, doi:10.4103/sni.sni_116_17 (2017).

44 Blinder, P. et al. The cortical angiome: an interconnected vascular network with noncolumnar patterns of blood flow. Nature neuroscience 16, 889-897, doi:10.1038/nn.3426 (2013).

45 Jankowsky, J. L. et al. Mutant presenilins specifically elevate the levels of the 42 residue beta-amyloid peptide in vivo: evidence for augmentation of a 42-specific gamma secretase. Hum Mol Genet 13, 159-170, doi:10.1093/hmg/ddh019 (2004).

46 Oakley, H. et al. Intraneuronal beta-amyloid aggregates, neurodegeneration, and neuron loss in transgenic mice with five familial Alzheimer's disease mutations: potential factors in amyloid plaque formation. The Journal of neuroscience : the official journal of the Society for Neuroscience 26, 10129-10140, doi:10.1523/JNEUROSCI.1202-06.2006 (2006).

47 Klunk, W. E. et al. Imaging Abeta plaques in living transgenic mice with multiphoton microscopy and methoxy-X04, a systemically administered Congo red derivative. J Neuropathol Exp Neurol 61, 797-805 (2002).

48 Pologruto, T. A., Sabatini, B. L. & Svoboda, K. ScanImage: flexible software for operating laser scanning microscopes. Biomed Eng Online 2, 13, doi:10.1186/1475-925X-2-13 (2003).

49 Dijkstra, E. W. A note on two problems in connexion with graphs. Numerische Mathematik Volume 1, 269-271, doi:10.1007/BF01386390 (1959).

50 Otsu, N. A threshold selection method from gray-level histogram. IEEE Trans. Syst. Man Cybern. 9, 62-66, doi:10.1109/TSMC.1979.4310076 (1979).

51 Team, R. C. R: A language and environment for statistical computing. Foundation for Statistical Computing (2013).

SUPPLEMENTARY MATERIALS

4.10 Materials and methods

4.10.1 Animals and surgical preparation

All animal procedures were approved by the Cornell Institutional Animal Care and Use Committee and were performed under the guidance of the Cornell Center for Animal Resources and Education. We used adult transgenic mice as mouse models of AD, including the APP/PS1 line (B6.Cg-Tg (APPswe, PSEN1dE9) 85Dbo/J; MMRRC_034832-JAX, The Jackson Laboratory)[45] and the 5xFAD line (B6SJL-Tg(APPSwFlLon,PSEN1 *M146L*L286V)6799Vas/Mmjax; MMRRC Stock No: 34840-JAX, The Jackson Laboratory)[46]. Littermate wild-type mice (C57BL/6) were used as controls. Animals were of both sexes and ranged in age from 12 to 100 weeks.

For cranial window implantation, mice were anesthetized under 3% isoflurane on a custom-built stereotactic surgery frame and then maintained on ~1.5% isoflurane in 100% oxygen. Once unresponsive to a toe pinch, mice were given 0.05 mg per 100 g of mouse weight of glycopyrrolate (Baxter Inc.) or 0.005 mg/100 g of atropine (54925-063-10, Med-Pharmex Inc.) to prevent lung secretions, 0.025 mg/100 g of dexamethasone (07-808-8194, Phoenix Pharm Inc.) to reduce post-surgical inflammation, and 0.5 mg/100 g of ketoprofen (Zoetis Inc.) to reduce post-surgical inflammation and provide post-surgical analgesia. Glycopyrrolate and ketoprofen were injected intramuscularly, while atropine and dexamethasone were injected subcutaneously. Bupivacaine (0.1 ml, 0.125%) (Hospira Inc.) was subcutaneously administered at the incision site to provide a local

nerve block. Animals were provided 1 ml per 100 g of mouse weight of 5% (w/v) glucose in normal saline subcutaneously every hour during the procedure. We used a thermometer and feedback-controlled heating blanket (40-90-8D DC, FHC) to maintain body temperature at 37 °C. The head was shaved and washed 3 times with alternating 70% (v/v) ethanol and iodine solutions (AgriLabs). A 6-mm diameter craniotomy was performed over the cerebral cortex using a high-speed drill (HP4-917-21, Fordom) using bits with diameters of 1.4, 0.9, 0.7, and 0.5 mm (Fine Science Tools) for different steps in the craniotomy procedure. The craniotomy was then covered with a sterile 8-mm diameter glass coverslip (11986309, Thermo Scientific), glued onto the remaining skull with cyanoacrylate adhesive (Loctite) and dental cement (Co-Oral-Ite Dental). All procedures were done using sterile technique.

Once the craniotomy was completed, mice were returned to their cages and given injections of 0.025 mg/100 g of dexamethasone and 0.5 mg/100 g of ketoprofen subcutaneously 1 and 2 days after surgery, and all cages were placed over a heating pad during this period. Animals were given at least two weeks to recover from cranial window implantation before experimentation to minimize inflammation from the surgical procedure.

Cranial window implantations were also performed in TgCRND8 mice (41-51 weeks of age, all female)[17]. These animals were housed at The Rockefeller University's Comparative Biosciences Center and treated in accordance with IACUC-approved protocols. The window implantation followed the same protocol as described above,

except that mice were anaesthetized using avertin (50 mg/100 g, intraperitoneal) and were given atropine (0.004 mg/100 g).

4.10.2 In vivo two-photon microscopy

During imaging sessions, mice were anesthetized with 3% isoflurane, placed on a custom stereotactic frame, and were given glycopyrrolate or atropine and glucose as described above. During imaging, anesthesia was maintained with ~1.5% isoflurane in 100% oxygen, with small adjustments to the isoflurane made to maintain the respiratory rate at ~1 Hz. The mouse was kept at 37 °C with a feedback-controlled heating pad.

To fluorescently label the microvasculature, Texas Red dextran (40 µl, 2.5%, MW = 70,000 kDA, Thermo Fisher Scientific) in saline was injected retro-orbitally immediately prior to imaging. In some animals, amyloid beta (Aβ) deposits were labeled using methoxy-X04[47]. In early experiments using methoxy-X04 obtained directly from Prof. Klunk at the University of Pittsburgh, we retro-orbitally injected 40 µL of 1 mg/ml methoxy-X04 in 0.9% saline (adjusted to pH 12 with 0.1 N NaOH) immediately prior to imaging. In later experiments using methoxy-X04 available commercially from Tocris, we intraperitoneally injected methoxy-X04 (dissolved in DMSO at 100 mM) one day prior to imaging at a dose of 1 mg/100 g. We observed no obvious differences in the amyloid labeling between these two administration approaches. In some animals, leukocytes and blood platelets were labeled with a retro-orbital injection of Rhodamine 6G (0.1 ml, 1 mg/ml in 0.9% saline, Acros Organics, Pure)[38] Leukocytes were distinguished from blood platelets with a retro-orbital injection of Hoechst 33342 (50 µl, 4.8 mg/ml in 0.9% saline, Thermo Fisher Scientific). Texas Red (and methoxy-X04, when

given retro-orbitally) were dosed in a single syringe, while Rhodamine 6G and Hoechst were dosed together in a second syringe.

Three-dimensional images of the cortical vasculature and measurement of red blood cell flow speeds in specific vessels were obtained via a custom-built two-photon excited fluorescence (2PEF) microscope. Imaging was done using 830-nm, 75-fs pulses from a Ti:Sapphire laser oscillator (MIRA HP pumped by a Verdi-V18 or Vision S, Coherent) and 900-nm, 75-fs pulses from a second Ti:Sapphire laser oscillator (Vision S, Coherent). Lasers were scanned by galvonometric scanners (1 frame/s) and focused into the sample using a 20× water-immersion objective lens for high-resolution imaging (numerical aperture (NA) = 1.0, Carl Zeiss Microscopy; or NA = 0.95, Olympus), or a 4× objective for mapping of the cortical surface vasculature (NA = 0.28, Olympus). The emitted fluorescence was detected on either a two-channel detection system or, for later data sets, on an upgraded four-channel detection system. On the two-channel system, the fluorescence was split by a 600-nm long pass dichroic and two successive image stacks were acquired first with 645/45 nm (center wavelength/bandwidth) and 575/25 nm bandpass filters to image Texas Red and Rhodamine 6G, respectively, and then with 645/65 nm and 460/50 nm filters to image Texas Red and both methoxy-X04 and Hoescht (on the same channel), all under 830-nm excitation. On the four-channel system, a secondary long-pass dichroic at 520 nm was followed by tertiary long-pass dichroics at 458 nm and one at either 562 or 605 nm. Emission was detected on four photomultiplier tubes through the following emission filters: 417/60 nm for Hoechst, 494/41 nm for methoxy-X04, 550/49 nm for Rhodamine 6G, and 641/75 nm for Texas Red. Laser excitation was 830 nm except when trying to image deep cortical tissue in animals where

only Texas Red was present in which case 900-nm excitation was used. Laser scanning and data acquisition was controlled by ScanImage software[48]. To visualize the cortical vasculature, stacks of images spaced by 1 μm axially were taken to a cortical depth of 300-500 μm.

For TgCRND8 mice, imaging was performed using a Fluoview 1000MPE two-photon laser scanning microscope (Olympus) equipped with a SpectraPhysics MaiTai DeepSee laser and a 25x/1.05 NA objective at The Rockefeller University Bio-Imaging Resource Center.

For imaging of neutrophils labeled with anti-Ly6G antibodies labeled with Alexa488, imaging was performed on a custom-built 2PEF microscope at the Wellman Center for Photomedicine. In these animals, neutrophils were labeled with a tail vein injection of anti-Ly6G-Alexa 488 (0.1 mg/kg animal weight, 127626-Biolegend) at the same time as the labeling of blood plasma with Texas Red dextran. Imaging was done using 750-nm, 80-fs pulses from a Ti:Sapphire laser oscillator (Spectra-Physics Mai Tai). The laser beam was scanned by polygon scanners (30 frames/s) and focused into the sample using a 40x water-immersion objective lens for high-resolution imaging (NA = 0.80, Olympus), or a 10x objective for mapping of the cortical surface vasculature (NA = 0.30, Olympus). The emitted fluorescence was detected on three photomultiplier tubes through the following emission filters: 525/50 nm for Alexa-488 and 605/50 nm for Texas Red. Laser scanning and data acquisition was controlled by custom built software. Stacks of images spaced by 1 μm axially were taken to a cortical depth of 100-200 μm.

4.10.3 Awake imaging

A subset of mice was imaged with 2PEF without anesthesia. During the craniotomy surgery, a 3D-printed skull-attached mounting frame was secured on top of the cranial window to allow for head fixation during anesthesia-free imaging. The 3D-printed frame was flanked by 4 screws (TX000-1-1/2 self tapping screws, Small Parts Inc., Miami Lakes, FL) inserted into the skull. The screws and appropriate parts of the frame were glued to the skull using Loctite and dental cement to firmly attach the mounting frame.

We adapted and modified the awake imaging system from Dombeck et al.[49], in which a large (8-inch diameter) Styrofoam ball (Floracraft) was levitated using a thin cushion of air between the ball and a custom made (3D printed) casting containing eight 0.25-inch diameter air jets, arranged symmetrically. The air pressure was adjusted to just float the ball when the mouse was on top of it.

We trained mice to remain in a calm state during awake, head-fixed imaging. During the first training session, mice were handled, with the room lights on, by a trainer wearing gloves for ~10 min or until the mice routinely ran from hand to hand. The mice were then transferred to the ball and allowed to move freely for ~10 min with the room lights on while the handler rotated the ball to keep the mice centered near the top. The second training session consisted of again allowing the mice to move freely on the ball for ~10–15 min, again with the room lights on. The third training session began by head restraining the mice on the ball in complete darkness for ~15–20 min. Typically it would take 5–10 min for the mouse to learn to balance and then begin to walk or run. Mice were

then head-fixed and placed on the ball during imaging under the microscope. Awake imaging lasted less than 30 min. Following awake imaging, mice were anesthetized as described above and imaging was repeated over the same cortical area to compare capillary physiology between the awake and anesthetized states.

4.10.4 Quantification of capillary network topology and capillary segment stalling

The 2PEF images of vascular networks were manually traced in three-dimensions to create a vectorized skeleton that represents the cortical vasculature using custom-written tracing software. The researchers producing these tracings were blinded to the genotype of the animal and any treatment it had received. Volumes of these image stacks where vessels could not be readily identified and traced were excluded from all analysis. These regions were typically deep and near the edges of the imaged volume, or occasionally directly underneath a large surface vessel. Vessel segments were classified as surface and penetrating arterioles, capillaries, or ascending and surface venules. All vessels smaller than 10 μm in diameter were classed as capillaries. Large surface arterioles were distinguished from large surface venules based on morphology (arterioles were smaller diameter, had smoother walls and less tortuosity, and tended to branch more symmetrically and in Y-shape junctions as compared to venules). Other arterioles or venules were classed by tracing their connectivity to these readily identifiable large vessels.

Each capillary segment in these images was then manually classed as either flowing or stalled based on the motion of RBCs during the entire time each capillary was visible in the 3D image stack. The Texas Red dextran labels the blood plasma, but not the

blood cells, so RBCs and other blood cells show up as dark patches in the vessel lumen. The motion of these dark patches indicates flowing blood cells. Each capillary segment was visible in a minimum of ~5 successive frames in the 3D image stack, or for ~5 s (capillaries not oriented parallel to the cortical surface were observed for significantly more frames). We scored a capillary segment as stalled if we did not see motion of the RBCs and other cells in the capillary segment over this observation time. This manual scoring of capillaries as flowing or stalled was performed with the researcher blinded to the genotype and treatment status of the animal. In addition, this scoring was performed using only the image data visible on the Texas Red imaging channel. All animals had at least 800 capillary segments scored as flowing or stalled.

Using the traced vascular network, the topologically shortest path from each flowing or stalled capillary to the nearest penetrating arteriole and ascending venule was calculated using Dijkstra's algorithm[50].

For the data on the fraction of capillaries stalled in the 5xFAD mice, individual capillary segments for categorization as flowing or stalled were identified using a more automated approach. Briefly, the image stack was preprocessed to the remove motion artifacts and noises. Then the vasculature network in the image stack was segmented using deep convolutional neural network followed by the post-processing procedure to extract the vectorized vasculature network. Finally, each identified capillary segment was manually classified as either flowing or stalled[32].

4.10.5 Distinguishing causes of capillary stalls

In some animals, once capillary stalls were identified we used the additional fluorescent labels to determine what was blocking blood flow in the capillary segment. Stalled capillary segments with a cell-shaped object labeled with both Rhodamine 6G and Hoechst present were scored as having a leukocyte. Stalled segments with punctate objects labeled with Rhodamine 6G alone were scored as having platelet aggregates. Stalled capillary segments with only RBCs present were classed as RBC stalls. We determined what fraction of stalled capillaries had only a leukocyte, a leukocyte with one or more RBCs present, only platelet aggregates, platelet aggregates with RBCs, and only RBCs. With this labeling scheme, we were unable to reliably distinguish platelet aggregates when a leukocyte was present. Additional experiments used a low-dose of Alexa 488 labeled anti-Ly6G antibodies to assess the type of leukocyte associated with capillary stalls.

We assessed if the diameter of flowing and stalled capillaries was different, on average. To reduce the salt and pepper noise in the vascular images, we filtered using a 3D 5 x 5 x 5 pixel Gaussian filter. We then corrected for unevenness in the image intensity by filtering the image (85 x 85 pixel sized mean filter) and subtracting this from the Gaussian filtered image. The resulting image was binarized using Otsu's method[51]. Finally, objects smaller than 1000 voxels were eliminated, where voxels were considered part of the same connected object whenever they shared at least a corner. We then used this binarized image to correct the manual tracing of the vasculature by shifting the centerline, so it was equidistant from the vessel boundaries (done within a 10-μm

neighborhood to avoid confusion between neighboring capillaries). Every 5 µm along the centerline of each capillary segment, we estimated the vessel radius by finding the closest distance from the centerline to the vessel boundary. Measurements of less than 2 µm or more than 10 µm were excluded as they likely reflected imaging artifacts, and we averaged across all measurements for each capillary segment.

4.10.6 Amyloid plaque segmentation and density analysis

2PEF images of methoxy-X04 labeled amyloid plaques were filtered and binarized. Briefly, we first reduced the background signal in a line-by-line fashion by subtracting the median of each line. Salt and pepper image noise was reduced using the adaptive Wiener method with a 3 x 3 pixel kernel[52]. The image was then binarized using a manually-determined threshold (99% of the intensity distribution) and smoothed with a 3 x 3 pixel median filter. Objects smaller than 25 voxels were then removed, with object connectivity here defined as voxels sharing a face. The volume fraction of amyloid either globally or in a tube that follows the centerline of each capillary segment was then calculated from this binarized image. The tube volume was generated by swaying a sphere with a specified radius along the centerline of the capillary segment from one end to the other.

4.10.7 Kinetics of capillary stalling

To determine the short-term fate of capillaries that stalled, we repeatedly imaged the same capillary bed at baseline and at 5, 10, and 15 min later in APP/PS1 mice (n= 6 animals), and tracked the fate of all the capillaries that were stalled at baseline. If a vessel

was observed as stalled at all subsequent imaging time points, it was scored as remaining stalled, and if flow had resumed the stall was scored to have resolved. If the originally stalled capillary resumed flow, then re-stalled at a later time point that was scored as re-stalled. In some animals, we further determined the cause of capillary stalls at each of these time points.

To evaluate the longer-term fate of capillaries that were stalled, we imaged APP/PS1 mice (n= 5 animals) at baseline and then 1, 3, 7, and 14 days later and determined what fraction of the capillaries stalled at baseline were stalled at any subsequent imaging session.

We estimated how frequently we would observe capillaries stalled at baseline to be stalled at any subsequent imaging session assuming that no stalls lasted long enough to stay stalled between imaging sessions and that each capillary segment was equally likely to stall. With this model, the probability, P_c, of the capillaries stalled at baseline to be stalled at any subsequent imaging session is:

$$P_c = 1 - (1 - r)^N \qquad (S1)$$

where r is the fraction of capillaries with stalled blood flow and N is the number of observations after the baseline imaging.

4.10.8 Administration of antibodies against Ly6G and impact on neutrophil population

We treated APP/PS1 mice (n = 9, 12-25 weeks old) with intraperitoneal injections of monoclonal antibodies against lymphocyte antigen 6 complex, locus G (Ly6G) (α-

Ly6G, clone 1A8, 4 mg/kg, BD Biosciences) or an isotype control antibody (n = 6, Rat IgG2a, κ, 4 mg/kg, BD Biosciences). The same cortical capillary bed was imaged in anesthetized mice immediately before and at 30-60 min and 60-90 min after treatment. Quantification of stalled capillaries was performed blinded to imaging time and treatment type.

To determine the impact of α-Ly6G on neutrophil number, we used flow cytometry to determine neutrophil counts 3, 6 and 24 hr after a single treatment (4 mg/kg) and after one month of treatment every three days (2 mg/kg).

Blood from APP/PS1 and wt mice was collected from the submandibular vein and mixed with 1x RBC lysis buffer (00-4300-54, ThermoFisher Scientific). After incubation at room temperature for 10 min, the sample was centrifuged at 500 g for 5 min and the supernatant was removed. The cell pellet was re-suspended in 500 uL of Hank's balanced salt solution (HBSS) supplemented with 1% bovine serum albumin (BSA) and centrifuged again; this washing procedure was repeated 3 times. Following isolation, neutrophils were re-suspended at a density of 10^7 cells per ml in HBSS supplemented with 1% BSA. The cell samples were labeled at room temperature for 45 min with the following anti-mouse antibodies: anti-CD45 (560695, BD Bioscience), anti-CD11b (557686, BD Bioscience) and anti-Ly6G (551460, BD Bioscience). After washing the samples with HBSS samples have been re-suspended in FACS buffer (1% BSA and 2mM EDTA in PBS), the remaining leukocytes were analyzed by flow cytometry using a Guava easyCyte Flow Cytometer (EMD Millipore Corporation). Data were analyzed using FlowJo software (FlowJo LLC). The neutrophil population was identified based on the

side and forward scatter and later gated for $CD45^{high}$, $CD11b^{high}$, and $Ly6G^{high}$ using FlowJo.

4.10.9 Measurement of volumetric blood flow in penetrating arterioles

To quantify blood flow in cortical penetrating arterioles, we measured the vessel diameter from image stacks and the centerline RBC flow speed from line-scan measurements, as described in Santisakultarm *T.P.* et al.[53]. The volumetric blood flow, *F*, was calculated as:

$$F = \frac{\pi v r^2}{2} \qquad (S2)$$

where *v* is the time-averaged centerline RBC speed and *r* is the vessel radius. To correlate the impact of the number of capillaries stalled on penetrating arteriole blood flow, we imaged the same capillaries and measured blood flow in the same six to eight penetrating arterioles in both young APP/PS1 and wt mice (ages 3-4 months) and older APP/PS1 mice (age 11-14 months) treated with antibodies against Ly6G or with isotype control antibodies. Images to determine capillary stalling and line scans to determine penetrating arteriole blood flow speed were taken at baseline and at 30-60 and 60-90 min after treatment. All analysis was conducted blinded to the animal genotype, age, treatment, and imaging time point.

4.10.10Measurement of global blood flow using ASL-MRI

Imaging was performed on a 7.0 Tesla small animal MRI system with 450 mT/m gradient amplitude and a 4500 T/m/s slew rate (Biospec 70/30, Bruker). The animals were

anesthetized with isoflurane in oxygen and immobilized in the MRI using a nose cone and bite ring. A volume coil was used for transmission and a surface coil for reception. We imaged APP/PS1 and wt mice (age 7-9 months) at baseline. About 48 hrs later, animals were given an intraperiotenial injection of α-Ly6G or isotype control antibodies (4 mg/kg) and a second set of images were acquired between 2-6 hr after injection.

Anatomical images were acquired to find a coronal slice at a location approximately 1 mm caudal to Bregma[54]. This position was used for subsequent ASL imaging, which was based on a FAIR-RARE pulse sequence that labeled the inflowing blood by global inversion of the equilibrium magnetization[55]. In this method, inversion recovery data from the imaging slice are acquired after selective inversion of the slice and after inversion of both the slice and the surrounding tissue. The difference of the apparent R1 relaxation rate images then yields a measure of the CBF[56]. Three averages of one axial slice were acquired with a field of view of 15 × 15 mm, spatial resolution of 0.23 × 0.23 × 2 mm^3, echo time TE of 5.36 ms, effective TE of 26.84 ms, repeat time TR of 10 s, and a RARE factor of 36. This resulted in a total scan time for the CBF images of about 25 min. Turbo-RARE anatomical images were acquired with the following parameters: 10 averages of 14 slices with the same field-of-view and orientation as the ASL images, resolution = 0.078 × 0.078 × 1 mm^3, TE = 48 ms, TR = 2000 ms, and a RARE factor of 10. The total scan time was about 6 min.

For computation of CBF, the Bruker ASL perfusion processing macro was used. It uses the model and includes steps to mask out the background and ventricles described in Kober, et al.[57]. The masked CBF images were exported to Analyze format on the MRI

console. We then used the anatomical image to create a mask that outlined the entire cortical region, excluding the sinus, and averaged the CBF measurement across this region for each animal at each imaging time point. Analysis of ASL-MRI data was conducted blinded to animal genotype and treatment.

4.10.11Multi-Exposure Laser Speckle Imaging

Mice were anesthetized for imaging using 3% isoflurane for induction and were given atropine and glucose each hour as described above. Depth of anesthesia was monitored using a force-sensitive square resistor placed below the mouse to detect respiration. For imaging, anesthesia was reduced to 1.5% in medical air and then adjusted to maintain a respiration rate between 65-75 breaths per minute. The mouse temperature was maintained at 37°C with a feedback-controlled heating pad.

Multi-exposure laser speckle contrast imaging quantifies the degree of blurring of a laser speckle pattern due to moving scatterers for different image exposure times[58]. In the cortex, moving red blood cells are the primary moving scatterers, so this technique yields a measure of cerebral blood flow. Images were taken using a near-IR camera (Basler) through a 4x objective (NA=0.28, Olympus) with a 786-nm stabilized laser diode (LD785-SEV300, ThorLabs), intensity modulated using an acousto-optic modulator (AOMO 3100-125 and AODR 1110AF-AEFO-1.5, Gooch & Housego). Laser speckle images were taken at 15 exposure times ranging across three decades from 50 μs to 80 ms, as described by Kaszmi et al.[59], with a calibrated laser intensity for each exposure time. Images were taken at ~10 fps with 30 images for each exposure time at each time point.

Mice were imaged for 20 minutes prior to antibody injection in order to ensure stabilization under anesthesia. Animals received either α-Ly6G or isotype control antibodies (4mg/kg, intraperitoneal). The mice were imaged for 3 hours post-injection.

Speckle contrast values, *K*, were fitted to the equation:

$$K^2(T,\tau_c) = \beta\rho^2 \frac{e^{-2x} - 1 + 2x}{2x^2} + 4\beta\rho(1-\rho)\frac{e^{-x} - 1 + x}{x^2} + v_e \qquad (S3)$$

with $x = \frac{T}{\tau_c}$, where τ_c is the correlation time, considered to be inversely proportional to average speed of moving scatterers in the sample, *T* is the exposure time, ρ is the fraction of dynamically scattered light, v_e accounts for any noise in the system, and β is a normalization constant indicating the mismatch between speckle and pixel sizes. The β parameter is estimated using the simpler form of the equation where ρ is considered to be 1:

$$K^2(T,\tau_c) = \beta \frac{e^{-2\frac{T}{\tau_c}} - 1 + 2\frac{T}{\tau_c}}{2\left(\frac{T}{\tau_c}\right)^2} + v_e \qquad (4)$$

Fractional blood flow changes are proportional to the inverse of the correlation time image divided by a baseline image taken immediately before antibody injection.

4.10.12Extraction of network topology and vessel diameters from mouse anatomical dataset

One large postmortem dataset from the vibrissa primary sensory (vS1) cortex in mouse previously obtained by Tsai et al[21] and Blinder et al.[44], was used for this study (~1 mm^3 and ~15,000 vessel segments). In brief, this dataset was obtained by filling the vessels with a fluorescent indicator, extracting the brain and imaging with 2PEF from the pial surface to near the bottom of cortex. In this dataset, penetrating arterioles and ascending venules that reached the pial surface were identified by following their connections to a large cerebral arteriole or venule. We further labeled subsurface vessels in three classes: arterioles, capillaries, and venules. Starting with the surface and penetrating arterioles (venules) vessels were classified by iteratively seeking all vessels with diameter above 6 μm connected to any previously labeled arteriole (venule). All remaining vessels were labeled as capillaries. The diameter threshold was manually chosen as the smallest integer diameter value which resulted in arteriolar and venular trees that exhibited no loops, in contrast to the very looped capillary network.

Due to post-mortem shrinkage, vessel diameters in this mouse dataset were smaller than those measured *in-vivo*, so required rescaling[21,44,53]. As blood flow is highly dependent on vessel diameters, two successive corrections were applied. First, a monotonically increasing function, which tends to one at large diameter, was applied to all vessel diameters:

$$d = d_0 + A\cos\left(\tan^{-1}\left(\frac{d_0}{B}\right)\right), A > 0, B > \frac{2}{3}A\sin\left(\tan^{-1}\left(\frac{1}{\sqrt{2}}\right)\right) \quad \text{(S5)}$$

where d is the corrected diameter and d_0 is the diameter extracted from the image stack. A and B are constrained parameters calculated so that the corrected vessel diameter distribution matched *in vivo* measurements from two photon microscopy[12], as shown in Extended Data Figure S 4.22. This function ensures that the hierarchy of diameters in the network is preserved and the larger vessels are not rescaled. For the network represented in Figure 6a, A=1.4 and B=10.3, so that the diameter threshold for capillary vessels becomes 7.2 µm. A second depth-dependent correction was then applied to the diameter of arterioles and venules:

$$d = d_0(az + b) \quad \text{Eq. 6}$$

where z is the depth below the cortical surface and a and b are parameters determined so that the diameters of the trunks of the penetrating arterioles and ascending venules matched *in-vivo* measurements[60]. For the network represented in Figure 4.6.a, these parameters were a=-0.0014 µm^{-1} (-9.36e-4 µm^{-1}) and b=2.54 (2.02) for arterioles (venules).

4.10.13Extraction of network topology and vessel diameters from human anatomical dataset

The dataset used was previously obtained by Cassot et al.[61] and Lauwers et al.[22] from thick sections (300 µm) of a human brain injected with India ink from the Duvernoy collection[53]. The brain came from a 60-year old female who died from an abdominal lymphoma with no known vascular or cerebral disease. It corresponds to a large volume (6.4 mm^3 of cerebral cortex) extending across 20.8 mm^2 along the lateral part of the

collateral sulcus (fisiform gyrus) extracted from Section S2 in Lauwers et al.[22], and includes a total of 27,340 vessel segments. The mean radius and length of each segment were rescaled by a factor of 1.1 to account for the shrinkage of the anatomical preparation. The main vascular trunks were identified manually and divided into arterioles and venules according to their morphological features, following Duvernoy's classification[62,63]. Following Lauwers et al.[22] and Lorthois et al[23] (*1*) as in the mouse data sets, arterioles (venules) were defined by iteratively seeking all vessels with diameter above 9.9 µm connected to any previously identified arteriole (venule), so that no loops were present. All remaining vessels were classified as capillaries.

4.10.14Synthetic network generation

The synthetic periodic network of order three (i.e. three edges per node) was generated to match the mouse network parameters. A 1-mm^3 vascular network was constructed by replication of a simple periodic network (Extended Data Figure S 4.21). Capillary diameters and lengths were uniform and were set to the averages for the mouse network. A single penetrating arteriole and ascending venule (with diameters set to the averages from the mouse network) served as inlet/outlet. The distance between the inlet and outlet corresponded to the average distance between penetrating arterioles and ascending venules from the mouse dataset.

4.10.15Blood flow simulations

The methodology for simulating blood flow in these intra-cortical vascular networks has been presented in detail in Lorthois et al.[23]. Briefly, the network was

represented by a graph in which edges represent vessel segments between branches that are characterized by an average diameter and length. We used a one-dimensional (analogous to electric circuit models) nonlinear network model that was slightly modified from Pries et al.[64] to handle large networks for the flow simulations. Using an iterative procedure, the model takes into account the complex rheological properties of blood flow in the microcirculation (Fåhræus, Fåhræus-Lindqvist, and phase separation effects). These effects are modeled using empirical descriptions[65,66] deduced from experiments in rats. The model was used to calculate the flow and hematocrit in each vessel and the pressure at each intersection of vessels. For the human dataset, the parameters for the empirical descriptions of the Fåhræus, Fåhræus -Lindqvist and phase separation effects were re-scaled in order to account for the difference in characteristic size between human and rat RBCs, as proposed by Lorthois et al.[23] and Roman et al.[67]. This simulation approach has no free parameters.

Boundary conditions: Physiologically realistic pressure drops of 60 mmHg, as measured in rats[68] and estimated in humans[23], were imposed between all arteriolar and venular trunks feeding and draining the computational volume, while a no-flow condition was imposed on deeper arteriolar or venular vessels that intersected the lateral boundaries of the simulated volume. A constant discharge hematocrit of 0.45, corresponding to a typical value of the systemic hematocrit, was also imposed in arteriolar trunks. Moreover, a pseudo-periodic boundary condition was applied to all capillaries at the lateral boundaries, as illustrated in Extended Data Figure S 4.23. Fictitious vessels were created that link capillaries intersecting opposing faces in a semi random fashion. A grid was created on the two faces and refined until, for a given cell, each capillary on one face was

matched with at most 2 capillaries on the opposing face, allowing the creation of fictitious bifurcations. Once the optimal grid was found, the closest neighboring vessels from the opposing faces were connected together. The length of the resulting fictitious vessels was set to 50 µm and their diameters to the average diameters of the connected capillaries. This pseudo-periodic boundary condition is similar in spirit but simpler and more computationally effective than the one recently introduced by Schmid et al.[69]. Finally, a no-flow boundary condition was applied to all vessels intersecting the bottom face of the domain. We also compared the results with no-flow boundary conditions for all capillaries at the lateral boundaries.

Simulating stalls: In order to study the influence of capillary stalling on cerebral blood flow, a given proportion of capillaries in each network was randomly occluded. To simulate occlusion, the radius of the selected vessels was divided by 100. This resulted in a large increase of the hemodynamic resistance, of order 10^8, and a similar decrease of the computed flow through these vessels. At least five repetitions were performed for each proportion of stalled capillaries and each set of conditions considered. On the mouse data, 1000 simulations in total were run on a 32-core Intel(R) Xeon E5-2680 v2 @ 3.3 GHz for a total computational time of ~170 hours. For human data set, about 100 simulations were run on the same machine for a total computational time of ~50 hours.

4.10.16Behavior experiments

All experiments were performed under red light in an isolated room. The position of the mouse's nose was automatically traced by Viewer III software (Biobserve, Bonn, Germany). In addition to the automatic results obtained by Viewer III software, a blinded

experimenter independently scored mouse behavior manually. Animals were taken into the behavior room one-hour prior to the experiment. Behavioral analysis was conducted at baseline and at 3 and 24 h after injection with α-Ly6G, α-LFA-1, or isotype control antibodies (IP 4 mg/kg). The α-Ly6G treated APP/PS1 mice were then treated every three days for four weeks (IP 2 mg/kg) and behavior experiments were repeated. The OR, Y-maze, balance beam walk, and forced swim tests were performed at all time points. The NOR task was performed only at baseline and the 4-week time point to avoid animals becoming accustomed to the objects. For experiments with APP/PS1 mice and α-Ly6G, animals were ~11 months of age at the start of the experiment (APP/PS1, α-Ly6G n=11; APP/PS1 Iso-Ctl, n=9; wt α-Ly6G, n=10; and wt Iso-Ctl, n=10). For experiments with APP/PS1 mice and α-LFA-1, animals were 11-13 months of age (APP/PS1, α-LFA-1 n=10; APP/PS1 Iso-Ctl, n=10; wt α-LFA-1, n=7; and wt Iso-Ctl, n=8). For experiments with 5xFAD mice and α-Ly6G, animals were 5-6 months of age (5xFAD, α-Ly6G n=8; 5xFAD Iso-Ctl, n=8; and wt α-Ly6G, n=10).

Object replacement test: The object replacement (OR) task evaluated spatial memory performance. All objects were validated in a separate cohort of mice to ensure that no intrinsic preference or aversion was observed, and animals explored all objects similarly. Exploration time for the objects was defined as any time when there was physical contact with an object (whisking, sniffing, rearing on, or touching the object) or when the animal was oriented toward the object and the head was within 2 cm of the object. In trial 1, mice were allowed to explore two identical objects for 10 min in the arena and then returned to their home cage for 60 min. Mice were then returned to the testing arena for 3 min with one object moved to a novel location (trial 2). Care was taken

to ensure that the change of placement alters both the intrinsic relationship between objects (e.g. a rotation of the moved object) and the position relative to internal visual cues (e.g. new location in the arena; one wall of testing arena had a pattern). In addition to using the tracking software to determine the object exploration times, the time spent at each object was manually scored by an independent experimenter who was blinded to the genotype and treatment. The preference score (%) for OR tasks was calculated as ([exploration time of the novel object]/[exploration time of both objects]) × 100 from the data in trial 2. Automated tracking and manual scoring yielded similar results across groups, so we report the automated tracking results.

Y-Maze: The Y-Maze task was used to measure working memory by quantifying spontaneous alternation between arms of the maze. The Y-maze consisted of three arms at 120° and was made of light grey plastic. Each arm was 6-cm wide and 36-cm long and had 12.5-cm high walls. The maze was cleaned with 70% ethanol after each mouse. A mouse was placed in the Y-maze and allowed to explore for 6 min. Mouse behavior was monitored, recorded, and analyzed using the Viewer software. A mouse was considered to have entered an arm if the whole body (except for the tail) entered the arm and to have exited if the whole body (except for the tail) exited the arm. If an animal consecutively entered three different arms, it was counted as an alternating trial. Because the maximum number of triads is the total number of arm entries minus 2, the spontaneous alternation score was calculated as (number of alternating triads)/ (total number of arm entries − 2).

Forced swim test: The forced swim test measured depression-like behavior. Mice were individually placed in a 4-L glass beaker filled with 2.5 L of 25°C water. Mice were

allowed to adjust for 1 min and then were evaluated for 6 min. An experimenter blind to the genotype and treatment analyzed the videotaped behavior and scored the immobility time, defined by the absence of active, escape-oriented behaviors such as swimming, jumping, rearing, sniffing, or diving.

Balance beam walk: The balance beam walk measured motor coordination and balance by scoring the ability of the mice to traverse a graded series of narrow beams to reach an enclosed safety platform. The beams consisted of long strips of wood (80 cm) with a round cross section of 12- or 6-mm diameter. The beams were placed horizontally, 40 cm above the floor, with one end mounted on a narrow support and the other end attached to an enclosed platform. Bright light illuminated the end of the beam where the mice started. Mice received three consecutive trials on each of the round beams, in each case progressing from the widest to the narrowest beam (15 min between each trial). Mice were allowed up to 60 s to traverse each beam. The time to traverse each beam and the number of times either hind paw slipped off each beam were recorded for each trial. Analysis of each measure was based on the mean score across all trials for that mouse at that time point. Experimenters were blinded to the genotype and the treatment of the mice.

Novel object recognition test: The novel object recognition (NOR) task measures recognition memory and is based on rodents' innate preference for exploring novel objects. This test was conducted only in the animals at baseline and after 4 weeks of treatment. The testing approach was identical to the OR task, but with a novel object placed at the location of one of the initial objects in trial 2.

4.10.17ELISA assay

After the conclusion of the behavior experiments, the APP/PS1 animals that had received α-Ly6G or isotype control antibodies every 3 days for a month were sacrificed by lethal injection of pentobarbital (5 mg/100 g). Brains were quickly extracted and divided along the centerline. One half was immersed in 4% paraformaldehyde in phosphate buffered saline (PBS) for later histological analysis and the other half was snap frozen in liquid nitrogen.

The frozen APP/PS1 mouse hemi-brains (Iso-Ctr: n=6, 11.5-12.5 months old; α-Ly6G: n=7, 11.5-12.5 months old) were weighed and homogenized in 1 ml PBS containing complete protease inhibitor (Roche Applied Science) and 1 mM AEBSF (Sigma) using a Dounce homogenizer. The homogenates were then sonicated and centrifuged at 14,000 g for 30 min at 4° C. The supernatant (PBS-soluble fraction) was removed and stored at −80° C. The pellet was re-dissolved in 0.5 ml 70% formic acid, sonicated, and centrifuged at 14,000 g for 30 min at 4° C, and the supernatant was removed and neutralized using 1M Tris buffer at pH 11. Protein concentration was measured in the PBS soluble fraction and the formic acid soluble fraction using the Pierce BCA Protein Assay (Thermo Fischer Scientific). The PBS soluble fraction extracts were diluted 1:5. Formic acid extracts were diluted 1:1 after neutralization. These brain extracts were analyzed by sandwich ELISA for Aβ1-40, Aβ1-42, and Aβ aggregates using commercial ELISA kits and following the manufacturer's protocol (Aβ1-40: KHB3481; Aβ1-42: KHB3441; Aβ aggregates: KHB3491, Thermo Fisher Scientific). The Aβ concentration was calculated by comparing the sample absorbance with the absorbance

of known concentrations of synthetic Aβ1–40 and Aβ1–42 standards on the same plate. Data was acquired with a Synergy HT plate reader (Biotek) and analyzed using Gen5 software (BioTek) and Prism (Graphpad).

4.10.18Histopathology

Immunohistochemistry was performed on the brains of mice chronically treated every third day for 4 weeks with either α-Ly6G antibody or isotype control (Iso-Ctr n=5, α-Ly6G n=4). A single paraformaldehyde-fixed hemisphere of each brain was cut into 40 μm thick sagittal sections.

Every sixth section from each mouse was stained with 1% Thioflavin-S (T1892**,** Sigma) for 10 min at room temperature and washed twice with 80% ethanol for 2 min. The sections were mounted using Fluoroshield with DAPI (F6057, Sigma). Images were taken using confocal microscopy (Zeiss Examiner.D1 AXIO). For each image, the background was subtracted using the ImageJ background subtraction plugin (Rolling ball with 7 μm radius). Images were then manually thresholded, using the same threshold for all sections from a given mouse. Appropriate thresholds varied mouse to mouse and were set to ensure that the smallest Thioflavin-S labeled objects that morphologically appeared to be an amyloid plaque remained above threshold. Cortical and hippocampal regions of interest were defined in each section anatomically, and the fraction of pixels above threshold was determined across all sections for these regions of interest. All image processing was done blinded to treatment group. As a second measure of amyloid deposition, we manually counting the number of Thioflavin-S positive amyloid plaques in the cortex and hippocampus, again across all sections and while blinded to the

treatment group. All sections were stained and imaged in parallel. Artifacts such as bubbles were eliminated from analysis by manually excluding these regions.

4.10.19Statistical analysis

Boxplots were created using Prism7 (GraphPad). The box extends between the values for the 25th and 75th percentile of the data. The whiskers extend 1.5 times the difference between the value of the 75th and 25th percentile of the data from the top and bottom of the box. Values lying outside the whiskers were defined as outliers and the mean was computed excluding these outliers. The median is indicated with a black horizontal line inside the box, while the mean is indicated with a red horizontal line. Violin plots were created using the statistical software package, R[70].

Data in all groups was tested for normality using D'Agostino-Pearson omnibus normality test. Parametric statistics were used only if the data in all groups in the comparison were normally distributed. The statistical significance of differences between multiple groups was determined using one-way analysis of variance (ANOVA) followed by Tukey's multiple comparison correction for normally distributed data, and using Kruskal-Wallis one-way ANOVA followed by Dunn's multiple comparison correction for data with a non-normal distribution. Statistical comparisons between two groups were performed using the Student's t test or paired t test for normally distributed data, or using the Mann-Whitney test or Wilcoxon matched-pairs test for data with a non-normal distribution. P-values smaller than 0.05 were considered statistically significant. All statistical analysis was performed using Prism7 (GraphPad).

We use a standardized set of significance indicators across all figures in this manuscript. For comparisons between groups: *p<0.05, **p<0.01, ***p<0.001, ****p<0.0001. For matched comparisons before and after treatment: +p<0.05, ++p<0.01. Supplementary Table 1 provides details of the groups compared, animal and capillary numbers, statistical tests, and explanatory notes for individual panels in the main figures. This information is included in the caption of supplementary figures.

4.10.20Supplementary text on numerical simulations of cerebral blood flow changes induced by capillary occlusions

In previous work, we studied how the occlusion of a single cortical capillary influenced blood flow in downstream vessels[11] and found strong reductions in blood flow (10% of baseline value 1 branch downstream; 25% at 2 branches; 50% at 3 and 4 branches), suggesting that even the small fraction of occluded capillaries we observed in APP/PS1 mice could cause a significant decrease in overall brain blood flow. To test this idea, we simulated blood flow in anatomically accurate blood vessel networks from mice and humans and examined how flow changed when we occluded a random selection of capillaries.

4.10.21Validation of simulations by comparison to in vivo measurements in mouse:

As described in the Materials and Methods above, our simulations resulted in calculated values for flow (Extended Data Figure S 4.24.a), pressure (Extended Data Figure S 4.24.b), and hematocrit (Extended Data Figure S 4.24.c) in each vessel segment in the volume. We validated the simulation by comparing *in vivo* measurements of blood

flow at different levels in the microvascular hierarchy acquired by 2PEF from the top 300 µm of mouse cortex (data from Santisakultarm, *et al.*[48]) with the simulation predictions. The simulation results are highly dependent on the boundary conditions imposed on capillaries at the lateral edges of the simulation volume. The calculated velocity distribution using pseudo-periodic boundary conditions in capillaries up to 300 µm in depth and using the vessel diameter corrections described above matches the experimental distribution well (Extended Data Figure S 4.24.d). For comparison, the velocity distribution calculated using diameters from the raw datasets (without correction for the difference in vessel size between *in vivo* and post mortem measurements) and that calculated using a no-flow boundary condition both led to an order of magnitude underestimation of capillary flow speeds (Extended Data Figure S 4.24.d). Our new pseudo-periodic boundary condition, together with the correction of vessel diameters, led to a velocity distribution that approaches the distribution of experimental velocities. The experimental distribution has a sharper peak, which might be due to experimental bias associated with the limited number of vessels in which these measurements have been performed (147 *in vivo* measurements vs. 3,400 capillaries in the simulations). The simulated speeds in penetrating arterioles and ascending venules as a function of their diameters also closely matched experimental results from Santisakultarm, et al.[48] and from Taylor, et al.[60] (Extended Data Figure S 4.24.e).

Numerical simulation of cerebral blood flow reductions caused by capillary occlusions: The effect of occlusions in capillaries was investigated by randomly selecting a given proportion of capillaries and reducing their flow by imposing a 100-fold reduction in diameter (Extended Data Figure S 4.25.a, Figure 4.6.a). To quantify the effects of the

occlusions, we calculated the normalized cortical perfusion as the summed flow in the penetrating arterioles feeding the region, normalized by the value calculated with no capillary occlusions (Figure 4.6.c). While the magnitude of this summed flow is highly dependent on the boundary conditions, the decrease in flow due to capillary occlusions was much less sensitive to the choice of boundary conditions (Extended Data Figure S 4.25.b). For the mouse network shown in Figs. 6a and Extended Data 24a with pseudo-periodic boundary conditions and diameter correction, we found a linear decrease in the normalized perfusion with a slope S=-2.3±0.2 %baseline perfusion/% capillaries stalled (mean±SD) (Figure 4.6.c). This linear behavior was very robust to variations in the parameters chosen for the computations, with slopes equal to -2.2±0.1 (-2.1±0.2) with no-flow boundary conditions and diameter correction (no diameter correction). In order to evaluate the influence of boundary conditions with regard to the size of the simulated volume, 300 µm-thick sub-volumes of the mouse anatomical datasets were randomly extracted. The decrease in blood flow with increasing numbers of stalled capillaries was slightly larger when 300 µm-thick sub-volumes of the datasets were used (-2.6±0.4 and -2.9±0.5 with the pseudo-periodic boundary condition and the no-flow boundary condition, respectively), as compared to the full ~1 mm-thick volume. In Figure 4.6.c, only computations on the maximum simulation volume with the corrected diameters and pseudo-periodic boundary conditions are presented.

The simulations in the human network (Figure 4.6.b) using pseudo-periodic boundary conditions yielded a slope of S=-2.3±0.6, very similar to the mouse results. This linear decrease was also observed in synthetic periodic networks of order three (i.e. three edges per node; S=-2.9, Figure 4.6.c).

Limitations and methodological considerations: The human dataset used in the simulations was only 300 μm thick, raising concerns about the influence of boundary conditions. The broad agreement between simulation results in mouse datasets with 1-mm and 300-μm thickness reduces this concern. The simulations predicted a similar CBF increase across mouse and human vascular networks when stalls were reduced, suggesting that the blood flow improvements we observed in APP/PS1 mice may be achievable in humans.

The simulations predicted a smaller impact of capillary stalling on CBF than we observed experimentally. One possible explanation is that the simulations used vascular networks from wt mice, while AD mouse models have different vascular densities and topologies[71] that may influence the sensitivity of CBF to capillary stalls, although the vascular density differences between APP/PS1 and wt mice have been reported to be relatively minor. In addition, increased leukocyte adhesion in APP/PS1 mice may lead not only to complete stalls, but also to slowed flow in some capillaries when a leukocyte is present in the segment, which is not captured in the simulations.

4.11 Supplementary figures

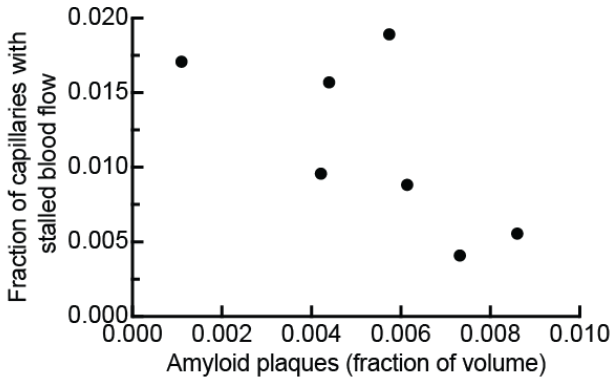

Figure S 4.1. The fraction of capillaries with stalled blood flow did not increase with increasing cortical amyloid plaque density in APP/PS1 mice.

Fraction of capillaries with stalled blood flow as a function of the cortical volume fraction that was labeled by methoxy-X04. Mice ranged from 50 to 64 weeks of age.

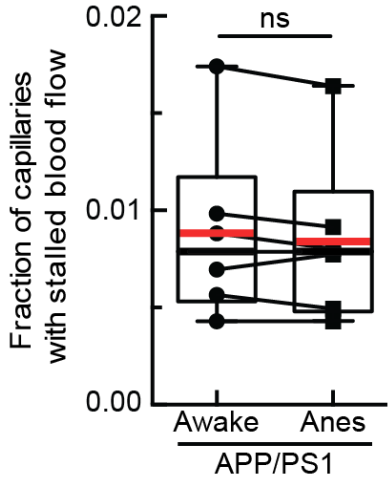

Figure S 4.2. Plot of the fraction of capillaries with stalled blood flow in mice imaged while anesthetized and awake.

Lines connecting data points indicate data from the same animal. Animals were first trained to remain calm while head fixed and standing on a spherical treadmill. On the day of imaging, animals were briefly anesthetized to enable retro-orbital injection of Texas-Red dextran and were then allowed to wake up. We imaged these animals first while awake and then while anesthetized under 1.5% isoflurane, with both imaging sessions occurring on the same day (n = 6 mice, no significant difference by Wilcoxon test).

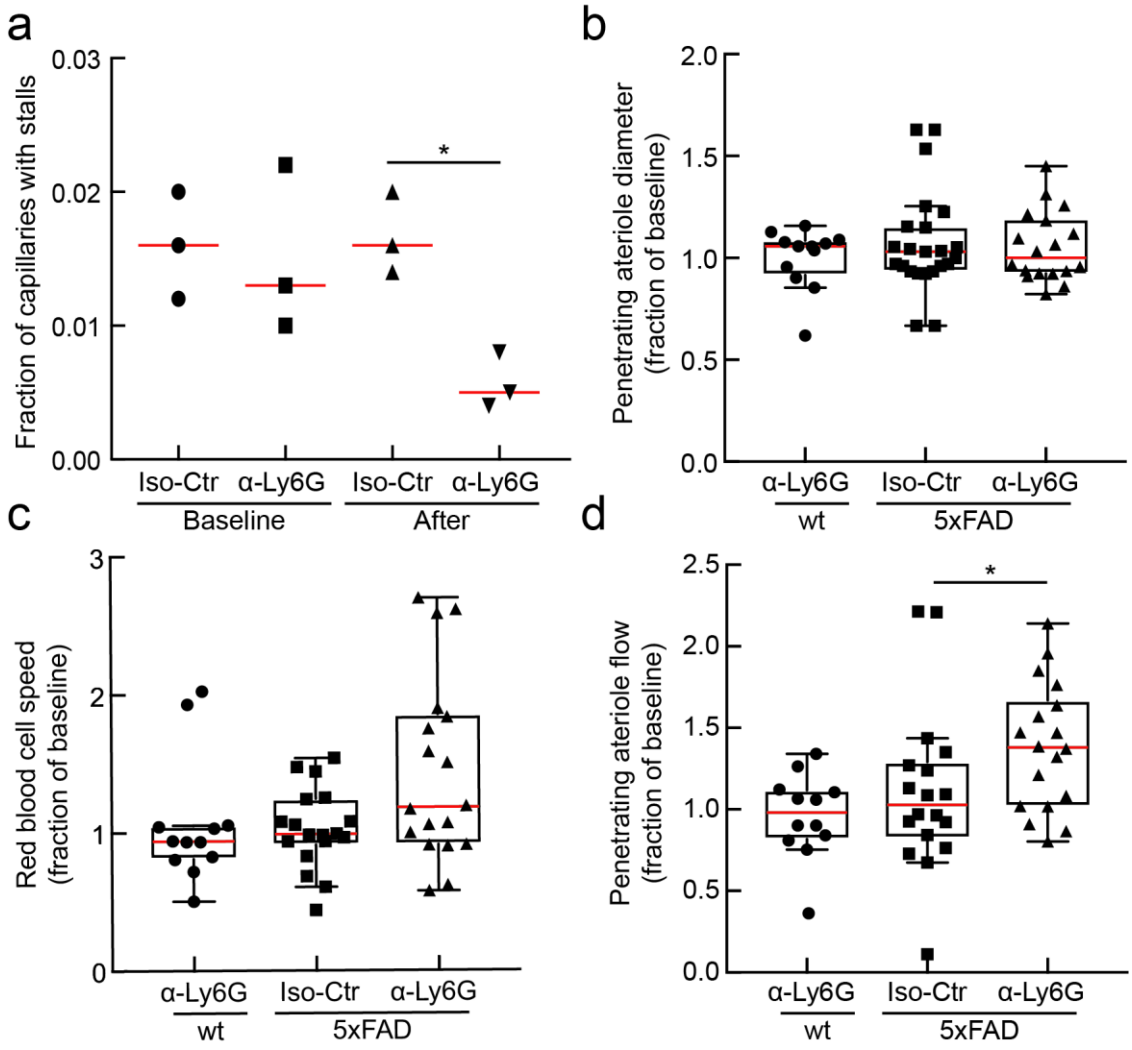

Figure S 4.3. α-Ly6G administration reduced the number of cortical capillary stalls and increased penetrating arteriole blood flow in 5xFAD mice.

(a) Fraction of capillaries with stalled blood flow in 5-7 month old 5xFAD mice at baseline and at about one hour after injection of α-Ly6G or isotype control antibodies. (b) Vessel diameter, (c) RBC flow speed, and (d) RBC volumetric blood flow from cortical penetrating arterioles after α-Ly6G or isotype control antibody administration, shown as a fraction of the baseline value, in 5xFAD or wt mice (wt α-Ly6G: 3 mice, 13 arterioles; 5xFAD Iso-Ctr: 3 mice, 18 arterioles; and 5xFAD α-Ly6G: 3 mice, 19 arterioles; * $p<0.05$, Kruskal-Wallis one-way ANOVA with post-hoc pair-wise comparisons using Dunn's multiple comparison test).

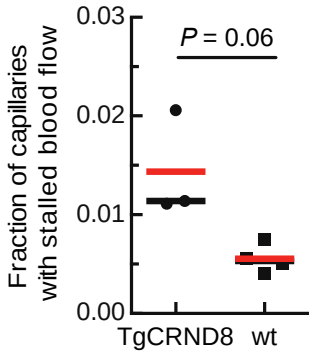

Figure S 4.4. 2PEF imaging of cortical vasculature reveals a higher fraction of stalled capillaries in TgCRND8 mice as compared to wt mice.

Fraction of capillaries with stalled blood flow in TgCRND8 and age-matched wild type littermates (TgCRND8: 3 mice, 3,028 capillaries; wild type: 4 mice, ~4,062 capillaries; p=0.06, Mann-Whitney).

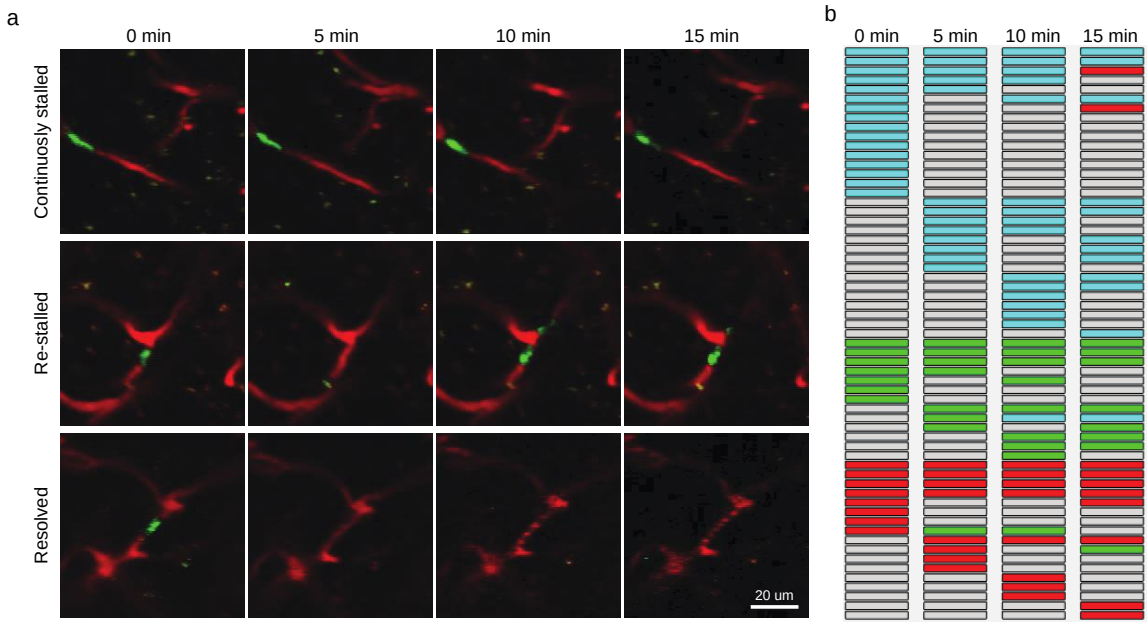

Figure S 4.5. Characterization of capillary stall dynamics in APP/PS1 mice.

(a) Repeated 2PEF imaging over 15 min of capillaries that were stalled at the baseline measurement and (top) remained stalled, (middle) began flowing and then re-stalled and (bottom) resolved and remained flowing. Blood plasma labeled with Texas-Red dextran (red) and leukocytes labeled with Rhodamine 6G (green). (b) Characterization of the fate of individual capillaries observed as being stalled across four image stacks taken at baseline and 5, 10, and 15 min later. Each row represents an individual capillary and the color of the box for each capillary at each time point indicates the status: flowing (grey), stalled with a leukocyte present (cyan), stalled with platelet aggregates present (green), and stalled with only RBCs (red). Note that unlike the results shown in Figure 4.3.b, we do not separate cases where RBCs are present along with a leukocyte or platelet aggregates.

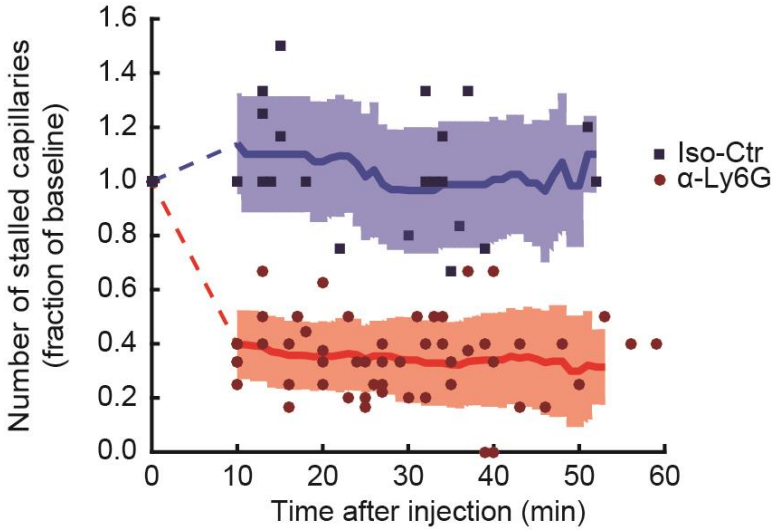

Figure S 4.6. Extended Data Figure 6. Number of stalled capillaries in APP/PS1 mice dropped rapidly after α-Ly6G administration.

2PEF image stacks were taken repeatedly over an hour after α-Ly6G or isotype control antibody injection and the number of stalled capillaries determined at each time point (α-Ly6G: n=6 mice; Iso-Ctr: n=4; each mouse imaged 2 to 6 times over the hour).

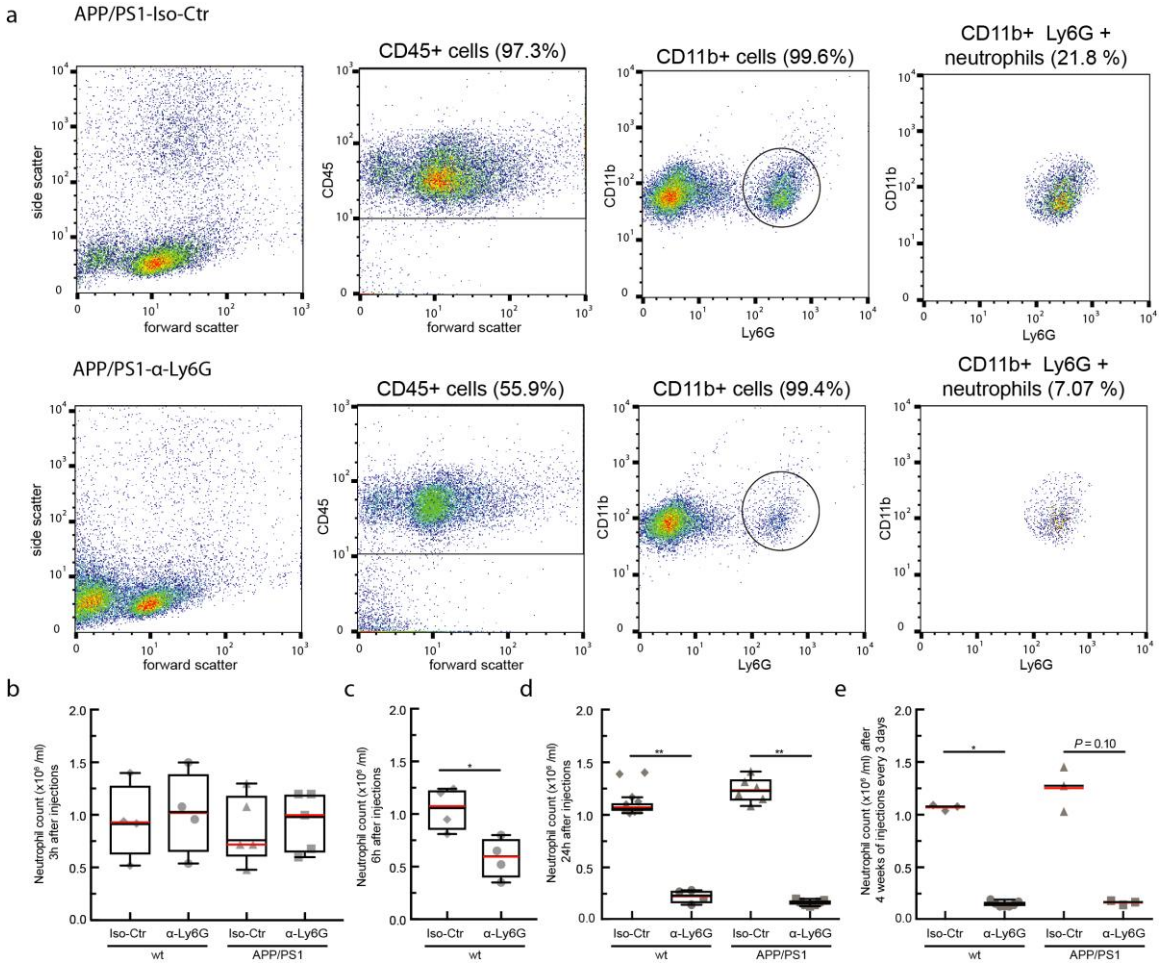
a
APP/PS1-Iso-Ctr
CD45+ cells (97.3%)
CD11b+ cells (99.6%)
CD11b+ Ly6G + neutrophils (21.8 %)
side scatter
forward scatter
CD45
CD11b
Ly6G
APP/PS1-α-Ly6G
CD45+ cells (55.9%)
CD11b+ cells (99.4%)
CD11b+ Ly6G + neutrophils (7.07 %)
b
c
d
e
Neutrophil count (x10⁶ /ml) 3h after injections
Neutrophil count (x10⁶ /ml) 6h after injections
Neutrophil count (x10⁶ /ml) 24h after injections
Neutrophil count (x10⁶ /ml) after 4 weeks of injections every 3 days
P = 0.10
Iso-Ctr
α-Ly6G
wt
APP/PS1

Figure S 4.7. Treatment with α-Ly6G leads to neutrophil depletion in both APP/PS1 and wildtype control mice, beginning within three hours after administration.

(a) Representative flow cytometry data for blood drawn from APP/PS1 mice 24 hours after treatment with isotype control antibodies (top row) and α-Ly6G (bottom row). Left column shows forward and side scattering from entire population of blood cells (after lysing and removing red blood cells). The second column shows the gate on CD45+ cells, indicating leukocytes. The third column shows expression of CD11b (high for monocytes and neutrophils) and Ly6G (high for neutrophils) for the CD45+ cells. Cells with high expression levels of both CD11b and Ly6G were considered to be neutrophils (right column). (b-d) Neutrophil counts for APP/PS1 and wt mice 3, 6, and 24 hr after a single treatment with α-Ly6G or isotype control antibodies, respectively. (3 hr data: wt Iso-Ctr: n=4 mice; wt Ly6G: n=4; APP/PS1 Iso-Ctr: n=4; APP/PS1 Ly6G: n=5; 6 hr data: wt Iso-Ctr: n=4 mice; wt Ly6G: n=4; 24 hr data: wt Iso-Ctr: n=9 mice; wt Ly6G: n=4; APP/PS1 Iso-Ctr: n=6; APP/PS1 Ly6G: n=7) (e) Neutrophil counts for APP/PS1 and wt mice after one month of treatment with α-Ly6G or isotype control antibodies every three days (4 week data: wt Iso-Ctr: n=3; wt Ly6G: n=7; APP/PS1 Iso-Ctr: n=3; APP/PS1 Ly6G: n=3) (*$p<0.05$, **$p<0.01$, Mann-Whitney comparison between Iso-Ctr and Ly6G treated animals.)

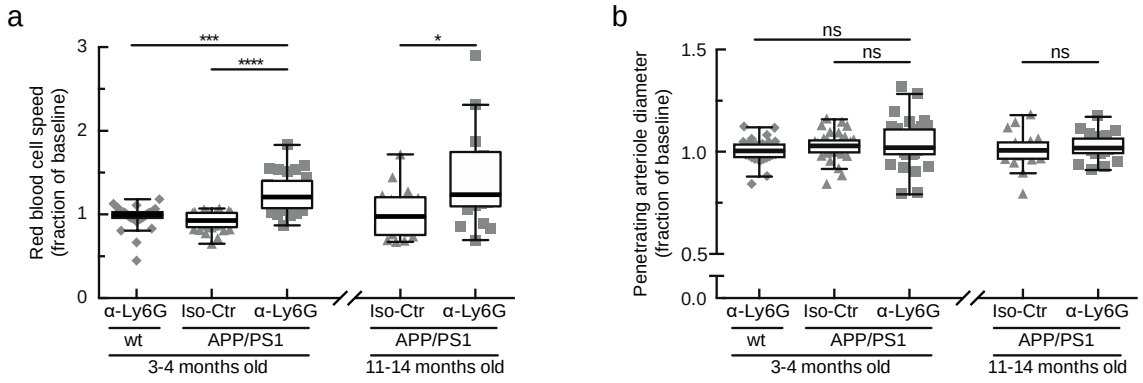

Figure S 4.8. Administration of antibodies against Ly6G increased the RBC flow speed but did not alter the diameter of cortical penetrating arterioles in APP/PS1 mice.

(a) RBC flow speed and (b) vessel diameter after α-Ly6G or isotype control antibody administration in young (3-4 months) and old (11-14 months) APP/PS1 mice and wt control animals shown as a fraction of baseline (young wt α-Ly6G: 5 mice, 30 arterioles; young APP/PS1 Iso-Ctr: 5 mice, 32 arterioles; young APP/PS1 α-Ly6G: 5 mice, 33 arterioles; old APP/PS1 Iso-Ctr: 3 mice, 18 arterioles; old APP/PS1 α-Ly6G: 3 mice, 22 arterioles; * $p<0.05$, ** $p<0.01$, *** $p<0.001$, **** $p<0.0001$, Kruskal-Wallis one-way ANOVA with post-hoc pair-wise comparisons using Dunn's multiple comparison test).

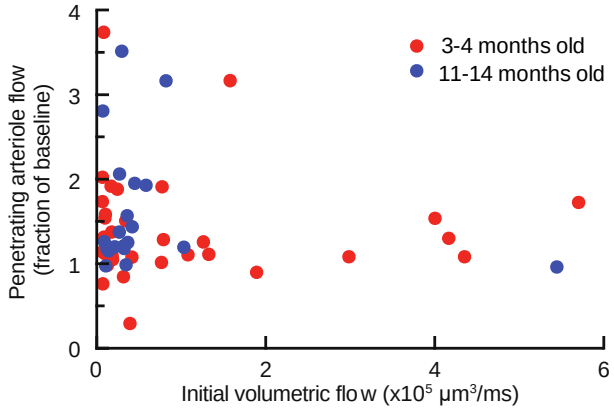

Figure S 4.9. Penetrating arterioles with slower initial flow tended to increase flow speed more after α-Ly6G injection in APP/PS1 mice.

Plot of penetrating arteriole flow after α-Ly6G antibody administration in young (3-4 months) and old (11-14 months) APP/PS1 mice shown as a fraction of baseline flow. Same data as shown in Figure 3C.

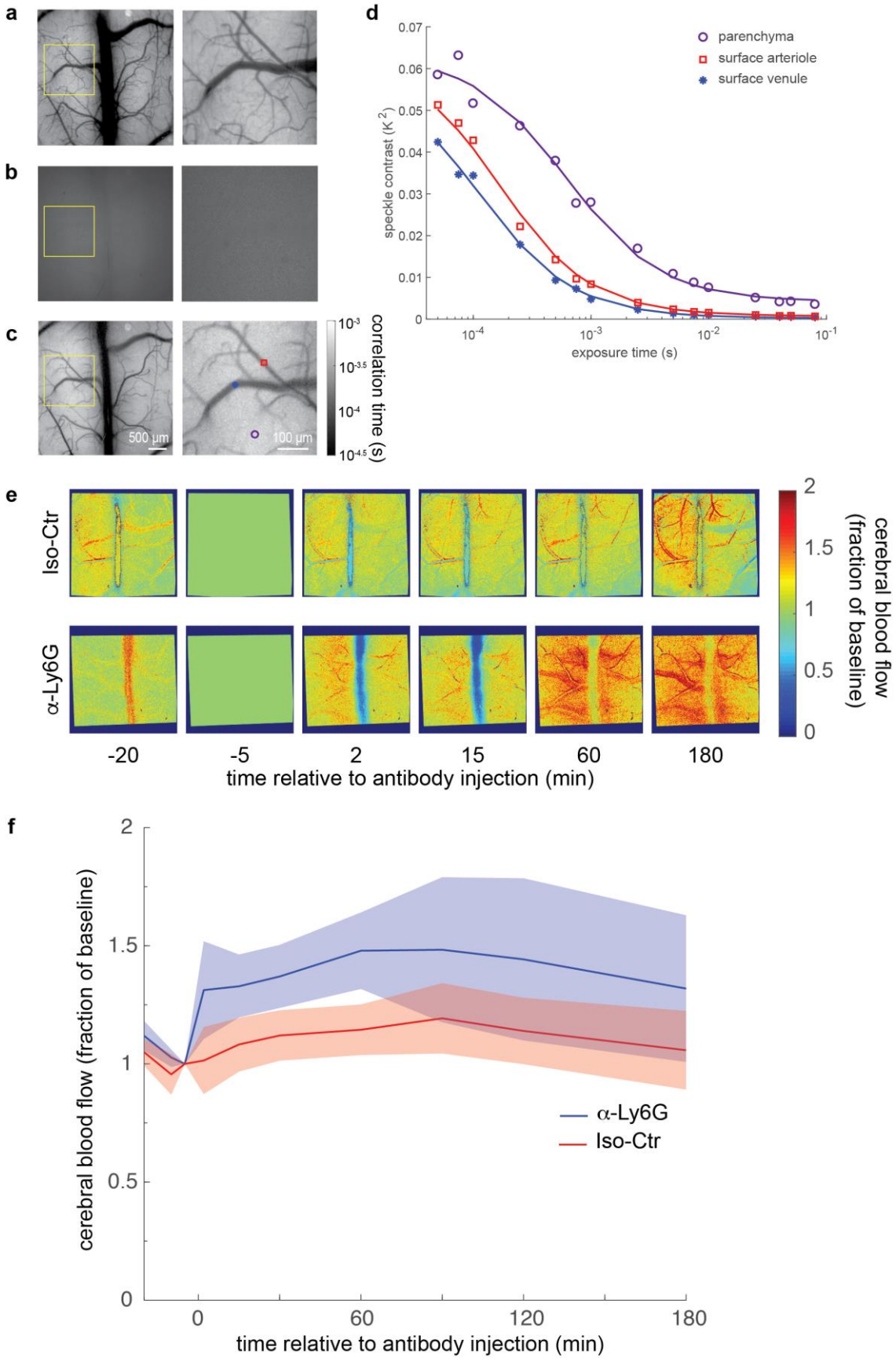
a
b
c
d
e
f
parenchyma
surface arteriole
surface venule
speckle contrast (K²)
exposure time (s)
correlation time (s)
500 μm
100 μm
Iso-Ctr
α-Ly6G
cerebral blood flow (fraction of baseline)
-20
-5
2
15
60
180
time relative to antibody injection (min)
α-Ly6G
Iso-Ctr
cerebral blood flow (fraction of baseline)
time relative to antibody injection (min)

Figure S 4.10. Multi-exposure laser speckle imaging revealed CBF increased in APP/PS1 mice within minutes of α-Ly6G administration.

(a) Green light reflectance image of parietal cortex of APP/PS1 mouse. Image to the right is a expanded view of the region outlined with a yellow box. (b) Raw laser speckle image of the same region as (a) with a 10 ms exposure time. (c) Correlation time image of the same region as (a). (d) Speckle contrast values as a function of image exposure time, showing fits for regions of interest located in a surface arteriole, surface venule, or parenchymal region. The corresponding symbols in the expanded view of (c) show the locations for each fit. (e) Images and (f) plot of cerebral blood flow as a function of time after antibody injection, expressed as a fraction of the value at 5 minutes before injection for APP/PS1 mice treated with isotype control antibodies or α-Ly6G. (APP/PS1 α-LFA1: 5 mice; APP/PS1 Iso-Ctrl: 5 mice; age range 9-19 months)

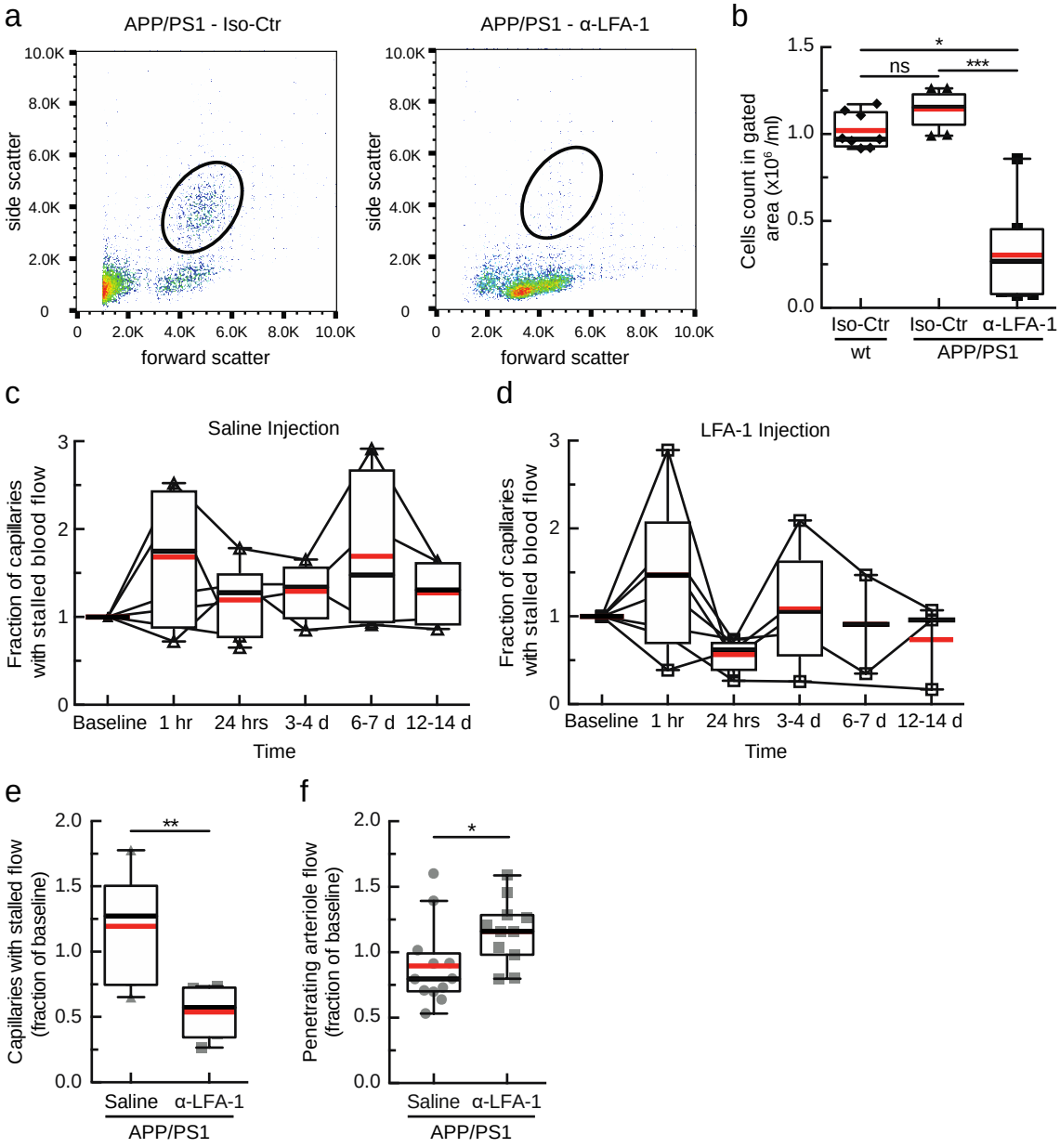

Figure S 4.11. Treating APP/PS1 mice with α-LFA-1 reduced the number of stalled capillaries and improved arterial blood flow after 24 hours.

(a) Flow cytometry scatter plots for APP/PS1 mice 24 hours after injection of isotype control antibodies (left) or with antibodies against Lymphocyte Functional Antigen 1 (α-LFA-1; M17/4 clone, BD Biosciences; 4 mg/kg, retro-orbital injection). Circles depict the gate used to identify leukocytes. (b) Leukocyte concentration in the blood 24 hours after treatment with α-LFA-1 or isotype control antibodies in APP/PS1 and

wt mice. Leukocytes counts in the gating area were decreased by 84% after α-LFA-1 as compared to the isotype control in APP/PS1 mice (Iso-Ctr in wt: 8 mice, Iso-Ctr in APP/PS1: 9 mice, α-LFA-1 in APP/PS1: 7 mice; *p<0.05, ***p<0.001, Kruskal-Wallis one-way ANOVA with post-hoc pair-wise comparisons using Dunn's multiple comparison test). (c and c) Fraction of capillaries with stalled blood flow as a function of time after a single retro-orbital treatment with 0.9% saline (c) or α-LFA-1 antibodies (d) in APP/PS1 mice (saline: n = 6 mice; α-LFA-1: n = 7 mice, 4 mg/kg). We observed a transient increase in the number of capillaries with stalled blood flow at about 1 hr after treatment in both groups. There was a significant decrease in the fraction of stalled capillaries 24 hours after injection in the α-LFA-1 group. Images were collected over the same capillary bed on each imaging day, and the fraction of capillaries stalled was determined for each time point, with the analysis performed blinded to treatment day and treatment type. (e) Number of stalled capillaries, expressed as a fraction of the baseline number, 24 hrs after administration of α-LFA-1 or saline. α-LFA-1 reduced capillary stalls by 65% as compared to the saline control. (*n* = 6 mice per treatment group. **p<0.01, Mann-Whitney test). (f) Fraction of baseline arteriole flow in penetrating arterioles from APP/PS1 mice 24 hours after α-LFA-1 or saline treatment. Each point represents a single arteriole in one mouse. The blood flow was increased after α-LFA-1 treatment by 29% compared with saline controls (APP/PS1 α-LFA1: 4 mice, 11 arterioles; APP/PS1 saline: 4 mice, 12 arterioles; *p<0.05, Mann- Whitney test).

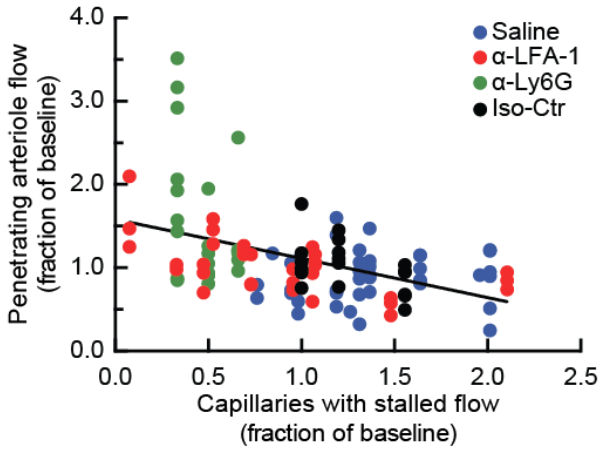

Figure S 4.12. Brain penetrating arteriole blood flow negatively correlates with the number of capillaries stalled in underlying capillary beds in APP/PS1 mice.

To correlate the effect of capillary stalling on penetrating arteriole blood flow, we imaged the same capillaries and measured blood flow in the same penetrating arterioles in APP/PS1 mice multiple times before and after administration of saline, α-LFA-1, α-Ly6G, and isotype control antibodies. For saline and α-LFA-1 animals, there were measurements at multiple time points over two weeks (data in Extended Data Figure S 4.9). For α-Ly6G and isotype control animals there were measurements only at baseline and ~1 hr after administration (data in Figure 4.3.c and Extended Data Figure 4.7 and 4.8). For each penetrating arteriole at each imaged time point, we plotted the volumetric flow, expressed as a fraction of the baseline volumetric flow, as a function of the number of capillaries stalled at that time point, expressed as a fraction of the baseline number of capillaries stalled (APP/PS1 α-LFA1: 4 mice, 11 arterioles; APP/PS1 saline: 4 mice, 12 arterioles; APP/PS1 α-Ly6G: 3 mice, 22 arterioles; APP/PS1 Iso-Ctr: 3 mice, 18 arterioles). These data confirm the sensitive dependence of penetrating arteriole blood flow on the fraction of capillaries with stalled flow across several different manipulations that led to either increases or decreases in the fraction of capillaries that are stalled. The linear regression is defined by: Y = -0.47 X + 1.6 (R^2 = 0.2, goodness of fit test; 95% confidence interval on slope: -0.65 – -0.29).

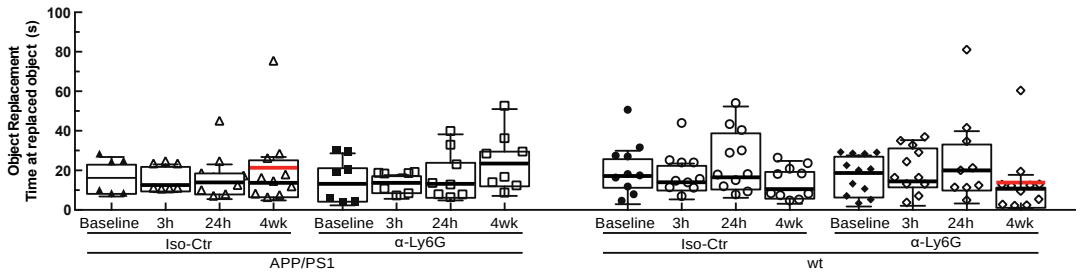

Figure S 4.13. Time spent at the replaced object in wild type controls and APP/PS1 animals treated with α-Ly6G or isotype control antibodies.

Time spent at the replaced object measured over 6 minutes for APP/PS1 and wt mice at baseline and at 3h and 24h after a single administration of α-Ly6G or isotype control antibodies, and after 4 weeks of treatment every three days (APP/PS1 Iso-Ctr: 10 mice; APP/PS1 α-Ly6G: 10 mice; wt Iso-Ctr: 11 mice; wt α-Ly6G: 11 mice; no significant differences among groups as determined by Kruskal-Wallis one-way ANOVA).

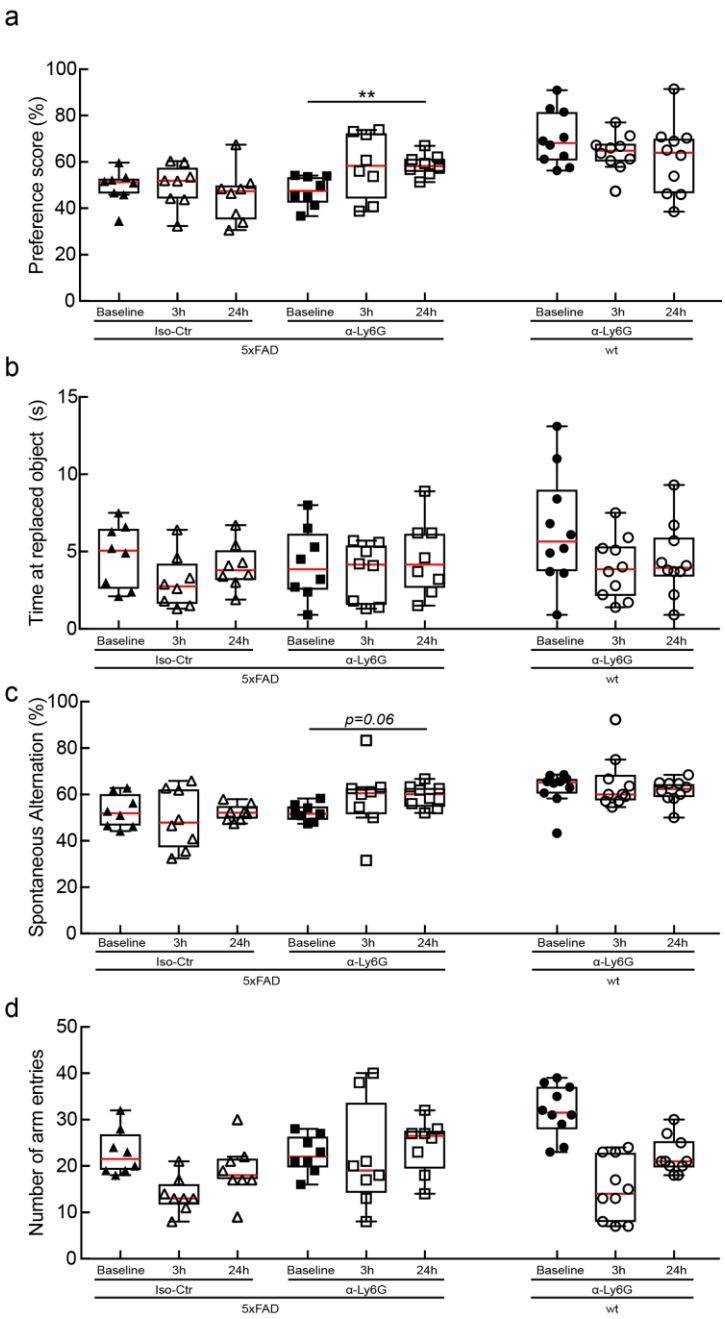
a
Preference score (%)
100
80
60
40
20
0
**
Baseline
3h
24h
Baseline
3h
24h
Baseline
3h
24h
Iso-Ctr
α-Ly6G
α-Ly6G
5xFAD
wt
b
Time at replaced object (s)
15
10
5
0
Baseline
3h
24h
Baseline
3h
24h
Baseline
3h
24h
Iso-Ctr
α-Ly6G
α-Ly6G
5xFAD
wt
c
Spontaneous Alternation (%)
100
80
60
40
20
0
p=0.06
Baseline
3h
24h
Baseline
3h
24h
Baseline
3h
24h
Iso-Ctr
α-Ly6G
α-Ly6G
5xFAD
wt
d
Number of arm entries
50
40
30
20
10
0
Baseline
3h
24h
Baseline
3h
24h
Baseline
3h
24h
Iso-Ctr
α-Ly6G
α-Ly6G
5xFAD
wt

Figure S 4.14. Administration of α-Ly6G improves performance of 5xFAD mice on object replacement and Y-maze tests of spatial and working memory.

(a) Preference score in OR task at baseline and at 3 hr and 24 hr after a single administration of α-Ly6G or Iso-Ctr antibodies. (b) Time spent at the replaced object measured over 3 minutes for 5xFAD and wt mice at baseline and at 3h and 24h after a single administration of α-Ly6G or isotype control antibodies. (c) Spontaneous alternation in Y-Maze task at baseline and at 3 hr and 24 hr after a single administration of α-Ly6G or Iso-Ctr antibodies. (d) Number of arm entries in the Y-maze measured for 6 minutes for 5xFAD and wt mice at baseline and at 3h and 24h after a single administration of α-Ly6G or isotype control antibodies. (5xFAD α-Ly6G: 8 mice; 5xFAD Iso-Ctr: 8 mice; and wt α-Ly6G: 10 mice; ** $p < 0.01$, Kruskal-Wallis one-way ANOVA with post-hoc pair-wise comparisons using Dunn's multiple comparison test).

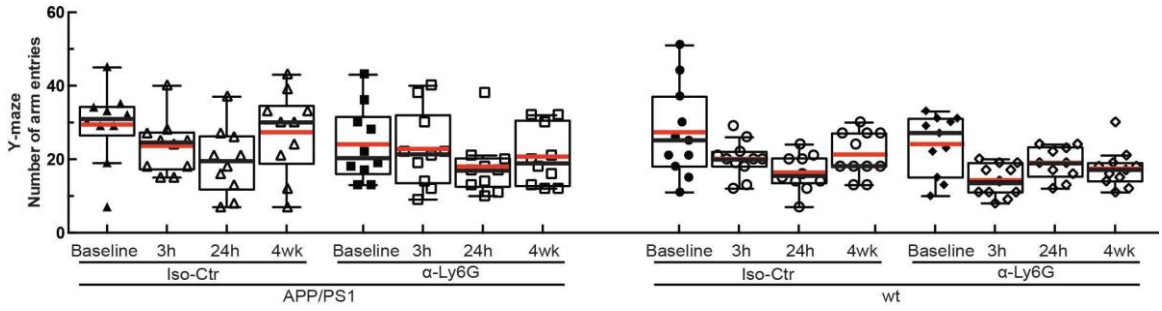

Figure S 4.15. Number of arm entries in the Y-maze for wild type controls and APP/PS1 animals treated with α-Ly6G or isotype control antibodies.

Number of arm entries in the Y-maze measured for 6 minutes for APP/PS1 and wt mice at baseline and at 3h and 24h after a single administration of α-Ly6G or isotype control antibodies, and after 4 weeks of treatment every three days (APP/PS1 Iso-Ctr: 10 mice; APP/PS1 α-Ly6G: 10 mice; wt Iso-Ctr: 11 mice; wt α-Ly6G: 11 mice; no significant differences among groups as determined by Kruskal-Wallis one-way ANOVA).

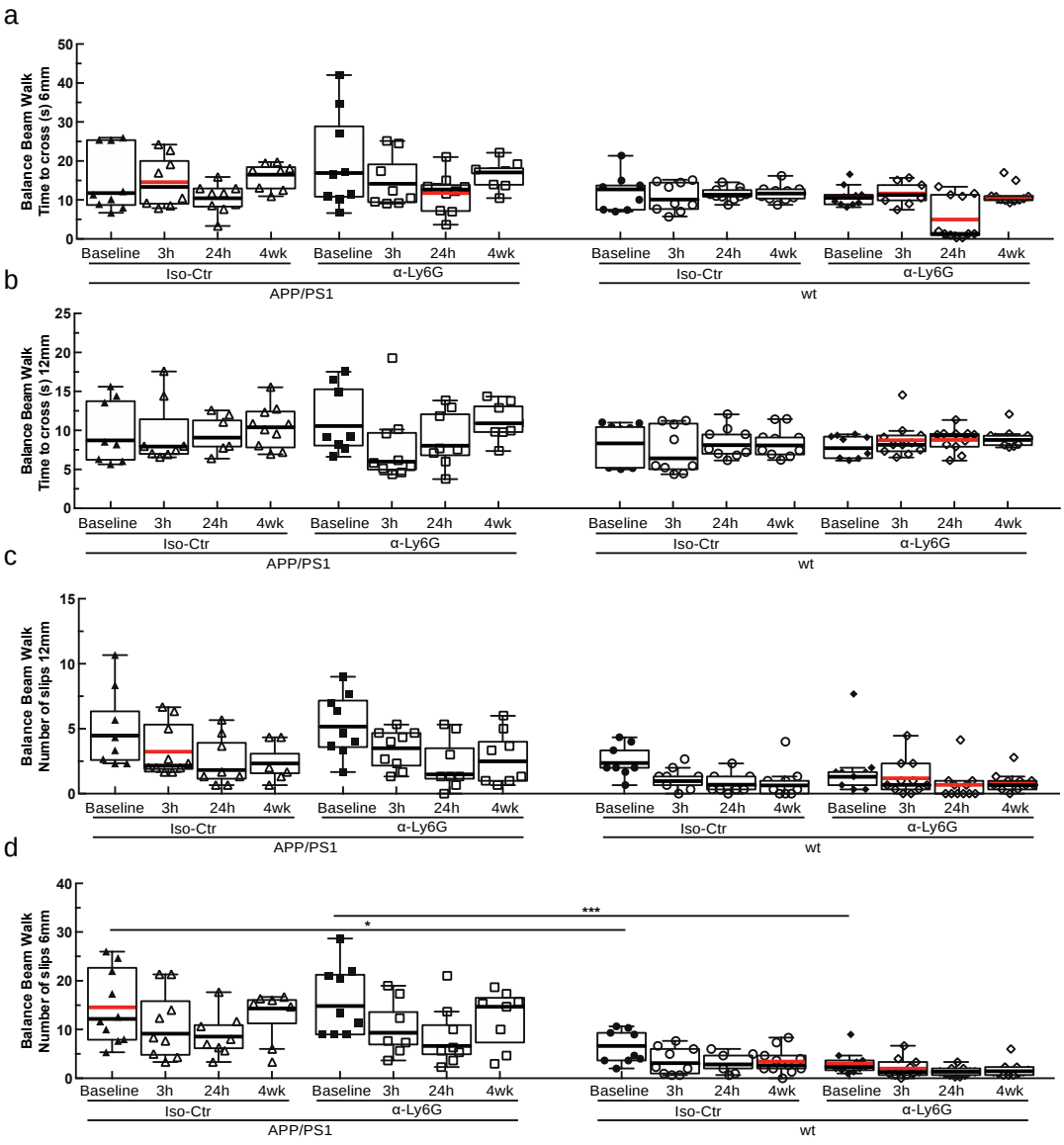
a
Balance Beam Walk
Time to cross (s) 6mm
b
Balance Beam Walk
Time to cross (s) 12mm
c
Balance Beam Walk
Number of slips 12mm
d
Balance Beam Walk
Number of slips 6mm
*
***
Baseline
3h
24h
4wk
Iso-Ctr
α-Ly6G
APP/PS1
wt

Figure S 4.16. Balance beam walk (BBW) to measure motor coordination in wildtype controls and APP/PS1 animals treated with α-Ly6G or isotype control antibodies.

(a and b) BBW time to cross on a 6- and 12-mm diameter beam, respectively, for APP/PS1 and wild type mice at baseline and at 3h and 24h after a single administration of α-Ly6G or isotype control antibodies, and after 4 weeks of treatment every three days. APP/PS1 mice showed a modest trend toward taking more time to cross the 6-mm diameter beam as compared to wt controls. (c and d). Number of slips on the BBW for a 6- and 12-mm diameter beam, respectively, for APP/PS1 and wild type mice at baseline and at 3h and 24h after a single administration of α-Ly6G or isotype control antibodies, and after 4 weeks of treatment every three days. For both beam diameters, APP/PS1 mice showed significantly more slips while crossing the beam as compared to wt animals, suggesting a motor deficit in the APP/PS1 mice. All animal groups showed a reduction in the number of slips with subsequent trials, suggesting improved motor coordination with practice. This improvement did not appear different between α-Ly6G and isotype control treated APP/PS1 mice, suggesting that increases in brain blood flow did not influence the motor learning underlying the reduction in the number of slips (APP/PS1 Iso-Ctr: 10 mice; APP/PS1 α-Ly6G: 10 mice; wt Iso-Ctr: 11 mice; wt α-Ly6G: 11 mice; * $p < 0.05$, *** $p < 0.001$, Kruskal-Wallis one-way ANOVA with post-hoc pair-wise comparisons using Dunn's multiple comparison test)

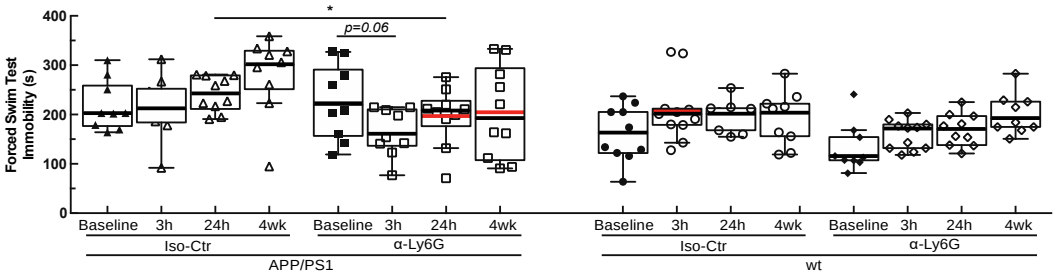

Figure S 4.17.. Depression-like behavior measured as immobility time in a forced swim test for wild type controls and APP/PS1 animals treated with α-Ly6G or isotype control antibodies.

Immobility time in forced swim test measured over 6 minutes for APP/PS1 and wt mice at baseline and at 3h and 24h after a single administration of α-Ly6G or isotype control antibodies, and after 4 weeks of treatment every three days (APP/PS1 Iso-Ctr: 10 mice; APP/PS1 α-Ly6G: 10 mice; wt Iso-Ctr: 11 mice; wt α-Ly6G: 11 mice; * $p < 0.05$, Kruskal-Wallis one-way ANOVA with post-hoc pair-wise comparisons using Dunn's multiple comparison test; p=0.06 comparison between baseline and 3h for APP/PS1 α-Ly6G, Wilcoxon matched-pairs signed rank test relative to baseline).

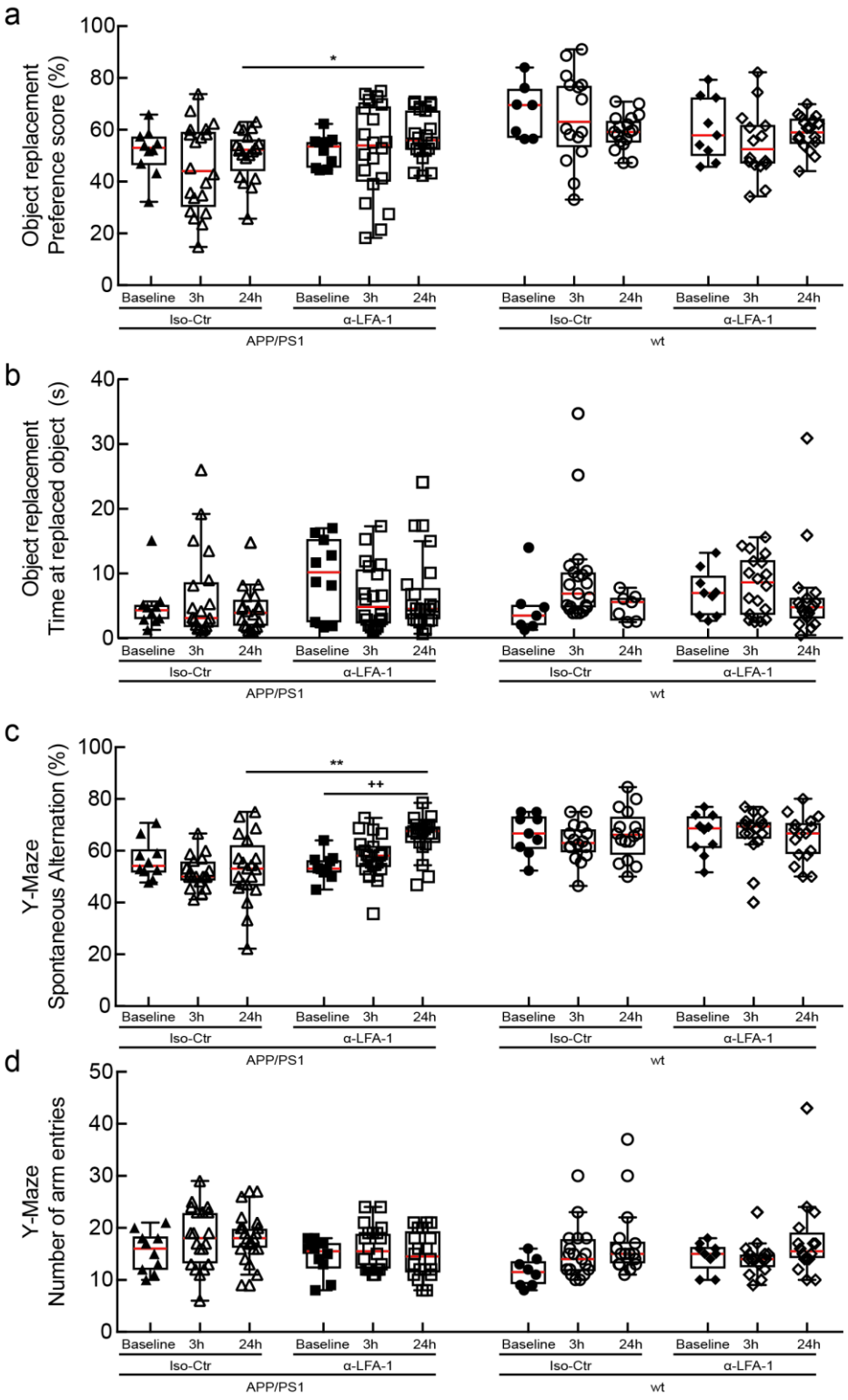
a
Object replacement
Preference score (%)
100
80
60
40
20
0
*
Baseline 3h 24h Baseline 3h 24h Baseline 3h 24h Baseline 3h 24h
Iso-Ctr α-LFA-1 Iso-Ctr α-LFA-1
APP/PS1 wt
b
Object replacement
Time at replaced object (s)
40
30
20
10
0
Baseline 3h 24h Baseline 3h 24h Baseline 3h 24h Baseline 3h 24h
Iso-Ctr α-LFA-1 Iso-Ctr α-LFA-1
APP/PS1 wt
c
Y-Maze
Spontaneous Alternation (%)
100
80
60
40
20
0
**
++
Baseline 3h 24h Baseline 3h 24h Baseline 3h 24h Baseline 3h 24h
Iso-Ctr α-LFA-1 Iso-Ctr α-LFA-1
APP/PS1 wt
d
Y-Maze
Number of arm entries
50
40
30
20
10
0
Baseline 3h 24h Baseline 3h 24h Baseline 3h 24h Baseline 3h 24h
Iso-Ctr α-LFA-1 Iso-Ctr α-LFA-1
APP/PS1 wt

Figure S 4.18. Administration of α-LFA-1 improves performance of APP/PS1 mice on object replacement and Y-maze tests of spatial and working memory.

(a) Preference score in OR task at baseline and at 3 hr and 24 hr after a single administration of α-LFA-1 or Iso-Ctr antibodies in 11-13 month old APP/PS1 and wt mice. (b) Time spent at the replaced object measured over 3 minutes these mice at baseline and at 3h and 24h after a single administration of α-LFA-1 or isotype control antibodies. (c) Spontaneous alternation in Y-Maze task at baseline and at 3 hr and 24 hr after a single administration of α-LFA-1or Iso-Ctr antibodies. (d) Number of arm entries in the Y-maze measured for 6 minutes for APP/PS1 and wt mice at baseline and at 3h and 24h after a single administration of α-LFA-1 or isotype control antibodies. (APP/PS1 α-LFA-1: 10 mice; APP/PS1 Iso-Ctr: 10 mice; wt α-LFA-1: 8 mice; wt Iso-Ctr: 7 mice; * $p<0.05$, ** $p<0.01$, Kruskal-Wallis one-way ANOVA with post-hoc pair-wise comparisons using Dunn's multiple comparison test).

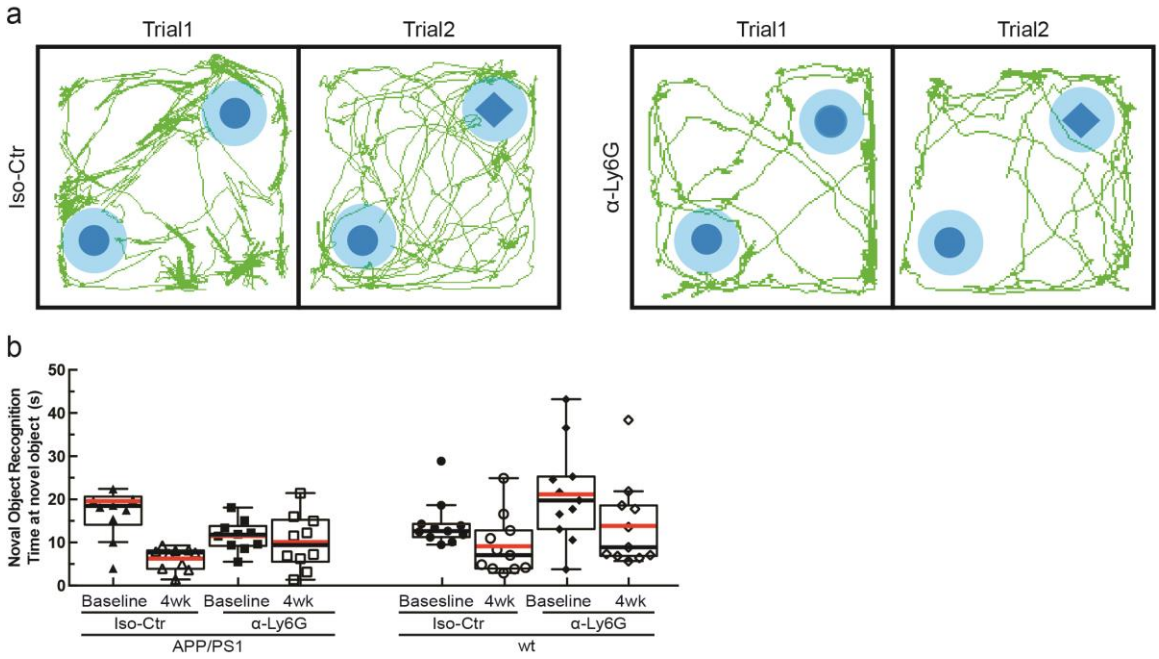

Figure S 4.19. Representative map of animal location and time spent at the novel object in wild type controls and APP/PS1 animals treated with α-Ly6G or isotype control antibodies.

(a) Tracking of mouse nose location from video recording during training and trial phases of novel object recognition task taken 4 weeks after administration of α-Ly6G or isotype control antibodies every three days in APP/PS1 mice. (b) Time spent at the novel object (APP/PS1 Iso-Ctr: 10 mice; APP/PS1 α-Ly6G: 10 mice; wt Iso-Ctr: 11 mice; wt α-Ly6G: 11 mice; no significant differences among groups as determined by Kruskal-Wallis one-way ANOVA).

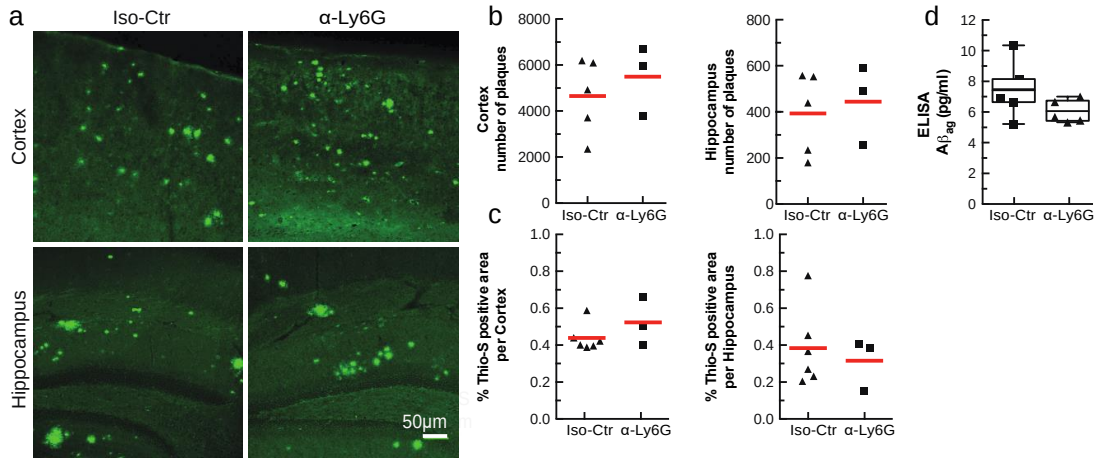

Figure S 4.20. Amyloid plaque density and concentration of amyloid-beta oligomers were not changed in 11-month-old APP/PS1 animals treated with α-Ly6G every three days for a month.

(a) Thioflavin-S staining of amyloid plaques in representative cortical sections (upper 2 panels) and hippocampal sections (lower 2 panels) for APP/PS1 mice treated with isotype control antibodies (left panels) or α-Ly6G (right panels). (b) Number of amyloid plaques in the cortex (left) and hippocampus (right) for APP/PS1 mice after one month of treatment (Iso-Ctr: 5 mice; α-Ly6G: 3 mice). (c) Percentage of tissue section positive for Thioflavin-S in the cortex (left) and hippocampus (right) (Iso-Ctr: 6 mice; α-Ly6G: 3 mice). (d) ELISA measurements of Aβ aggregate concentrations after 4 weeks of treatment with α-Ly6G or isotype control antibodies every three days (Iso-Ctr: 7 mice; α-Ly6G: 6 mice).

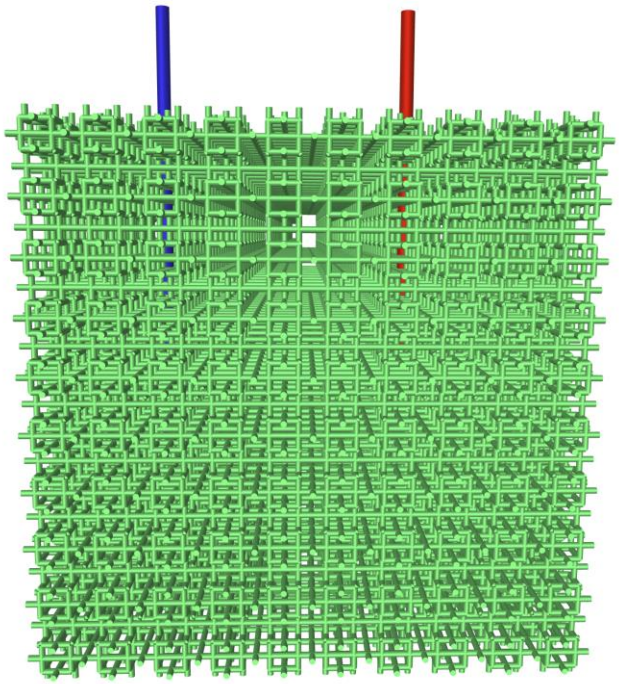

Figure S 4.21. Synthetic capillary network of order three.

Capillaries are indicated in green, while red and blue indicate the single feeding arteriole and draining venule, respectively.

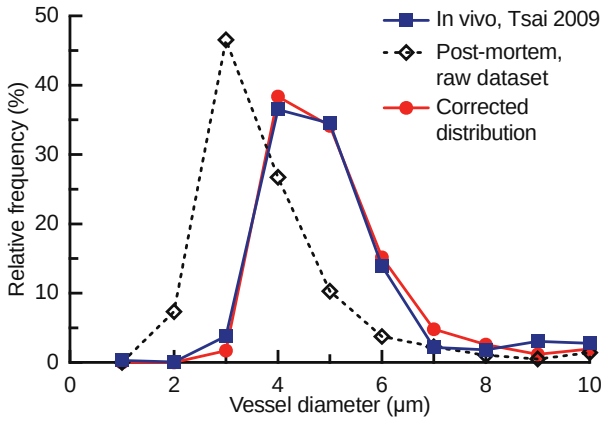

Figure S 4.22. Histogram of mouse capillary diameters from *in vivo* measurements and post-mortem vascular casts.

The diameter correction described in Eq. 3 closely aligned the post mortem diameters to the *in vivo* data.

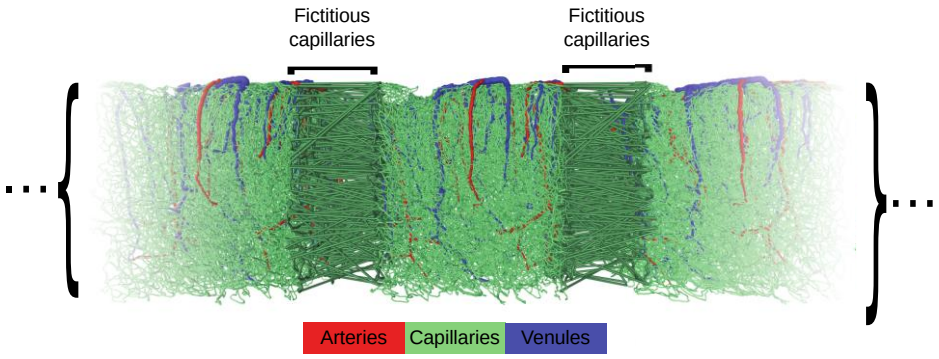

Figure S 4.23. Illustration of the pseudo-periodic boundary conditions.

Vessels categorized as arterioles are labeled in red, venules in blue, and capillaries in green.

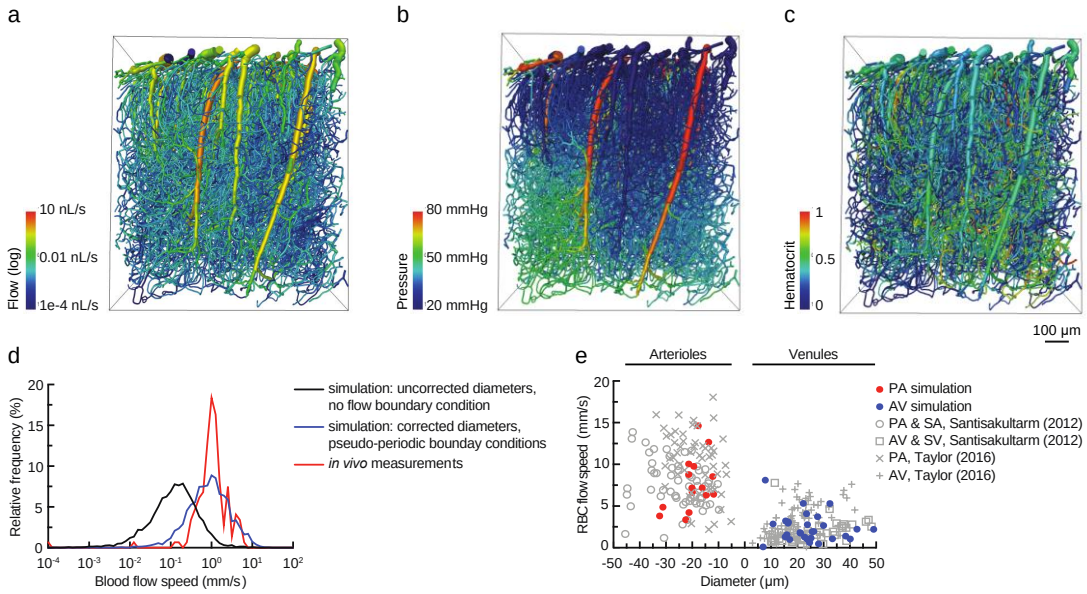

Figure S 4.24. Validation of simulations.

Spatial distribution of simulated blood flow (a), pressure (b), and hematocrit (c) in each vessel in the mouse vascular network. (d) Comparison of red blood cell velocities in capillaries in the top 300-µm of mouse cortex from experimental, *in vivo* measurements (red line), simulations with pseudo-periodic boundary conditions with corrected diameters (blue line), and no-flow boundary conditions without corrected diameters (black line). (e) Relationship between red blood cell speed and vessel diameter in arterioles and venules in calculations (solid red and blue dots) and experimental measurements (grey points).

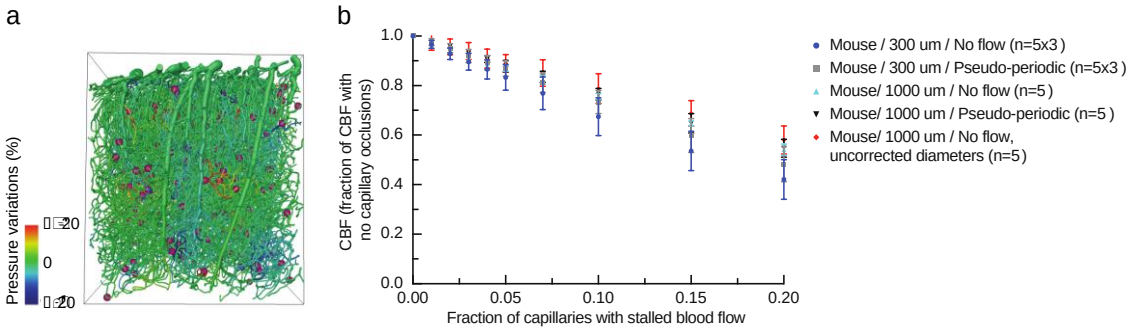

Figure S 4.25. Calculated blood flow decreases due to capillary stalls was robust with respect to simulation parameters.

(a) Pressure changes in mouse cortical vessel network due to randomly placed occlusions in 2% of capillaries. The corresponding flow changes are shown in Figure 4.1.J. (b) Calculated flow changes due to the occlusion of varying proportions of the capillaries using the full mouse dataset (1000 µm) or truncated datasets (1000x300 µm) with periodic or no flow boundary conditions, and with or without corrected vessel diameters. Error bars represent SD across n independent simulations (whole domain: n=5; 300 µm slices: n=5 for each of 3 slices).

4.12 Supplementary table

Table S 4-1. Group sizes, statistical tests, and notes for main Figure panels.

Figure panel	Groups compared	Statistical tests and Notes
4.1c, d	APP/PS1: 28 mice, ~22,400 capillaries wt: 12 mice, ~9,600 capillaries	Mann-Whitney, ****p<0.0001 Each data point represents one mouse in which > 800 capillaries were scored as flowing or stalled. The lines in panel D represent a sliding average with a 10-week window and the shaded areas represent 95% confidence intervals.
4.1f	APP/PS1: 7 mice Stalled: n ~ 120 Flowing: n = ~ 8,700	
4.1g	APP/PS1: 7 mice Stalled: n ~ 120 Flowing: n = ~ 8,600	
4.2b	APP/PS1: 6 mice, 106 stalled capillaries	Error bars represent 95% confidence intervals based on binomial statistics.

4.2d	Stalled: n = 116 Flowing: n = 8,431	Mann-Whitney, ****p<0.0001
4.2e	APP/PS1: 7 mice Stalled: n ~ 120 Flowing: n ~ 9,000	
4.2f	APP/PS1: 3 mice, 31 capillaries	
4.2h	APP/PS1: 4 mice, 49 stalled capillaries followed from first imaging session	
4.3a	α-Ly6G: 6 mice, ~4,800 capillaries Iso-Ctr: 6 mice, ~4,800 capillaries	Mann-Whitney, **p<0.01
4.3c	young APP/PS1 Iso-Ctr: 5 mice, 32 arterioles old APP/PS1 Iso-Ctr: 3 mice, 18 arterioles young wt α-Ly6G: 5 mice, 30 arterioles	Kruskal-Wallis one-way ANOVA with post-hoc using Dunn's multiple comparison correction, **p<0.01 and ***p<0.001

	young APP/PS1 α-Ly6G: 5 mice, 33 arterioles old APP/PS1 α-Ly6G: 3 mice, 22 arterioles	
4.3e	wt α-Ly6G: 10 mice APP/PS1 α-Ly6G: 10 mice APP/PS1 Iso-Ctr: 10 mice	Ordinary one-way ANOVA with post hoc using Tukey's multiple comparison correction to compare across groups, *p<0.05 Paired t-test to compare baseline and after treatment within a group, ++p<0.01 Each data point indicates a single mouse and lines connecting baseline and after measurements indicate the same animal.
4.4c, d, e	APP/PS1 Iso-Ctr: 10 mice APP/PS1 α-Ly6G: 10 mice wt α-Ly6G: 11 mice wt Iso-Ctr: 11 mice	Kruskal-Wallis one-way ANOVA with post-hoc using Dunn's multiple comparison correction to compare across groups, *p<0.05 and **p<0.01 Wilcoxon matched-pairs signed rank test relative to the baseline measurement to compare baseline and after treatment within a group, +p<0.05 and ++p<0.01
4.5a, b	Iso-Ctr: 6 mice	Mann-Whitney

	α-Ly6G: 7 mice	**p <0.01
4.6c		Error bars represent SD across for five independent simulations.

4.13 Supplementary movies

Movie S 4.1. Two-photon image stacks of fluorescently labeled blood vessels from APP/PS1 mice. Capillaries with stalled blood flow are indicated with red circles.

Movie S 4.2. Two-photon image stacks of fluorescently labeled blood vessels from wt mice. Capillaries with stalled blood flow are indicated with red circles.

Movie S 4.3. Two-photon image stacks of fluorescently-labeled blood vessels APP/PS1 mouse when anesthetized. Capillaries with stalled blood flow are indicated with red circles. Animal was anesthetized by breathing 1.5% isoflurane.

Movie S 4.4. Two-photon image stacks of fluorescently-labeled blood vessels from the same APP/PS1 mouse (Movie. S3) when awake. Capillaries with stalled blood flow are indicated with red circles.

REFERENCES

1 Wang, J., Gu, B. J., Masters, C. L. & Wang, Y. J. A systemic view of Alzheimer disease - insights from amyloid-beta metabolism beyond the brain. *Nature reviews. Neurology* **13**, 612-623, doi:10.1038/nrneurol.2017.111 (2017).

2 Santos, C. Y. *et al.* Pathophysiologic relationship between Alzheimer's disease, cerebrovascular disease, and cardiovascular risk: A review and synthesis. *Alzheimer's & dementia* **7**, 69-87, doi:10.1016/j.dadm.2017.01.005 (2017).

3 Iturria-Medina, Y. *et al.* Early role of vascular dysregulation on late-onset Alzheimer's disease based on multifactorial data-driven analysis. *Nature communications* **7**, 11934, doi:10.1038/ncomms11934 (2016).

4 Dai, W. *et al.* Mild cognitive impairment and alzheimer disease: patterns of altered cerebral blood flow at MR imaging. *Radiology* **250**, 856-866, doi:10.1148/radiol.2503080751 (2009).

5 Wolters, F. J. *et al.* Cerebral Perfusion and the Risk of Dementia: A Population-Based Study. *Circulation*, doi:10.1161/CIRCULATIONAHA.117.027448 (2017).

6 Wiesmann, M. *et al.* Hypertension, cerebrovascular impairment, and cognitive decline in aged AbetaPP/PS1 mice. *Theranostics* **7**, 1277-1289, doi:10.7150/thno.18509 (2017).

7 Li, H. *et al.* Vascular and parenchymal amyloid pathology in an Alzheimer disease knock-in mouse model: interplay with cerebral blood flow. *Molecular neurodegeneration* **9**, 28, doi:10.1186/1750-1326-9-28 (2014).

8 Niwa, K., Kazama, K., Younkin, S. G., Carlson, G. A. & Iadecola, C. Alterations in cerebral blood flow and glucose utilization in mice overexpressing the amyloid precursor protein. *Neurobiology of disease* **9**, 61-68, doi:10.1006/nbdi.2001.0460 (2002).

9 Niwa, K. *et al.* A beta-peptides enhance vasoconstriction in cerebral circulation. *American journal of physiology. Heart and circulatory physiology* **281**, H2417-2424 (2001).

10 Farkas, E. & Luiten, P. G. Cerebral microvascular pathology in aging and Alzheimer's disease. *Progress in neurobiology* **64**, 575-611 (2001).

11 Chen, Y. *et al.* Voxel-level comparison of arterial spin-labeled perfusion MRI and FDG-PET in Alzheimer disease. *Neurology* **77**, 1977-1985, doi:10.1212/WNL.0b013e31823a0ef7 (2011).

12 Royea, J., Zhang, L., Tong, X. K. & Hamel, E. Angiotensin IV Receptors Mediate the Cognitive and Cerebrovascular Benefits of Losartan in a Mouse Model of Alzheimer's Disease. *The Journal of neuroscience : the official journal of the Society for Neuroscience* **37**, 5562-5573, doi:10.1523/JNEUROSCI.0329-17.2017 (2017).

13 Marshall, R. S. *et al.* Recovery of brain function during induced cerebral hypoperfusion. *Brain : a journal of neurology* **124**, 1208-1217 (2001).

14 Wang, L. *et al.* Chronic cerebral hypoperfusion induces memory deficits and facilitates Abeta generation in C57BL/6J mice. *Experimental neurology* **283**, 353-364, doi:10.1016/j.expneurol.2016.07.006 (2016).

15 Hattori, Y. *et al.* Gradual Carotid Artery Stenosis in Mice Closely Replicates Hypoperfusive Vascular Dementia in Humans. *Journal of the American Heart Association* **5**, doi:10.1161/JAHA.115.002757 (2016).

16 Radde, R. *et al.* Abeta42-driven cerebral amyloidosis in transgenic mice reveals early and robust pathology. *EMBO reports* **7**, 940-946, doi:10.1038/sj.embor.7400784 (2006).

17 Chishti, M. A. *et al.* Early-onset amyloid deposition and cognitive deficits in transgenic mice expressing a double mutant form of amyloid precursor protein 695. *The Journal of biological chemistry* **276**, 21562-21570, doi:10.1074/jbc.M100710200 (2001).

18 Hasenberg, A. *et al.* Catchup: a mouse model for imaging-based tracking and modulation of neutrophil granulocytes. *Nature methods* **12**, 445-452, doi:10.1038/nmeth.3322 (2015).

19 Deane, R., Bell, R. D., Sagare, A. & Zlokovic, B. V. Clearance of amyloid-beta peptide across the blood-brain barrier: implication for therapies in Alzheimer's disease. *CNS & neurological disorders drug targets* **8**, 16-30 (2009).

20 Nishimura, N. *et al.* Targeted insult to subsurface cortical blood vessels using ultrashort laser pulses: three models of stroke. *Nature methods* **3**, 99-108, doi:10.1038/nmeth844 (2006).

21 Tsai, P. S. *et al.* Correlations of neuronal and microvascular densities in murine cortex revealed by direct counting and colocalization of nuclei and vessels. *The Journal of neuroscience : the official journal of the Society for Neuroscience* **29**, 14553-14570, doi:10.1523/JNEUROSCI.3287-09.2009 (2009).

22 Lauwers, F., Cassot, F., Lauwers-Cances, V., Puwanarajah, P. & Duvernoy, H. Morphometry of the human cerebral cortex microcirculation: general characteristics and space-related profiles. *NeuroImage* **39**, 936-948, doi:10.1016/j.neuroimage.2007.09.024 (2008).

23 Lorthois, S., Cassot, F. & Lauwers, F. Simulation study of brain blood flow regulation by intra-cortical arterioles in an anatomically accurate large human vascular network. Part II: flow variations induced by global or localized modifications of arteriolar diameters. *NeuroImage* **54**, 2840-2853, doi:10.1016/j.neuroimage.2010.10.040 (2011).

24 Roher, A. E. *et al.* Cerebral blood flow in Alzheimer's disease. *Vascular health and risk management* **8**, 599-611, doi:10.2147/VHRM.S34874 (2012).

25 Iadecola, C. The Neurovascular Unit Coming of Age: A Journey through Neurovascular Coupling in Health and Disease. *Neuron* **96**, 17-42, doi:10.1016/j.neuron.2017.07.030 (2017).

26 Park, L. *et al.* Nox2-derived radicals contribute to neurovascular and behavioral dysfunction in mice overexpressing the amyloid precursor protein. *Proceedings*

of the National Academy of Sciences of the United States of America **105**, 1347-1352, doi:10.1073/pnas.0711568105 (2008).

27 Park, L. *et al.* Innate immunity receptor CD36 promotes cerebral amyloid angiopathy. *Proceedings of the National Academy of Sciences of the United States of America* **110**, 3089-3094, doi:10.1073/pnas.1300021110 (2013).

28 Wang, J. X. *et al.* Ly6G ligation blocks recruitment of neutrophils via a beta2-integrin-dependent mechanism. *Blood* **120**, 1489-1498, doi:10.1182/blood-2012-01-404046 (2012).

29 Daley, J. M., Thomay, A. A., Connolly, M. D., Reichner, J. S. & Albina, J. E. Use of Ly6G-specific monoclonal antibody to deplete neutrophils in mice. *Journal of leukocyte biology* **83**, 64-70, doi:10.1189/jlb.0407247 (2008).

30 Lavkan, A. H., Astiz, M. E. & Rackow, E. C. Effects of proinflammatory cytokines and bacterial toxins on neutrophil rheologic properties. *Critical care medicine* **26**, 1677-1682 (1998).

31 Bennett, R. E. *et al.* Tau induces blood vessel abnormalities and angiogenesis-related gene expression in P301L transgenic mice and human Alzheimer's disease. *Proceedings of the National Academy of Sciences of the United States of America* **115**, E1289-E1298, doi:10.1073/pnas.1710329115 (2018).

32 Mohammad Haft-Javaherian, L. F., Victorine Muse, Chris B. Schaffer, Nozomi Nishimura, Mert R. Sabuncu. *Deep convolutional neural networks for segmenting 3D in vivo multiphoton images of vasculature in Alzheimer disease mouse models. arXiv preprint arXiv:1801.00880* (2018).

33 Villringer, A. *et al.* Imaging of leukocytes within the rat brain cortex in vivo. *Microvascular research* **42**, 305-315 (1991).

34 Ishikawa, M. *et al.* Leukocyte plugging and cortical capillary flow after subarachnoid hemorrhage. *Acta neurochirurgica* **158**, 1057-1067, doi:10.1007/s00701-016-2792-6 (2016).

35 Kloner, R. A. No-reflow phenomenon: maintaining vascular integrity. *Journal of cardiovascular pharmacology and therapeutics* **16**, 244-250, doi:10.1177/1074248411405990 (2011).

36 Engler, R. L., Schmid-Schonbein, G. W. & Pavelec, R. S. Leukocyte capillary plugging in myocardial ischemia and reperfusion in the dog. *The American journal of pathology* **111**, 98-111 (1983).

37 Chibber, R., Ben-Mahmud, B. M., Chibber, S. & Kohner, E. M. Leukocytes in diabetic retinopathy. *Current diabetes reviews* **3**, 3-14 (2007).

38 Santisakultarm, T. P. *et al.* Stalled cerebral capillary blood flow in mouse models of essential thrombocythemia and polycythemia vera revealed by in vivo two-photon imaging. *Journal of thrombosis and haemostasis : JTH* **12**, 2120-2130, doi:10.1111/jth.12738 (2014).

39 Ilesanmi, O. O. Pathological basis of symptoms and crises in sickle cell disorder: implications for counseling and psychotherapy. *Hematology reports* **2**, e2, doi:10.4081/hr.2010.e2 (2010).

40 Zuliani, G. *et al.* Markers of endothelial dysfunction in older subjects with late onset Alzheimer's disease or vascular dementia. *Journal of the neurological sciences* **272**, 164-170, doi:10.1016/j.jns.2008.05.020 (2008).

41 Iadecola, C. Vascular and Metabolic Factors in Alzheimer's Disease and Related Dementias: Introduction. *Cellular and molecular neurobiology* **36**, 151-154, doi:10.1007/s10571-015-0319-y (2016).

42 Zenaro, E. *et al.* Neutrophils promote Alzheimer's disease-like pathology and cognitive decline via LFA-1 integrin. *Nature medicine* **21**, 880-886, doi:10.1038/nm.3913 (2015).

43 Goldsmith, H. S. Alzheimer's disease can be treated: Why the delay? *Surgical neurology international* **8**, 133, doi:10.4103/sni.sni_116_17 (2017).

44 Blinder, P. *et al.* The cortical angiome: an interconnected vascular network with noncolumnar patterns of blood flow. *Nature neuroscience* **16**, 889-897, doi:10.1038/nn.3426 (2013).

45 Jankowsky, J. L. *et al.* Mutant presenilins specifically elevate the levels of the 42 residue beta-amyloid peptide in vivo: evidence for augmentation of a 42-specific gamma secretase. *Human molecular genetics* **13**, 159-170, doi:10.1093/hmg/ddh019 (2004).

46 Oakley, H. *et al.* Intraneuronal beta-amyloid aggregates, neurodegeneration, and neuron loss in transgenic mice with five familial Alzheimer's disease mutations: potential factors in amyloid plaque formation. *The Journal of neuroscience : the official journal of the Society for Neuroscience* **26**, 10129-10140, doi:10.1523/JNEUROSCI.1202-06.2006 (2006).

47 Klunk, W. E. *et al.* Imaging Abeta plaques in living transgenic mice with multiphoton microscopy and methoxy-X04, a systemically administered Congo red derivative. *Journal of neuropathology and experimental neurology* **61**, 797-805 (2002).

48 Pologruto, T. A., Sabatini, B. L. & Svoboda, K. ScanImage: flexible software for operating laser scanning microscopes. *Biomedical engineering online* **2**, 13, doi:10.1186/1475-925X-2-13 (2003).

49 Dombeck, D. A., Khabbaz, A. N., Collman, F., Adelman, T. L. & Tank, D. W. Imaging large-scale neural activity with cellular resolution in awake, mobile mice. *Neuron* **56**, 43-57, doi:10.1016/j.neuron.2007.08.003 (2007).

50 Dijkstra, E. W. A note on two problems in connexion with graphs. *Numerische Mathematik* **Volume 1**, pp 269–271, doi:doi:10.1007/BF01386390 (1959).

51 Otsu, N. A threshold selection method from gray-level histogram. *IEEE Trans. Syst. Man Cybern.* **vol. 9**, pp. 62-66, doi:10.1109/TSMC.1979.4310076 (1979).

52 Lim, J. Two-Dimensional Signal and Image Processing. *NJ, Englewood Cliffs:Prentice Hall* (1990).

53 Santisakultarm, T. P. *et al.* In vivo two-photon excited fluorescence microscopy reveals cardiac- and respiration-dependent pulsatile blood flow in cortical blood vessels in mice. *American journal of physiology. Heart and circulatory physiology* **302**, H1367-1377, doi:10.1152/ajpheart.00417.2011 (2012).

54 Paxinos, G. & Franklin, K. The mouse brain in stereotaxic coordinate. *Elsevier Academic Press* (2004).

55 Kim, S. G. Quantification of relative cerebral blood flow change by flow-sensitive alternating inversion recovery (FAIR) technique: application to functional mapping. *Magnetic resonance in medicine* **34**, 293-301 (1995).

56 Herscovitch, P. & Raichle, M. E. What is the correct value for the brain--blood partition coefficient for water? *Journal of cerebral blood flow and metabolism : official journal of the International Society of Cerebral Blood Flow and Metabolism* **5**, 65-69, doi:10.1038/jcbfm.1985.9 (1985).

57 Kober, F. *et al.* High-resolution myocardial perfusion mapping in small animals in vivo by spin-labeling gradient-echo imaging. *Magnetic resonance in medicine* **51**, 62-67, doi:10.1002/mrm.10676 (2004).

58 Dunn, A. K. Laser speckle contrast imaging of cerebral blood flow. *Annals of biomedical engineering* **40**, 367-377, doi:10.1007/s10439-011-0469-0 (2012).

59 Kazmi, S. M., Parthasarthy, A. B., Song, N. E., Jones, T. A. & Dunn, A. K. Chronic imaging of cortical blood flow using Multi-Exposure Speckle Imaging. *Journal of cerebral blood flow and metabolism : official journal of the International Society of Cerebral Blood Flow and Metabolism* **33**, 798-808, doi:10.1038/jcbfm.2013.57 (2013).

60 Taylor, Z. J. *et al.* Microvascular basis for growth of small infarcts following occlusion of single penetrating arterioles in mouse cortex. *Journal of cerebral blood flow and metabolism : official journal of the International Society of Cerebral Blood Flow and Metabolism* **36**, 1357-1373, doi:10.1177/0271678X15608388 (2016).

61 Cassot, F., Lauwers, F., Fouard, C., Prohaska, S. & Lauwers-Cances, V. A novel three-dimensional computer-assisted method for a quantitative study of microvascular networks of the human cerebral cortex. *Microcirculation* **13**, 1-18, doi:10.1080/10739680500383407 (2006).

62 Duvernoy, H. M., Delon, S. & Vannson, J. L. Cortical blood vessels of the human brain. *Brain research bulletin* **7**, 519-579 (1981).

63 Reina-De La Torre, F., Rodriguez-Baeza, A. & Sahuquillo-Barris, J. Morphological characteristics and distribution pattern of the arterial vessels in human cerebral cortex: a scanning electron microscope study. *The Anatomical record* **251**, 87-96 (1998).

64 Pries, A. R., Secomb, T. W., Gaehtgens, P. & Gross, J. F. Blood flow in microvascular networks. Experiments and simulation. *Circulation research* **67**, 826-834 (1990).

65 Pries, A. R., Secomb, T. W. & Gaehtgens, P. Biophysical aspects of blood flow in the microvasculature. *Cardiovascular research* **32**, 654-667 (1996).

66 Pries, A. R., Reglin, B. & Secomb, T. W. Structural response of microcirculatory networks to changes in demand: information transfer by shear stress. *American journal of physiology. Heart and circulatory physiology* **284**, H2204-2212, doi:10.1152/ajpheart.00757.2002 (2003).

67 Roman, S., Merlo, A., Duru, P., Risso, F. & Lorthois, S. Going beyond 20 mum-sized channels for studying red blood cell phase separation in microfluidic bifurcations. *Biomicrofluidics* **10**, 034103, doi:10.1063/1.4948955 (2016).

68 Bragin, D. E., Bush, R. C., Muller, W. S. & Nemoto, E. M. High intracranial pressure effects on cerebral cortical microvascular flow in rats. *Journal of neurotrauma* **28**, 775-785, doi:10.1089/neu.2010.1692 (2011).

69 Schmid, F., Tsai, P. S., Kleinfeld, D., Jenny, P. & Weber, B. Depth-dependent flow and pressure characteristics in cortical microvascular networks. *PLoS computational biology* **13**, e1005392, doi:10.1371/journal.pcbi.1005392 (2017).

70 Team, R. C. R: A language and environment for statistical computing. R Foundation for Statistical Computing. (2013).

71 Brown, W. R. & Thore, C. R. Review: cerebral microvascular pathology in ageing and neurodegeneration. *Neuropathology and applied neurobiology* **37**, 56-74, doi:10.1111/j.1365-2990.2010.01139.x (2011).

CHAPTER 5

APPLICATION OF CROWDSOURCING CITIZEN SCIENCE IN STUDYING BRAIN CAPILLARIES IN ALZHEIMER'S DISEASE

5.1 Introduction

Alzheimer's disease (AD), the leading cause of dementia in the elderly, is known to be caused by the aggregates of amyloid beta proteins and neurofibrillary tangles in the brain. Since the cerebrovascular dysregulation is a feature of neurodegenerative diseases (Iadecola, 2004), we are interested in studying the interaction between brain microvasculature dysfunction and AD. Recently, we observed a significantly increased rate of spontaneous transient capillary stalls in the cortical microvasculature of AD mice compared to wild-type littermates, which is correlated with the brain blood flow reduction seen in these mouse models of APP overexpression (Cruz Hernández et al., 2019). This study similar to other research projects that investigate the interaction between brain blood flow and neurodegenerative diseases depends heavily on both imaging techniques such as multiphoton microscopy and fMRI and image analysis methods such as registration, segmentation, and blood flow stalling detection (Bennett et al., 2018; Cruz Hernández et al., 2019; T. P. Santisakultarm et al., 2014; Thom P. Santisakultarm et al., 2012).

The brain vasculature network imaging and blood flow measurements can be done by *in vivo* two-photon excited fluorescence (2PEF) microscopy (Kleinfeld, Mitra,

Helmchen, & Denk, 1998; Thom P. Santisakultarm et al., 2012), which allows us to map the architecture of the vasculature throughout the top 500 μm of the mouse cortex, as well as measure the blood flow velocity in individual vessels. Briefly, the blood plasma of an anesthetized mouse is fluorescently labeled. A low-energy femtosecond laser pulse is tightly focused, through a craniotomy, into the cortex of the mouse. There is no linear absorption at the laser wavelength by the dye, so fluorescence is produced only at the focus, where the laser intensity is high enough to excite the dye through the two-photon absorption process. The fluorescence intensity is then recorded while the position of the laser focus is scanned throughout the brain, providing a three-dimensional image of the vasculature (Denk, Strickler, & Webb, 1990). To determine the flow velocity in individual vessels based on the fact that the dye labels only the blood plasma, the motion of the non-fluorescent red blood cells can be determined by tracking the dark patches produced in the 2PEF image (Kleinfeld et al., 1998).

The acquired brain vasculature network images and blood flow measurements require various image analyses to quantitatively measure different geometrical and topological metrics in order to examine the proposed scientific hypothesis. For instance, our stalled capillary research study requires two main image processing tasks of 3D vessel segmentation and stalled vs. flowing capillary classification to identify each capillary with end points, centerline, and a unique identifier because we accumulate the data from multiple people for each vessel. Since manual image analysis tasks including both segmentation and classification are time-consuming and become bottleneck processes, researchers pursued different automated or semi-automated techniques to tackle this

problem. Alternatively, researchers tried to combine computational power and human wisdom through a process called “citizen science”.

Citizen science is a mechanism in which citizens are participating alongside the professional scientists in different aspects of scientific research projects (e.g. crowdsourcing projects) such as environmental DNA data collection (Biggs et al., 2015), avian biological pattern monitoring (Sullivan et al., 2009), and interstellar dust particle detection (Westphal et al., 2014), and medical image analysis (Heim et al., 2018). Every year, more than 2 million volunteers participate in thousands of crowdsourcing projects around the world with an estimated value of $2.5B for their time investment (Theobald et al., 2015). Without the power of the crowd, the scientific community cannot tackle these research questions due to logistical and financial limitations (Bird et al., 2014).

The “EyesOnALZ” initiative (involves Human Computation Institute, Cornell University, University of California at Berkeley, and Princeton University) proposed to use citizen science for both two main image processing tasks required for our stalled capillary research study (3D vessel segmentation and stalled vs. flowing capillary classification).

Our proposed method for stalled vs. flowing capillary classifications starts with utilizing the acquired segmentation results to create image samples that each one outlines a particular vessel segment in the image and then, citizen scientists classify each vessel segment as a stalled or flowing capillary. This method was inspired by “Stardust@home”, a citizen science project developed by the Space Sciences Laboratory at U. C. Berkeley,

that analyzes samples collected by the Stardust spacecraft to detect interstellar dust particles (Westphal et al., 2014).

In this chapter, we describe the manual solutions developed by Schaffer-Nishimura labs for these image segmentation and classification tasks prior to EyesOnALZ initiative. Then, we discuss the complete pipeline including automated image segmentation and StallCatchers samples generation. In addition, we present a study on the StallCatchers' performance and methodology validation based on the collected data. Finally, we present the results of a novel study produced by StallCatchers and conclude the chapter with the discussions of the StallCatchers' powers and limitations to discuss the possibility of its adaptation by other researchers.

5.2 Method

5.2.1 General pipeline

Based on the StallCathers' crowdsourcing design, each player at each round of the game receives a 3D image stack that encompasses a particular vessel to target for the classification task between flowing vs. stalled. Users view the acquired 3D images through movies that show one plane at a time. Since vessels have different 3D orientation and many vessels are visible in an image stack, we need to indicate the targeted vessel segment to the user. Therefore, we need to identify each vessel segment within the 3D image stack and generate a movie that encompasses a particular targeted segment and includes a visual indicator to the segment for the user. A database is generated to save the

information about the generated movies for all vessel segments identified in each image stack.

Each particular vessel is assigned to several players to score and their results are aggregated to form the crowd answer. The StallCatchers pipeline (Figure 5.1) starts with the imaging of a mouse brain using the multiphoton microscopy and followed by the vessel segmentation and the centerline detection as well as the single vessel movie generation. The pipeline is concluded by the user task assignment and the crowd result aggregation. In this section, we elaborate on each step of this pipeline and the rationale for the approaches in detail.

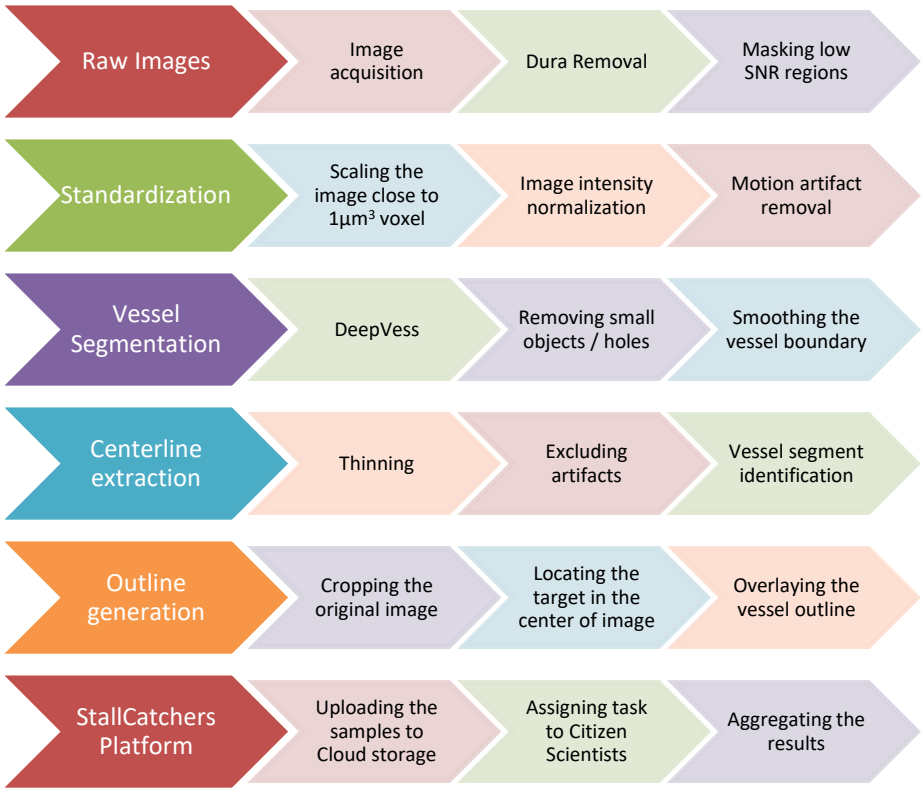

Figure 5.1. StallCatchers complete pipeline. Each row represents one of the objectives (first column) and processes required to achieve it (other columns).

5.2.2 Manual tracing and scoring

We developed an in-house software package (Cruz Hernández et al., 2019) to facilitate the image analysis of *in vivo* multiphoton microscopy images of brain vasculature networks. Furthermore, this tool was adopted for the StallCatchers' validation study. Researchers load the 3D images and start with inserting a node at the location of vessel bifurcations or the end of the vessel segments. Next, the vessel centerlines can be drawn as a set of 3D center points between two vessel ends. Finally, each vessel is classified as one of the defined vessel classes (i.e. surface venule, surface arteriole, ascending venule, penetrating arteriole, flowing capillary, or stalled capillary). The final graph representation of the vasculature network within the image is saved in an XML file including the properties of all node' and edges.

5.2.3 DeepVess

The manual tracing of brain vasculature network in a 3D image stack can take 20-30 hours, depend on the researchers' experience level. In order to remove this bottleneck, we developed a convolutional neural network model, called *DeepVess* (Haft-Javaherian et al., 2018), that performs the whole segmentation task automatically. In brief, DeepVess is a convolutional neural network with optimized architecture that uses a greedy search over each subgroup of the hyperparameters in addition to a new customized loss function to tackle the fact that the segmentation labels are highly unbalanced (i.e. vessels are within than 10% of the imaged brain volume). DeepVess consists of preprocessing, segmentation, and postprocessing. DeepVess' preprocessing includes splitting the image channels, resizing the image close to 1 μm^3 voxel, image intensity normalization, and

motion artifact removal. DeepVess' postprocessing includes removing of small objects and holes, smoothing vessel boundaries, and automatic vessel centerline extraction. Small vessels connected to the boundary of the image were excluded from the analysis due to lack of information for the classification.

The centerline extraction task is a challenging and essential task, which removes centerline artifacts such as hairs (i.e. tiny vessels with one end not connected to any vessels caused by noise bulge at vessel boundaries). Since images includes regions outside the brain (the dura) which have highly fluorescent structures that are not vessels, the slices captured outside the brain require manual rejection. Similarly, parts of the images need to be manually masked and excluded from the analysis pipeline when the signal-to-noise ratio (SNR) drops intensely due to light scattering caused by big vessel optical obstructions or highly inflamed tissues in the disease animal models.

5.2.4 Vessel outlines and movie presentation for the StallCatchers user

At each round of the game, each player examines a movie for a particular vessel, which is part of a 3D image stack with indications to the targeted vessel segment by showing one plane at a time. The movie generation step utilizes the segmentation and centerline information to generate movies for each identified vessel segment. A movie for each vessel segment was generated from sub-volume of the original image stack with a fixed aspect ratio and variable depth in z. The target vessel was located as close as possible to the centroid with some margin proportional to the vessel diameter, which is measure using the segmentation results along the vessel centerline. Infrequently, the original images were rotated 90 degrees or resized to obtain a better view of the vessel.

The displayed image intensity within the cropped box was normalized to utilize the entire available intensity range. Feedback from trained users suggests that contrast and saturation are critical in the ability to discriminate red blood cell motion. In our laboratory, users adjust the image contrast for each image stack independently and dynamically, but we made the decision to simplify the game delivery and choose a fixed contrast range determined by an internal multi-case multi-reader survey.

The single channel 3D image is then converted to a 3-channel RGB image. Based on the vessel centerline and diameter an outline was overlaid on the image to annotate the target vessel (Figure 5.2). Initially, the outline hue was set to the green similar to the Stardust@home design. Six months after the public lunch in October, we received negative feedback from citizen scientists on the green hue. Subsequently, we did an external and internal multi-case multi-reader study to set an optimum hue, saturation and lightness that resulted in the selection of blaze orange (24° hue, 100% saturation, and 50% lightness).

In the same way, the shape of the outline was optimized with an internal multi-case multi-reader study and was selected to meet the UI/UX design criteria of minimal user distraction caused by static annotation in the movie compare to other dynamic annotations. To annotate the target vessel with the circular cross-sectional pipes along the projection of vessels in 2D, the vessel centerline was projected into the x-y plane, two mathematical dilation morphological operations with disk structuring elements were applied to the projected centerline independently. The first disk structuring element has a fixed radius and the second disk structuring element has a radius equal to the radius of

the first disk added to a fixed value as the outline thickness. The logical operation of exclusive disjunction applied to these two dilated centerlines generates the final outcome. Next, a median filter was applied to smooth the outline and the results were overlaid on the original images in RGB format.

Finally, A unique 128-bit immutable universally unique identifier (UUID) was assigned to each vessel and all the information about the vessel geometry and movie generation steps added to a metadata record. The metadata for each particular vessel includes the vessel's UUID, the imaged animal ID, the image stack ID, the image intensity ranges based on the intensity normalization, the vessel centroid coordinate, the coordinate of the movie within the original image stack, the original size of the movie, and the rotation of the movie. Finally, the movie was saved either as a sequence of JPEG images, multi-page TIFF file, and/or MP4 movies.

5.2.5 Amazon AWS & Microsoft Azure

Later in the project, we expedited the image analysis process by utilizing the NC series virtual machines on the Microsoft Azure cloud service. The generated vessel samples in Microsoft Azure were transferred to Amazon AWS S3 storage shared between Stardust@home and StallCatchers projects. Finally, the StallCatchers frontend and backend was redeveloped using PHP and MySQL. Since 2016, the entire StallCatchers' pipeline has been optimized for higher accuracy and performance continuously.

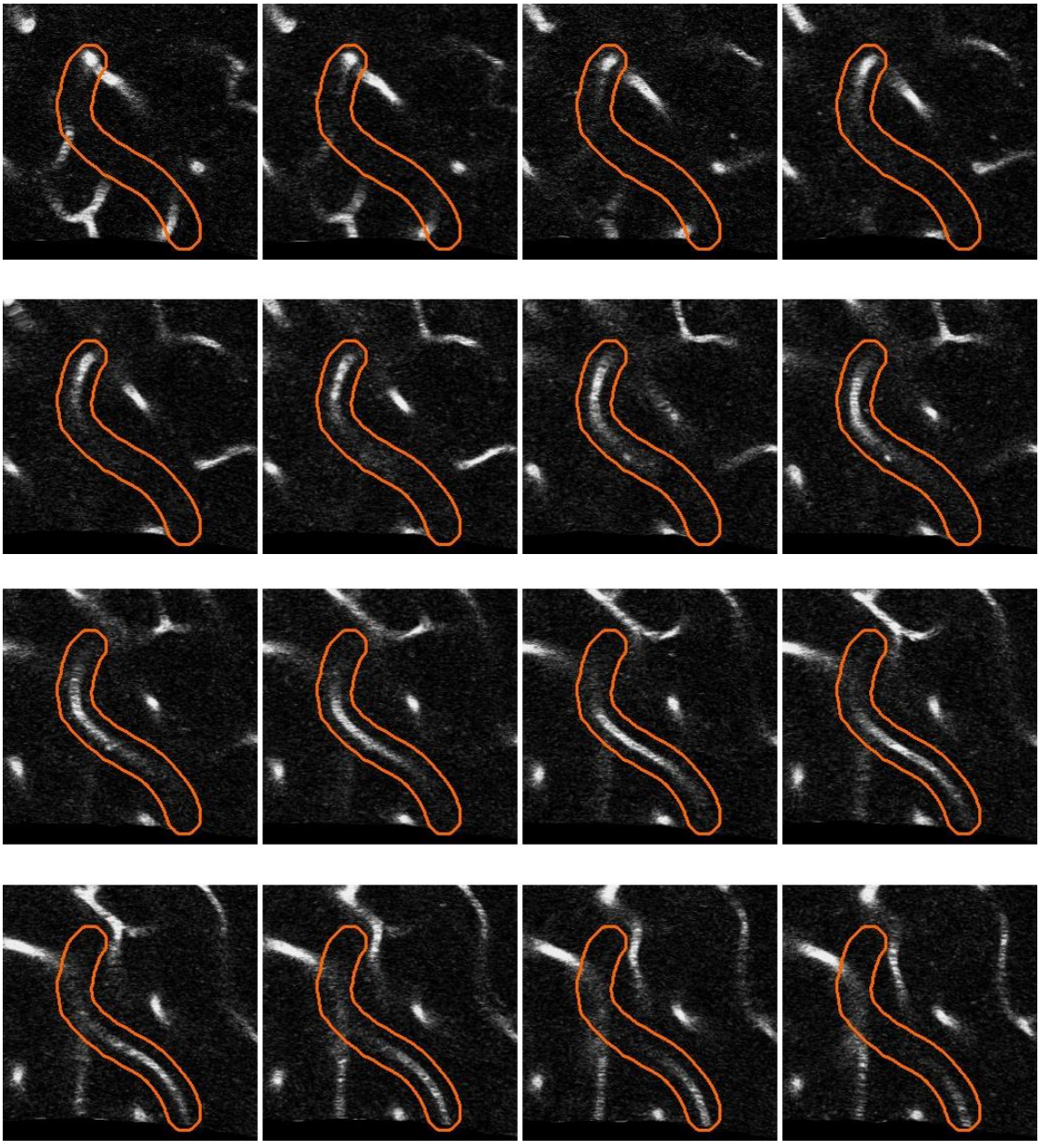

Figure 5.2. Example of frames from a StallCatchers movie showing a vessel that traverses along the third dimension.

The movie starts at the top left frame and finishes at the bottom right frame, with the images going gradually deeper into the brain.

5.3 Results and discussions

5.3.1 Alpha test Discussions

StallCatchers was launched publicly in October 2016. Prior to the public lunch, the Alpha test was performed in September 2019 with contributions from several communities such as biomedical researchers, Cornell University Alzheimer's Help and Awareness Club, and other Alzheimer's disease advocates who already have been involved in this project since 2015. For the Alpha test, we prepared a calibration dataset with 133 capillaries (100 flowing and 33 stalled capillaries) to be used for the training and the user calibration process during the game. These 133 capillaries are sampled from a few datasets due to the low incident rate of capillary stalling. Furthermore, a dataset with 1000 capillaries (750 flowing and 250 stalled capillaries) was prepared as the validation dataset. All flowing capillary were extracted from datasets based on the study done by Cruz Hernández et al. (Cruz Hernández et al., 2019). In contrast, since only a small fraction of vessels are stalled in that study, additional image data from stalled vessels were added from other studies (T. P. Santisakultarm et al., 2014; Thom P. Santisakultarm et al., 2012). An expert reconfirmed all the capillaries' stalled vs. flowing classification.

The alpha test had a two-fold goal: the user interface/experience design (UI/UX) feedback and hyperparameter optimization for crowd data aggregation algorithm. Crowd results can be aggregated using a weighted average with associating a weight to each user base on "d prime" (Eq. (1), as a user accuracy metric, where Z is the inverse of the cumulative distribution function of Gaussian distribution (Raykar et al., 2009).

$$d' = Z_{hit\ rate} - Z_{false\ alarm\ rate} \quad (1)$$

Based on the results of the Alpha test (Figure 5.3) and the StallCatchers' design criteria of 95% sensitivity, 20 annotations per vessel is required for each vessel.

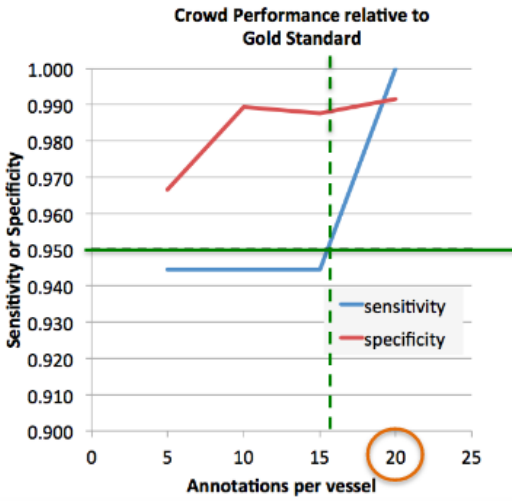

Figure 5.3. Alpha test results for the different numbers of annotations per vessel.
For the StallCatchers' design criteria of 95% sensitivity, 20 annotators per vessel are required.

On the other hand, the measured users' d prime can be utilized for task completion determination. The cumulative sum of the d prime of the users who classified a particular vessel is a good indicator of the task completion. We defined an empirical threshold to determine the task completion based on the for the cumulative sum of the d prime.

5.3.2 Validation Study

After the public launch, the first dataset for validation of Alpha test findings was prepared and uploaded to StallCatchers. This dataset, called *plaque proximity dataset*,

served two purposes: the validation of Alpha test findings and the investigation of the scientific question whether the amyloid beta plaque density in the vessel vicinity is correlated with stalled capillary phenomena. Internally, we used our in-house manual tracing and scoring software package to locate the vessel segments and classify them as stalled or flowing. Independently, the detected stalled vessels by StallCatchers were reconfirmed by an expert to determine the final StallCatchers result. Based on our internal results and StallCatchers' results as the confirmation, we concluded there is no significant difference in terms of plaque density in the vessel vicinity and the occurrence of capillary stalling (Cruz Hernández et al., 2019). Additionally, after conducting the analysis, we used this dataset for the future crowd aggregation algorithm development. The centerline in this dataset was extracted and all the vessels were classified manually to generate the ground truth for this dataset.

After the reinvestigation of the crowd aggregation method parameters with this larger dataset compare to the Alpha test, we concluded that 7 annotations per vessels are required to obtain the StallCatchers' design criteria of 95% sensitivity (Figure 5.4). The new criterion increases the StallCatchers throughput rate by 3-fold. We incorporated all UI/UX feedbacks and developed the second generation of StallCatchers (Figure 5.5).

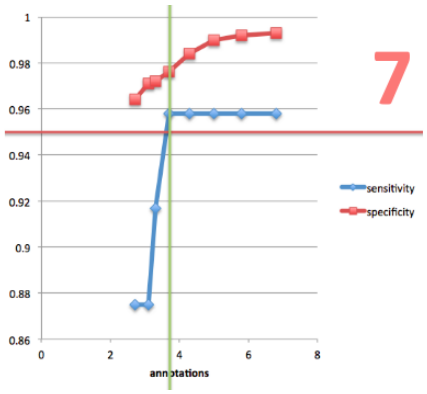

Figure 5.4. Validation study results for the different numbers of annotations per vessel based on the plaque proximity dataset.

For the StallCatchers' design criteria of 95% sensitivity, 7 annotators per vessel are required, which is a 3-fold improvement compare to Alpha test's results.

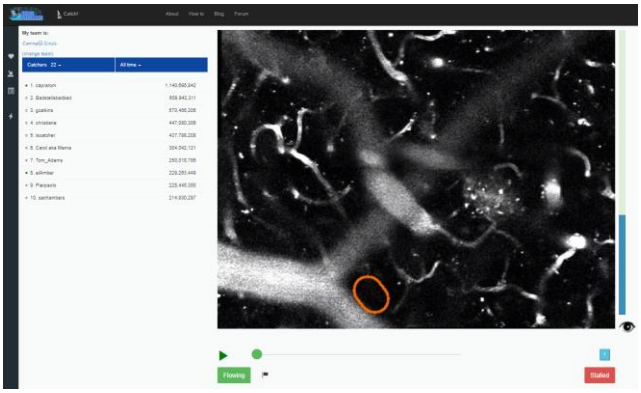

Figure 5.5. StallCatchers current user interface.

UI includes the virtual microscope with a sliding bar for moving through the movie and decision buttons in addition to the leaderboard.

5.3.3 High Fat Project

The first study that utilized the complete StallCatchers pipeline investigated the effect of high-fat diet (HFD) and AD on the capillary stalls. Obesity is correlated with

severe dementia and AD (Cova et al., 2016). For instance, late-life dementia can be correlated in a dose-dependent manner to cardiovascular-risk factors such as diabetes, smoking, hypertension, and high cholesterol (Alosco et al., 2012). To answer this question, we studied the correlation between stall capillary phenomenon and HFD in AD and wild type mice. AD mice and WT mice were fed a western HFD or a control diet for 11 months (6 mice per group, total of 24 mice) and then their brain vasculature was imaged using in vivo multiphoton microscopy and the capillary stalling rate was measured using StallCatchers. An expert reviewed the capillaries detected as stalled by StallCatchers with high probability after the data collection to reconfirm the results. As shown in Figure 5.6, this dataset suffers from poor image quality and low SNR compared to data in the previous StallCatchers testing and in the calibration data. This is a common phenomenon observed in the data of studies, which are dealing with mouse models with different diseases.

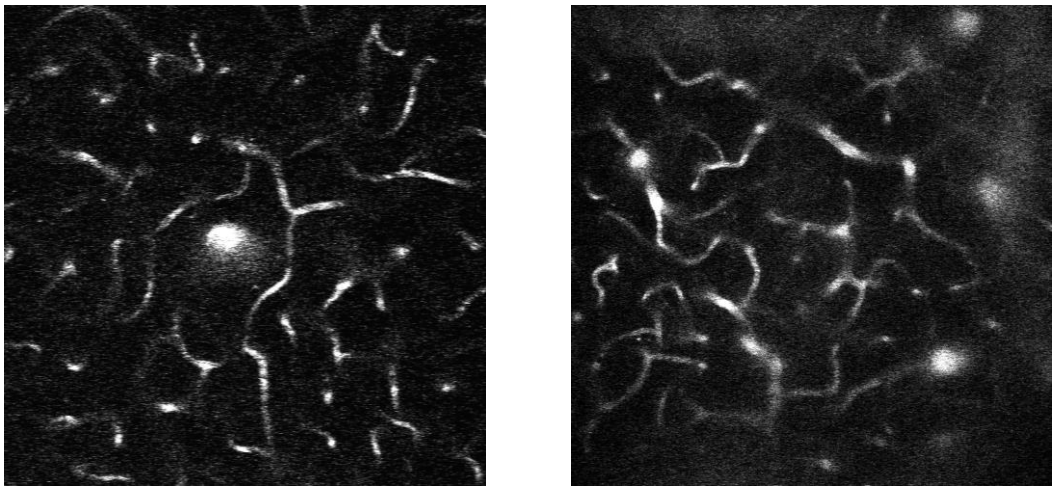

(A) (B)

Figure 5.6. Comparison of image quality between a normal (A) and an HFD image stack (B).

Due to inflammation caused by AD and/or HFD, images suffer from poor image quality and low SNR.

5.3.4 Post-hoc expert stall reconfirmation

Since the occurrence probability of capillary stalling is less than 0.5% and 2% in WT and APP/PS1 AD mouse models, the false positive rate can be reduced significantly using the second-round quality control of positive detection by researchers with a reasonable time cost. On the other hand, identifying false negatives are not tractable even with the second-round quality control due to the very large number of negative results.

5.3.5 Power of StallCatchers

The stalled vs. flowing capillary classification is a challenging task and time-consuming. Currently, there is no fully automated computer algorithm that can perform this task with an acceptable accuracy to eliminate the need for the manual classification. StallCatchers enables us to perform this classification task ~30 times faster compared to the traditional time-consuming manual classification, which delays the scientific research progress, with up to 30 times faster.

5.3.6 Different stall-rate metrics

The stalled capillary phenomenon can be characterized using different metrics depending on the stall detection methodology. The first category of the detection methods is based on examining the whole complete 3D image stack while scrolling through slices and the evaluator is not directed to check every vessel. This category has two variants. The image can be examined using the raw acquired image or it can be examined after overlaying the vessel centerlines on the image. Note that the vessel centerline also can be extracted manually or automatically using DeepVess. The second category of the detection methods is based on examining a sub-volume of the original 3D image stack with annotation identifying the targeted vessel. This category also has two variants. The examination can be done manually by an expert or it can be done using StallCatchers followed by manually reconfirmation of the vessel classification for vessels with high stalling probability.

On the other hand, the stall rate can be measured in two ways. The total number of stalled vessels can be normalized by the total number of vessels in the image or by total number slices in the image stack depending on the availability of the total number of vessels in the image.

5.3.7 Comparison between StallCatchers and human manual classifications

Concerned that the difference in image quality could compromise results, we selected 4 mice from the HFD project with ~5000 vessels total to perform vessel-by-vessel accuracy comparisons between StallCatchers and expert manual classifications in addition to the inter-reader and reader vs. panel accuracies. Two trained researchers reviewed the vessel movies generated by StallCatchers pipeline one-by-one and marked 144 vessels as stalled capillary candidates. First, one expert examined the candidates and then independently, a panel of experts met and examined the same candidates together. We used absolute mean difference (AMD), which is the absolute difference total number of detected stalled vessels divided by the arithmetic mean, as the accuracy metric. Note that a lower AMD value shows higher agreement between two measurements with AMD value of 0 means complete agreement. Additionally, we ran these vessels through StallCatchers and an expert reviewed top 6% of vessels in terms of stalling probability. StallCatchers and the panel agreed better with the AMD value of 0.06, than StallCatchers and the expert or StallCatchers and the manual classification with the AMD values of 0.29 and 0.25, respectively.

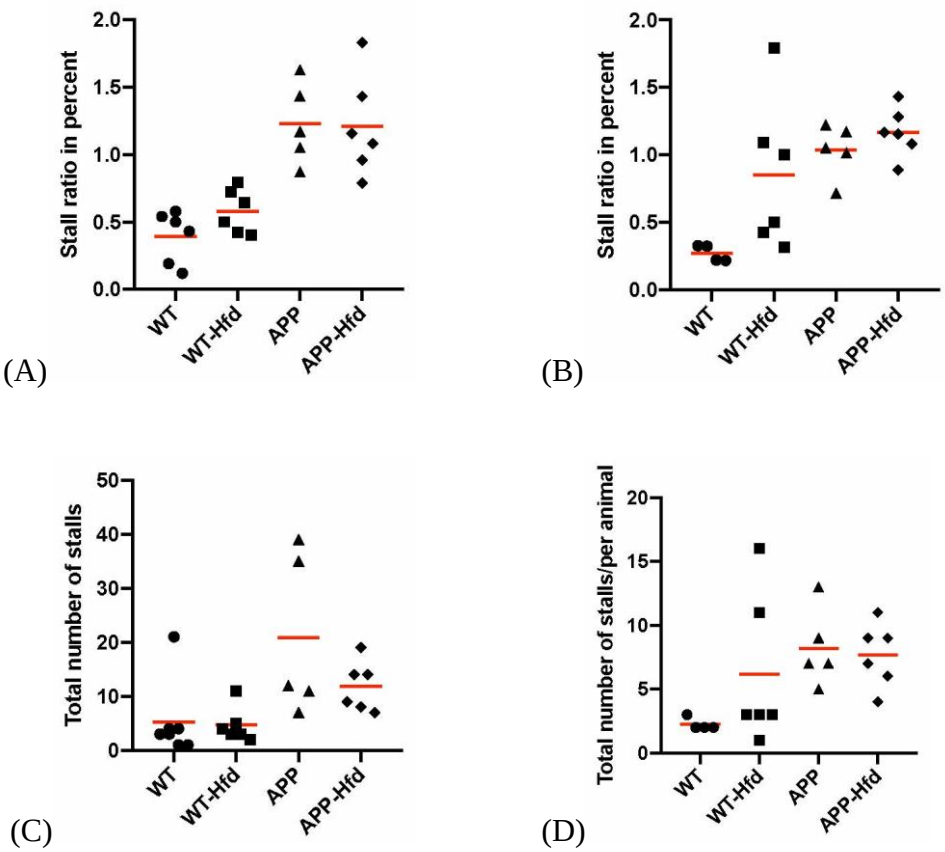

Figure 5.7. The stalled capillary phenomenon in AD and HFD.

The percentage (A, B) or total number (C, D) of capillary stalls in wildtype and AD mice with 11 months HFD or control diet based on StallCatchers' results with post hoc expert reconfirmation (A, C) or manual detection of stalls in the raw 3D images (B, D). Each data point represents an averaged value of four 3D image stacks acquired from an animal. The manual ratio is the total number of stalls divided by the total number of image slices and the StallCatchers ratio is the total number of stalls divided by the total number of detected vessels in the image.

(A)

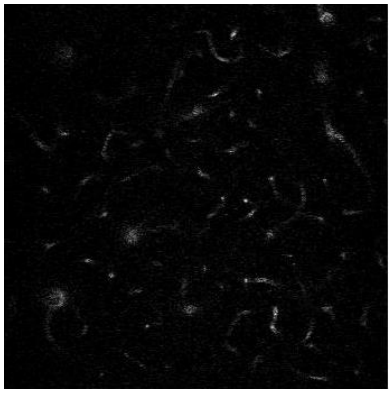

(B)

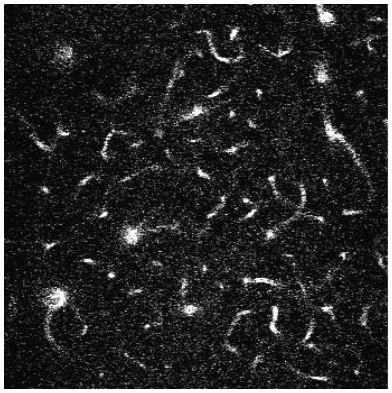

(C)

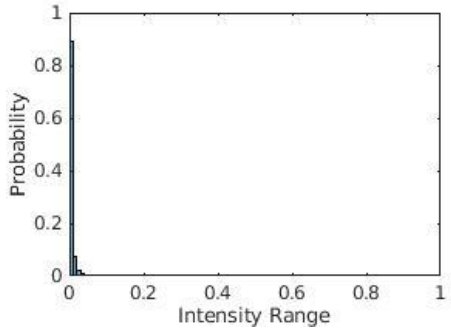
Probability
Intensity Range
0
0.2
0.4
0.6
0.8
1

(D)

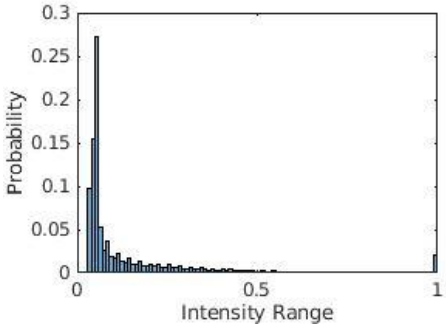
Probability
Intensity Range
0
0.05
0.1
0.15
0.2
0.25
0.3
0.5
1

(E)

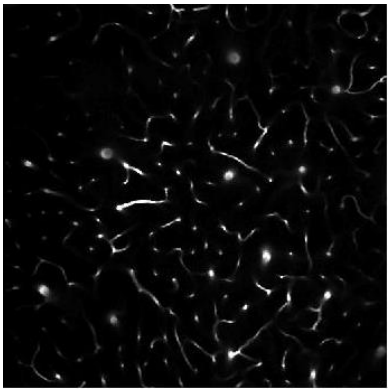

(F)

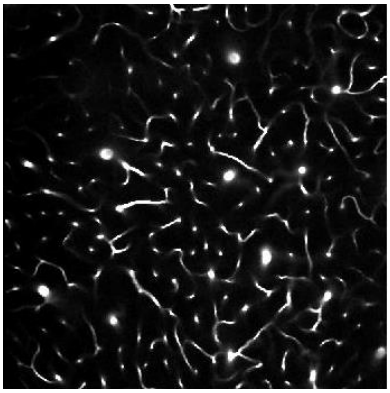

(G)

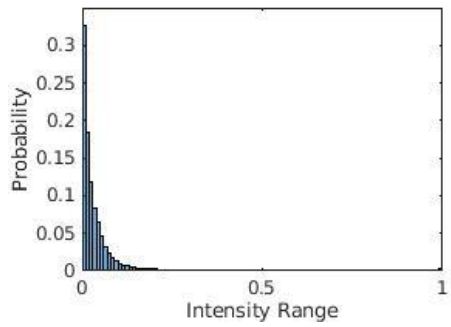
Probability
Intensity Range
0
0.05
0.1
0.15
0.2
0.25
0.3
0.5
1

(H)

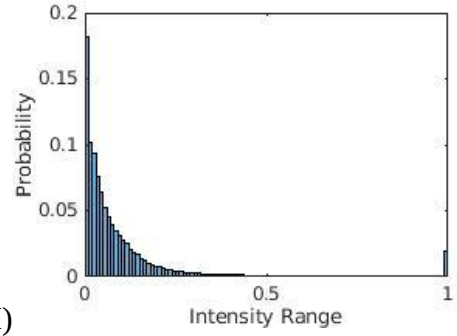
Probability
Intensity Range
0
0.05
0.1
0.15
0.2
0.5
1

Figure 5.8. Image Intensity normalization for two different datasets.

SN Lab (A-D) and Boas Lab (E-H), before (A, C, E, G) and after (B, D, F, H) intensity normalization illustrated as the grayscale image (A-B, E-F) and image intensity histogram (C-D, G-H).

5.3.8 HFD results

We also compared the results between a trained user evaluating full stacks and the StallCatchers result. An expert looks at the raw 3D images and identified the stalled vessels. Alternatively, an expert reviewed the stalled vessels detected by StallCatchers with high probability and reconfirmed the results similar to the previous section. The results of this study (shown in Figure 5.7) suggests HFD increases stall rates but does not have a synergistic effect with AD.

5.3.9 Exceptional dataset

A new dataset from an independent laboratory (Boas Lab, Boston University) was acquired to study the generalization of the preprocessing steps to images acquired using different microscopes and acquisition settings. These data had differences from previous used data in terms of the different levels of noise, the pixel size, and the frame rate.

In order to utilize the current pipeline, the only hyperparameter of DeepVess that required fine-tuning was the image intensity normalization percentile used for the standardization. Typically, most of the intensity range can be utilized by performing 1% saturation at the two ends of the intensity range. In contrast, the new dataset required 2%

saturation at the high-intensity range in order to utilize most of the intensity range (Figure 5.8). The level of saturation was determined in an empirical optimization fashion based on intensity histogram and DeepVess' results. Figure 5.8 shows the effect of the intensity normalization process with having intensity distributions with the fat tail that utilizes most of the intensity range.

As described in the last section, since the image intensity distribution depends on the microscope and acquisition systems, the only hyperparameter that needs fine tuning is the image normalization percentile, which maximizes the intensity range utilization.

5.4 Conclusions

5.4.1 Future work

The crowd response aggregation algorithm can be improved to decrease the required number of responses per vessel and leads to a higher throughput rate. Additionally, the vessel assignment can be done in a more adaptive fashion in order to utilize the valuable time of the experienced users in more challenging cases.

Furthermore, the StallCatchers' results can be re-utilized as the ground truth dataset for training more sophisticated machine learning algorithm with the goal of performing this classification task in a semi- or fully-automated manner in the near future.

REFERENCES

Alosco, M. L., Spitznagel, M. B., Raz, N., Cohen, R., Sweet, L. H., Colbert, L. H., … Gunstad, J. (2012). Obesity Interacts with Cerebral Hypoperfusion to Exacerbate Cognitive Impairment in Older Adults with Heart Failure. Cerebrovascular Diseases Extra, 2(1), 88–98. https://doi.org/10.1159/000343222

Bennett, R. E., Robbins, A. B., Hu, M., Cao, X., Betensky, R. A., Clark, T., … Hyman, B. T. (2018). Tau induces blood vessel abnormalities and angiogenesis-related gene expression in P301L transgenic mice and human Alzheimer's disease. Proceedings of the National Academy of Sciences, 115(6), E1289–E1298. https://doi.org/10.1073/pnas.1710329115

Biggs, J., Ewald, N., Valentini, A., Gaboriaud, C., Dejean, T., Griffiths, R. A., … Dunn, F. (2015). Using eDNA to develop a national citizen science-based monitoring programme for the great crested newt (Triturus cristatus). Biological Conservation, 183, 19–28. https://doi.org/10.1016/j.biocon.2014.11.029

Bird, T. J., Bates, A. E., Lefcheck, J. S., Hill, N. A., Thomson, R. J., Edgar, G. J., … Frusher, S. (2014). Statistical solutions for error and bias in global citizen science datasets. Biological Conservation, 173, 144–154. https://doi.org/10.1016/j.biocon.2013.07.037

Cova, I., Clerici, F., Rossi, A., Cucumo, V., Ghiretti, R., Maggiore, L., … Caracciolo, B. (2016). Weight Loss Predicts Progression of Mild Cognitive Impairment to Alzheimer's Disease. PLOS ONE, 11(3), e0151710. https://doi.org/10.1371/journal.pone.0151710

Cruz Hernández, J. C., Bracko, O., Kersbergen, C. J., Muse, V., Haft-Javaherian, M., Berg, M., … Schaffer, C. B. (2019). Neutrophil adhesion in brain capillaries reduces cortical blood flow and impairs memory function in Alzheimer's disease mouse models. Nature Neuroscience, 22(3), 413–420. https://doi.org/10.1038/s41593-018-0329-4

Denk, W., Strickler, J. H., & Webb, W. W. (1990). Two-photon laser scanning fluorescence microscopy. Science, 248(4951), 73–76.

Haft-Javaherian, M., Fang, L., Muse, V., Schaffer, C. B., Nishimura, N., & Sabuncu, M. R. (2018). Deep convolutional neural networks for segmenting 3D in vivo multiphoton images of vasculature in Alzheimer disease mouse models. ArXiv:1801.00880 [Cs]. Retrieved from http://arxiv.org/abs/1801.00880

Heim, E., Roß, T., Seitel, A., März, K., Stieltjes, B., Eisenmann, M., … Maier-Hein, L. (2018). Large-scale medical image annotation with crowd-powered algorithms. Journal of Medical Imaging, 5(3), 034002. https://doi.org/10.1117/1.JMI.5.3.034002

Iadecola, C. (2004). Neurovascular regulation in the normal brain and in Alzheimer's disease. Nature Reviews Neuroscience, 5(5), 347–360. https://doi.org/10.1038/nrn1387

Kleinfeld, D., Mitra, P. P., Helmchen, F., & Denk, W. (1998). Fluctuations and stimulus-induced changes in blood flow observed in individual capillaries in layers 2 through 4 of rat neocortex. Proceedings of the National Academy of Sciences, 95(26), 15741–15746.

Raykar, V. C., Yu, S., Zhao, L. H., Jerebko, A., Florin, C., Valadez, G. H., … Moy, L. (2009). Supervised Learning from Multiple Experts: Whom to Trust when Everyone Lies a Bit. Proceedings of the 26th Annual International Conference on Machine Learning, 889–896. https://doi.org/10.1145/1553374.1553488

Santisakultarm, T. P., Paduano, C. Q., Stokol, T., Southard, T. L., Nishimura, N., Skoda, R. C., … Schaffer, C. B. (2014). Stalled cerebral capillary blood flow in mouse models of essential thrombocythemia and polycythemia vera revealed by in vivo two-photon imaging. Journal of Thrombosis and Haemostasis, 12(12), 2120–2130. https://doi.org/10.1111/jth.12738

Santisakultarm, Thom P., Cornelius, N. R., Nishimura, N., Schafer, A. I., Silver, R. T., Doerschuk, P. C., … Schaffer, C. B. (2012). In vivo two-photon excited fluorescence microscopy reveals cardiac- and respiration-dependent pulsatile blood flow in cortical blood vessels in mice. American Journal of Physiology-

Heart and Circulatory Physiology, 302(7), H1367–H1377. https://doi.org/10.1152/ajpheart.00417.2011

Sullivan, B. L., Wood, C. L., Iliff, M. J., Bonney, R. E., Fink, D., & Kelling, S. (2009). eBird: A citizen-based bird observation network in the biological sciences. Biological Conservation, 142(10), 2282–2292. https://doi.org/10.1016/j.biocon.2009.05.006

Theobald, E. J., Ettinger, A. K., Burgess, H. K., DeBey, L. B., Schmidt, N. R., Froehlich, H. E., … Parrish, J. K. (2015). Global change and local solutions: Tapping the unrealized potential of citizen science for biodiversity research. Biological Conservation, 181, 236–244. https://doi.org/10.1016/j.biocon.2014.10.021

Westphal, A. J., Stroud, R. M., Bechtel, H. A., Brenker, F. E., Butterworth, A. L., Flynn, G. J., … Dusters, 30714 Stardust@home. (2014). Evidence for interstellar origin of seven dust particles collected by the Stardust spacecraft. Science, 345(6198), 786–791. https://doi.org/10.1126/science.1252496

CHAPTER 6

XYLEM VESSEL CONNECTIVITY IN THE RING AND DIFFUSE POROUS TREES

6.1 Introduction

The world is full of transport networks ranging from biological to engineered. Despite differences in their nature and purpose, networks share similar structures and dynamics (Watts & Strogatz 1998). To model and understand these dynamics, networks are often simplified and studied as graphs, structures comprising of nodes and edges, where nodes represent the main elements of the network and edges represent the connections or pathways between the elements. The specific arrangement of nodes and pathways within the network determines both the overall topology and the functional efficiency of the structure (Watts & Strogatz 1998; Latora & Marchiori 2001). With respect to biological fluid transport networks, the topology can also impact the vulnerability of the system in response to external stresses (Zimmermann 1983). Topology regulates the total throughput of the network in terms of the hydraulic conductance and the fluid transport distributions throughout the network. As a result, the ability to accurately map physical networks into well-defined networks is a crucial step toward understanding the dynamics of these complex systems. Previously, the methodologies based on the network analysis have been utilized to study brain vascular networks (Cruz Hernández et al. 2019).

One network that has been understudied is the water transport system in plants: the xylem network. The anatomy of this network provides reliable water transport in plants. These networks consist of water conducting, tube-shaped vessels, called xylem vessels,

that are connected through intervessel pit connections, that form between two adjacent vessels (Figure 6.1). Pits are porous membranes with pore sizes ranging from 1-10 nm that are many-fold smaller than the diameters of xylem vessels, whose diameters range from 5-500 µm (Venturas, Sperry & Hacke 2017). Intervessel connections between two adjacent xylem vessels occur in regions so that there are spans of vessels that are connected by many pores. The pores in intervessel connections are numerous so that they contribute substantially to water conductance despite their small size relative to the xylem vessels. Water flow through the network of xylem vessels is limited by both vessel diameter and intervessel connections (Sperry, Hacke & Wheeler 2005), stressing the importance that both anatomical features have on the water transport efficiency through xylem vessels.

Intervessel connections between xylem vessels can provide redundant pathways for water transport that confer robustness against loss of xylem vessels. However, these connections can also threaten water transport efficiency during drought stress periods, because intervessel connections are not only permeable to water but also gases. During water shortages, the water tension within the xylem increases continuously, which can cause the metastable water to cavitate spontaneously, resulting in the formation of small air bubbles (Tyree & Dixon 1986). After which, air from cavitation events can expand across an entire xylem vessel, forming so-called embolism events that block the water flow through that segment of the xylem vessel. When water potentials continue to decline, local embolism events have the tendency to spread via intervessel connections through the vascular system, which decreases the hydraulic conductivity of the xylem network and diminishes the water supply to distal plant organs (Zimmermann 1983). Embolism vulnerability of single vessels is well examined and can be attributed to anatomical traits

such as vessel diameter, vessel wall thickness and intervessel connection structures (Jacobsen, Ewers, Pratt, Paddock III & Davis 2005; Wheeler, Sperry, Hacke & Hoang 2005; Jansen, Choat & Pletsers 2009). Even though research has failed to provide direct evidence of an existing tradeoff between water efficiency and safety on a single intervessel connection level, data show that larger volume vessels are more likely to embolize because of the positive correlation between intervessel areas and vessel surface areas, based on which the likelihood of having a leaky intervessel connection increases with vessel size (Wheeler *et al.* 2005). Thus, vessel connectivity and vessel size are not only important anatomical characteristics for water transport efficiency but also embolism resistance.

A. 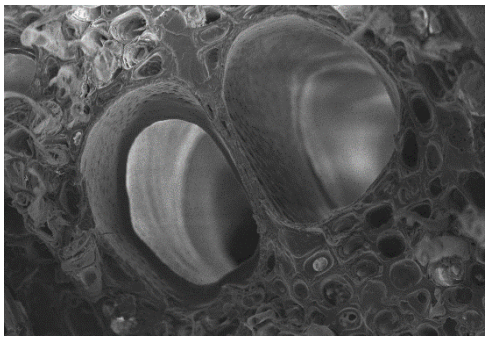 B. 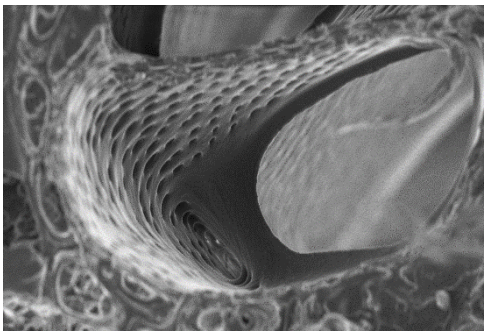

Figure 6.1. SEM images of a xylem intervessel connection.
The intervessel connection between two adjacent xylems (A), which is a porous membrane between two xylems (B).

Network connectivity is a major component of network robustness. However, the effects of water delivery efficiency on the drought survival and embolism spread are unknown. There is an ongoing debate on how xylem vessel topology relates to drought tolerance and whether higher vessel connectivity leads to a xylem network with higher resistant to embolism or if the opposite is the case. Both hypotheses are reasonably argued

and supported: Loepfe et al. 2007 suggested that higher xylem vessel connectivity impedes the network resistance to embolism because of the high network connectivity due to the intervessel connections facilities the spread of embolisms throughout the system. Indirect support for Loepe's results is given by an empirical study conducted on eighteen North American and Asian temperate trees and shrubs (Zanne, Sweeney, Sharma & Orians 2006) which focused on drought tolerance. This study showed that plants with a higher drought tolerance have less integrated, i.e., less number of intervessel connections, xylem pathways (Zanne *et al.* 2006). Contrarily, the counter-theory proposes that interconnected xylem networks are more resistant to drought stress because, in the case of an embolism event, a highly interconnected xylem network benefits from having several pathways through which water can be redirected. Thus, embolism events will have less impact on hydraulic conductance in a well-connected network. Support for this theory is given by an empirical data set on six different Acer taxa, that showed that intervessel connectivity leads to a more resistant xylem network (Lens *et al.* 2011). These two contrary arguments highlight the necessity for characterizing the architecture of xylem networks to identify networks traits affecting embolism resistance. However, both vessel topology and vessel connections are difficult to map due to technical limitations and therefore are poorly understood. As a result, we are far away from understanding how network connectivity affects xylem network vulnerability to embolism.

An established method for quantifying xylem network resistance to embolisms without the characterization of anatomical traits is the hydraulic vulnerability curves (PLC curves), which characterize the percent loss of hydraulic conductivity of a tissue segment as a function of the water potential within the tissue. There is an implicit assumption that

the water potential within the tissue is correlated with the degree of embolism within the vessel network and PLC curves (Cochard *et al.* 2013). Using the PLC curves, the P50 value is the water potential corresponding to a 50% hydraulic conductance loss through the xylem and is commonly used to compare drought resistance across plants. P50 values typically range in trees from -0.2 MPa to -14.0 MPa, with more negative values corresponding to greater tolerance to drought (Maherali, Pockman & Jackson 2004). How the overall shape of the PLC curve is directly linked to the relevant network characteristics remains unknown.

To address a number of these unknowns, in this manuscript we utilized laser ablation tomography (LATscan), a method that produces three-dimensional structural images, to explore the anatomical network characteristics of three ring-porous and three diffuse-porous tree species. Diffuse-porous tree species typically exhibit a tight vessel size distribution (around 40 μm in diameter) across year rings, while ring-porous tree species typically exhibit a bimodal vessel distribution, with large vessels (<500 μm) in the spring wood and small vessels (>20 μm) in the late wood. Ring-porous tree species have a higher maximum hydraulic efficiency than diffuse porous tree species due to the larger vessels in the early growth periods of the season in comparison to diffuse porous tree species (Carlquist 1988). However, these large vessels are particularly vulnerable to air embolisms due to the inverse correlation between vessel size and intervessel quantity and the likelihood of gas penetrating through the intervessel connection (Zimmermann 1983; Wheeler *et al.* 2005; Christman, Sperry & Smith 2012). We investigated the relationship between the intervessel quantity and the embolism likelihood by tracing and reconstructing the xylem networks of all six species using a deep neural network to segment images and

then quantify the overall network connectivity and vessel topology to identify network characteristics for these two wood types. We then simulated the robustness of the water flow in the network against blocked vessels and correlated these findings to P50 values. Comparing the different vessel arrangements of these two wood types with vulnerability curves aims towards a better understanding of the different vulnerabilities of embolism spread in the ring and diffuse-porous trees and will allow us to examine if xylem network connectivity contributes to the high embolism vulnerability of large early wood vessels in ring-porous tree species.

6.2 Material and Methods

6.2.1 Plant material

Two two-year-old branches of three individual trees of either three diffuse-porous (*Fagus sylvatica, Populus x canadensis, Liriodendron tulipifera)* or three ring-porous (*Quercus montana, Fraxinus excelsior, Carya ovata)* tree species were harvested for each measurement between April 2016 and June 2017. Selected tree species were grown on Cornell Campus, and tree replicates were chosen based on their proximity to each other (Ithaca, NY; lat. 42.44° N, long. 76.44° W). Ithaca has a continental moderate climate with an average annual temperature of 8.5 °C and an average annual rainfall of 982 mm (Northeast Regional Climate Center 2019).

6.2.2 Percent loss of hydraulic conductivity

Vulnerability curves were performed using the bench-top dry down method (Tyree & Dixon 1986). Around 60 cm long branches were cut around midnight, immediately

double bagged, brought to the lab, and the cut end was put into water. The following morning, the branches were spread out on the bench-top, single leaves were bagged for allowing leaf water potential (Ψ_{leaf}) to equilibrate with the branch water potential (Ψ_{branch}) and dried down for varying amounts of time to archive a range of different (Ψ_{leaf}). During this timeframe, Ψ_{leaf} was taken on the bagged leaves with a water status console (Soilmoisture Equipment Corp., Goleta, CA). After reaching the desired Ψ_{leaf}, branches were double bagged, equilibrated for 12 hours, and remeasured. Then, branches were cut under water to 15 cm long segments and inserted into a custom-built low-pressure flow meter (Melcher *et al.* 2012) by attaching one end of the branch segment to a reservoir that was filled with a (0.1 µm) filtered 20 mM KCl of perfusion solution, and the other end of the branch segment to an analytical balance (HR-200, A&D, Elk Grove, Il). Then, the initial flow rate (Q) was measured. The hydraulic pressure difference between sample and solution reservoir was kept constant species dependent between 1.5 kPa and 3.0 kPa during the measurements. Afterward, branch segments were flushed for 1 hour at 100 kPa with the perfusion solution, and the max flow rate was measured by reinserting the stem segments in the low-pressure flow meter. The unit-length hydraulic conductivity (K) was determined by:

$$\mathrm{K} = \mathrm{Q}\,\frac{L}{\Delta \mathrm{P}} \tag{1}$$

Where, L is the length of the sample, and ΔP is the hydraulic pressure gradient. After the measurements, the xylem cross-sectional area was determined with a caliper and the specific hydraulic conductivity determined by dividing the K by the cross-sectional areas. Lastly, the percent of hydraulic loss of conductivity (PLC) was calculated by:

$$\mathrm{PLC} = \frac{100}{1 - \frac{K_{max}}{K_{min}}} \quad (2)$$

Where, K_{max} is the maximum specific conductivity after flushing, and K_{in} is the initial specific hydraulic conductivity. The PLC data were fitted with an exponential sigmoidal equation of:

$$\mathrm{PLC} = \frac{100}{1 + exp\big(a + (\Psi - \mathrm{b})\big)} \quad (3)$$

Where, a and b are fitting parameters, whereby a describes the slope of the curve and b represents the position of the curve on the x-axis at 50% PLC (Pammenter & Van der Willigen 1998). The significance levels of the parameters were calculated based on this fit.

6.2.3 Vessel length distribution

Vessel length distribution was calculated based on the silicon injection technique (Sperry *et al.* 2005; Wheeler *et al.* 2005). Six branches (~60 cm) per species were cut, brought into the lab, and flushed for 1 hour at 70 kPa with a 20 mM KCL solution to remove native embolisms (Sperry, Donnelly & Tyree 1988). Then, basal ends of the branches were connected via silicon tubing to a nitrogen gas tank and injected with a 10:1 two-component silicon elastomers (RTV141 A&B, distributed by Hisco, Somerset, NJ, USA) at 70 kPa overnight. Prior to injection, the silicon mixture was degassed under vacuum and infused with a UV stain that was dissolved in chloroform (Ciba Uvitex OB, Ciba Specialty Chemicals, Tarrytown, NY) in order to separate silicon injected xylem vessels from empty vessels for imaging analysis. After the silicon cured (~2 days), branches were sectioned at six cutting distances from the injection site with a sliding microtome (American Optical,

680 sliding microtome, Spencer Lens Co., Buffalo, NY). The respective cutting distances (L_i) were determined with the following equation:

$$L_i = L_{min}\left(\frac{L_{max}}{L_{min}}\right)^{\left[\frac{i-1}{N-1}\right]} \quad (4)$$

With L_{min} the cross section at 0.5 cm after the injection point, and L_{max} the cross-section at which 2% of the vessels were detected under the fluorescence microscope, and N the total amount of cuts. Then, cross sections mounted in glycerol, magnified with a 10x/04 objective and imaged a with a fluorescence microscope (Olympus BX50, Olympus Scientific Solutions, Waltham, MA, US) to which a camera was attached (Retiga Exi CCD camera, QImagig, Burnaby, BC, Canada). Fluorescent silicon injected vessels from the most recent formed year ring were counted and averaged over species. Lastly, the vessel length distribution and the average vessel length was calculated for each species on the basis of equations reported by Christmann et al. and Christman et al. (Christmann, Weiler, Steudle & Grill 2007; Christman, Sperry & Adler 2009). The objective was to fit the silicon-injected vessel counts with a Weibull function and to use the best fit to calculate the second derivate, from which the vessel length distribution was calculated.

6.2.4 Laser ablation tomography

In this study, the laser source of the Laser ablation tomography scan (LATscan) system was a Coherent Avia 355-7000 Q-switched ultraviolet laser (Coherent, 5100 Patrick Henry Drive, Santa Clara, CA 95054 USA) with a pulse repetition rate of 25 KHz and wavelength of 355 nm. The pulse duration of the laser was less than 30 ns and supplied pulse energy of approximately 200 mJ. The galvanometer used to scan the laser beam to make the ablation plane was a Scanlab HurryScan 10 (Scanlab, Siemensstr 2a, 82178

Puchheim, Germany). Samples were fixed to a cantilever and connected to the mechanical stage along its travel axis, then fed into the ablation plane using an Aerotech linear drive stage (Aerotech, Inc., 101 Zeta Dr, Pittsburgh, PA 15238, USA), with the distance between sections ranging from 35 µm to 50 µm. Images were captured via a Canon 70D camera equipped with a Canon Macro Photo Lens MP-E 65 mm 1:2.8 1-5X. The images were 5472 x 3648 pixels at a resolution of 1 micron per pixel.

F. sylvatica

L. tulipifera

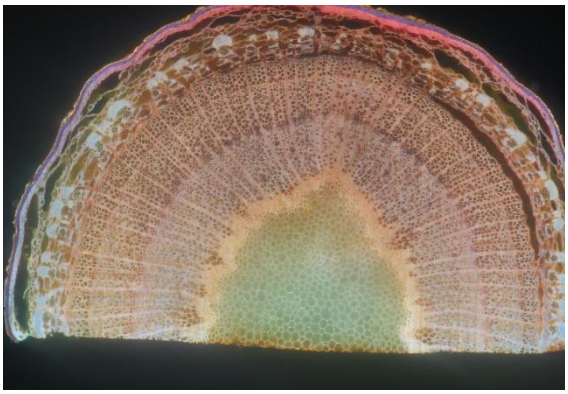

P. x canadensis

C. ovata

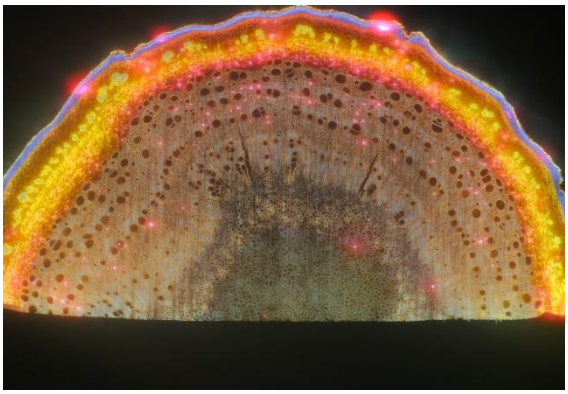

F. pennsylvanica

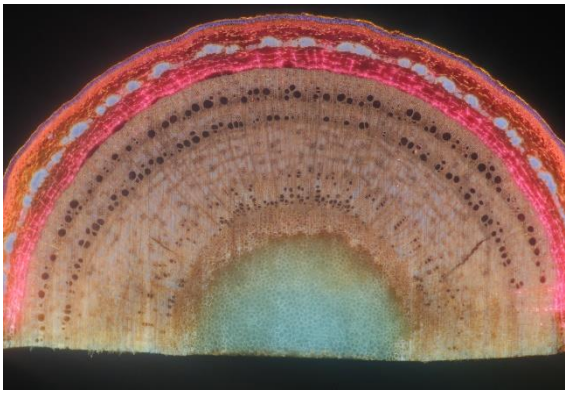

Q. montana

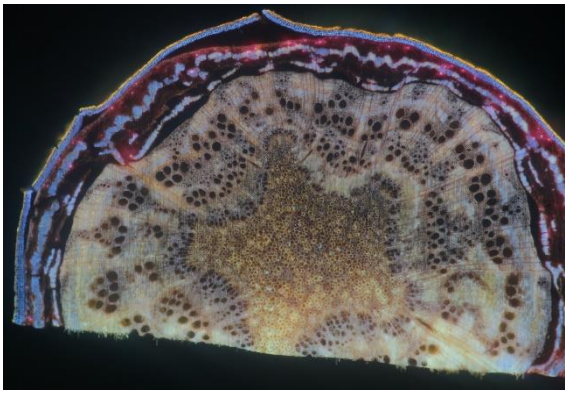

Figure 6.2. Samples of 3D LATscan images of tree branch cross-sections of different species.

6.2.5 Selecting vessel length and cutting distance for analysis

The maximum sample length was restricted by a combination of technical limitation and sample trait. The digital camera tended to overheat with increasing sample length due to the amount of image taken. Additionally, the degree of natural bending of the branches increased with sample length. Consequently, samples tended to move out of the imaging plane with increasing sample length and we were unable to realign the sample with imaging plane by simply pushing the sample back in the imaging plane. To ensure image quality we chose maximum sample length to be the 75^{th} percentile of vessel class length, that was determined by vessel length distribution, for diffuse-porous tree species and 50^{th} percentile for ring-porous tree species (Figure S 6.1). To determine the maximum distance between cuttings, we performed a preliminary experiment in which we ablated 31 slices of a sample of all six tree species into the minimum cutting distance (5 μm and total length of 150 μm) and manually segmented 100 vessels per species using ImageJ (Rueden *et al.* 2017) using the procedure described by Haft-Javaherian et al. (Haft-Javaherian et al. 2019). We then measured the segmentation similarity between the first slice and the following slices based on the ratio of the intersection area of two adjacent vessel cross-sections and the first slice vessel cross-section area averaged over all detected vessels to determine the maximum distance between two images such that we observed at least 50% averaged cross-sectional overlaps with an upper limit of 50 μm. We found this distance to be 50 μm for all ring-porous tree species, 40 μm for *F. sylvatica*, 35 μm for *P. x canadensis*, and 50 μm for *L. tulipifera*. These cutting distances were then used for all further analysis (Table 6-1).

Table 6-1. The geometrical characteristic of tree species samples.

Wood type	Tree species	Slice thickness (μm)	Total Length (mm)	Intervessel threshold (μm)
Diffuse-porous	*F. sylvatica*	40	70	2
	L. tulipifera	50	62.9	3
	P. x canadensis	35	46	3
Ring-porous	*C. ovata*	50	98	4
	F. pennsylvanica	50	271.4	5
	Q. montana	50	167	5

6.2.6 Determining intervessel wall thickness

Scanning electron microscopy (SEM, Zeiss 1550) was used to measure intervessel wall thickness as the distance between two adjacent vessels to determine the minimum distance at which two vessels are connected and to be used as the vessel connectivity criteria. Three branches per individual tree (nine branches per tree species), were harvested and cut into 5 mm samples with a sliding microtome (American Optical, 680 sliding microtome, Spencer Lens Co, Buffalo, NY). Then, samples were dehydrated in a series of 25%, 50%, 70%, 95%, and 100% ETOH, and then dried down at room temperature. Samples were coated with gold-palladium for 20 seconds at a current of 20 mA and imaged at a voltage of 3.0kV and a current of 0.21nA. The intervessel wall thickness was measured in ImageJ (Rueden *et al.* 2017) based on a minimum of 60 adjacent vessels. The 95^{th} percentile of each data set was calculated and set as the criterion for intervessel connectivity. Intervessel distances equal to or smaller than the 95^{th} percentile was counted as been connected (Table 1).

6.2.7 The study-design image processing pipeline

We developed a graphical user interface (GUI) in Matlab for image processing and network analysis to facilitate the preliminary study analysis and the study design (e.g., cutting distance determinations and methodological feasibility risk analysis). The GUI allows the user to load a 3D stack of images and select the region of interest in addition to tuning the image processing parameters. The image processing pipeline started with the application of a top hat filter followed by a bottom hat filter. Top hat filter subtracts the morphological opening of the image from the original image and similarly bottom hat filter subtract the original image from the morphological closing of the image. The morphological opening consists of an erosion of image followed by dilation, and in contrast, morphological closing consists of a dilation followed by an erosion. The erosion and dilation are the two basic mathematical morphology operations, which require a structuring element (i.e., kernel) to operate. The combination of top hat and bottom hat filters treat small objects with very high or low intensity. Next, we sharpened the image by subtracting the smoothed image (using a Gaussian lowpass filter multiplied by a constant) from the original image. Next step the grayscale image is binarized using an adaptive threshold defined using Otsu's method (Otsu 1979) in addition to ensuring the preservation of the boundaries between adjacent vessels. Finally, the small isolated objects were removed, and the holes were filled. The vessel cross-section centroids were identified to produce the graph representation of vasculature networks using the binary segmentation results. The GUI save the segmentation, graph representation, and the adjacency matrix of vessel connections to the output data file.

6.2.8 Motion artifact compensation

Motion artifact is one of the main challenges for images processing of 3D vasculature network images. Apparent motion can be caused by any combination of gradual shift, sudden shift or rotation, poor focus, and burned cross-section (see Figure 6.3). In order to compensate for these different motion artifact cases, we utilized two different methods and optimized their hyperparameter based on our images and sources of motion artifacts. Due to the size of our dataset, the computational complexity and scalability is the other important factor that needs to be considered because the 3D images could contain up to 5000 slices along their third dimension. Since there are no local distortion and motion artifacts in the images, a rigid registration (i.e., translation and rotation) is sufficient for this task. A registration method consists of a similarity metric as an input to the cost function and an optimizer to optimize the cost function finding the optimal registration parameters. The first method used mean square error (Eq. 5) as the similarity metric and the regular step gradient descent optimization, which follows the gradient of the cost function to in the direction of extrema with reducing the step function when the gradient changes direction.

$$MSE = \frac{1}{N \times M} \sum_{i=1}^{N} \sum_{j=1}^{M} \left(I_{i,j} - I'_{i,j} \right)^2 \tag{5}$$

We used a random grid search to find the optimal hyperparameters for the optimizer and found two optimal sets of hyperparameters. The ensemble of two optimizers based on the optimal sets of hyperparameters was able to handle most of the cases, and it was successful when applied to the test cases with small sample sizes. The failure modes include uneven illuminations, laser-burned cross-sections, color-distorted images, and

sudden dramatic changes. On the other hand, even after multi-thread parallelization, this method has a long run time, besides, to the need for required manual treatments of the remaining failure cases.

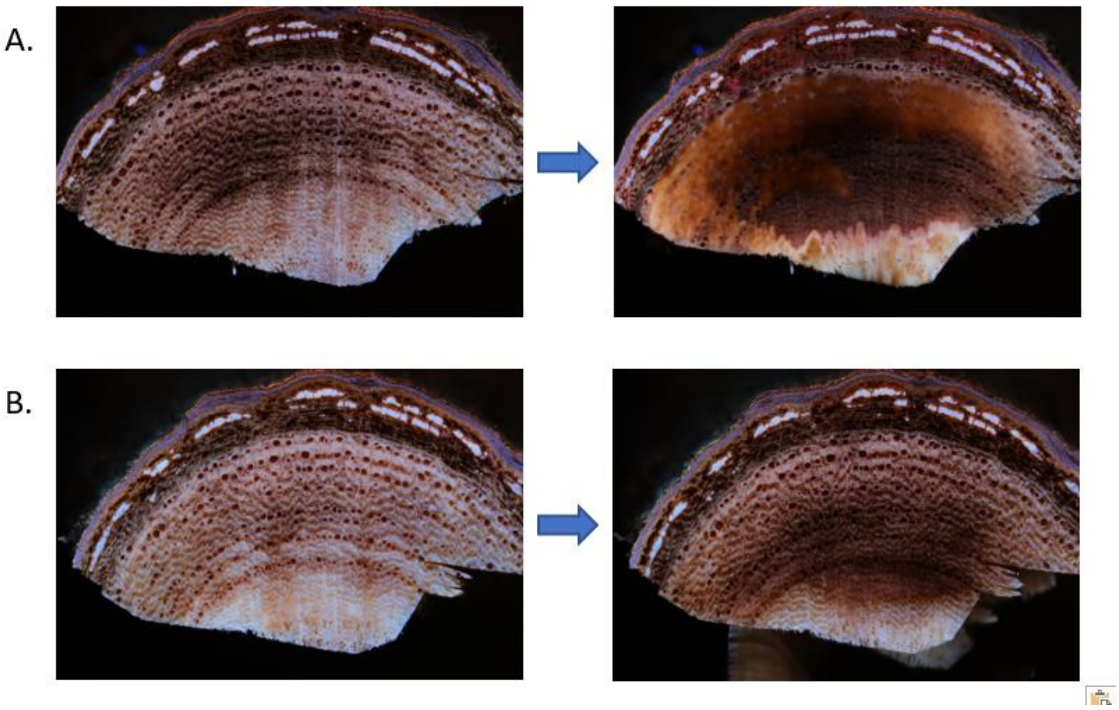

Figure 6.3. Examples of motion artifacts due to the residuals of last cross-section (A) and the laser ablation signs in addition to the reflection (B).

We devised the second method is based on the work by Evangelidis and Psarakis (Evangelidis & Psarakis 2008) to overcome the drawbacks of the first method specifically for samples with large sample sizes. They adopted the enhanced correlation coefficient (Psarakis & Evangelidis 2005) as the similarity measure. This measure has preferable characteristics such as being invariant to contrast and brightness differences (i.e., photometric distortions) as well as having a corresponding linear approximation expression with a closed-form solution, which facilitates the optimization of the original non-linear

measure. Additionally, Evangelidis and Psarakis proposed an iterative gradient based (e.g., forward additive refinement algorithm) to optimize the original non-linear measure using the linear approximation (Evangelidis & Psarakis 2008). In order to tackle multi-scale motion artifacts, we estimated the transformation parameters in a pyramid fashion using 10X scaled-down versions of the two images and then fine-tune the parameters using the original resolutions. Since the images do not suffer from local motion artifacts, only the estimation of the global transformation parameters within two consecutive images is required.

In order to parallelize the process, images were divided into groups of 10 consecutive images and registered independently based on the first image in the group. Then, sequentially starting from the second image group, the first image of each image group was aligned to the last image of the preceding image group and the rest of the images within the group were warped using the same transformation. Finally, we implemented a failure detector using the mean structural similarity index (Wang, Bovik, Sheikh & Simoncelli 2004) between two consecutive images. Within every 11 consecutive pairs of images, the middle pair is considered as a failure case if its similarity index is at least 5% lower than the median of the 11 similarity indexes. The failure cases were registered again using the same algorithm (or in rare cases manually if the algorithm failed repeatedly) followed by warping all the following images using the same transformation parameters. This process was repeated until no failure cases were detected.

6.2.9 Segmentation

We extracted three 3D samples per species including at least 31 consecutive images that were manually annotated as the ground truth. At least 100 vessels were manually segmented through the depth of each sample using the manual segmentation protocol developed by Haft-Javaherian et al. (Haft-Javaherian *et al.* 2019). Due to the significant anatomical differences between different species vessel morphologies and size distributions, we trained a separate segmentation model for each species. We adopted the architecture and training scheme of DeepVess (Haft-Javaherian *et al.* 2019), that is a convolutional neural network (CNN) model with an optimal architecture for the 3D vasculature segmentation task and a customized cost function, and trained the model for each species using the ground truth.

Since each sample had between 1000 and 5000 images, each 500-image stack was stored in a separate HDF5 binary data format to be segmented using the CNN model. After the segmentation task, the binarized segmentation results were concatenated to form the complete segmentation results for each sample. In order to remove minimal segmentation artifacts, we applied a dilation morphological image filter with a disk kernel of radius 1 to remove the boundary of vessels followed by a 3D median filter with a 3-voxel box kernel to smooth the vessel boundary and fill the holes within the vessels. The complete image processing pipeline is illustrated in Figure 6.4.

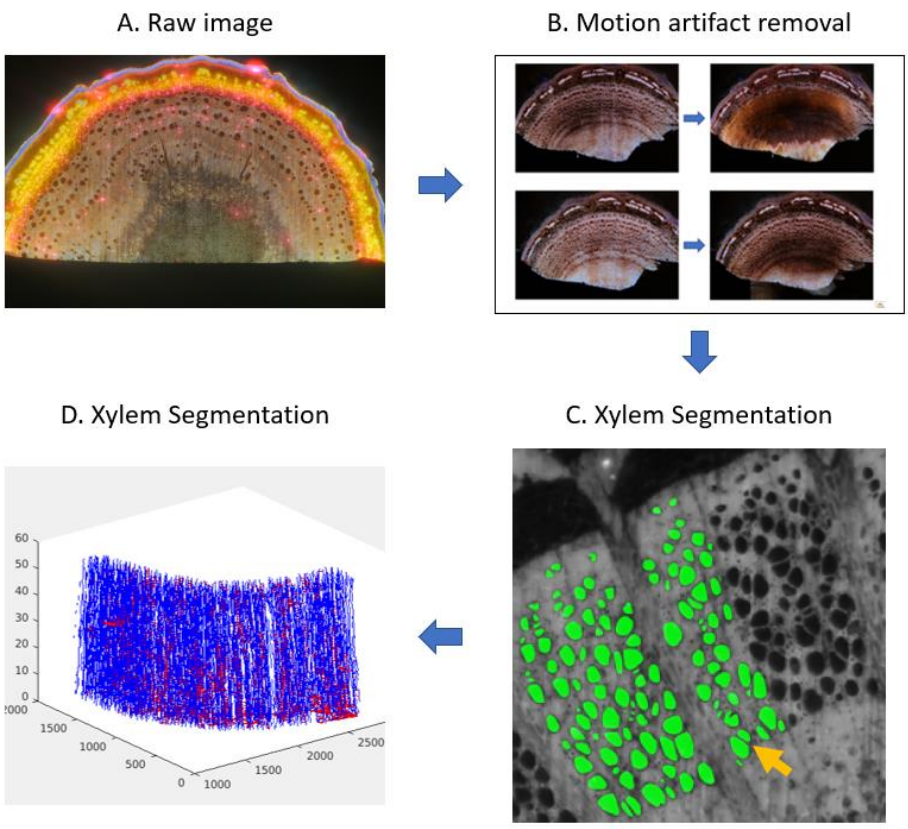

Figure 6.4. Complete image processing pipeline.

Raw images (A) are preprocessed for intensity normalization and motion artifact removal (B). The preprocessed images are segmented, and the xylem cross sections and intervessel connections (such as the intervessel connection between the two xylems indicated by the yellow arrow) are detected (C). The segmentation and detection results are represented in the graph representation (D). For example, the graph representation of 50 slices of images are illustrated in D. The xylem segment edges are in blue, and the intervessel connections are in red.

6.2.10 Computational fluid dynamics and embolism simulation

The pressure drops within a 3D xylem segment can be modeled based on the Hagen–Poiseuille law as a circular cross-sectional pipe with laminar flow of water, which

is an incompressible and Newtonian fluid, correlating the fluid flow within the pipe (Q) with the pressure drop (ΔP) as formulated in Eq. 6. Hence, the segment resistance is defined as Eq. 7, where, μ is the dynamic viscosity of water at 25°C, D is the xylem segment diameter, and L is the xylem segment length.

$$Q = \frac{\pi D^4 \Delta P}{128 \mu L} \tag{6}$$

$$R_x = \frac{\Delta P}{Q} = \frac{128 \mu L}{\pi D^4} \tag{7}$$

Sperry and Hacke (Sperry & Hacke 2004) modeled the resistance of the intervessel connections (R_i) as infinitely thin plates with perfectly circular pores with resistance as a function of the equivalent pore size (D_e) and the number of pores in the intervessel connection (n_p) defined in Eq. 8. Since we can assume that n_p is proportional to the intervessel connection length (L_i in Eq. 9), which are measured based on 3D images of samples, we modeled the intervessel connection resistance (R_i) as a function of L_i, which is a proxy for the n_p (Eq. 10).

$$R_i = \frac{24 \mu}{D_e^3 n_p} \tag{8}$$

$$D_e^3 n_p = \alpha L_i \tag{9}$$

$$R_i = \frac{24 \mu}{\alpha L_i} \tag{10}$$

The hydraulic network based on the xylem segments and intervessel connections was modeled using Eq. 7 and Eq. 10. The system then is represented in a linear system of equations, and the solution was acquired using one of the sparse systems of linear equation solver methods (e.g., Cholesky solver) depend on the characteristics of the linear systems. A unit pressure difference was applied between the two ends of the longest connected

segment within each tree sample, and the flow within the sample was measured to calculate the sample conductance ($Q/\Delta P$). Thirty simulations were conducted for each dropout percentile ranging from 0% to 100% in order to simulate different embolism events. The relative conductance, which is the ratio of conductance to the baseline conductance at 0% dropout was reported for each sample.

6.2.11 Statistics

Statistical analysis was performed in JMP Pro 14.0.0 (SAS Institute Inc., Cary, NC.) or Matlab. All tests were performed with probability level $p < 0.05$. Differences between tree pieces were calculated using ANOVA, and multi-comparison corrections were done using the Tukey-Kramer method. For calculating differences in intervessel wall thickness among tree types, the dependent variable was log transformed to fulfill model assumptions.

6.3 Results and Discussions

Graphs and networks are mathematical tools that represent a set of relationships or processes (edges) between a set of objects (vertices) and facilitate quantitative analysis of the objects in the context of their relationships. We utilized the xylem segmentation results to generate the graph representation of xylem networks to study and characterize them using network analysis and fluid mechanics.

Since 3D xylem vessels extend the length of the branch, the xylems appear in cross-section in each image slice. The segmented image slices identified connected voxels that together represent a distinct cross-section of a xylem vessel. Xylem vessels are connected

by two types of connections. First xylem vessels merged and bifurcated as they traverse the length of the branch. Xylem segments were defined to start and end with a junction. Two cross-sections located within two adjacent slices were defined as belonging to the same 3D xylem segment if they are overlapped (Figure 6.5). Conversely, the xylem junctions happen when more than one xylem merge into one xylem, or one xylem divides into more than one xylem. The junction is apparent in images when a cross-section from an image slice is overlapped with more than one cross-section in the preceding or proceeding adjacent image slice. Therefore, depending on the cross-sectional overlaps in the segmented images, the 3D xylem segments and their junctions are identifiable. Second, because the intervessel connections are not directly visible in the images, they were identified based on the thickness of the wall between two xylem vessels. The intervessel connection occurs in places where the distance between the boundaries of two separate cross-sections within an image slice is less than the intervessel threshold (Table 6-1 and Figure 6.5.A).

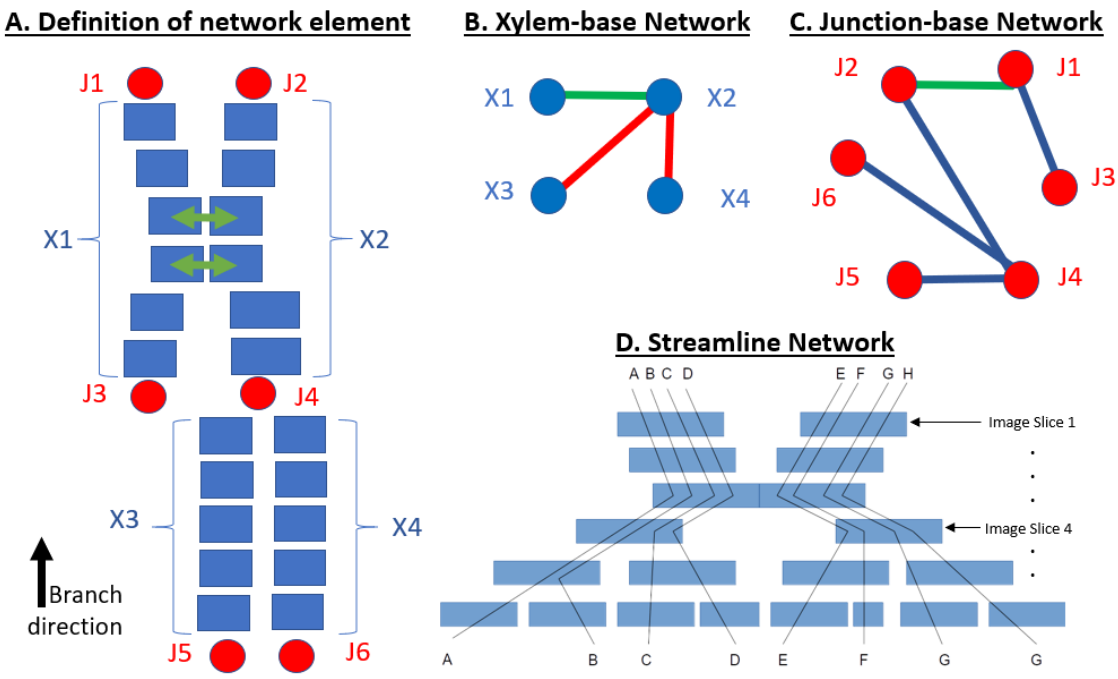

Figure 6.5. Three graph representations of xylem networks.

(A) The Blue boxes represent a segmented xylem cross-section, and each row of the blue boxes represents an image slice. 3D xylem segments (X1-X4) begin and end at junctions (J1-J6). Some xylem vessels were connected by intervessel connections (green arrows and graph edges) that are identified as region where two xylem segments are closer than the threshold distances found in SEM images. The (B) xylem-based and (C) junction-based graph representations assign xylems and junctions to the vertices, respectively. (D) In the streamline network representation, streamlines were defined as all possible paths for water to traverse the sample using junctions.

We represented the combination of 3D xylem segments, junctions, and intervessel connections using three different network representations (i.e., xylem-based, junction-based, and streamline representations). The xylem-based network (Figure 6.5.B) represents the 3D xylem segments as the graph vertices, while the junction-based network (Figure

6.5.C) represents the junctions as the graph vertices. Consequently, the xylem-based network represents the junctions and intervessel connections using the graph edges, while the junction-based network represents 3D xylem segments and intervessel connections using the graph edges. Alternatively, the streamline network (Figure 6.5.D) traces all the possible distinct water streamlines between the first and last image slices based on the junctions. Therefore, streamline network represents the streamlines as the graph vertices and the intervessel connections between streamlines as the graph edges.

In order to characterize these networks using geometrical measures, each cross-section was fit to a centroid, and the shortest distance to the boundary was defined as the diameter. The diameter of each xylem vessel was defined as the median of the measured cross-sections. Correspondingly, the xylem length, number of intervessel connections, and total length of intervessel connections are measured for each xylem vessel.

Topological metrics characterize the graphs in terms of the relationships within the vertices. Topological metrics are measured on the graph as a whole (e.g., density) or measured for each vertex or edge independently (i.e., closeness). The edge- or vertex-based topological metrics results in measurement distributions, which can be summarized in terms of their mean (μ) and standard deviation (σ). The implications of the topological metrics can be illustrated using an analogy based on the United States Highway System (USHS).

The *density* measures the degree of connectedness within the network based on the ratio of the current number of edges and the maximum possible number of edges. In USHS,

the number of highways in the current system that connects cities is compared to the case of maximum density in which each city is connected to all other cities directly.

The *centrality* metrics are topological metrics measuring the importance of edges, vertices, or paths. The centrality metrics utilize the identified shortest path between all pairs of vertices. The *edge*- and *vertex-betweenness* measure the number of shortest paths that include an edge or vertex, respectively. Similarly, *closeness* measures the average shortest path to other vertices demonstrating the level of influence of this vertex on other vertices. In USHS, betweenness illustrates the magnitude of effects in the case of city entrances or a highway closure due to constructions or catastrophic events. The betweenness is the number of shortest paths that are eliminated by the closure. Correspondingly, closeness shows the importance of a city and how congestion in that city may have a ripple effect on other cities.

The *clustering* and *assortativity* measure the amount of the closed loop within the system and the level of clustering with similar edge types. In USHS, when a city is connected to two different cities, whether those two cities are connected is correlated with the level of interconnections and clustering in the network. The assortativity measures how similar highways are connected for instance main highways vs. controlled access highways (e.g., US I-95 vs. US I-495).

The graph connection can be recorded using the *adjacency matrix*, whose indices represents the vertices and the entry are non-zero when there is an edge between the corresponding vertices. The maximum *eigenvalue* and its eigenvector of the adjacency

matrices represent the importance of the main pattern of edge connections within the graph and *Katz* utilized the same concept to measure the relative degree of influence of vertices.

6.3.1 Geometrical comparisons

Figure 6.6 and Table S 6-1 summarized the geometrical comparisons between species based on the 3D segment graph representation. F. pennsylvanica and Q. montana have larger average xylem diameters compare to the other four species, with both being about double the diffuse-porous trees. Similarly, C. ovata has a larger average xylem diameter compared to diffuse-porous species. Nevertheless, only F. pennsylvanica has a significantly larger average xylem segment length compare to all other species. In terms of intervessel connections, F. sylvatica and P. x canadensis have larger average xylem intervessel frequency per xylem segment compared to C. ovata and F. pennsylvanica, while, just P. x canadensis has a larger average xylem intervessel frequency compared to L. tulipifera and Q. montana. Likewise, F. pennsylvania has a significantly larger average xylem intervessel length (Total length of intervessel connections per xylem segment) compare to all other species. On the other hand, Figure 6.7 and Table S 6-2 summarized the geometrical comparisons between species based on the streamline graph representation. While xylem diameters results based on the streamline representations imitate the results based on the 3D segment graph representations, other three geometrical metrics are not significantly different between species except for the intervessel frequency of C. ovata.

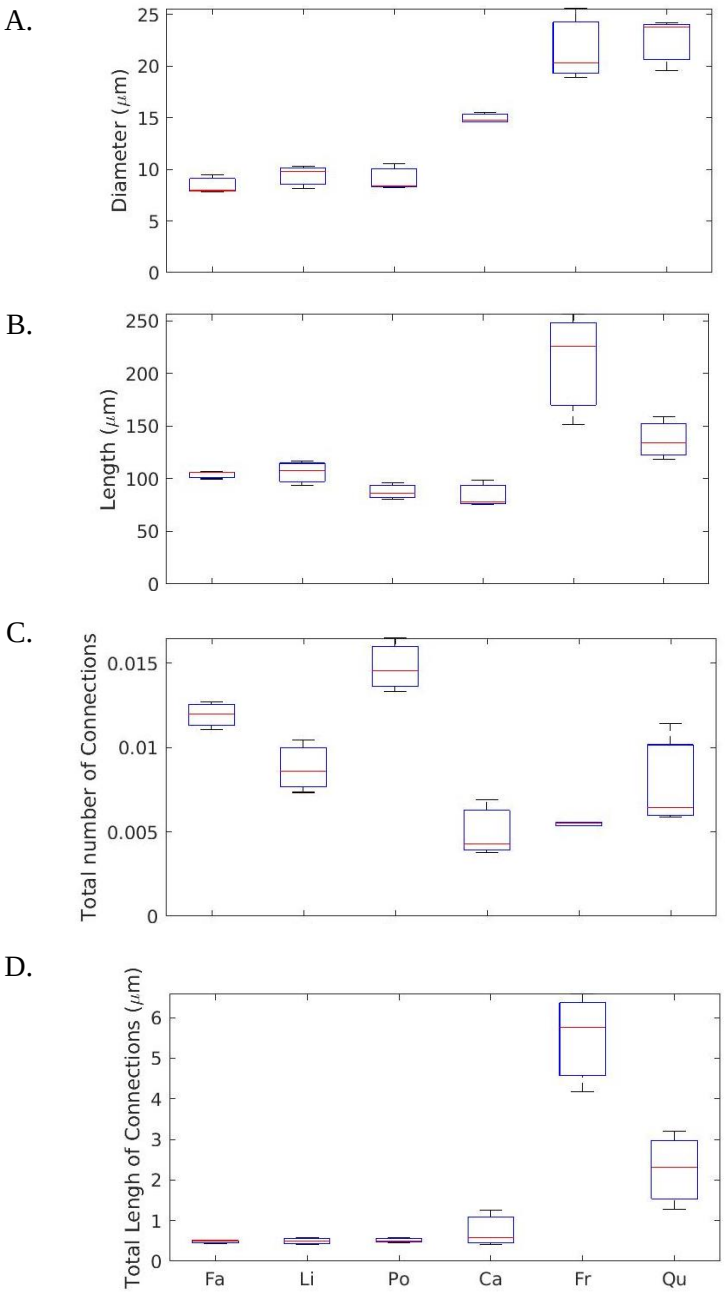

Figure 6.6. Anatomical characteristics based on the 3D segment representation.

Comparison of vessel diameters (A), vessel lengths (B), total number of intervessel connections (C), and total length of intervessel connections (D) per vessel segment between *Fagus sylvatica* (Fa), *Liriodendron tulipifera* (Li), *Poulus x canadensis* (Po), *Carya ovata* (Ca), *Fraxinus pennsylvanica* (Fr), and *Quercus montana* (Qu). Calculations are based on the 3D segment analysis. Statistical differences are given in Table S 6-1.

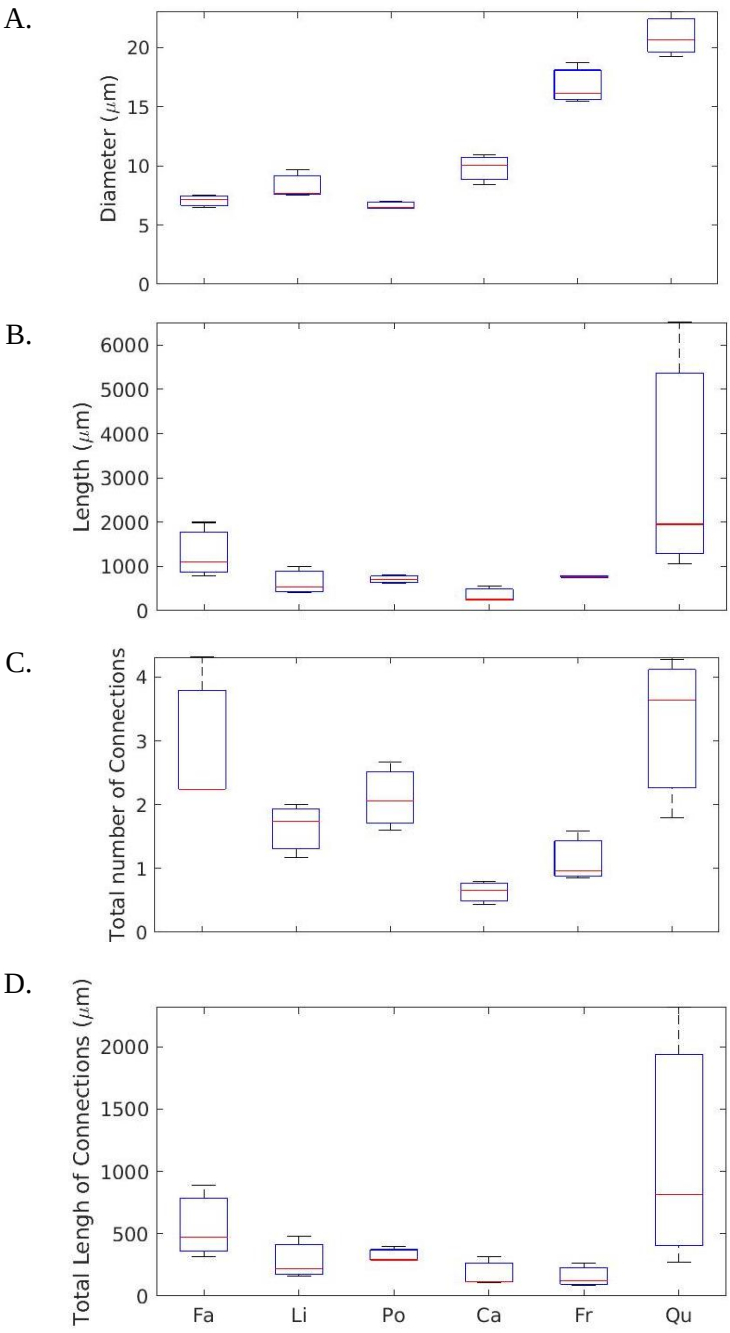

Figure 6.7. Anatomical characteristics based on the streamline representation.

Comparison of vessel diameters (A), vessel lengths (B), total number of intervessel connections (C), and total length of intervessel connections (D) per streamline between *Fagus sylvatica* (Fa), *Liriodendron tulipifera* (Li), *Poulus x canadensis* (Po), *Carya ovata* (Ca), *Fraxinus pennsylvanica* (Fr), and *Quercus montana* (Qu). Calculations are based on the streamline analysis. Statistical differences are given in Table S 6-2.

6.3.2 Topological comparisons

The geometrical comparison results describe the noticeable visual differed between samples of species qualitatively. In contrast, topological comparisons quantify the differences that are not detectable by visual inspections because they result from aggregate network properties. Figure 6.8 summarizes the topological comparisons based on the metrics described in the network analysis method section measured on the 3D segment graph representations. While it is evident that ring-porous species have a higher density, compare to diffuse-porous species due to the extremely lower number of xylems at each image, Katz, clustering, and assortativity demonstrates similar discrimination between wood types. On the other hand, C. ovata, P. x canadensis, Q. montana have higher centrality metrics such as closeness and betweenness compare to the other three species. This division cannot be described based on wood types or other geometrical or topological differences.

On the other hand, the topological comparisons measured on the streamline graph representations (Figure 6.10), show an additional aspect of the topological differences between species. For instance, only Q. montana has a higher density compared to all other species based on this representation, while only F. sylvatica has a high eigenvalue compare to all other species. These differences were not observed in the topological comparison based on the 3D segment representations. Instead, Katz, clustering, and assortativity still discriminate between wood types except for C. ovata. In contrast, the closeness metric in this representation discriminates between wood types in the opposite direction.

Another way to visualize the nature of the networks is to use circle graphs by aligning all the nodes along the circle and draw the edges between nodes. Even though,

the intervessel connectivity depicted in the Figure 6.9 and Figure 6.11 illustrate the evident difference between wood types in terms of amount of connectivity shown as a high number of edges, location variation of connectivity shown as edges closer to the center of the circle, and strength of the connections shown as the width of the edges perpendicular to the perimeter. These observations match with the visual assessments of the images of the species and serve as a confirmation of the various analysis pipelines proposed in this study.

A.

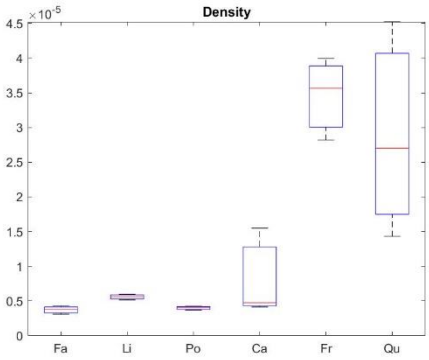
Density
×10^-5
4.5
4
3.5
3
2.5
2
1.5
1
0.5
0
Fa
Li
Po
Ca
Fr
Qu

B.

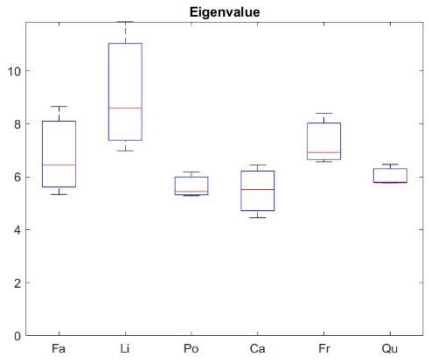
Eigenvalue
10
8
6
4
2
0
Fa
Li
Po
Ca
Fr
Qu

C.

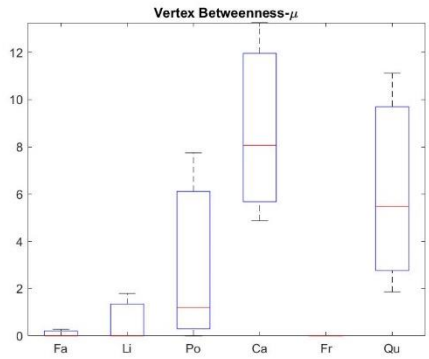
Vertex Betweenness-μ
12
10
8
6
4
2
0
Fa
Li
Po
Ca
Fr
Qu

D.

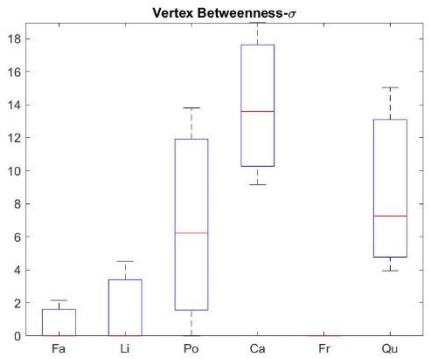
Vertex Betweenness-σ
18
16
14
12
10
8
6
4
2
0
Fa
Li
Po
Ca
Fr
Qu

E.

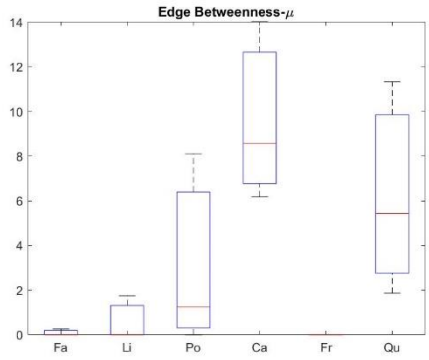
Edge Betweenness-μ
14
12
10
8
6
4
2
0
Fa
Li
Po
Ca
Fr
Qu

F.

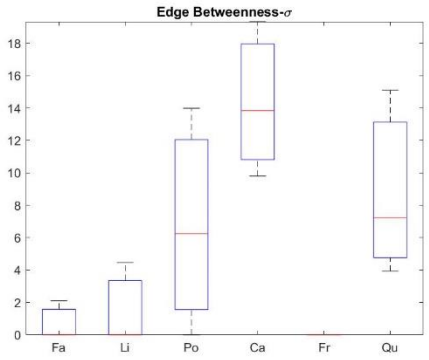
Edge Betweenness-σ
18
16
14
12
10
8
6
4
2
0
Fa
Li
Po
Ca
Fr
Qu

G.

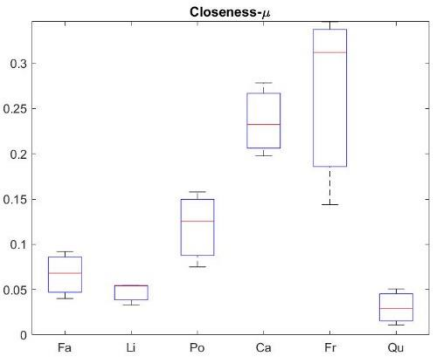
Closeness-μ
0.3
0.25
0.2
0.15
0.1
0.05
0
Fa
Li
Po
Ca
Fr
Qu

H.

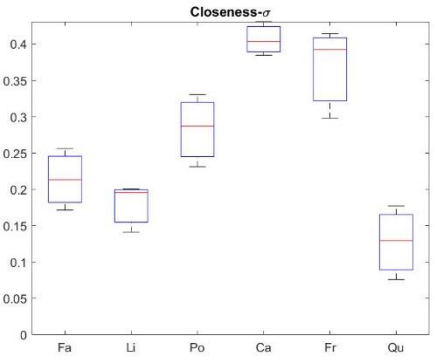
Closeness-σ
0.4
0.35
0.3
0.25
0.2
0.15
0.1
0.05
0
Fa
Li
Po
Ca
Fr
Qu

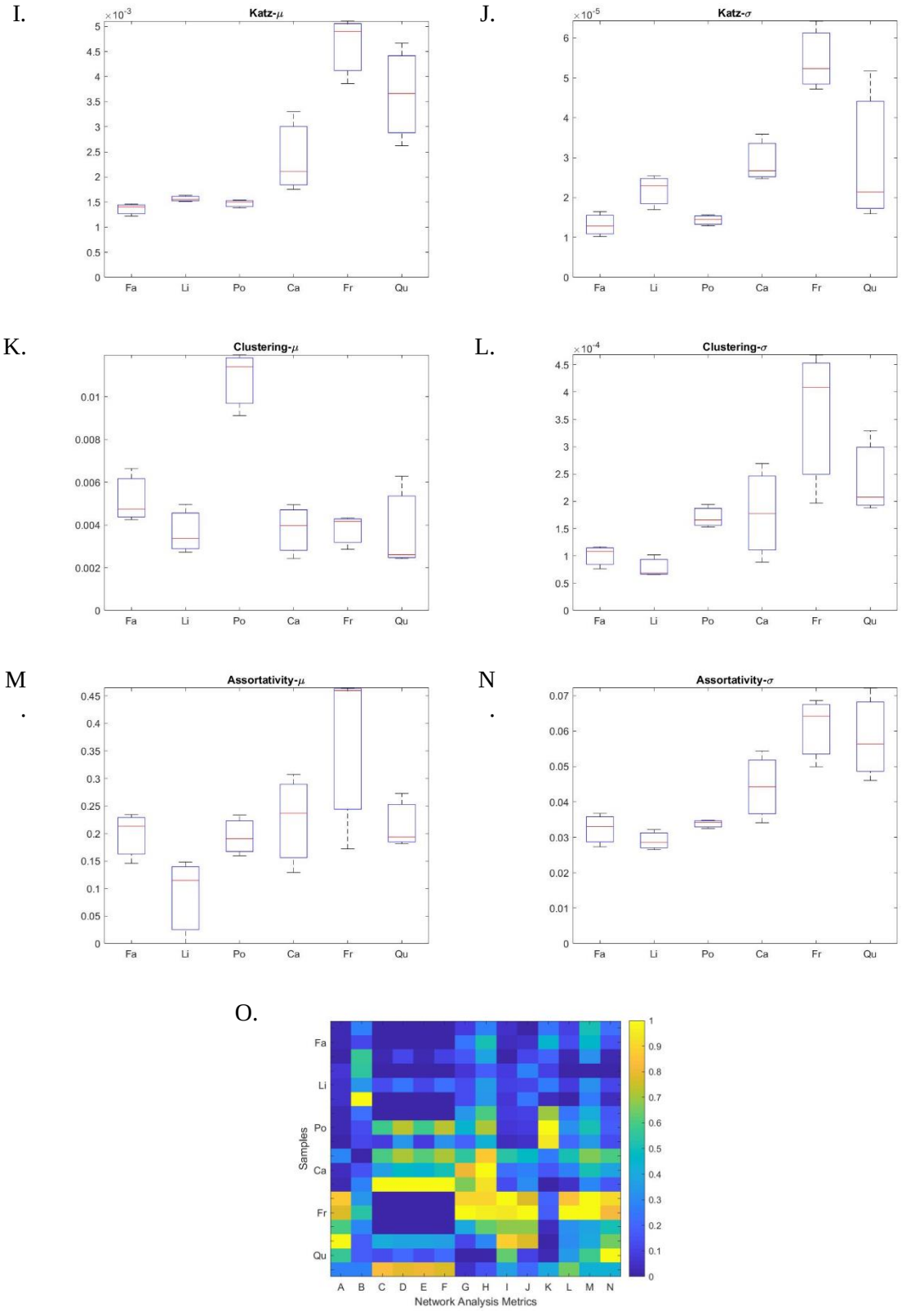

Figure 6.8. Network analysis based on the 3D segment representation.

Boxplots of fourteen network metrics (A-N) are characterizing the xylem network of *Fagus sylvatica* (Fa), *Liriodendron tulipifera* (L), *Poulus x canadensis* (P), *Carya ovata* (C), *Fraxinus pennsylvanica* (Fr), and *Quercus montana* (Q). Data are calculated based on the 3D network analysis. All matrices are combined in a heat map (O) in which each row represents a sample and each column one of the network metrics (A-N). Data in the heatmap are normalized (0-1) based on data range and the warmer color correspond to higher values.

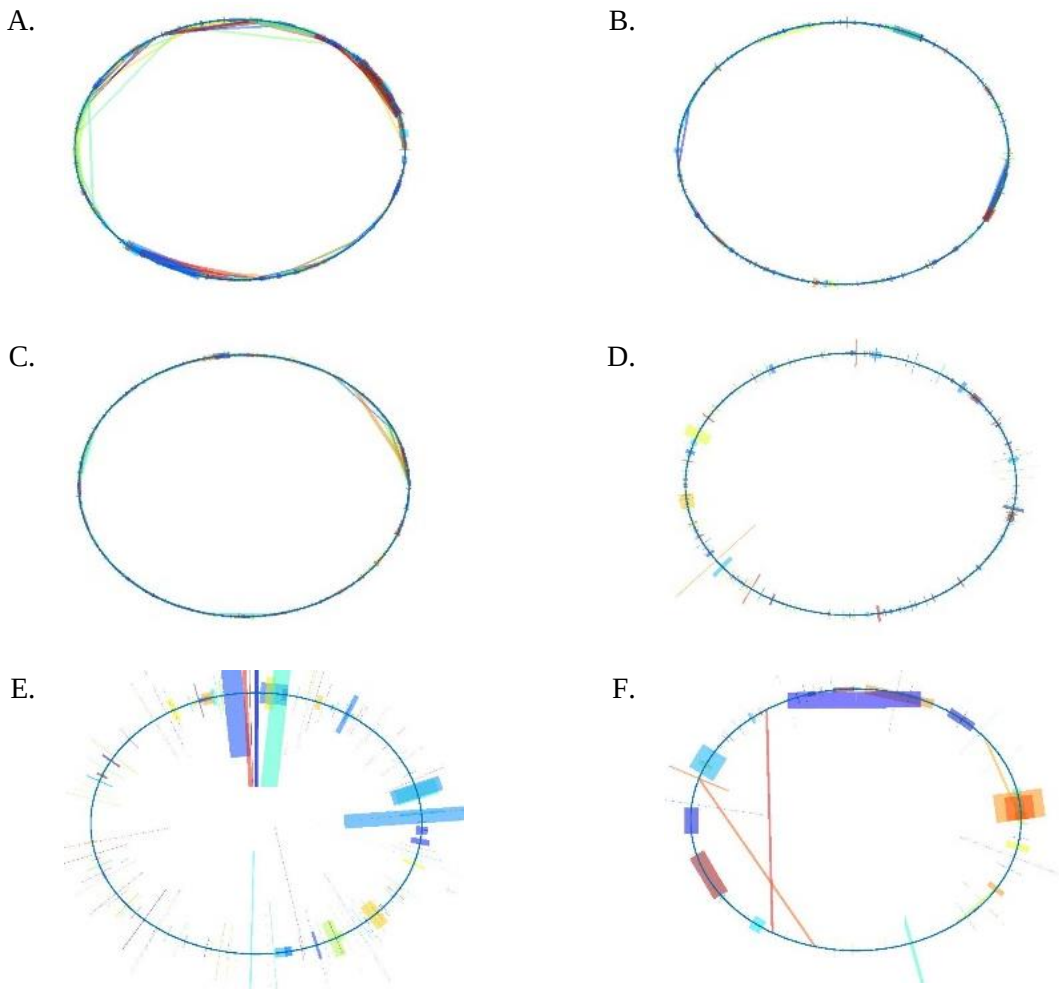

Figure 6.9. Graph illustration based on the 3D segment representation.

Network presentations of *Fagus sylvatica* (a), *Liriodendron tulipifera* (b), *Poulus x canadensis* (c), *Carya ovata* (d), *Fraxinus pennsylvanica* (e), and *Quercus montana (f)* based on 3D network analysis. One representative network per species is show. Network resentations for all replicates are in the supporting information (Figure S 6.5). All vertices are aligned along the circle perimeter and edges drawn between vertices. The edge thickness perpendicular to the circle perimeter is proportional to the sum of the length of the intervessel connections between two connected vertices.

A.

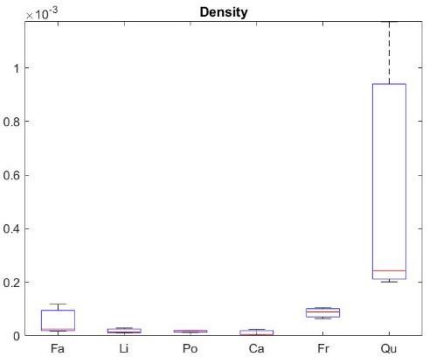
Density
×10^-3
1
0.8
0.6
0.4
0.2
0
Fa
Li
Po
Ca
Fr
Qu

B.

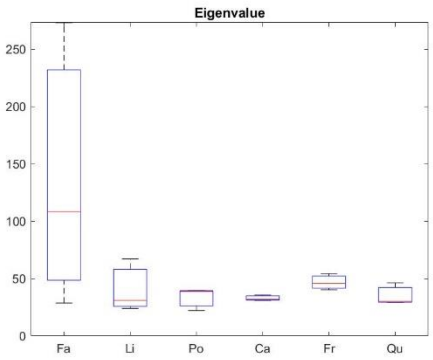
Eigenvalue
250
200
150
100
50
0
Fa
Li
Po
Ca
Fr
Qu

C.

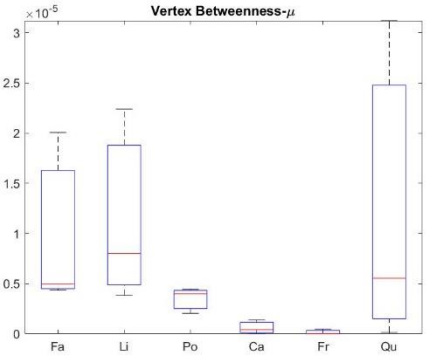
Vertex Betweenness-μ
×10^-5
3
2.5
2
1.5
1
0.5
0
Fa
Li
Po
Ca
Fr
Qu

D.

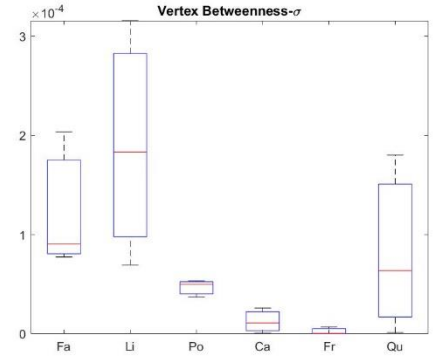
Vertex Betweenness-σ
×10^-4
3
2
1
0
Fa
Li
Po
Ca
Fr
Qu

E.

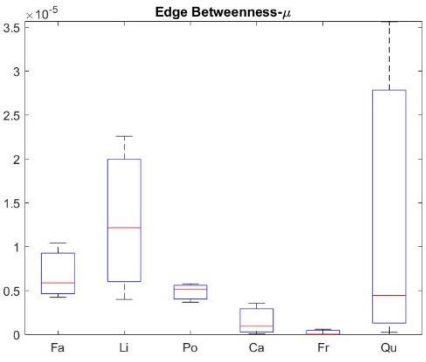
Edge Betweenness-μ
×10^-5
3.5
3
2.5
2
1.5
1
0.5
0
Fa
Li
Po
Ca
Fr
Qu

F.

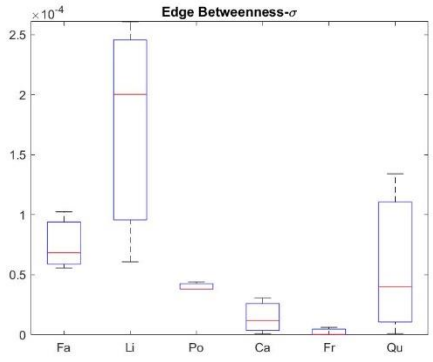
Edge Betweenness-σ
×10^-4
2.5
2
1.5
1
0.5
0
Fa
Li
Po
Ca
Fr
Qu

G.

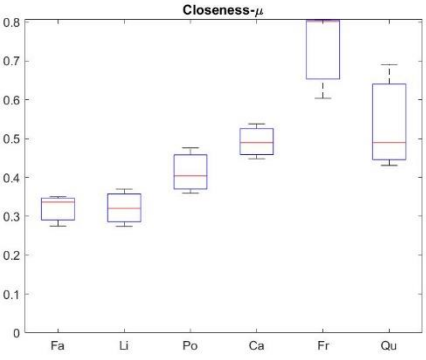
Closeness-μ
0.8
0.7
0.6
0.5
0.4
0.3
0.2
0.1
0
Fa
Li
Po
Ca
Fr
Qu

H.

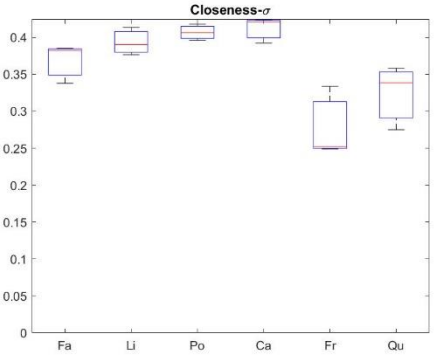
Closeness-σ
0.4
0.35
0.3
0.25
0.2
0.15
0.1
0.05
0
Fa
Li
Po
Ca
Fr
Qu

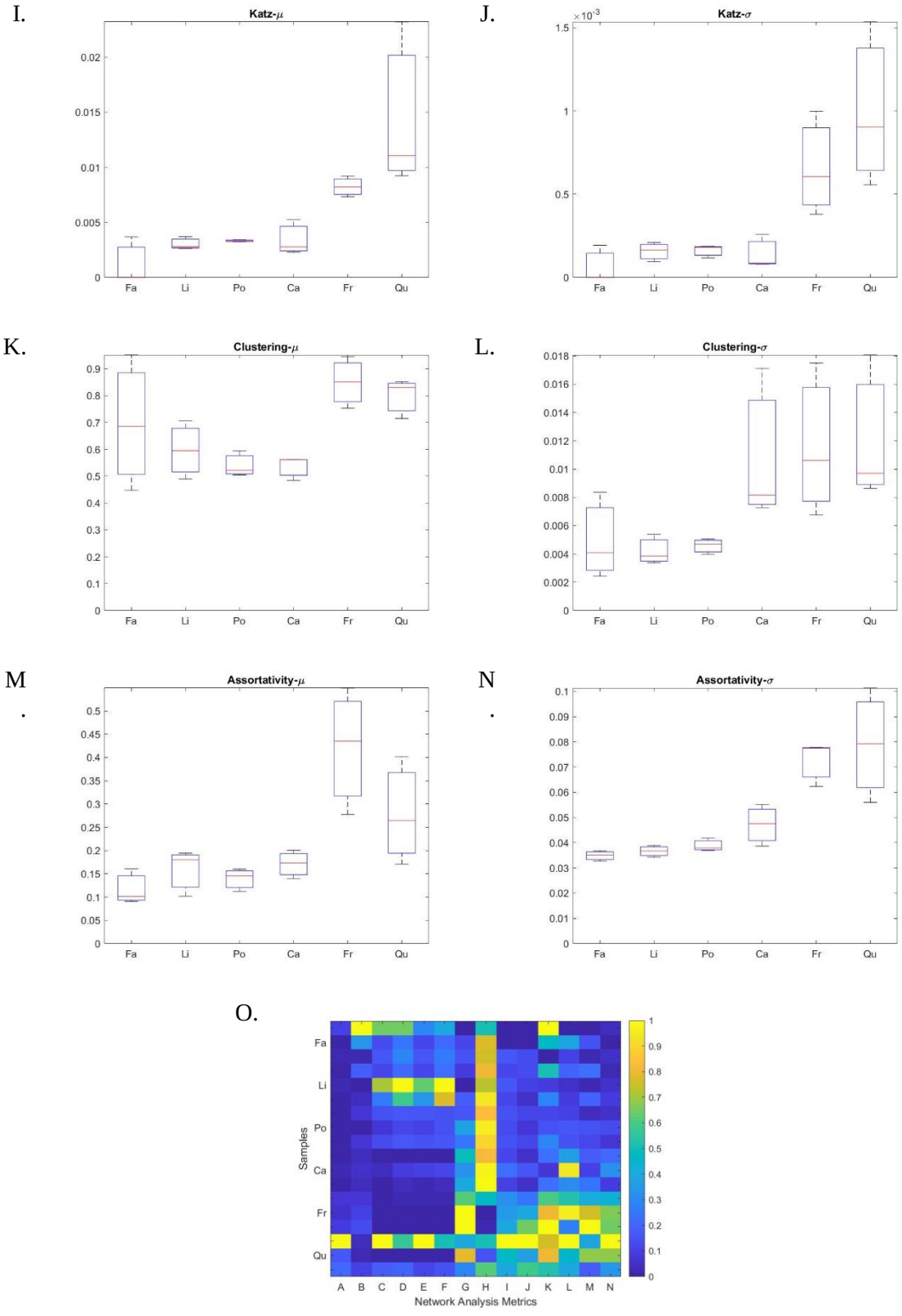

Figure 6.10. Network analysis based on the streamline segment representation.

Boxplots of fourteen network metrics (A-N) are characterizing the xylem network of *Fagus sylvatica* (Fa), *Liriodendron tulipifera* (L), *Poulus x canadensis* (P), *Carya ovata* (C), *Fraxinus pennsylvanica* (Fr), and *Quercus montana* (Q). Data are calculated based on the streamline analysis. All matrices are combined in a heat map (O) in which each row represents a sample and each column one of the network metrics (A-N). Data in the heatmap are normalized (0-1) based on the data range and the warmer color correspond to higher values.

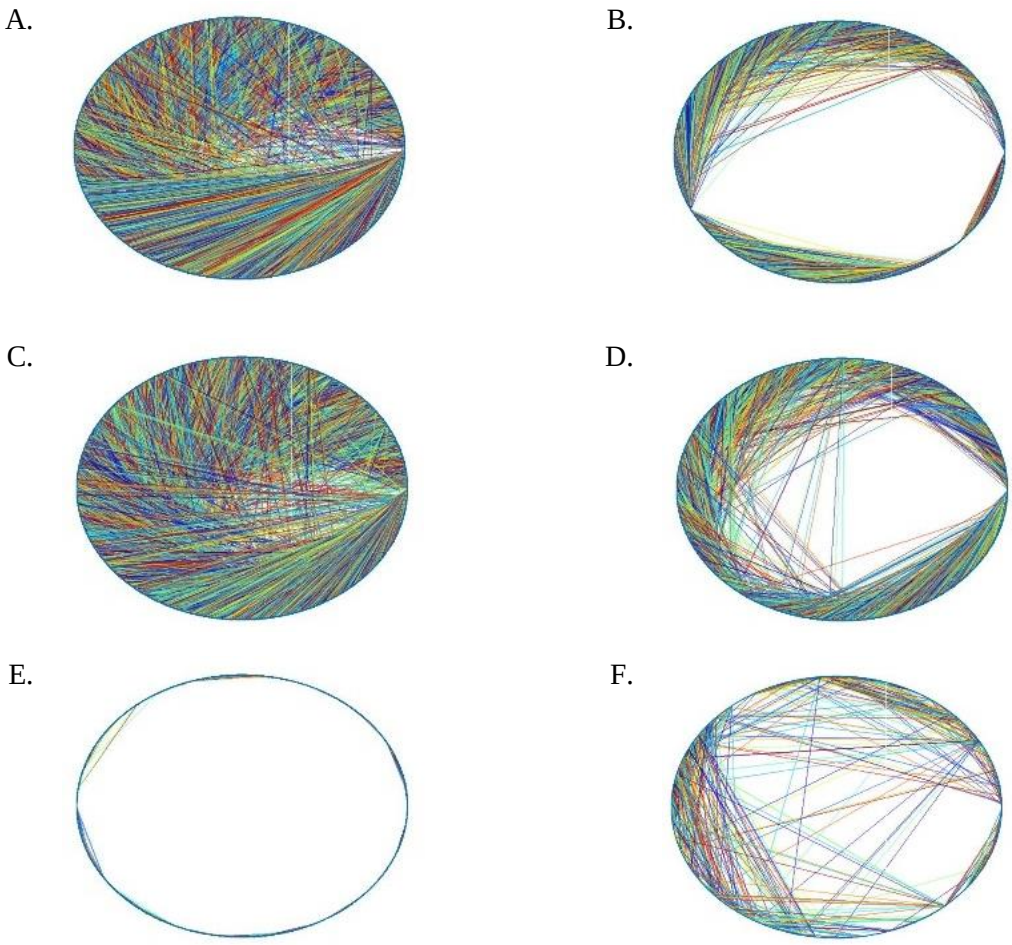

Figure 6.11. Graph illustration based on the 3D segment representation.

Network presentations of *Fagus sylvatica* (A), *Liriodendron tulipifera* (B), *Poulus x canadensis* (C), *Carya ovata* (D), *Fraxinus pennsylvanica* (E), and *Quercus montana (F)* based on the streamline analysis. One network per species is shown representative for the species. Network presentations for all replicates are in the supporting information (Figure S 6.6). All vertices are aligned along the circle perimeter and edge drawn between vertices. The edge thickness perpendicular to the circle perimeter is proportional to the total length of the connection between two connected vertices.

6.3.3 Fluid simulations and P50 comparisons

As a measure of robustness, we used computational fluid dynamics methods to simulate the flow of water through a sample at constant pressure and characterized the change in flow due to the elimination of increasing fractions of randomly selected xylem vessels (dropout). Relative conductance decreased in all networks with an increasing vessel dropout probability (Figure 6.12). The ring-porous tree species *C. ovata* and *Q. montana* showed the highest decreasing rate in relative conductance, with a 100% conductance loss at a vessel dropout rate of 2% (Figure 6.12.D & F). In contrast, the dropout probability that causes a 100% conductance loss in *F. pennsylvanica* varies between 1-90 % due to the high variability within the three replicates (Figure 6.12.E). In the diffuse porous tree species, *F. sylvatica* and *P. x canadensis* show a total conductance loss at 10% vessel dropout (Figure 6.12.A & C), while the 100% conductance loss of *L. tulipifera* varies between 10% and 38% due to the variability within the samples (Figure 6.12.B).

Empirical P50 values range from – 0.02 MPa for *F. pennsylvanica* to -2.07 MPa for *F. sylvatica* (Figure 6.14). Ring-porous tree species have higher P50 values than diffuse porous tree species, with the exception of *C. ovata* and *P. canadensis*. *C. ovata* is with a P50 value of -0.9 MPa more drought resistant than *P. canadensis* that has a P50 value of -0.69 MPa. Fitting parameter a and b are all highly significant, except fitting parameter b for *F. pennsylvanica*, indicating that a more simplistic model fit would have been sufficient for this species (Table S 6-3).

The simulated P10 and P50 values are calculated based on the decrease in relative conductance with increasing vessel dropout. Both P10 and P50 are not significantly

different between the species (Figure 6.13.A & B). Simulated mean P10 values are reached between 0.002 % and 0.005% vessel dropout (Figure 6.13.B), while simulated P50 values are reached between 0.01% and 0.04% vessel dropout probability (Figure 6.13.A). The simulated dropout rate (the exponential decay rate of dropout curves) does not differ either between tree species (Figure 6.13.C).

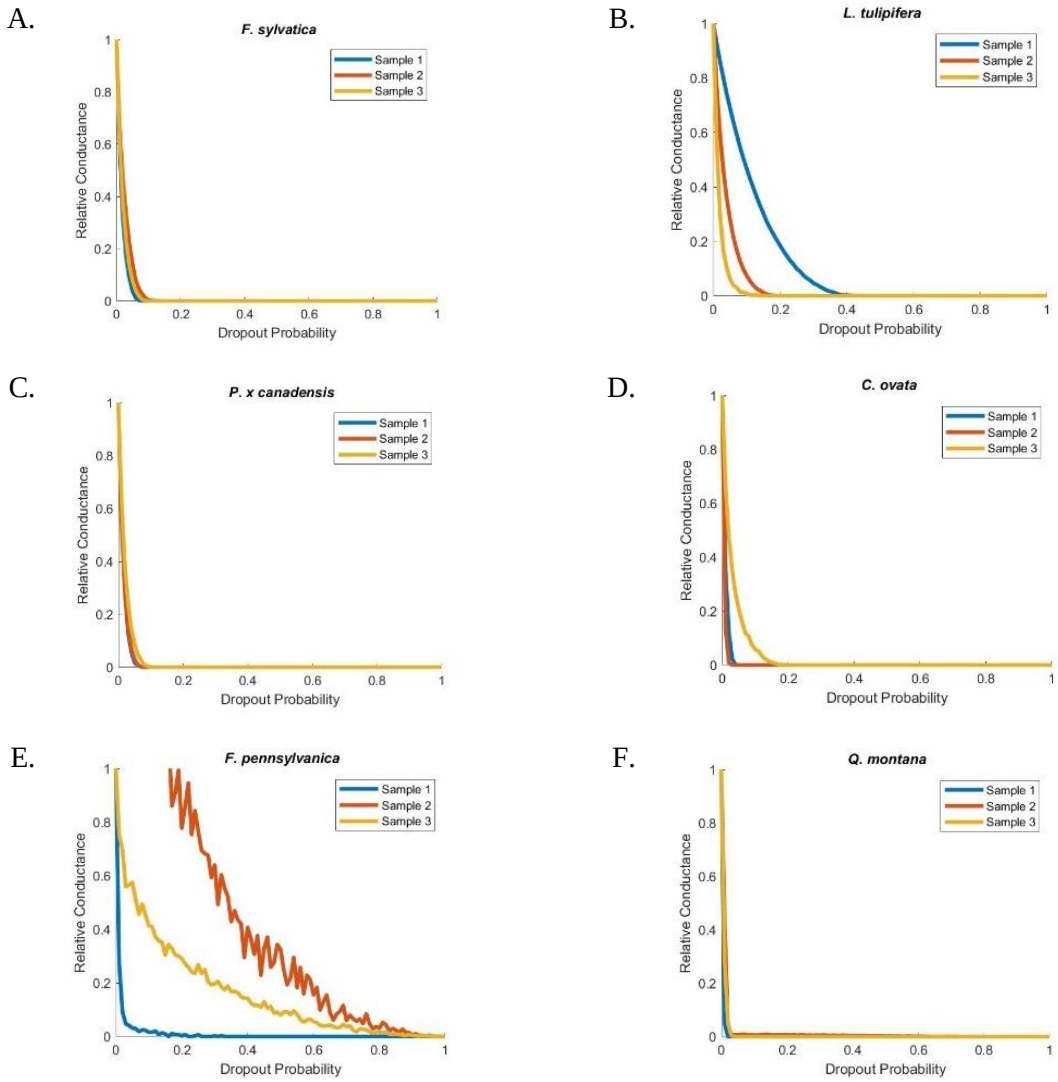

Figure 6.12. Computational fluid dynamics and embolism simulation:

Relation between relative conductance of xylem networks of *Fagus sylvatica* (A), *Liriodendron tulipifera* (B), *Poulus x canadensis* (C), *Carya ovata* (D), *Fraxinus pennsylvanica* (E), and *Quercus montana (F)* and increasing vessel dropout probability (3 replicates per species). Quercus montana sample 2 has a higher average conductance compare to based line for droput rates less than 20%.

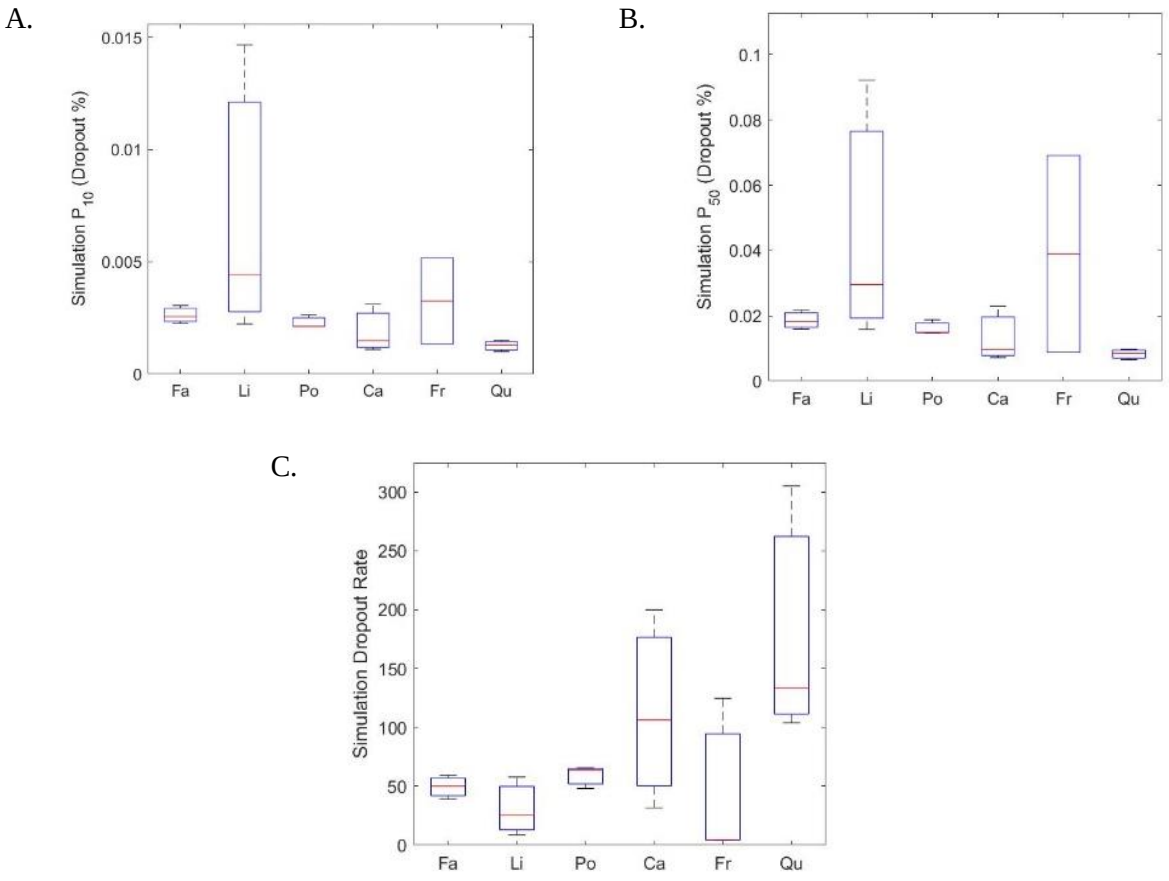

Figure 6.13. Comparison between simulations and experientially measured P50.

Relation between simulated P10 (A), P50 (B), and dropout rate (C), which is the exponetntial decay rate of dropout curves, based on embolism simulation analysis and P50 values calculate based on hydraulic conductance measurements of Fagus sylvatica, Liriodendron tulipifera, Poulus x canadensis, Carya ovata, Fraxinus pennsylvanica, and Quercus montana (three replicates per species).

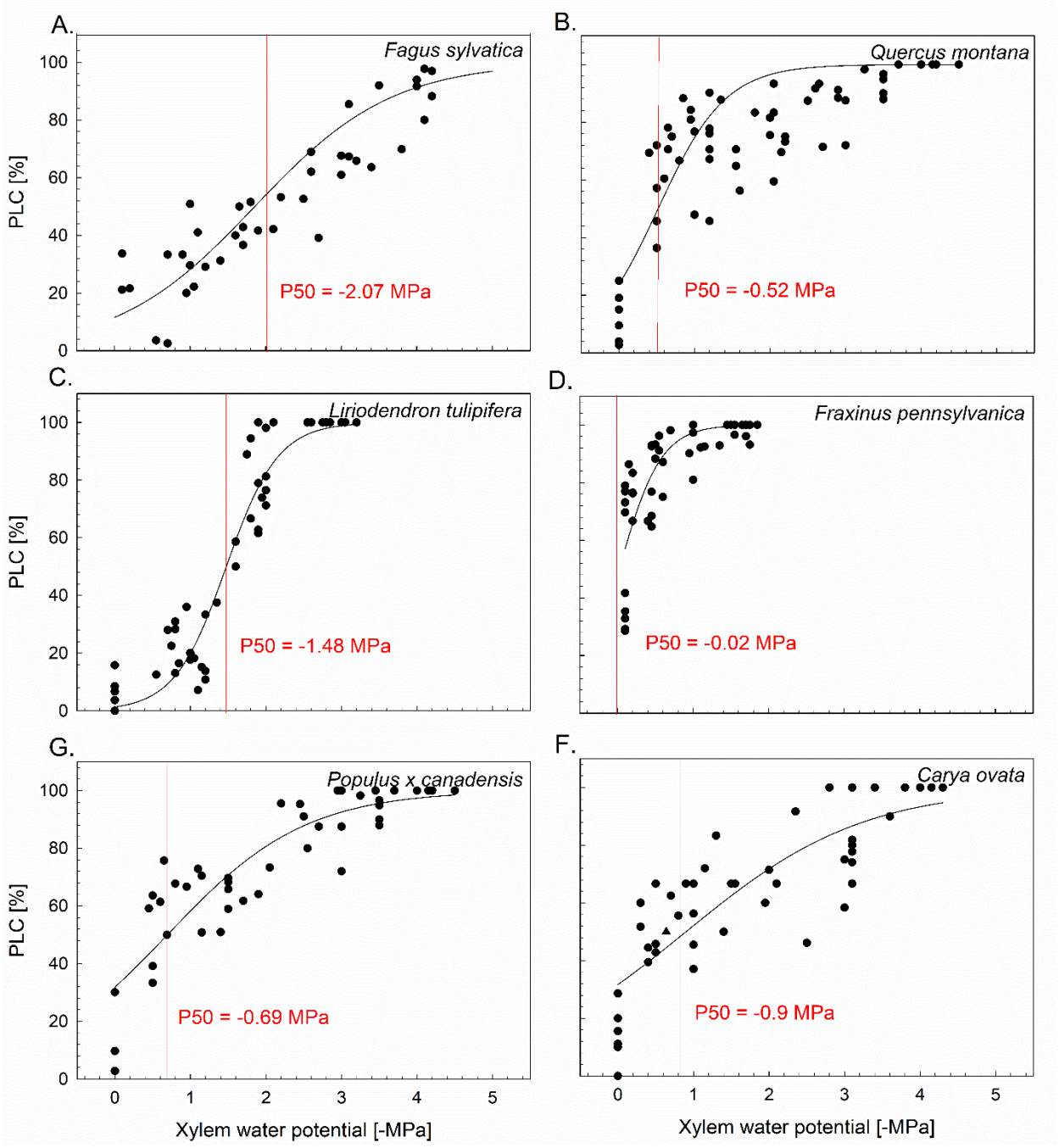

Figure 6.14. Percent loss of hydraulic conductivity (PLC).

Fitted lines were obtained by fitting the exponential sigmoidal equation PLC = 100/ (1 + exp{a[Ψ_x -b]}), to the data, where a describes the slope of the curve and b is the water potential (Ψ_x) at which PLC is reduced 50% (P50, red line) (Pammenter and Vander Willigen, 1998). Values for a, b, are given in table 3.

6.4 Discussion

3D segment analysis and streamline analysis provide two different topological analyses to characterize xylem networks (Figure 3 and 4). While 3D segmentation looks at anatomical characteristics of xylem vessels, the streamline analysis focuses on network characteristics based on potential water pathways (streamlines), which will traverse through multiple different xylem segments. For example, the 3D segment analysis revealed that F. pennsylvanica has the widest vessel diameter and the longest vessel length in this study. However, when considering anatomical characteristics on a network level, we can see that the average streamline length is 10-fold higher than the average 3D segment length. The dichotomy of these two results is important because it highlights the degree to which the factors impacting network robustness remain unknown.

In order to evaluate differences between the xylem networks, we calculated different centrality parameters based on the 3D segment analysis and the streamline analysis. The advantage of these metrics is that they are normalized, which facilitates comparison between the different xylem networks. For example, the density parameter revealed that the xylem network of *F. pennsylvanica* is relatively well connected compared to the other tree species, even though the 3D segment analysis revealed that *F. pennsylvanica* has relatively few connections between the xylem vessels.

Overall, we can see a lower variability in the standard deviation of the network metrics from the streamline analysis, making it a stronger analysis. However, the heat maps of both analyses showed that there is high variability within the samples, stressing that

more replicates are needed to make better predictions about the actual value of these matrices and reduce the variability within the tree species.

All species show an exponential decline in their relative conductance with increasing vessel dropout. Because vessel dropout was assigned randomly in the simulation, these results correspond to randomly occurring cavitation events within the pore network. However, the model does not include the effects of air embolisms propagation from air seeding, and therefore, at this time we are unable to conclude if higher connectivity leads to more embolism resistant networks or more vulnerable networks. In order to simulate air-seeding in xylem networks, we will perform a follow-up simulation in which randomly dropped vessels will also trigger the removal of all vessels in connection to this one. The lack of strong differences in the simulated P10 and P50 values, the decreasing rate of relative conductance, and the experimentally determined P50 value based on hydraulic conductance measurements might be due to the variability between samples. However, differences in experimental P50 values based on hydraulic measurements were also not observed. Nevertheless, the conductance loss of 50% (simulated P50) occurred between 0.01-0.04% dropout probability. This value seems low in comparison to other biological networks such as mouse and human cortical capillary networks in which a 50% reduction in blood flow occurred when 20% capillaries are stalled with blood flow (Cruz Hernández *et al.* 2019).

Combinations of geometrical and topological differences based on both graph representations reveal the complexity of this correlation between the xylem network characteristics and drought vulnerability. For each species, we can consider each of these characteristics as an agent, which may strengthen or weaken the tree during drought

incidents. The result is a multi-agent complex system with various stochastic processes, which determine the probability of survival at a given drought episode speculation.

In this study, we were able for the first time to produce a large data set and to reconstruct xylem networks based on actual data. Furthermore, we presented different metrics to characterize vessel and streamline topology with which we can characterize differences between xylem networks. However, to identify network metrics that are specific to ring- and diffuse porous xylem networks, we need more specific analysis, for example, the suggested air seeding dropout simulation.

6.5 Supporting information

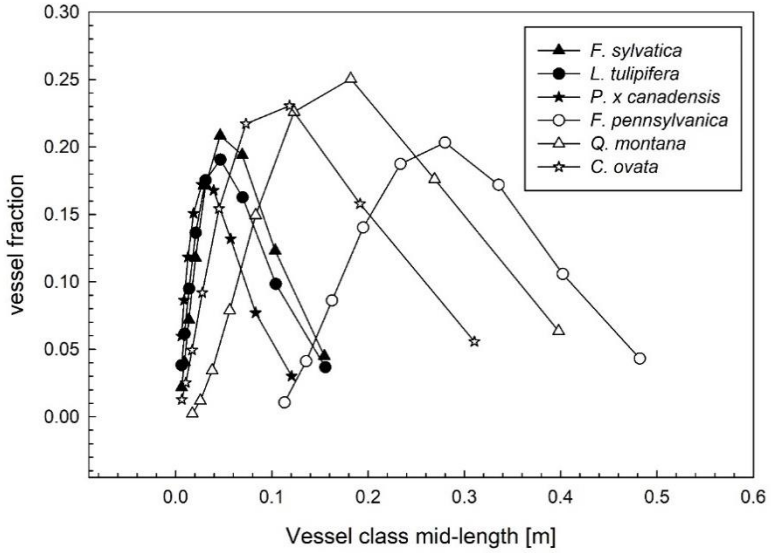

Figure S 6.1. Vessel length distribution of three diffuse porous (filled symbols) and three ring-porous (unfilled symbols) tree species.

Per species six branches were sampled and compiled before fitting vessel distribution according to Christmann et al. 2009.)

Table S 6-1. Comparisons between means of vessel diameter, vessel length, intervessel connection frequency and connection length of three ring- (*F. sylvatica, P. x canadensis, L. tuilipifera*) and three diffuse-porous tree species (*C. ovata, Q. montana, F. pennsylvanica*) based on the 3D segment analysis (ANOVA and Tukey-Kramer multi-comparison correction).

3D Segment Networks		Diameter (µm)		Length (µm)		Connection Frequency		Connection Length (µm)	
Species 1	**Species 2**	**Δµ**	**P**	**Δµ**	**P**	**Δµ**	**P**	**Δµ**	**P**
F. sylvatica	*L. tulipifera*	-0.99	0.987	-2.13	1.000	3.14E-3	0.292	-0.01	1.000
F. sylvatica	*P. x canadensis*	-0.65	0.998	16.64	0.958	-2.85E-3	0.385	-0.03	1.000
F. sylvatica	*C. ovata*	-6.54	0.014 *	20.08	0.912	6.94E-3	0.004 **	-0.26	0.996
F. sylvatica	*F. pennsylvanica*	-13.17	<.001 ***	-106.97	0.002 **	6.47E-3	0.006 **	-5.02	<.001 ***
F. sylvatica	*Q. montana*	-14.07	<.001 ***	-32.97	0.597	4.04E-3	0.112	-1.78	0.056
L. tulipifera	*P. x canadensis*	0.34	1.000	18.77	0.932	-5.99E-3	0.011 *	-0.02	1.000
L. tulipifera	*C. ovata*	-5.56	0.039 *	22.20	0.874	3.80E-3	0.147	-0.25	0.997
L. tulipifera	*F. pennsylvanica*	-12.19	<.001 ***	-104.84	0.002 **	3.32E-3	0.244	-5.01	<.001 ***
L. tulipifera	*Q. montana*	-13.09	<.001 ***	-30.84	0.658	8.99E-4	0.986	-1.76	0.058
P. x canadensis	*C. ovata*	-5.89	0.028 *	3.43	1.000	9.79E-3	<.001 ***	-0.23	0.997
P. x canadensis	*F. pennsylvanica*	-12.53	<.001 ***	-123.61	<.001 ***	9.32E-3	<.001 ***	-4.99	<.001 ***
P. x canadensis	*Q. montana*	-13.43	<.001 ***	-49.61	0.214	6.89E-3	0.004 **	-1.75	0.061
C. ovata	*F. pennsylvanica*	-6.63	0.013 *	-127.04	<.001 ***	-4.75E-4	0.999	-4.75	<.001 ***
C. ovata	*Q. montana*	-7.53	0.005 **	-53.05	0.166	-2.90E-3	0.368	-1.51	0.123
F. pennsylvanica	*Q. montana*	-0.90	0.991	73.99	0.030 *	-2.42E-3	0.545	3.24	<.001 ***

Table S 6-2. Comparisons between means of streamline diameter, streamline length, intervessel connection frequency and connection length of three ring- (*F. sylvatica, P. x canadensis, L. tuilipifera*) and three diffuse-porous tree species (*C. ovata, Q. montana, F. pennsylvanica*) based on the streamline analysis (ANOVA and Tukey-Kramer multi-comparison correction).

Streamline Networks		Diameter (µm)		Length (µm)		Connection Frequency		Connection Length (µm)	
Species 1	**Species 2**	**Δµ**	**P**	**Δµ**	**P**	**Δµ**	**P**	**Δµ**	**P**
F. sylvatica	*L. tulipifera*	-1.25	0.833	642.79	0.985	1.30E+0	0.391	275.25	0.973
F. sylvatica	*P. x canadensis*	0.42	0.998	586.31	0.990	8.26E-1	0.789	235.66	0.986
F. sylvatica	*C. ovata*	-2.74	0.169	941.26	0.929	2.30E+0	0.035 *	379.40	0.905
F. sylvatica	*F. pennsylvanica*	-9.73	<.001 ***	526.58	0.994	1.80E+0	0.127	402.89	0.882
F. sylvatica	*Q. montana*	-13.93	<.001 ***	-1885.4	0.458	-3.06E-1	0.996	-571.80	0.655
L. tulipifera	*P. x canadensis*	1.67	0.618	-56.48	1.000	-4.69E-1	0.974	-39.59	1.000
L. tulipifera	*C. ovata*	-1.49	0.717	298.47	1.000	1.01E+0	0.634	104.15	1.000
L. tulipifera	*F. pennsylvanica*	-8.48	<.001 ***	-116.2	1.000	5.01E-1	0.966	127.64	0.999
L. tulipifera	*Q. montana*	-12.68	<.001 ***	-2528.2	0.193	-1.60E+0	0.203	-847.05	0.280
P. x canadensis	*C. ovata*	-3.16	0.089	354.95	0.999	1.48E+0	0.268	143.74	0.999
P. x canadensis	*F. pennsylvanica*	-10.15	<.001 ***	-59.73	1.000	9.70E-1	0.667	167.23	0.997
P. x canadensis	*Q. montana*	-14.35	<.001 ***	-2471.7	0.210	-1.13E+0	0.523	-807.46	0.323
C. ovata	*F. pennsylvanica*	-6.99	<.001 ***	-414.68	0.998	-5.07E-1	0.965	23.49	1.000
C. ovata	*Q. montana*	-11.19	<.001 ***	-2826.6	0.122	-2.61E+0	0.016 *	-951.19	0.187
F. pennsylvanica	*Q. montana*	-4.20	0.017 *	-2411.9	0.229	-2.10E+0	0.059	-974.69	0.170

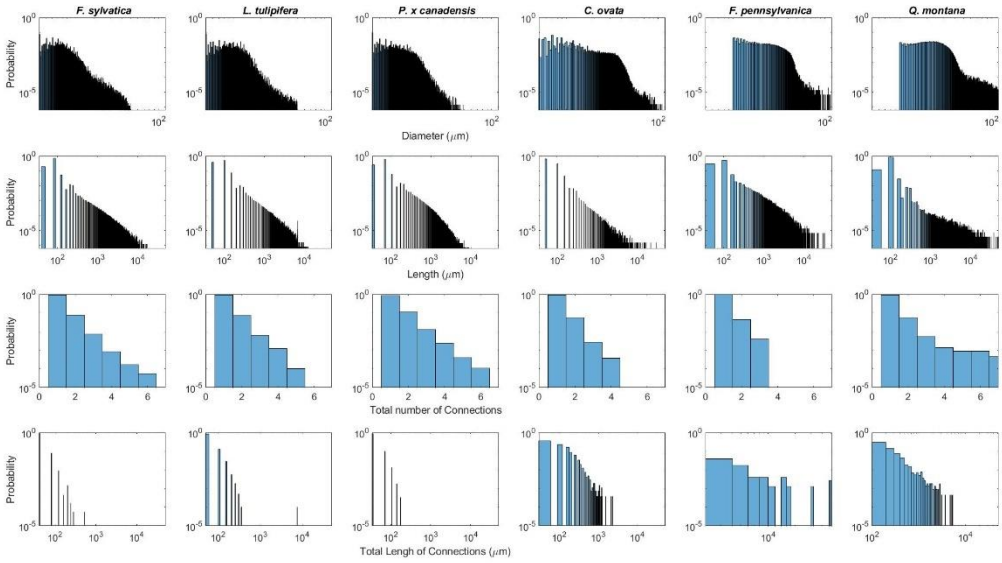

Figure S 6.2. Characteristics of xylem vessels and their connections of *Fagus sylvatica, Liriodendron tulipifera, Poulus x canadensis, Carya ovata, Fraxinus pennsylvanica,* and *Quercus montana*. Calculations are based on the 3D segment analysis. All data are represented on a log scale with the exception of the total number of connections per xylem vessel.

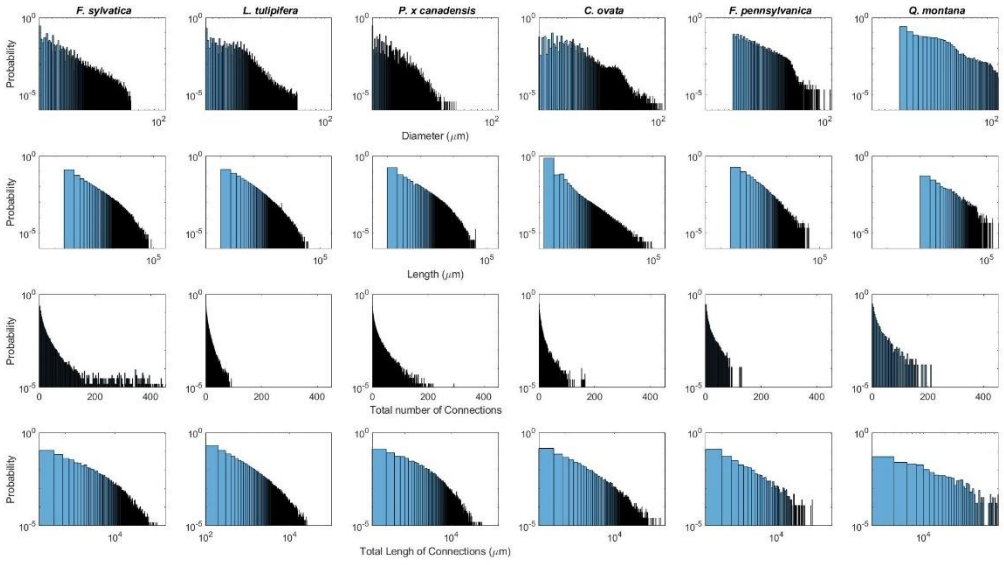

Figure S 6.3. Characteristics of xylem vessels and their connections of *Fagus sylvatica, Liriodendron tulipifera, Poulus x canadensis, Carya ovata, Fraxinus pennsylvanica,* and *Quercus montana*. Calculations are based on the streamline analysis. All data are represented on a log scale with the exception of the total number of connections per xylem vessel.

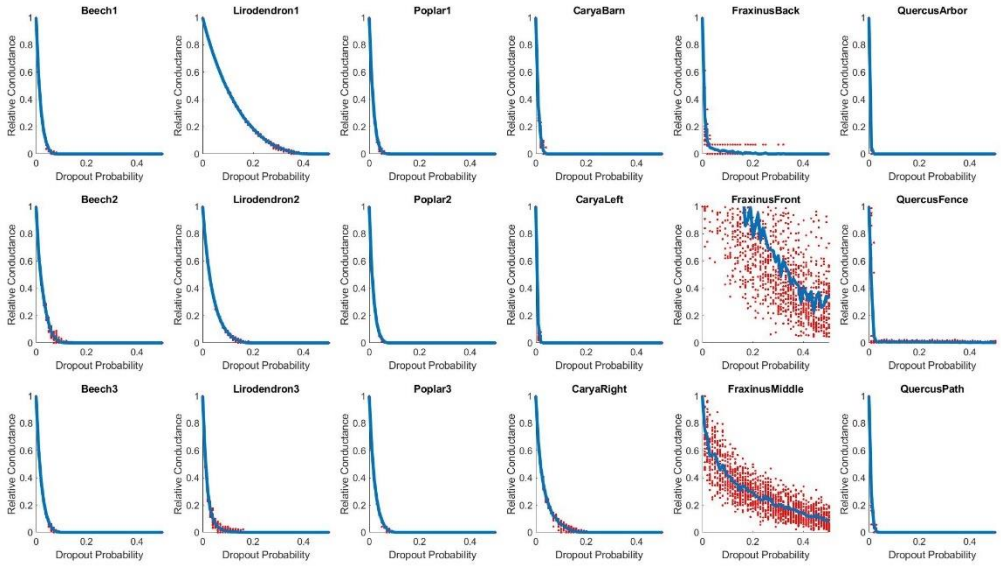

Figure S 6.4. Relation between relative conductance of xylem networks of *Fagus sylvatica* (A), *Liriodendron tulipifera* (B), *Poulus x canadensis* (C), *Carya ovata* (D), *Fraxinus pennsylvanica* (E), and *Quercus montana (F)* and increasing vessel dropout probability. Each species is represented by three individual samples (three panels).

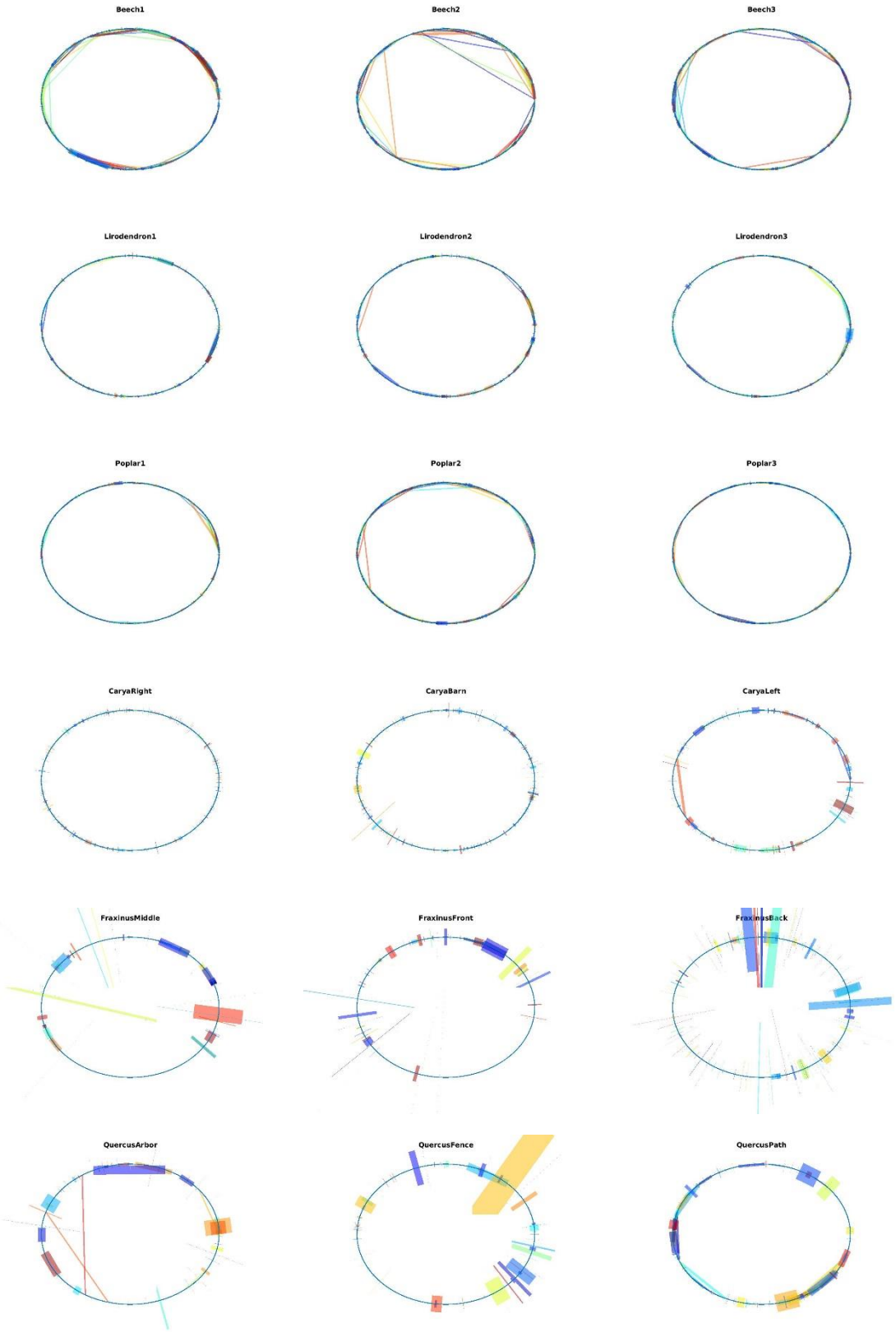

Figure S 6.5. Network presentations

of *Fagus sylvatica* (a), *Liriodendron tulipifera* (b), *Poulus x canadensis* (c), *Carya ovata* (d), *Fraxinus pennsylvanica* (e), and *Quercus montana (f)* based on 3D network analysis. Circle representation can be read as described in Methods and Results. Each species is represented by three individual samples (three panels).

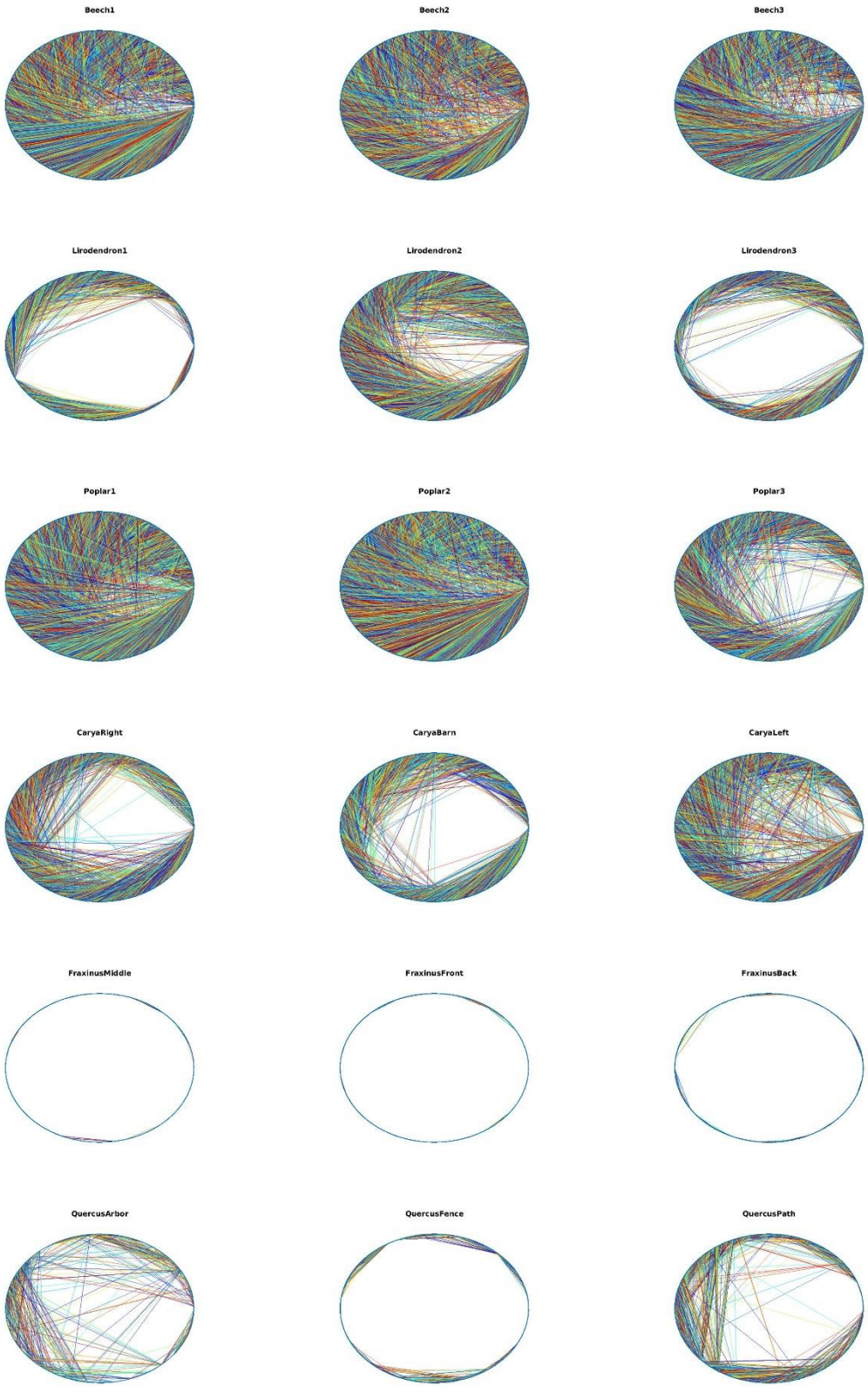

Figure S 6.6. Network presentations

of *Fagus sylvatica* (a), *Liriodendron tulipifera* (b), *Poulus x canadensis* (c), *Carya ovata* (d), *Fraxinus pennsylvanica* (e), and *Quercus montana (f)* based on streamline analysis. Circle representation can be read as described in Methods and Results. Each species is represented by three individual samples (three panels).

Table S 6-3. Values of coefficients a and b from Equation 2,
where a describes the slope of vulnerability curves presented in Figure 1 and b is the predicted water potential at which 50% loss in hydraulic conductance occur. Significant parameters are marked by asterisks (* = P<0.0001).**

Tree species	a	b
F. sylvatica	0.84***	-2.07***
L. tulipifera	2.92***	-1.47***
P. canadensis	1.07***	0.69***
Q. montana	1.13***	-0.51***
F. pennsylvanica	3.64***	-0.02
C. ovata	0.85***	-0.90***

REFERENCES

Carlquist S. (1988) Comparative wood anatomy: systematic, ecological, and evolutionary aspects of dycotyledon wood. Springer-Verlag, Berlin, Heidelberg.

Christman M. a, Sperry J.S. & Smith D.D. (2012) Rare pits, large vessels and extreme vulnerability to cavitation in a ring-porous tree species. New Phytologist 193, 713–720.

Christman M.A., Sperry J.S. & Adler F.R. (2009) Testing the "rare pit" hypothesis for xylem cavitation resistance in three species of Acer. New Phytologist 182, 664–74.

Christmann A., Weiler E.W., Steudle E. & Grill E. (2007) A hydraulic signal in root-to-shoot signalling of water shortage. The Plant Journal 52, 167–174.

Cochard H., Badel E., Herbette S., Delzon S., Choat B. & Jansen S. (2013) Methods for measuring plant vulnerability to cavitation: a critical review. Journal of Experimental Botany 64, 4779–4791.

Cruz Hernández J.C., Bracko O., Kersbergen C.J., Muse V., Haft-Javaherian M., Berg M., … Schaffer C.B. (2019) Neutrophil adhesion in brain capillaries reduces cortical blood flow and impairs memory function in Alzheimer's disease mouse models. Nature Neuroscience 22, 413–420.

Evangelidis G. & Psarakis E. (2008) Parametric image alignment using enhanced correlation coefficient maximization. IEEE Transactions on Pattern Analysis and Machine Intelligence 30, 1858–1865.

Haft-Javaherian M., Fang L., Muse V., Schaffer C.B., Nishimura N. & Sabuncu M.R. (2019) Deep convolutional neural networks for segmenting 3D in vivo multiphoton images of vasculature in Alzheimer disease mouse models. PloS one 14, e0213539.

Jacobsen A.L., Ewers F.W., Pratt R.B., Paddock III W.A. & Davis S.D. (2005) Do xylem fibers affect vessel cavitation resistance ? Plant Physiology 139, 546–556.

Jansen S., Choat B. & Pletsers A. (2009) Morphological variation of intervessel pit membranes and implications to xylem function in angiosperms. American Journal of Botany 96, 409–419.

Latora V. & Marchiori M. (2001) Efficient Behavior of Small-World Networks. Physical Review Letters 87, 3–6.

Lens F., Sperry J.S., Christman M. a, Choat B., Rabaey D. & Jansen S. (2011) Testing hypotheses that link wood anatomy to cavitation resistance and hydraulic conductivity in the genus Acer. New Phytologist 190, 709–723.

Maherali H., Pockman W. & Jackson R.B. (2004) Adaptive variation in the vulnerability of woody plants to xylem cavitation. Ecology 85, 2184–2199.

Melcher P.J., Michele Holbrook N., Burns M.J., Zwieniecki M.A., Cobb A.R., Brodribb T.J., … Sack L. (2012) Measurements of stem xylem hydraulic conductivity in the laboratory and field. Methods in Ecology and Evolution 3, 685–694.

Northeast Regional Climate Center (2019) NRCC The Ithaca Climate Page.

Otsu N. (1979) A threshold selection method from gray-level histograms. IEEE Tansactions on Systems, Man, and Cybernetics 9, 62–66.

Pammenter N.W. & Van der Willigen C. (1998) A mathematical and statistical analysis of the curves illustrating vulnerability of xylem to cavitation. Tree Physiology 18, 589–593.

Psarakis E. & Evangelidis G. (2005) An enhanced correlation-based method for stereo correspondence with sub-pixel accuracy. In Computer Vision, 2005. ICCV 2005. Tenth IEEE International Conference on. pp. 907–912. IEEE, Beijing, China.

Rueden C.T., Schindelin J., Hiner M.C., DeZonia B.E., Walter A.E., Arena E.T. & Eliceiri K.W. (2017) ImageJ2: ImageJ for the next generation of scientific image data. BMC Bioinformatics 18, 1–26.

Sperry J.S., Donnelly J.R. & Tyree M.T. (1988) Seasonal occurrence of xylem embolism in sugar maple (Acer saccharum). American Journal of Botany 75, 1212–1218.

Sperry J.S. & Hacke U.G. (2004) Analysis of circular bordered pit function I. Angiosperm vessels with homogenous pit membranes. American Journal of Botany 91, 369–385.

Sperry J.S., Hacke U.G. & Wheeler J.K. (2005) Comparative analysis of end wall resistivity in xylem conduits. Plant, Cell and Environment 28, 456–465.

Tyree M.T. & Dixon M.A. (1986) Water stress induced cavitation and embolism in some woody plants. Physiologia Plantarum 66, 397–405.

Venturas M.D., Sperry J.S. & Hacke U.G. (2017) Plant xylem hydraulics: what we understand, current research, and future challenges. Journal of Integrative Plant Biology 59, 356–389.

Wang Z., Bovik A.C., Sheikh H.R. & Simoncelli E.P. (2004) Image quality assessment: from error visibility to structural similarity. IEEE Transactions on Image Processing 13, 600–612.

Watts D. & Strogatz S. (1998) Collective dynamics of networks. Nature 393, 440–442.

Wheeler J.K., Sperry J.S., Hacke U.G. & Hoang N. (2005) Inter-vessel pitting and cavitation in woody Rosaceae and other vesselled plants: a basis for a safety versus efficiency trade-off in xylem transport. Plant, Cell and Environment 28, 800–812.

Zanne a. E., Sweeney K., Sharma M. & Orians C.M. (2006) Patterns and consequences of differential vascular sectoriality in 18 temperate tree and shrub species. Functional Ecology 20, 200–206.

Zimmermann M.H. (1983) Xylem structure and the ascent of sap. Springer Verlag, New York.

CHAPTER 7

CONCLUSIONS AND FUTURE DIRECTIONS

Quantitative analysis of various biomedical data modalities such as images is an essential part of the research and medical settings. This dissertation focused on image processing and network analysis of brain vasculature network. Many image analysis tasks such as segmentation and object identifications are bottlenecks of biomedical research progress and medical diagnosis throughputs. The applicability and effectiveness of the developed techniques were demonstrated in studies focused on Alzheimer's disease using mouse models of the disease. Alzheimer's disease is the sixth leading cause of death in the US, and it kills more than breast and prostate cancer combined. Moreover, Alzheimer's is the only leading cause of death increasing every year. Therefore, investigation of Alzheimer's is indispensable.

Chapter 2 is a review of the recent advancement in vessel segmentation and centerline extraction. There are different categories of image segmentation methods with different pros and cons that allow the researchers and practitioner to choose based on the target application. The details of vascular segmentation of different organs and vessel segments in health and disease states were discussed as well.

In Chapter 3, DeepVess, a deep convolutional neural network solution for fast and fully automated segmentation of brain vasculature and centerline extraction was discussed. I developed new open-source algorithms and software packages using machine learning and complex network analysis to compare and describe different vascular networks and to study the interactions between brain blood flow and diseases using the properties of

vascular networks extracted from mouse models. The resulting software, DeepVess, allows researchers to extract vascular networks with unprecedented speed, finally enabling various geometrical and topological measurements in large volumes across many samples. These data are critical for next level analysis such as computational fluid dynamics and network analysis. DeepVess can be applied to other organs and imaging modalities with minimal interventions or fine-tuning. There is still room for improvement in obtaining the vessel centerlines directly form algorithms instead of as the byproduct of the segmentation results.

Chapter 4 describes the discovery of the high incidents of stalling capillaries in mouse models of Alzheimer's disease due to the adhesion of the leukocyte. I developed different analysis and image analysis methods for this paper including vessel and amyloid-beta plaques detection, segmentation, and quantification in terms of topological and geometrical measurements. DeepVess was used in one section of this study as well. The downstream mechanism of the leukocyte adhesion in stalled capillaries still is unknown and required further investigation.

In Chapter 5, our crowdsourcing citizen science project called StallCatchers was described. This project was developed to facilitate the stalled capillary detection task with the power of citizen science. I was involved in the development of the image processing pipeline for this project and investigation of crowd response aggregation methods. This project utilized DeepVess as well, and it has more than fifteen thousand users at this time. Next steps include the improvement of methods to aggregate the crowd response and the addition of methods for the smart distributions of tasks based on the user experiences.

In Chapter 6, we tested the application of DeepVess on a very different vasculature network than mouse brain vasculature. We studied big datasets of images of xylem networks from six different tree species from two categories of trees. In addition to use of the DeepVess, computationally efficient preprocessing methods required for big data and efficient network analysis metrics were developed. Furthermore, various network representations were introduced to facilitate studying these xylem networks from different points of views. Finally, a computational fluid dynamic simulation was conducted to study the vulnerability of these trees to drought events and embolism incidents. This study paves the road for further investigation for more extensive experimental data and other species.